UNIVERSITAT DE BARCELONA

Design of novel compositionally controlled hybrid and ternary nanostructures

Mariona Dalmases Solé

DESIGN OF NOVEL COMPOSITIONALLY CONTROLLED HYBRID AND TERNARY NANOSTRUCTURES

Mariona Dalmases Solé

UNIVERSITAT DE BARCELONA

Programa de Doctorat en Nanociències

Design of novel compositionally controlled hybrid and ternary nanostructures

Mariona Dalmases Solé

Tesi presentada per optar al títol de Doctor per la Universitat de Barcelona

Director: Dr. Albert Figuerola Silvestre

Tutor: Dr. Guillem Aromí Bedmar

Departament de Química Inorgànica i Orgànica: Secció de Química Inorgànica

Institut de Nanociència i Nanotecnologia

INSTITUT DE NANOCIÈNCIA I NANOTECNOLOGIA

UNIVERSITAT DE BARCELONA

Contents

Agraïments

Aquesta tesi que teniu a les mans és un recull de tota la feina que he estat fent els últims 5 anys. Com la majoria de coses, ha estat una mescla de moments bons i dolents: motivació, treball, aprenentatge, satisfacció i una mica d'estrès (sobretot al final). No ha estat un camí fàcil però, per sort, no l'he fet tota sola. I ara que ja estic al final, ha arribat el moment d'agraïr a totes les persones que ho han fet possible.

En primer lloc, i un dels més importants, al meu director de tesi. Moltes gràcies Albert per donar-me la oportunitat de poder ser la teva primera estudiant de doctorat, per totes les reunions, presentacions, planificacions d'experiments, discussions de resultats, congressos... Seguint el teu exemple, he après com ser una bona científica. Encara recordo el primer dia que vaig entrar al teu despatx, quan encara era una estudiant de la carrera a punt per començar el TFG. En aquell moment no tenia clar que volia fer a continuació, però els teus ensenyaments, la teva paciència i, sobretot, la teva dedicació i motivació, em van obrir la porta al món de la recerca i la nanociència i em van encaminar cap a aquest moment. També vull agrair-te el suport i la confiança que m'has donat durant tot aquest temps, ha ajudat a que aquesta tesi hagi arribat a bon port.

A la Lidia, per ser la meva companya de laboratori, però sobretot, per convertir-te en la meva amiga, per compartir amb mi els bons i els mals moments i (el que és més important) les galetes. Han sigut moltes hores juntes (et veia més a tu que a la meva família!) i moltes experiències. És molt difícil plasmar aquí tot el que hem viscut, però et puc dir que del nostre laboratori, a part de tota la recerca, m'enduc una capsa plena de records inoblidables (la nostra paret de la fama ho demostra) i alguna que altra rascada (les teves xancletes no passaran mai a l'oblit).

Al Raul i la Rosa perquè tot i que a vegades se'ls hi envà la pinça, són els millors! No hagués estat el mateix sense vosaltres.

A tots els membres del grup GMMF (Guillem, Carolina, Leo, Vero, David, Jorge, Ivana, Mohanad, Marta, Carlos), sempre m'he sentit part d'aquesta gran família. Ha estat un plaer poder compartir laboratoris, group meetings, calçotades, excursions... amb tots vosaltres.

A tots els estudiants amb qui he compartit laboratori (Adri, Eugènia, Martí, Joan, Lluís, Joaquín, Andrés, Saul, Samira, Albert, Azar, Guillem, Mengxi), de tots i cadascun de vosaltres he après alguna cosa i heu fet que l'ambient al laboratori fos sempre divertit. I especialment a la Mariona, perquè no només compartim el nom, sinó moltes més coses!

Al Guillem, la Berta, l'Albert, la Laia, la Beltzane, l'Arnald i tota la gent del departament/secció, gràcies per tots els moments viscuts, ja sigui a dins o fora de la universitat.

A la Eli i la Laura, per tots els moments compartits amb el DAPTA, va ser una gran oportunitat per conèixer la recerca del vostre grup i fer un gran treball en equip. Al Fran, simplement per les grans converses (a vegades sense sentit) que hem tingut i sobretot, per tot el suport que m'has donat, especialment, ara al final (un cafè que val or!).

A l'Andrea, per un dels congressos més divertits, i pels experiments més simples i alhora més complicats de la història. També pels "petits" *breaks* d'una hora, als quals més, tard també s'hi van unir l'Àlex i l'Ari. La nostra estada a l'Alba va ser un punt d'unió entre nosaltres, que espero que puguem mantenir.

To Dr. Andrea Falqui for giving me the great opportunity of doing a stay in his group in KAUST. Also to Sergio, Efisio and Alberto, for making me feel like home. And to Clara, for being the best housemate and for all the amazing moments we lived in Saudi Arabia.

Als microscopistes, el Pau, la Sònia i la Paqui, per veure i "fotografiar" sempre el costat bo de les meves nanopartícules. I al Víctor, per ajudar-me sempre, tant als meus inicis en la recerca, com durant una etapa d'aquesta tesi.

A la Maria, de DRX, per la seva gran professionalitat i paciència i sobretot, per tenir sempre un somriure quan hi anava.

Als meus companys de "taula", l'Stuart, l'Ari, la Marina, la Roser, l'Héctor i tota la resta, perquè els dinars, si són amb bona compayia, són més deliciosos. I al Manel, perquè tot i que només pugés de tant en tant, sempre ha sigut un més.

Al Javi i l'Alejandro, que ara fa 5 anys vam emprendre aquest viatge junts, perquè, tot i estar a orgànica, sempre ens hem entès i perquè, vulgui reconèixer-ho o no, en el fons, m'agraden els acudits dolents (les referències als Simpson ja no eh! No ens passem tampoc).

A la Raquel, l'Ari i la Tania, per tenir el super poder Topcuqui de saber sempre el que necessito. Encara que no hi estiguin escrites, les nostres quedades també formen part d'aquesta tesi. Al Xevi, que és una més de nosaltres! No sé si hauria sobreviscut a tant de drama sense les teves brometes! I a la resta dels meus amics de la universitat, el Miki, la Marta, la Patri, la Cristina i l'Àngels, perquè, tot i que no ens veiem gaire sovint, sempre heu estat al meu costat.

A la Gemma, l'Anna, la Laura, el Marc i el Gabri, per ser-hi sempre, per fer-me costat en totes les etapes de la meva vida, incloent aquesta. Perquè tot i que, probablement, moltes vegades no enteníeu de que anava la cosa, sempre m'heu escoltat i m'heu animat.

Als meus companys de cotxe, per aguantar tots els meus monòlegs! Sempre és un plaer viatjar amb vosaltres.

To my new friends from ICFO, for all the support you gave me these last months.

A la meva, família perquè sense ells no hauria arribat tant lluny. Especialment als meus germans, el Josep i el Joan, perquè encara que no ho noteu, la vostra aprovació i suport són molt importants per mi. Aviam si després de llegir-vos detingudament aquesta tesi, us acabeu creient (d'una vegada per totes) que treballo! I als meus pares, perquè tot i que no entenguin la meitat del que faig, mai han deixat de creure en mi i sé que passi el que passi, m'estimaran sempre.

Finalment, m'agradaria dedicar aquesta tesi als meus avis, que sempre han estat un referent per mi i que des de ben petita m'han ensenyat a apreciar el valor de la superació i la feina ben feta. Tot i que alguns d'ells ja no estan aquí, sé que sempre m'acompanyen. Iaia, avi, padrí, àvia Teresina, espero que estigueu orgullosos de mi.

Resum de la tesi

En els últims anys, els materials nanoestructurats han atret l'atenció en diversos camps, com ara l'emmagatzematge d'energia, l'optoelectrònica o la biomedicina, gràcies a les seves propietats físiques i químiques dependents de la mida/forma. Tot i que els semiconductors binaris han estat uns dels més estudiats fins ara, els semiconductors ternaris i quaternaris han començat a sorgir gràcies al gran ventall de composicions i, per tant, de propietats que ofereixen. La importància dels nanomaterials híbrids està creixent també. L'associació de més d'un material en una mateixa nanoestructura permet la preservació o, fins i tot la millora, de les diferents propietats que presenten els seus materials preliminars i les combina amb les noves, originades degut a la interacció entre els dos dominis.

Aquesta tesis està centrada en el disseny de noves nanoestructures ternàries i híbrides i està dividida en cinc capítols en funció dels diferents sistemes que s'han estat estudiant.

En els dos primers capítols (capítols 2 i 3) s'ha descrit un procediment simple a temperatura ambient per la síntesi de nanoestructures ternàries i híbrides d'Ag-Au-Se i d'Ag-Au-S. El mètode consisteix en la reacció entre nanopartícules d'Ag_2Se i Ag_2S sintetitzades prèviament i un precursor d'Au(III). El temps de reacció, la concentració del precursor d'or, la naturalesa del tensioactiu i la relació Ag:Au són els quatre paràmetres clau que permeten el control del producte final. Una caracterització estructural i química exhaustiva de les nanoestructures descrites en aquests capítols s'ha dut a terme per HRTEM, STEM, EELS, EDS i XPS. A partir d'aquesta caracterització s'ha pogut proposar un mecanisme de reacció segons el qual dos processos poden tenir lloc paral·lelament. Per un costat, quan una amina (dodecilamina, DDA) s'utilitza com a tensioactiu, aquesta redueix l'Au(III) a or metàl·lic, el qual es diposita a la superfície del semiconductor, formant un segon domini. Per l'altre, s'ha observat que l'anió Se^{-2}/S^{-2} és capaç de reduir l'Au(III) a Au(I), que seguidament difon dins de l'estructura del semiconductor binari, substituint parcialment els cations Ag(I) i formant un material ternari.

En el sistema Ag-Au-Se, nanopartícules (NPs) híbrides d'Au-Ag_2Se, NPs híbrides d'Au-Ag_3AuSe_2 i NPs d'Ag_3AuSe_2 han estat sintetitzades amb èxit. Quan s'utilitza un tensioactiu sense propietats reductores (bromur de tetraoctilamoni, TOAB) és possible suprimir el procés de reducció a or metàl·lic i obtenir NPs d'Ag_3AuSe_2. Mentre que, quan s'utilitza l'amina i un temps de reacció curt, la formació del material ternari es pot suprimir i obtenir les NPs híbrides d'Au-Ag_2Se.

Les NPs híbrides d'Au-Ag_3AuSe_2 van ser estudiades com a materials termoelèctrics, obtenint una resposta millorada en comparació amb el material binari (Ag_2Se). Les NPs d'Ag_3AuSe_2

van ser analitzades com a agent de contrast per tomografia computada, donant resultats prometedors en aquest camp.

En el sistema anàleg amb sofre (Ag-Au-S), la miscibilitat més alta entre l'or i el sofre ofereix un diagrama ternari més complex, que presenta dos materials ternaris amb diferent estequiometria: Ag_3AuS_2 i AgAuS. Mitjançant el mètode proposat, és factible la transformació gradual del Ag_2S a Au_2S, amb la possibilitat d'aïllar NPs híbrides d'Au-Ag_2S, NPs híbrides d'Au-Ag_3AuS_2, NPs híbrides d'Au-AgAuS, NPs híbrides d'Au-Au_2S i NPs foradades d'Au_2S. En aquest sistema, la supressió de la reducció de l'Au(III) a or metàl·lic no és possible utilitzant el tensioactiu sense propietats reductores, i tots els materials obtinguts presenten dos dominis, exceptuant les NPs foradades d'Au_2S. Quan es treballa amb una alta quantitat de complex Au(III)-TOAB, l'elevada concentració d'anions bromur a la dissolució pot desencadenar un augment de la velocitat de difusió dels cations Ag(I) cap a l'exterior de les NPs, provocant la formació de forats interns en les nanoestructures, seguint el que es coneix com a efecte Kirkendall.

La tercera secció (capítol 4) està centrada en un altre sistema ternari, format per Ag-Cu-S. Aquest sistema també presenta dues fases ternàries (Ag_3CuS_2 i AgCuS), tanmateix, el mètode d'injecció en calent proposat en aquesta tesi, només permet la formació del material amb estequiometria AgCuS. Depenent del precursor de coure utilitzat, es proposen dos mecanismes de síntesi diferents. Per un costat, l'ús dels clorurs de coure (I) i (II) indueixen la formació inicial de nanopartícules de Ag_2S, que gradualment pateixen intercanvi catiònic, donant lloc al material ternari. Per l'altre, quan s'utilitza el iodur de coure (I), es formen simultàniament els dos sulfurs binaris, que seguidament es combinen per formar el ternari. Aquest material també va ser caracteritzat termoelèctricament, tot i que no mostra resultats satisfactoris degut a la seva baixa conductivitat elèctrica.

En el capítol 5 es presenten quatre nanoestructures noves basades en Cu, Pt i Se. Aquestes nanoestructures van ser sintetitzades mitjançant una reacció a alta temperatura entre NPs de $Cu_{2-x}Se$ sintetitzades prèviament i un precursor de Pt(II). Els nanomaterials han estat detingudament caracteritzats estructural i morfològicament per estudiar l'impacte de la relació Pt:Cu utilitzada en la síntesi en el producte final. Els tres primers materials (amb quantitats més baixes de platí) presenten fases ternàries, mentre que l'últim (amb més quantitat de platí) està format només pels dos metalls (Pt i Cu). A mesura que la quantitat de platí augmenta en l'estructura, aquest es va introduint més eficientment en la xarxa cristal·lina del semiconductor de coure i seleni, expulsant gradual i lentament el seleni fins a la totalitat, augmentant així el caràcter metàl·lic de les nanoestructures finals.

Finalment, en el capítol 6, es descriuen uns compostos híbrids hidrofílics, formats a partir de NPs inorgàniques (Au, Ag, Ag_3AuSe_2 i Au@Fe_3O_4) i un complex d'Au(I) de baix pes molecular i altament fluorescent. Aquests nanocompostos es poden dispersar en dissolvents polars com l'aigua o l'etanol, i són estables durant un any, com a mínim, a diverses temperatures

dins el rang de 25 a 50ºC i entre pHs de 4 i 9. El seu acoblament està basat, essencialment, en interaccions aurofíliques/metal·lofíques entre els àtoms de la superfície de la nanopartícula i els àtoms d'Au(I) del complex. Aquestes interaccions formen petits agregats de nanopartícules embolcallades pel complex. La formació dels agregats s'ha estudiat per espectroscòpia d'absorció, seguint la variació de la banda de ressonància plasmònica localitzada, molt característica de les NPs d'or en dissolució. Addicionalment, els nanocompostos d'Au i Ag es van caracteritzar per espectroscòpia Raman. És ben sabut que quan una molècula està estretament lligada amb una nanopartícula amb propietats plasmòniques, la intensitat dels pics obtinguts per espectroscòpia Raman augmenta. Aquest fenomen és conegut com a SERS (Surface-Enhanced Raman Spectroscopy) i es va poder observar en ambdós materials.

En resum, en aquesta tesi s'han sintetitzat, caracteritzat i estudiat cinc sistemes híbrids i ternaris basats en materials amb una toxicitat baixa amb la intenció de trobar materials alternatius que, en un futur, es puguin aplicar en els camps de la la conversió d'energia i la biomedicina.

Abstract

The size/shape dependent and unique physical and chemical properties presented by nanostructured materials have attracted great attention in several fields such as energy harvesting, optoelectronics and biomedicine, among others. Even though binary semiconductors have been some of the most studied systems until now, ternary and quaternary semiconductors have started to stand out due to the wide variety of compositions and, as a result, of properties they offer. The importance of hybrid nanomaterials is growing as well: the association of more than one material in the same nanostructure usually allows the preservation or even, the enhancement, of the different properties of the preliminary materials and combines them with the new ones originated from the interaction between the two domains.

This thesis is focused on the design of novel compositionally controlled hybrid and ternary nanostructures and it is divided in five chapters regarding different systems. The studied materials have been chosen with the idea of working with low toxic materials, which might find, in a future, application in different fields.

In the first two sections (chapter 2 and 3) a simple procedure at room temperature is reported for the synthesis of hybrid and ternary nanostructures of Ag-Au-Se and Ag-Au-S. The method consists in the reaction between pre-synthesised Ag_2Se/Ag_2S nanoparticles (NPs) and a Au(III) precursor. The reaction time, the concentration of gold solution, the surfactant nature and the Ag:Au ratio are the four key parameters that allow the control of the final product. In-depth chemical and structural characterization of the nanostructures reported in these chapters were done by HRTEM, STEM, EELS, EDS and XPS. From this characterization a reaction mechanism was proposed in which two processes could have place concurrently. On the one side, when an amine (dodecylamine, DDA) is used as a surfactant, this reduces Au(III) cation to metallic gold, which heterogeneously nucleates on the surface of the semiconductor, and further grows forming a second domain. On the other, Se^{-2}/S^{-2} anions have been found to reduce Au(III) cations to Au(I) cations, which subsequently diffuse through the binary semiconductor structure, partially exchanging the Ag(I) cations of the guest material and consequently forming a ternary system.

Regarding the Ag-Au-Se system, Au-Ag_2Se hybrid nanoparticles (HNPs), Au-Ag_3AuSe_2 HNPs and Ag_3AuSe_2 NPs were successfully synthesised. When a non-reducing surfactant is used (tetraoctylammonium bromide, TOAB), the reduction of Au(III) to metallic gold is totally supressed, leading to the formation of Ag_3AuSe_2 NPs. Whereas, when the amine and a short

reaction time is used during the synthesis, the formation of the ternary material is supressed and it is possible to obtain Au-Ag_2Se HNPs.

In addition, Au-Ag_3AuSe_2 HNPs were tested as thermoelectric material, obtaining an improved response in comparison with the binary material (Ag_2Se). The potential of Ag_3AuSe_2 NPs as Computed Tomography contrast agents was also tested, obtaining promising results in this field.

Concerning to the analogous system with sulphur, the higher miscibility of Au and S offers a more complex ternary diagram, with two ternary materials with different stoichiometries: Ag_3AuS_2 and AgAuS. A gradual transformation of Ag_2S to Au_2S was achievable by the proposed method, with the possibility of isolating Au-Ag_2S HNPs, Au-Ag_3AuS_2 HNPs, Au-AgAuS HNPs, Au-Au_2S HNPs and hollow Au_2S NPs. In this system, the reduction of Au(III) to metallic gold cannot be avoided, even when using a non-reducing surfactant. All the obtained materials presented two domains, with the only exception of hollow Au_2S NPs. When using high amounts of Au(III)-TOAB complex as precursor the Kirkendall effect clearly manifested in the samples by forming hollow nanostructures: most probably, the high amount of bromides in the solution acts as a driving force for the accelerated outwards diffusion of Ag^+ cations from the Ag_2S host NPs, which provokes the formation of internal voids in the nanostructures.

The third section (chapter 4) is focused in another ternary system: Ag-Cu-S. Even though this system also presents two different ternary materials (Ag_3CuS_2 and AgCuS), the direct hot injection method proposed here only allows the formation of the AgCuS stoichiometry. Two different mechanisms are reported, depending on the precursor of copper used in the synthesis. On the one side, the use of copper (I) or (II) chlorides induces the early formation of Ag_2S NPs, which gradually suffer cationic exchange and convert to the ternary material. On the other side, the use of copper (I) iodide favours the early formation of the two binary materials and their subsequent combination. The material was thermoelectrically characterized as well, but without showing a proper performance.

Four novel nanostructures based on Cu-Pt-Se are described in Chapter 5. They were synthesised by a reaction at high temperature between pre-synthesised $Cu_{2-x}Se$ NPs and a Pt(II) precursor. The nanomaterials were thoroughly structurally and morphologically characterized to study the impact of the Pt:Cu ratio in the final product. The three first materials (with a lower Pt:Cu ratio) are composed by ternary phases, whereas the fourth material (with a high Pt:Cu ratio) is just formed by the two metals (platinum and copper). The larger the amount of platinum in the structure, the more efficient diffusion of the element occurs through the Cu-Se lattice, with the consequent and slow spell of selenium until its totality.

Finally, in chapter 6, hybrophilic hybrid inorganic-organic nanocomposites formed by inorganic NPs (Au, Ag, Ag_3AuSe_2 i $Au@Fe_3O_4$) and a highly fluorescent low molecular weight Au(I) metallogelator are presented. These nanocomposites can be dispersed in polar solvents such as water or ethanol, and they are stable for, at least, one year, at different temperatures in the range of 25-50°C and between pH 4 and pH 9. Their coupling is mainly based on aurophilic/metallophilic interactions between atoms in the surface of the NPs and Au(I) atoms from the complex. These interactions induce the formation of small aggregates of nanoparticles surrounded by an organic shell of complex. The formation of these aggregates has been studied by absorption spectroscopy, through the evolution of the localized surface plasmon resonance band characteristic of gold NPs. Additionally, the Ag and Au nanocomposites were characterized by Raman Spectroscopy. It is well known that when a molecule is strongly coupled to a plasmonic nanoparticle, the intensity of the Raman peaks of the molecule are intensified. This phenomenon is known as Surface-Enhanced Raman Spectroscopy (SERS) and could be observed in both materials.

In summary, in this thesis five hybrid and ternary nanostructured systems, based on low toxic materials, have been synthesised, characterized and studied, following the aim of investigate alternative materials, which, in a future, could be applied in energy conversion and biomedicine fields.

Contributions

In this thesis, some work has been done in collaboration with different research groups.

- HRTEM, FFT analyses, STEM-HAADF, EDX and EELS in Chapter 2 and 3 were done by Pau Torruella and Dr. Víctor Fernández-Altable, under the supervision of Dr. Sònia Estradé and Dr. Francesca Peiró. (Laboratory of Electron Nanoscopies (LENS)-MIND/IN^{2}UB, Departament d'Electrònica, Universitat de Barcelona).

- HRTEM, STEM-HAADF and EDS in Chapter 5 were done by Dr. Andrea Falqui and Dr. Alberto Casu (Biological and Environmental Sciences and Engineering (BESE) Division, King Abdullah University of Science and Technology (KAUST)).

- Thermoelectric characterization and XANES in Chapter 2 and 4 were done by Dr. Maria Ibáñez and Dr. Doris Cadavid, under the supervision of Dr. Andreu Cabot (Institut de Recerca en Energia de Catalunya (IREC)).

- Computed Tomography characterization in Chapter 2 was done by Carlos Caro, Dr. Manuel Pernia and Dr. María Luisa García-Martín (Andalusian Centre for Nanomedicine and Biotechnology (BIONAND).

- XPS and FESEM were carried out by Dr. Jordi Llorca (Institut de Tècniques Energètiques and Centre de Recerca en Ciència i Enginyeria Multiescala de Barcelona, Universitat Politècnica de Catalunya).

- Complex 1 was synthesised by Dr. Elisabet Aguiló under the supervision of Dr. Laura Rodríguez (Sistemes Supra i Nanoestructurats, Departament de Química Inorgànica i orgànica: Secció de Química Inorgànica, Universitat de Barcelona). The work reported in Chapter 6 was also done in collaboration with them.

Preface

The research reported in this thesis was developed in Grup de Magnetisme i Molècules Funcionals (GMMF) from the Departament de Química Inorgànica i Orgànica: Secció de Química Inorgànica de la Universitat de Barcelona. It was financially supported by a PhD fellowship from University of Barcelona (Ajuts de Personal Investigador pre-doctoral en Formació (APIF)) and by two different projects from Ministerio de Economía y Competitividad (MINECO):

1) Project "Moléculas, polímeros y nanoestructuras funcionales basadas en la química de coordinación: Diseño, preparación y estudio" from 2013 until 2015 (CTQ2012-32247)

2) Project "Materiales funcionales moleculares y nanoestructurados para aplicaciones nanotecnológicas" from 2016 until 2018 (CTQ2015-68370-P)

The research has been disseminated in several international conferences:

- E-MRS Fall Meeting 2015 (Warsaw, Poland): Poster communication entitled "Dimer-like Au-Ag3AuSe2 nanocrystals for thermoelectric applications"

- 13th International Conference on Nanoscience and Nanotechnologies, NN16 (Thessaloniki, Greece): Oral communication entitled "Exploiting metallophilicity for the assembly of inorganic nanocrystals and conjugated organic molecules"

- Applied Nanotechnology and Nanoscience International Conference 2016, ANNIC 2016 (Barcelona, Spain): Poster communication entitled "Controlled synthesis of Ag-Au-S ternary nanostructured semiconductors"

- II Workshop on Chemistry of Group 11 Elements (Barcelona, Spain): Oral communication entitled "Ag-Au-S ternary semiconductors: controlled synthesis of spherical and rod-like nanostructures"

- III International Symposium on Nanoparticles/Nanomaterials and Applications, ISN2A 2018 (Lisbon, Portugal): Shotgun and poster communications entitled "Shape and phase controlled synthesis of Ag-Au-S ternary nanostructured semiconductors"

Additionally, the research reported in Chapters 2, 3 and 6 has been already published and research reported in Chapters 4 and 5 will be published soon:

- Mariona Dalmases, Maria Ibáñez, Pau Torruella, Víctor Fernàndez-Altable, Lluís López-Conesa, Doris Cadavid, Laura Piveteau, Maarten Nachtegaal, Jordi Llorca, Maria Luisa Ruiz-González, Sònia Estradé, Francesca Peiró, Maksym V. Kovalenko, Andreu Cabot, and Albert Figuerola. Synthesis and Thermoelectric Properties of Noble Metal Ternary Chalcogenide Systems of Ag−Au−Se in the Forms of Alloyed Nanoparticles and Colloidal Nanoheterostructures. *Chemistry of Materials,* 2016, *28*, 7017-7208

- Mariona Dalmases, Elisabet Aguiló, Jordi Llorca, Laura Rodríguez, and Albert Figuerola. Exploiting Metallophilicity for the Assembly of Inorganic Nanocrystals and Conjugated Organic Molecules. *ChemPhysChem*, 2016, *17*, 2190-2196

- Carlos Caro, Mariona Dalmases, Albert Figuerola, María Luisa García-Martín and Manuel Pernia Leal. Highly water-stable rare ternary Ag–Au–Se nanocomposites as long blood circulation time X-ray computed tomography contrast agents. *Nanoscale,* 2017, *9*, 7242-7251

- Mariona Dalmases, Pau Torruella, Javier Blanco-Portals, Albert Vidal, Miguel Lopez-Haro, José Juan Calvino, Sonia Estradé, Francesca Peiró and Albert Figuerola. Gradual Transformation of Ag_2S to Au_2S Nanoparticles by Sequential Cation Exchange Reactions: Binary, Ternary, and Hybrid Compositions. *Chemistry of Materials*, 2018, *30*, 6893-6902

Abbreviations

BSE	Backscattered electrons
CT	Computed tomography
DDA	Dodecylamine
DLS	Dynamic light scattering
EDX/EDS	Energy-dispersive X-ray spectroscopy
EELS	Electron energy loss spectroscopy
FESEM	Field emission scanning electron microscopy
FFT	Fast fourier transform
FTIR	Fourier-transform infrared spectroscopy
HAADF	High-angle annular dark field
HNP	Hybrid nanoparticle
HRTEM	High resolution transmission electron microscopy
ICP-AES	Inductively coupled plasma atomic emission spectroscopy
LSPR	Localized surface plasmon resonance
NCP	Nanocomposite
NP	Nanoparticle
NR	Nanorod
OLAm	Oleylamine
QD	Quantum dot
SE	Secondary electrons
SEM	Scanning electron microscopy
SERS	Surface-enhanced Raman spectroscopy
STEM	Scanning transmission electron microscopy
TEM	Transmission electron microscopy
TOAB	Tetraoctylammonium bromide
XANES	X-Ray absorption near edge spectroscopy
XAS	X-Ray absorption spectroscopy
XPS	X-Ray photoelectron spectroscopy
XRD	X-Ray diffraction

Chapter 1 General Introduction

Nanotechnology is defined as the part of science, engineering and technology that works with materials in the nanoscale, between 1 nm and 100 nm. It comprises many different branches including physics, chemistry, biology, medicine, materials science. Even though the development of different techniques with the capacity of "seeing" the nanoparticles, such as transmission and scanning electron microscopy, has impulsed the field exponentially in the last decades, nanoparticles (NPs) have been used since centuries ago. For instance, roman glassmakers, in the fourth-century A.D., were fabricating colourful glasses that contained nanosized metals. The Lycurgus cup (Figure 1.1), exhibited in the British Museum, is one of the most famous examples. This cup is made of soda lime glass containing silver and gold nanocrystals and changes its colour from green, when it is lit from the front and reflects the light, to red, when it is lit from behind and transmits the light. Other examples, from the medieval age, are the colourful stained-glass windows of cathedrals, in which the colours are also attributable to the presence of metal NPs. Photography, as well, was a technology that depended on the formation of silver NPs and it emerged in the eighteenth century. The development of pictures consisted in a light decomposition of silver halides, which produced silver NPs, the pixels of the image.[1]

Figure 1.1: Lycurgus cup. Images extracted from the website of the British Museum.

The first publication about nanostructured materials was done by the English physicist and chemist Michael Faraday, in 1857, with his study entitled "Experimental Relations of Gold (and other Metals) to light".[2] However, it was not until 100 years later, in 1959, when nanotechnology started gaining importance. The lecture "There is a plenty of room at the bottom - an invitation to enter to a new field of physics", disseminated by the physicist Richard Feynman, was instrumental in raising its visibility.

Nanostructured materials are special in comparison with its homologous bulk materials because of their ability of changing their properties depending on the size and shape of the NPs. Usually, in the study of the properties of bulk materials, microscopic peculiarities become insignificant and, consequently, the properties measured are average properties. Nevertheless, when the material is nanostructured these peculiarities become important and can affect the final properties, leading to their size/shape-dependent tunability.[1,3] This dependence gives nanomaterials a wide variety of applications in several fields, for instance, medicine,[4] energy harvesting,[5] electronics,[6,7] among others.[8]

1.1 Nanostructured semiconductors

Semiconductor nanomaterials, also known as quantum dots (QDs), are one of the most studied nanostructured materials. As it is well known, a semiconductor is a material with a gap between the valence and the conduction band which has an energy (the band gap energy, E_g) closer to the thermal energy k_BT (K_B is Boltzmann's constant). Although at room temperature just a few electrons are excited to the conduction band and the electrical conductivity is low, with the proper stimuli it is possible to excite more electrons to the conduction band and the material can present significant values of electrical conductivity.

In these materials, when a photon is absorbed and one electron is promoted to the conduction band, a hole is created in the valence band, which is conductive like an electron, but with an effective positive charge. The negative electron, from the conduction band, and the positive hole, from the valence band, have an attractive force and form a weakly bonded pair, known as exciton, which usually moves through the lattice of the semiconductor material. However, when the size of the nanoparticle is reduced and gets closer to the distance between the electron and the hole, known as the characteristic Bohr radius (a_B) of each material, the optical properties of the nanomaterial become confined and size/shape dependent.[1,9,10] This is to say that, when NPs are smaller, the distance between the exciton components are shorter and, as a consequence, the energy gap (or bandgap) is more energetic and the probability of radiative recombination increases (Figure 1.2a). One of the most famous and beautiful examples of quantum confinement is the size-dependent absorption and photoluminescence of CdSe QDs covering the whole range of the visible spectrum[11] (Figure 1.2b and c).

Silicon is known to be the most used bulk semiconductor. However, concerning nanostructured semiconductors, II-VI, IV-VI and III-V binary materials have been the most studied in the last decades.[3,1213] II-VI semiconductor family includes Zn, Cd and Hg chalcogenides, whereas Sn and Pb chalcogenides are part of the IV-VI family. III-V semiconductors consist, basically, in In and Ga phosphides and arsenides.

The easy tunability of their optical properties make these materials perfect candidates to be applied in several fields[14] including energy conversion,[15–18] light-emitting,[19–21] optoelectronics,[22,23] sensing[24,25] and biomedicine.[26–28]

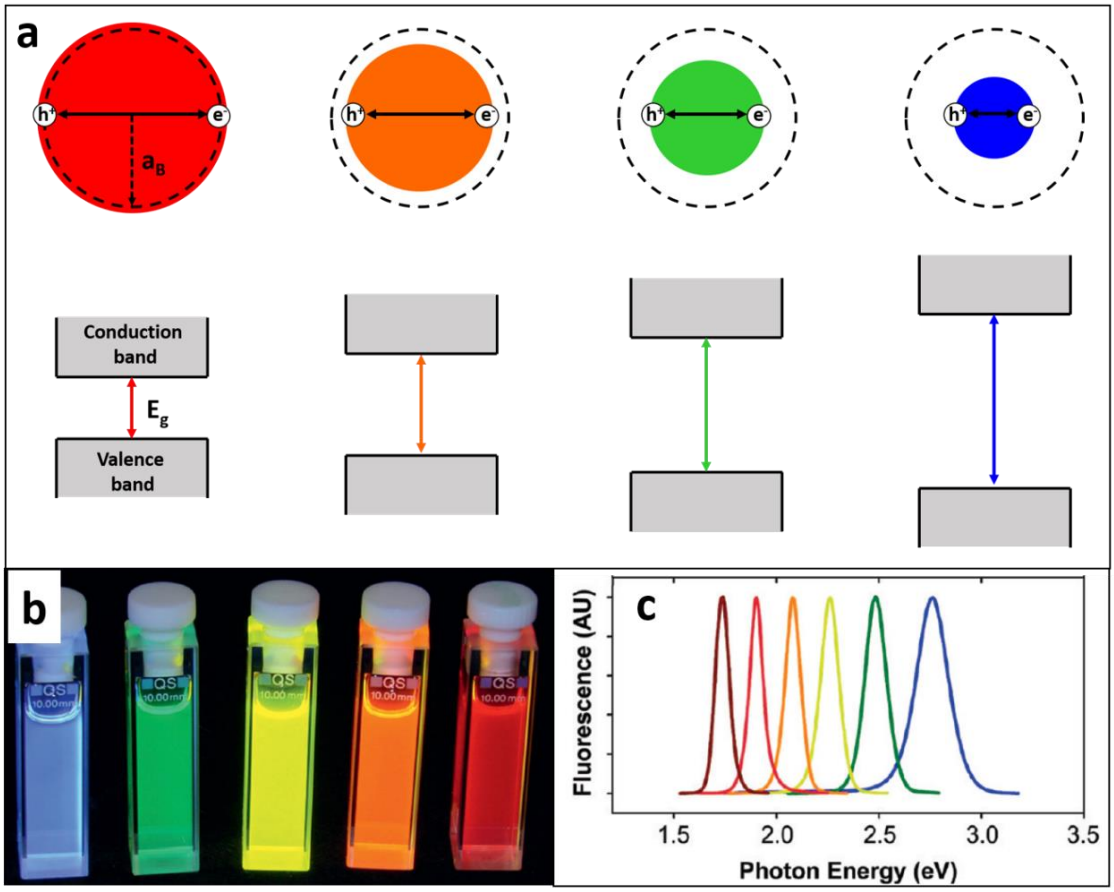

Figure 1.2: a) Illustration of the quantum confinement effect. b) Image and c) Fluorescence of CdSe QDs of different sizes. b) and c) extracted from Ref. 10 and 11.

Ternary and quaternary semiconductors

Even though the importance of cadmium chalcogenides and lead chalcogenides, which cover the visible and the near-infrared range respectively, is still growing, the increasing demand of more sophisticated devices and the concern of using toxic and environmentally non-friendly materials, forced scientists to start looking for alternative materials. Ternary and quaternary materials, also named multinary materials, have raised as suitable options.

These systems are composed of more than two elements and offer high flexibility for tuning the band gap with their composition, size and shape. Besides, many of these ternary/quaternary nanostructures have narrow band gaps, with energies of 1.55 eV (800 nm) or lower (near-infrared range), which are especially interesting for energy harvesting, optoelectronic and biomedical applications.[29–34] Their syntheses are not trivial due to the different possible stoichiometries that each material can present. Many groups have been working on them for the last decade.

Copper Indium sulphide ($CuInS_2$, CIS)[35,36] and selenide ($CuInSe_2$)[37] and Copper Indium Gallium selenide ($Cu(In,Ga)Se_2$, CIGS)[38,39] were some of the first studied materials. For instance, CIGS has been commercialized in thin film solar cells, with efficiencies up to 20%, proving the viability of these kind of materials in the actual market. Nowadays, the challenge consists on the use of non-toxic and earth-abundant elements and materials for current demanding technologies. For example, copper zinc tin sulphide (Cu_2ZnSnS_4, CZTS)[40–42] is now being studied as alternative.

1.2 Nanostructured noble-metals

Another family of materials which has been hugely studied is that of nanostructured noble-metals. As it was mentioned before, they were the first nanostructured materials that were studied and published by Michael Faraday.[2] Since then, the field has been remarkably developed. For instance, Johann Wolfgang Dobereiner, thought to be one of the founders of catalysis, discovered the catalytic capability of finely divided platinum, and from that moment, nanostructured platinum has been one of the most investigated catalysts.[43–45]

Silver and gold nanostructures[46,47] apart from being known as good catalysts, they also present interesting optical properties. These noble-metals, when going to the nanoscale, present a curious interaction with light, a phenomenon known as the Localised Surface Plasmon Resonance (LSPR). When the free-electron cloud of the metal, which is located on the surface of the material, interacts with an electromagnetic field of a particular frequency, it starts to oscillate, creating a plasma. They are known as surface plasmons. If the material is nanostructured, the amplitude of the oscillation is larger than the size of the objects and the oscillation affects all the electrons of the particle (Figure 1.3). As the induced plasma is confined to the nanoscale region, it can be said that the surface plasmon is localised. This phenomenon is highly affected by the size and shape of the NPs and the dielectric constant of the surrounding medium and it has two significant effects: 1) the optical absorption of the material presents a maximum at the plasmon resonance frequency and 2) there is an enhancement of the electrical fields close to the NPs.[48,49]

The nanostructured metals presenting LSPR are gold, silver and copper, which have a strong photoabsorption at 530 nm, 400 nm and 580 nm, respectively. This strong absorption is

responsible for their characteristic colour in solution: red for gold, yellow in the case of silver, and brown for copper. This phenomenon is exploited in several fields including catalysis,[50,51] sensing,[52–54] biomedicine,[55–57] among others.[58–60]

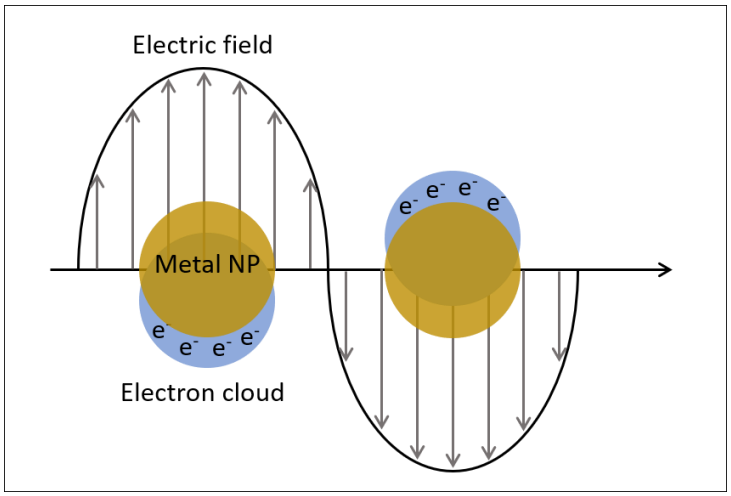

Figure 1.3: Illustration of the LSPR phenomenon.

1.3 Hybrid nanostructured materials

The flourishing interest in multifunctional materials leads to the development of hybrid materials. This kind of materials consists in two or more different materials joined in the same structure and thus, sharing an interface. They usually have the ability of preserving the different properties of the preliminary materials, which are combined in one structure. Besides, they can also exhibit some new properties and enhance some already existing ones, as a consequence of the formation of an interface and the interaction or coupling established between the two domains.[61–66] The fact that the size of this interface and the size of the nanodomains, in contrast to what happens in bulk interfaces, are in the same order of magnitude, enhances the synergetic effects between the two domains, increasing their relevance in the macroscopic properties of these hybrid materials.

Many different combinations have been studied: semiconductor-semiconductor,[67–71] metal-magnetic,[72,73] metal-semiconductor,[74–78] metal-metal,[70] magnetic-semiconductor[73] and so forth. As can be expected, each combination has its own special properties and is suitable for different applications. To give an example, the combination of two different semiconductors, depending on the bang gap, can lead to two different types of materials.

In type I materials the energy levels of one semiconductor is in between of the energy levels of the other. The holes and electrons are confined to the smaller band gap material, leading to higher photoluminescence quantum yields (Figure 1.4). In type II materials the energy levels of one semiconductor are higher than the energy levels of the other and, therefore, charge separation can occur on the interface: the hole is trapped in one semiconductor

while the electron is transferred to the other, avoiding this way their recombination and improving the efficiency of photovoltaic devices or photocatalysis (Figure 1.5).

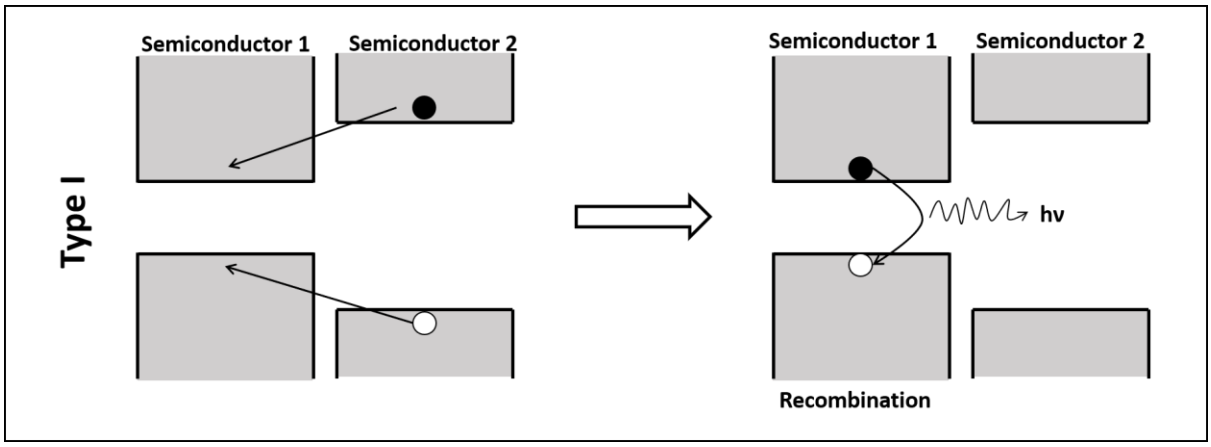

Figure 1.4: Illustration of type I semiconductor-semiconductor hybrid nanomaterials.

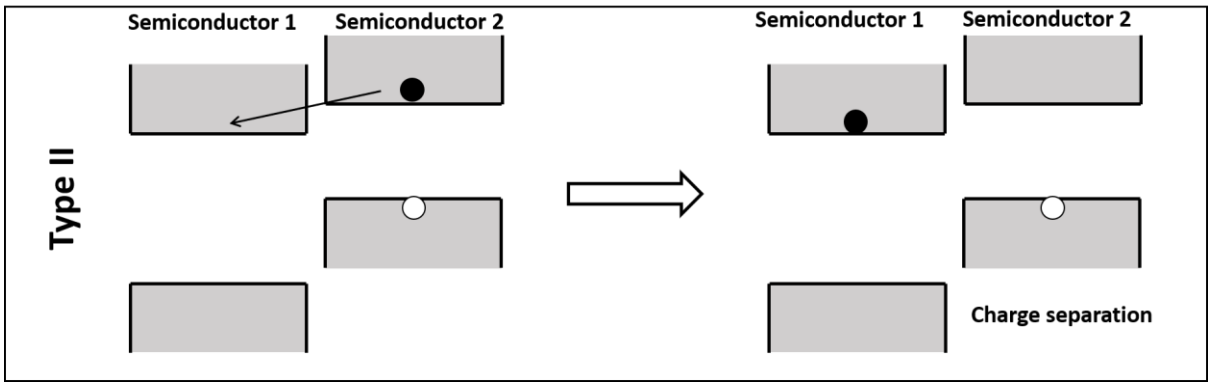

Figure 1.5: Illustration of type II semiconductor-semiconductor hybrid nanostructure.

The charge separation can also be induced in a metal-semiconductor hybrid nanoparticle (HNP), in which, additionally, the intimate interaction between the metal and the semiconductor can cause significant alterations in the optical and electrical behaviour of the sample. Besides, the metallic domain can operate as electrical contact in nanoelectrical devices.

Apart from the nature of the domains, the shape of the heteronanostructures or the relative spatial distribution of the two domains in the structure can also be designed. Core@shell,[79] hetero-dimers,[80] nanoflowers,[81] pine-apple,[82] nanoworms,[83] dumbbell[84] are some of the hybrid shapes that have been reported (Figure 1.6), thus leading to a wide variety of symmetric and non-symmetric heterocompounds with various properties.

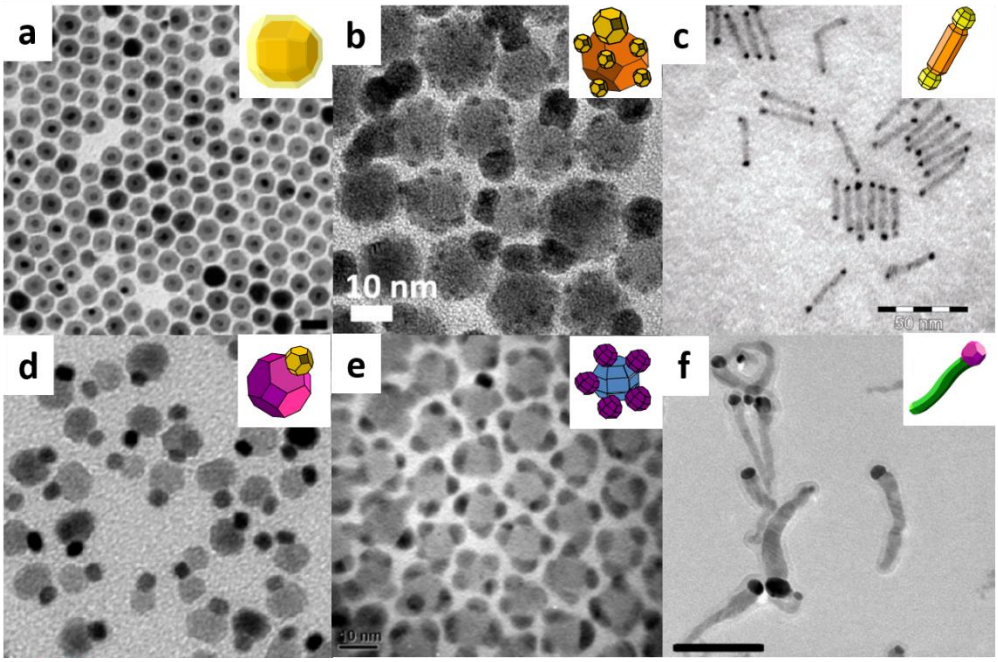

Figure 1.6: TEM images of a) core-shell Au-Fe_3O_4 HNPs, b) pine-apple-like Au-PbSe HNPs, c) dumbbell-like Au-CdSe HNPs, d) dimer-like Pt-Fe_3O_4 HNPs, e) flower-like Au-PbS HNPs and f) nanoworm-like Au-CdSe HNPs. Images extracted from Ref. 79-84.

1.4 Methods of synthesis

In order to achieve a high control on the properties of the materials to have an optimized performance in different applications, it is essential to control the size, shape and composition of the nanostructures, thus favouring the availability of highly homogeneous samples. Hence, the synthesis of the nanomaterials has become one of the biggest challenges of nanoscience.

Two general approaches for nanofabrication can be defined depending on their general procedure: top down or bottom up (Figure 1.7).[9,85] Top-down approaches lie in the formation of nanostructures from a bulk material, chipping away the macroscopic block to produce the nanomaterial. As an example, photolithography is the classic top-down method used for the fabrication of semiconductor computer chips. It consists on the printing of a pattern to a light sensitive polymeric substrate. The substrate is covered with a photomask (with the specific design) and is exposed to light. This exposition to radiation degrades the "uncovered" part of the substrate, leading to the designed structure. Other lithographic methods which use X-ray, mechanical processes or electron beam as degrading sources for the creation of the pattern have also been developed. Indeed, only the latter allows for obtaining nanostructured patterns. Micromachining is another important top-down approach. It consists in the removal of part of the bulk structure using an etching source such as a focused-ion beam, an electron beam or a femto-second laser. Traditional miniaturization methods, milling and drilling, are also considered as top down methods.

Bottom up approaches lie in the assembly or controlled aggregation of atoms or molecules to build the desired nanostructures. Inert gas condensation process, vacuum arc deposition, molecular beam epitaxy, metal-organic chemical vapor deposition, sol-gel deposition and wet-chemical colloidal synthesis are some examples of bottom up approaches.

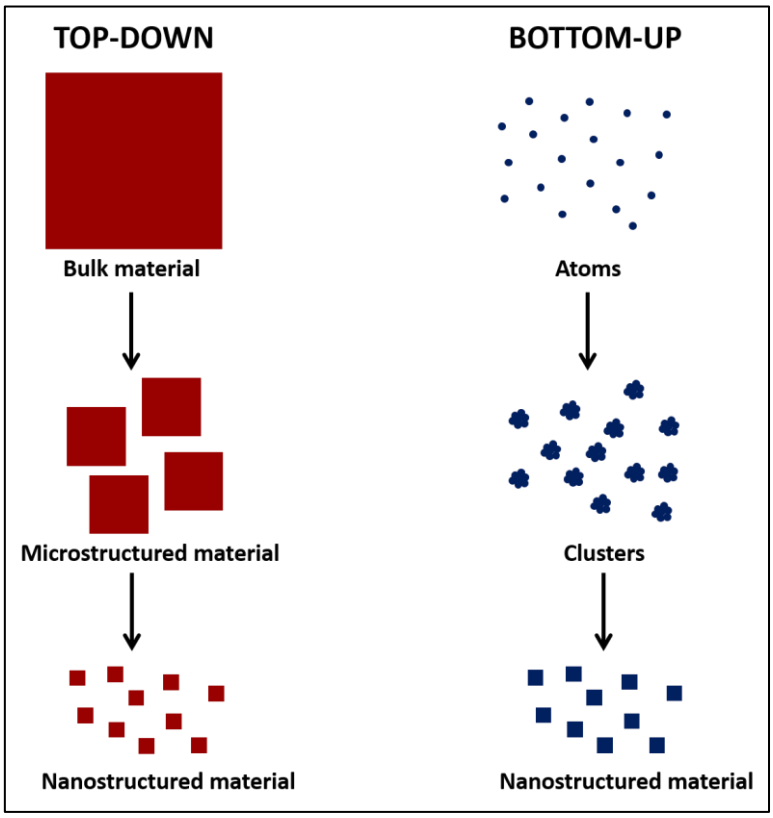

Figure 1.7: Schematic illustration of top-down and bottom-up manufacturing techniques.

Hot injection method

Wet-chemical colloidal methods are known to achieve a high control of the size and shape of the nanomaterials and to minimize the polydispersity of the samples. One of the approaches is the Hot Injection Method and it was first reported by Bawendi and co-workers in 1993.[86] Three basic chemical components are essential in this method: a high boiling point solvent, capable of holding on the high temperatures of the reaction; a surfactant, to control the size and shape of NPs and to avoid their aggregation, and precursor coordination or organometallic complexes, which at certain temperature are chemically transformed to an active atomic or molecular species, named monomers. In some cases, the surfactant can also be used as solvent.

These syntheses are usually done under inert atmosphere, using a Schlenck line and a round-bottom flask equipped with a thermocouple (Figure 1.8a). Basically, they consist on the injection of the organometallic precursor complexes at high temperature and their subsequent decomposition to form the NPs. The adsorption of the surfactant on the surface

of NPs allows the control of their shape and size and to stabilise the nanostructures in different liquid media for further processing.

The key point for the high control of the distribution of sizes and shapes is the reaction mechanism, which can be divided in three fundamental steps: burst nucleation, diffusion-controlled growth and Ostwald ripening. The nucleation and growth mechanism was first reported by LaMer in 1950.[87] The theory states that nucleation becomes a thermodynamically allowed process when the solution is supersaturated, this is to say that the concentration of the free monomer, [M], is higher than the critical nucleation concentration, [M_C]. At this point, monomers start to react between them to give place to very small particles (of a few atoms), named nucleus. The formation of these nuclei consumes part of the monomer, and, as a consequence, [M] drops below [M_C] and the nucleation process stops. However, as the [M] is still above the equilibrium monomer concentration, monomers keep reacting, in this case, with nuclei, enlarging their size (Figure 1.8b). This step is known as the diffusion-controlled growth. Finally, when [M] becomes lower than the equilibrium monomer concentration, the growth process ceases and Ostwald ripening takes control of the mechanism.

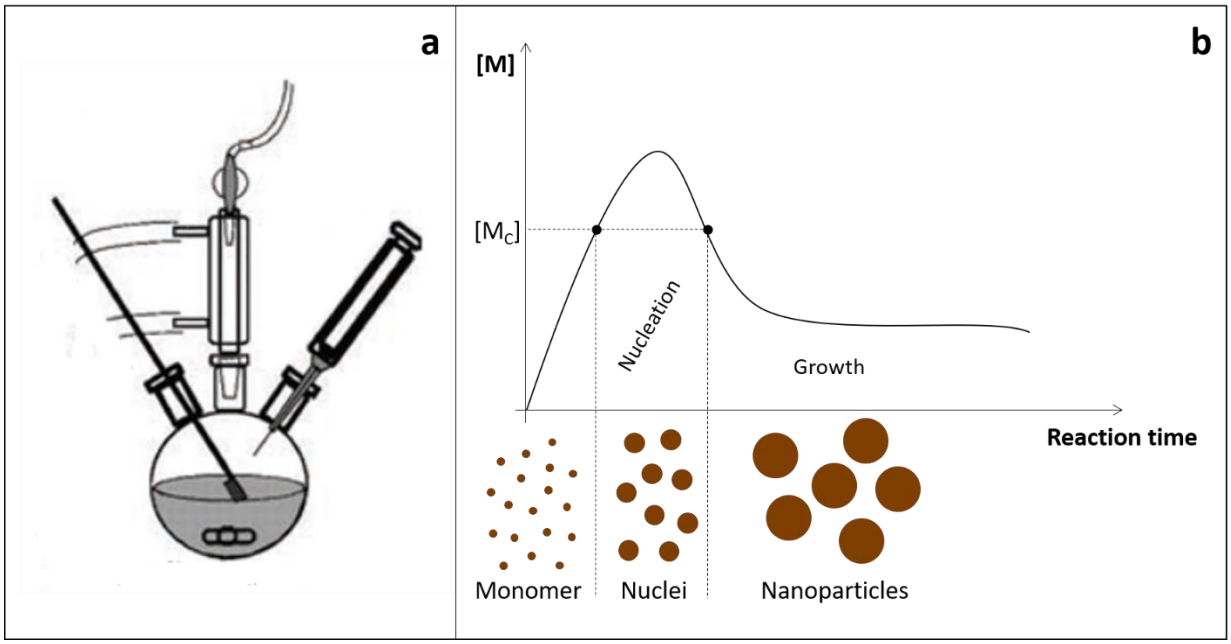

Figure 1.8: a) Draw of the hot injection method equipment (extracted from Ref. 90). b) Schematic representation of the formation mechanism of NPs by Hot Injection Method.

Ostwald ripening is a thermodynamically spontaneous process that was first described by the Latvian chemist Wilhelm Ostwald in 1896. Essentially, larger particles grow at the expenses of small particles. It is well known that atoms and molecules on the surface of a particle are energetically less stable than atoms/molecules of the interior. As a result, small particles, which have a large surface to volume ratio, are more unstable than big particles

and, trying to decrease their overall energy, atoms on their surface tend to detach, diffuse through the solution and deposit onto the surface of larger particles (Figure 1.9).

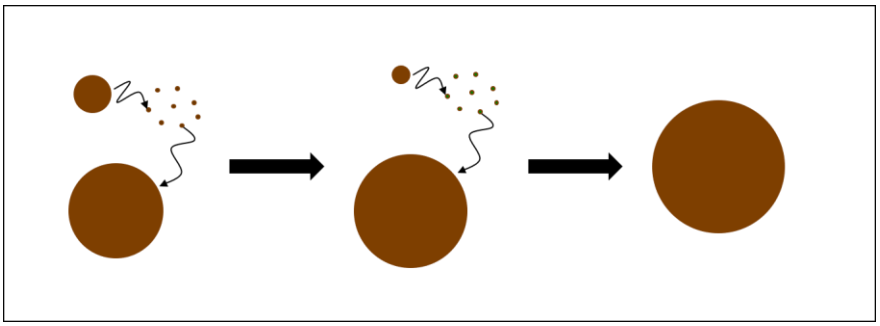

Figure 1.9: Schematic representation of Ostwald Ripening process.

The time-separation between the nucleation and growth processes, due to an initial burst nucleation event followed by a sudden decrease of [M], allows a high control of the size distribution of the sample.[88–90] Nevertheless, this synthetic method has some important requirements, such as good mixing of the sample and a controlled cooling time, that could complicate its scale up and possible industrialization. In addition, the injection step could also be difficult to manage when the volume of the injected solution became larger. A new method has been developed in the last years: the heat up method, also known as the "non-injection" method.

The basis of this procedure is similar to the hot injection method, but, instead of injecting part of the reactants, the initial solution has already all the reagents from the beginning. A controlled heating of these reactants induce the nucleation and the growth of NPs. However, the chemistry between ligands and precursors needs to be carefully controlled to ensure the rapidity of the nucleation step and the separation of the nucleation and growth steps in order to achieve a great control of the dispersity of samples.[91] Even though this method has been used in the synthesis of several materials, including semiconductor, metal and metal oxide nanocrystals, the hot injection method is, until now, one of the methods that allows a better control of the size and shape of the NPs.

Cation exchange

Cation exchange is a method that consists on the exchange of the cations of the host structure with different guest cations (Figure 1.10). It has stood out as a proper procedure to explore compositionally complex nanostructures or to synthesise metastable crystallographic phases.[92–95]

Solid-state cation exchange in bulk materials has been known for decades and it usually requires long times and high temperatures. However, in the nanoscale, the more accessible

surface and lower activation barriers of diffusion often enable the process to take place at room temperature and in a few seconds, confirming this as a "real" soft chemistry approach. The method entails first the synthesis of the host material acting as the template, which will preserve the size and the shape during the reaction, regardless of changes in chemical composition. Besides, the crystallographic structure is often also maintained, which allow the possibility of, for example, synthesising metastable phases. In some cases, the cation exchange is intentionally not completed and, as a result, the final product is a ternary/quaternary[96–99] or a doped material.[100,101] In other cases, new phases nucleate and grow at the interior or at a specific site of the nanocrystal due to selective cation exchange, allowing for the formation of multicomponent nanocrystals.[102–106] Anion exchange has also been studied and some interesting examples have been reported.[107,108] However, in general, low mobilities of anions require larger reaction times and high reaction temperatures and the obtention of high-quality materials is an issue.

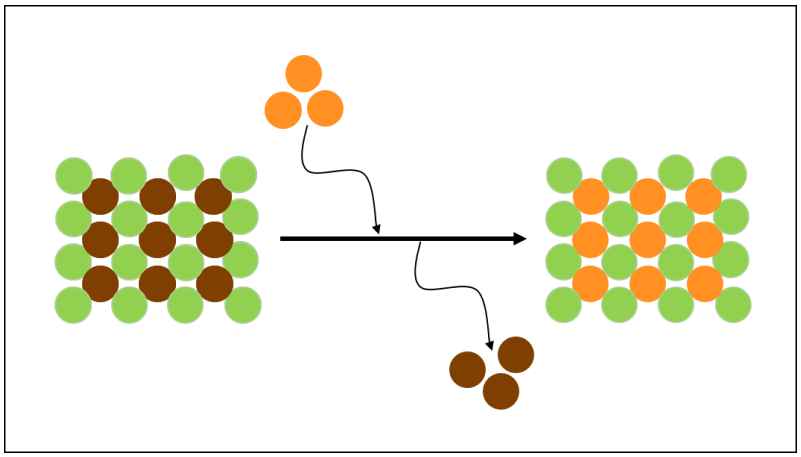

Figure 1.10: Schematic representation of cation exchange process.

1.5 Characterization methods

Controlling the size, the shape, the composition and the crystal structure is essential to control the properties of the nanocrystals; and this makes characterization of materials indispensable. Different techniques that have been used in this thesis are compiled in this section.[109] The characterization methods have been divided in three categories: morphological, structural and chemical.

Morphological characterization

Electron Microscopy is a group of techniques to study the morphology par excellence. It consists in the use of an accelerated electron beam as a source of illumination. Since the wavelength of an electron is shorter than the wavelength of visible light photons, its resolving power is higher and, as a result, it is possible to observe small objects such as

nanostructures. It is known that the wavelength of electrons depends on their velocity of travelling: the higher velocity, the shorter wavelength. So, when the accelerating voltage of the electron beam is increased, the resolution of the microscope is also increased. To control the electron beam, these microscopes use electromagnetic or electrostatic lenses.

When the electron beam interacts with the sample, different phenomena take place (Figure 1.11). Depending on the phenomenon studied, different information can be obtained. Mainly, there are two types of electron microscopes: Transmission Electron microscopes (TEM) and Scanning Electron microscopes (SEM).

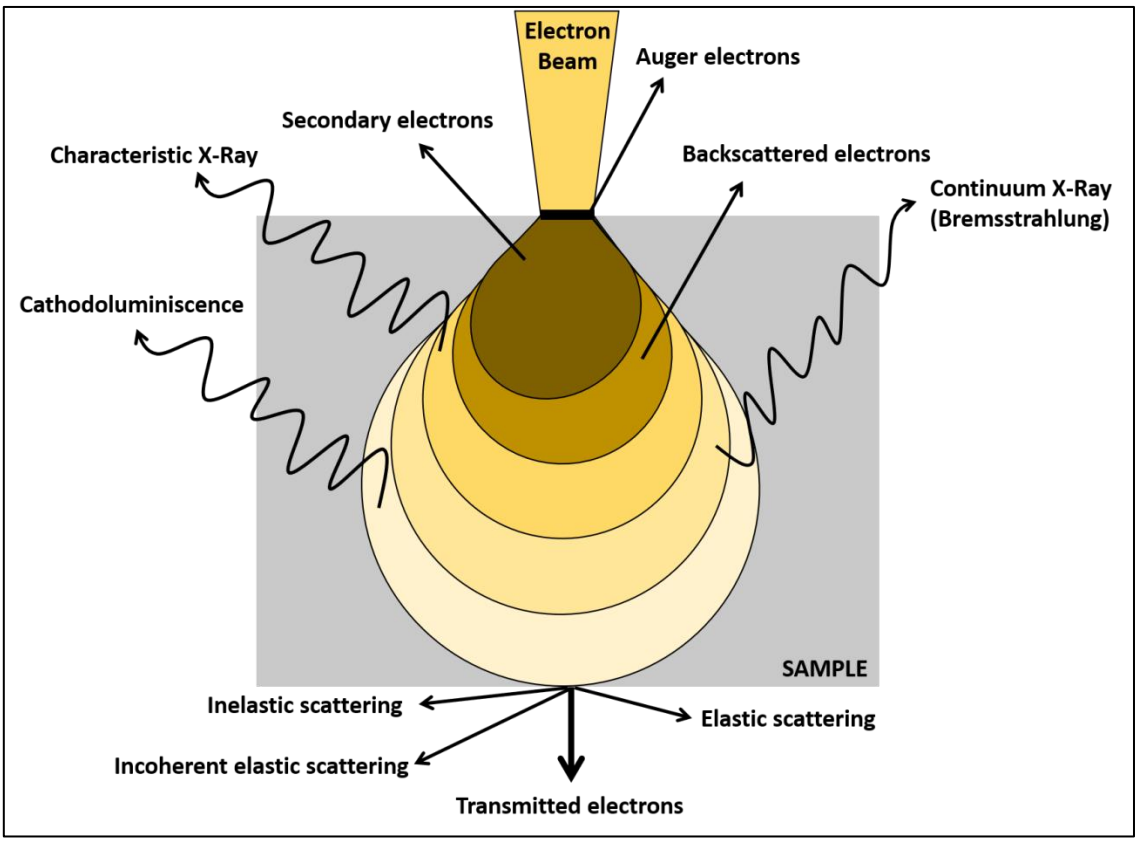

Figure 1.11: Schematic diagram of the phenomena resulting of the interaction of the electron beam with matter.

Transmission Electron Microscopy (TEM)

Transmission Electron microscopes have the detectors under the sample and analyse the electrons that have gone through it: the transmitted electrons. This technique provides two dimensional images in black and white, where the size and shape of the nanostructures can be studied. Similar to optical microscopes, TEM offers two different imaging modes: bright field and dark field.

Bright field mode uses the direct transmitted beam to create an image, in which contrast depends on the absorption and scattering of the sample: areas that absorb or scatter light

are darker than areas that transmit light, which appear brighter. The absorption and scattering of light can be due to three different factors: the atomic number (Z), the thickness and the crystallinity. Higher Z atoms and thicker samples have larger absorption and scattering, which lead to darker images. Additionally, crystalline areas efficiently scatter the electron beam, and thus they also appear darker than amorphous areas.

In the dark field mode, the elastically scattered electrons are used to produce the image. In order to collect only the scattered electrons and to avoid the main beam (used in the bright field mode), an objective aperture, placed in the diffraction plane, is used. Therefore, the black regions of images are those with no scattering, which is to say that the electron beam passes straight through the sample. This mode is Z-sensitive: the heavier the compound is, the brighter it appears. Besides, it is useful to observe crystal defects.

Scanning Electron Microscopy (SEM)

Scanning Electron microscopes has the detectors on top of the sample and scans the surface of the material, recollecting secondary and backscattered electrons. On the one side, secondary electrons (SE) come from the excitation of some atoms at the surface when interacting with the primary electron (PE) beam (Figure 1.12) and they are used to display an image of the topography of the sample. On the other side, backscattered electrons (BSE) are a result of the reflection of some high-energy electrons from the electron beam. They are used to study areas with different chemical compositions since elements with a high atomic number (heavy elements) backscatter electrons more intensely than low atomic number elements (light elements) and they appear brighter in the micrograph.

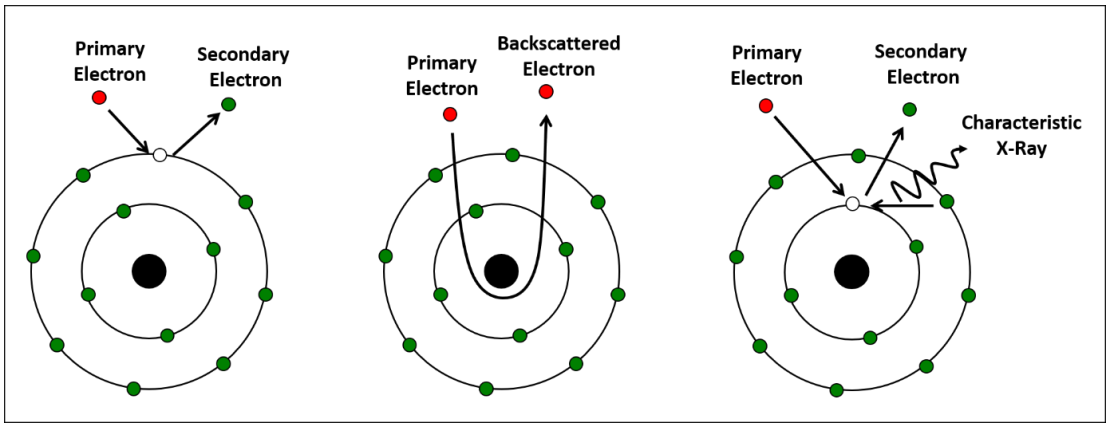

Figure 1.12: Schematic representations of the emission mechanisms of SE, BSE and characteristic X-Rays.

Scanning Transmission Electron Microscopy

Scanning Transmission Electron Microscope (STEM) is a type of TEM. It uses the transmitted electrons to create an image, but as the electron beam is focused in a fine spot a scanning of the sample is necessary to obtain the image. This concentrated beam allows a higher resolution of images in both modes (bright field and dark field). In addition, high angle incoherently scattered electrons are also detected by a high-angle annular dark field (HAADF) detector, which is highly sensitive to the atomic number of atoms and forms Z-contrast images.

Structural characterization

Crystalline structures consist in the repetition of a unit cell, which leads to a regular arrangement of atoms in 3D. Depending on the parameters of this unit cell (angles and lengths), structures can be divided in seven crystal systems: cubic, tetragonal, orthorhombic, hexagonal, trigonal, monoclinic and triclinic. This order of atoms can be represented as an array of points, known as lattice. From this pattern, different sets of rows can be established (Figure 1.13a). Each pair of adjacent rows has a characteristic distance (*d*). When the 3D structure is considered, these rows are converted in lattice planes, and two adjacent planes are separated by the interplanar *d*-spacing. In order to identify these lattice planes, three numbers (*hkl*), known as the Miller indices, are assigned to each set of planes.

Two different techniques have been used to study the crystallography of samples: powder X-Ray diffraction and Electron diffraction.

X-Ray Diffraction (XRD)

When X-Rays interact with matter two different phenomena take place: scattering and absorption. Absorption of X-Rays is used in two families of techniques: in X-Ray Absorption Spectroscopy (XAS), which will be briefly introduced in Chapter 2, and X-Ray fluorescence. The scattering phenomenon is used in XRD techniques.

Lawrence and William Henry Bragg, in 1913, proposed an approach to explain the fact that crystals reflected intensely the X-Ray radiation at certain specific incident angles and wavelengths. Bragg's law (Eq. 1.1) expresses the relation between the *d*-spacing (*d*), the angle of incidence (θ) and the X-Ray wavelength (λ).

$$n\lambda = 2dsin\theta \qquad (1.1)$$

Where n is a positive integer number. When the scattered beams satisfy Bragg's law, they are in-phase and interfere constructively, creating an intensive reflection (Figure 1.13b). Whereas, they are out-of-phase and destructive interference occurs when they do not follow the equation.

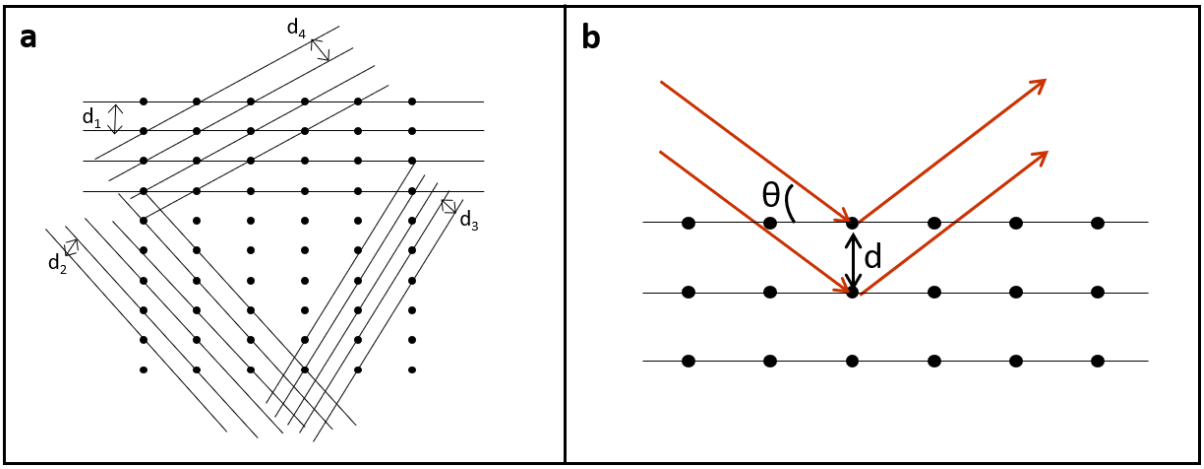

Figure 1.13: a) Lattice planes in projection. b) Schematic representation of a constructive interference.

By Bragg's equation it is possible to calculate the distance between the two equivalent planes and to identify the type of structure exhibited by the material. Generally, the angular positions and the intensity of the reflections are specific for each material, therefore, XRD patterns can be used as a fingerprint of a material. The majority of the known material's patterns are compiled by the Joint Committee of Powder Diffraction Standards (JCPDS). In this thesis, all the reference patterns have been taken from this database.

The size of the crystal is also an important factor that impacts on the width of the peaks. In 1918 Paul Scherrer reported an equation (Eq. 1.2) which related these two parameters, the smaller the particle is, the broader the peak becomes.

$$\tau = \frac{K\lambda}{\beta cos\theta} \qquad (1.2)$$

Where τ is the mean size of crystalline domains, K is the Scherrer constant, which is a shape factor, and β is the line broadening at a half the maximum intensity (FWHM) in radians.

Electron diffraction

Electrons strongly interact with matter, giving intense diffraction patterns, which make them suitable to be used for diffraction experiments. Electron diffraction is done in TEM and, in contrast to XRD, it performs local measurements in the sample, instead of bulk average measurements. The electron diffraction pattern consists in an array of dots

organized in concentric circles which capture the direction of the diffracted beam. Similar to XRD, each reflection (dot) can be assigned to a family of lattice planes and the distance between the equivalent planes can be estimated. Information of the lattice type and space symmetry can also be obtained.

Fast Fourier Transform analyses

The structural information of a specific crystal can also be studied from a high resolution TEM (HRTEM) image. If a Fast Fourier Transform (FFT) function is applied to a region of an HRTEM image, a pattern similar to the one of electron diffraction is obtained. However, in this case the measure is even more localized than in electron diffraction, the array only shows the spots of the family of planes that are exposed in the image, fulfilling the Bragg law. An example, extracted from the literature, of an FTT analysis is shown in Figure 1.14.

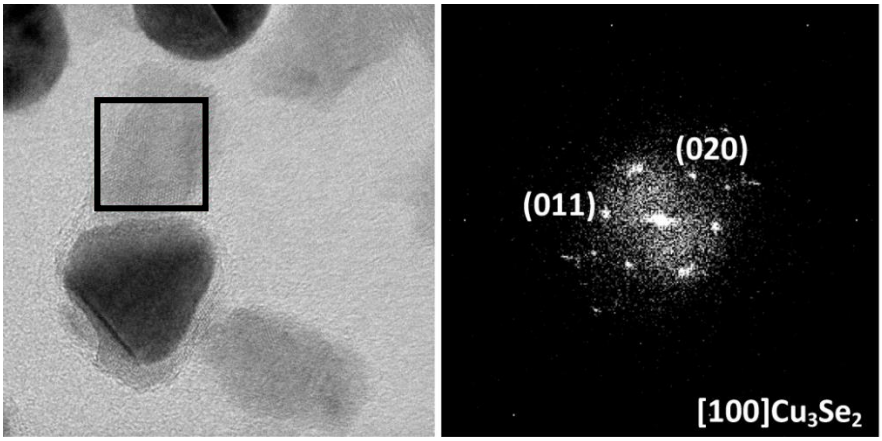

Figure 1.14: HRTEM image of an Au-Cu_3Se_2 HNP and indexed FFT of the highlighted area. Images extracted from Ref. 83.

Chemical Characterization

Chemical characterization was done basically by four different spectroscopic techniques: Electron Energy Loss Spectroscopy (EELS), Energy Dispersive X-Ray Spectroscopy (EDX or EDS), Inductively Coupled Plasma Atomic Emission Spectroscopy (ICP-AES) and X-Ray Photoelectron Spectroscopy (XPS).

Electron Energy Loss Spectroscopy

EELS uses the inelastically scattered electrons to obtain information about the chemical composition of the sample and it is done in the TEM. Some electrons of the beam interact with matter provoking inner shell ionizations. As a consequence, these electrons lose energy and their paths are slightly deflected. Since inner shell ionization energies are characteristic

of each element, the losses of energy can be associated to specific elements, obtaining a nanometer-level mapping of elemental distribution of the sample. The technique is specifically useful for low atomic number elements.

Energy Dispersive X-Ray Spectroscopy

The complementary technique of EELS, since it is more sensitive to heavier elements, is EDX. This technique can be operated in a SEM, a TEM or a STEM and detects the characteristic X-Ray emitted by matter when interacting with the electron beam. The ejection of inner-shell electrons and the subsequent relaxation of outer-shell electrons goes together with the emission of a characteristic X-Ray (Figure 1.12). This technique takes advantage of the fact that energy differences between inner and outer shells are characteristic of each element and associate the detected X-Ray with a specific element. Besides, the technique also allows to study the relative abundance of elements in the sample.

Inductively Coupled Plasma Atomic Emission Spectroscopy

ICP-AES has been used to determine the concentration of elements and composition of the nanomaterials in solution. In this analytical technique, excited atoms and ions which emit electromagnetic radiation are produced by inductively coupled plasma. The characteristic wavelength of each element and the possibility of making the method quantitative when the instrument has an appropriate calibration allow the determination of these two features. Compared to the two previous techniques, ICP-AES offers bulk average compositions instead of local and spatially-resolved measurements.

X-Ray Photoelectron Spectroscopy

Regarding to a more specific chemical information such as the oxidation of the elements on the structure, XPS can be a useful technique. Essentially, it consists in the irradiation of the sample with an X-Ray beam and the simultaneous measure of the kinetic energy of photoelectrons emitted by the sample. The identity of an element, its chemical environment and its quantification can be determined by the binding energy and the intensity of photoelectron peak. However, it is important to highlight that it is a surface-sensitive technique with an average depth of analysis of 5 nm approximately, which can significantly vary depending on several factors.

Optical characterization

Since the majority of the materials synthesised in this thesis are semiconductors or have plasmonic properties, the optical characterization by absorption spectroscopy was also important. This spectroscopic technique studies the response of the material in front of the electromagnetic radiation within the UV-Vis-NIR range. It measures the absorption of light as a function of the wavelength or the frequency.

Additional characterization

A few more techniques have been also used in this project, but as they are more specific for some application or material, they have been reported in following chapters. Specifically, thermoelectric characterization (Chapter 2 and 4), X-Ray attenuation (Chapter 2), X-Ray Absorption Spectroscopy (Chapter 2), Dynamic Light Scattering (Chapter 2 and 6), Fourier Transform Infrared Spectroscopy (Chapter 2 and 6), ^{1}H-Nuclear Magnetic Resonance (Chapter 2) and Raman Spectroscopy (Chapter 6).

1.6 Objectives

This thesis is focused in the design of novel compositionally controlled hybrid and ternary nanostructures based on low toxic elements and it is divided in two different blocks.

Chapters 2 to 5 constitute the first block, which is focused in semiconductor nanostructures.

The main objectives of this part of the project were:

- to develop a method to synthesise, with a high control, hybrid and ternary nanostructures based on four different combinations of elements: silver-gold-selenium (Chapter 2) and their analogous with sulphur (Chapter 3), the combination of silver-copper-selenium (Chapter 4) and, finally, the ternary system platinum-copper-selenium (Chapter 5)

- to characterise morphologically, structurally, compositionally and optically these systems

- to identify the reaction mechanisms responsible for the transformations

- and, to test them, in collaboration with other research groups, for possible future applications in the energy harvesting and biomedicine fields

Chapter 6 composes the second block, focalised in hybrid organic-inorganic nanostructured materials. The purposes of this section of the thesis were:

- to combine or assemble two materials of different nature (organometallic and inorganic) in one hybrid nanostructure by the design of a simple methodology

- to study the mechanism of assembly of the two domains through the deeply characterization of the nanostructures

- and, to study the optical properties derived from the coupling of the two building blocks

Chapter 2 Ag-Au-Se system

2.1 Introduction

Silver chalcogenides (Ag_2X) are known to be narrow bandgap semiconductors with bandgap energies of 0.9eV, 0.15eV and 0.67eV for Ag_2S, Ag_2Se and Ag_2Te, respectively. In recent years, they have been synthesised as nanomaterials and they have attracted much interest due to their promising optoelectronic properties that make them suitable in energy-related applications such as dye/quantum-dot-sensitized solar cells,[110–113] thermoelectric devices[114–117] and photocatalysis.[118–122] Their efficient charge transport, superionic character at high temperatures and high magnetoresistance[123,124] have motivated the study of their use as solid electrolytes for memory applications[125–128] as well as magnetic sensors.[129]

Apart from these excellent physical properties, their ultralow solubility product constant enables a minimal release of silver cations in biosystems compared with other materials, opening the possibility to apply them in the biomedicine field. Their low cytotoxicity and their emission in the NIR range make Ag_2X nanomaterials perfect candidates to be exploited in cancer imaging, photothermal therapy and controlled drug release.[130–132] Since the first publication of biocompatible Ag_2S quantum dots in 2012 by Zhang and co-workers,[133] multiple groups have been working on these applications, achieving promising results.[134–141] Besides, silver compounds have recognized antimicrobial and antibacterial properties,[122,142,143] which enlarge, even more, their suitability in the biomedicine field.

This chapter is focused in Ag_2Se nanomaterials and its ternary and hybrid compounds with gold.

Ag_2Se has two stable crystalline polymorphs, which present different physical and chemical properties, such as electrical conductivity or resistance, thermal conductivity and ionic conductivity. On the one hand, β-Ag_2Se is a narrow bandgap semiconductor which crystallizes in an orthorhombic phase and it is stable at low temperature. On the other, α-Ag_2Se, a cubic phase, is stable above 135°C and it is a superionic conductor.

The material has a first-order phase transition around 133-140°C. However, in nanosized Ag_2Se or in thin films there is another crystallographic polymorph, stable also at low temperatures: the tetragonal phase (*t*-Ag_2Se),[144–147] which is metastable and its stability depends on size, shape or method used to synthesise the material.[148,149]

Regarding Ag-Au-Se ternary materials, the phase diagram shows the existence of a room-temperature stable compound called *Fischesserite*, with chemical formula Ag_3AuSe_2. It was discovered and isolated from nature the first time in 1971 by Johan and coworkers[150] and it was synthesised and studied several times by different groups. It could be obtained by a reaction between Ag_2Se precipitates and thio-gold(I) complexes or by a direct solid-state reaction of the elements.[151] Electronic, ionic,[152] thermodynamic[153] and optoelectronic[154] properties of the material have been studied. It is a semiconductor with a band gap energy of 0.2eV[155] and with a phase transition from the cubic phase to a *bcc* at 270°C.[156] Nevertheless, in the nanoscale, there is just one publication, in which Liu and Zeng synthesised Au-Ag_3AuSe_2 hybrid nanoparticles by the reaction of an AgAu alloy with a selenium complex.[157]

2.2 Ag_2Se NPs: synthesis and morphological and structural characterization

Having a high control of the size and shape of the nanoparticles is one of the most important issues in the synthesis of nanomaterials. The hot injection method allows this control, so this was the method chosen for the synthesis of nanostructured Ag_2Se. The first attempt was done following the synthesis published by Norris and co-workers in 2011,[146] where octadecene was used as solvent and oleylamine and hexadecylamine as surfactants. $AgNO_3$ and Se, dissolved in trioctylphosphine, were used as precursors. The final sample was formed mostly by aggregated NPs with a large distribution of sizes.

Thus, another method, also published by Norris group, was tested.[147] In this case, octadecene was substituted by trioctylphosphine oxide and hexadecylamine was removed of the synthesis. The synthesised nanoparticles were spherical and of 7 nm of average diameter with a standard deviation of 4.3%.

The first idea of this part of the project was to synthesise hybrid Au-Ag_2Se nanostructures to test them as a thermoelectric material. The parameters that affect thermoelectric response and why this material could be an interesting option will be explained in section 2.5. For now, it is just necessary to consider that bigger particles of silver selenide were required.

In the former publication Norris and co-workers also studied the effect of the silver precursor nature in the synthesis and they proved that when AgCl is used instead of the nitrate, the nanoparticles grow larger. So, this change was introduced in the next synthesis. The obtained nanostructures were hexagonal and of 8.54 nm of average diameter with a standard deviation of 8.3%, as can be seen in TEM image of Figure 2.1. Although the shape and size were satisfactory, XRD, also displayed in Figure 2.1, showed the sample was not only formed of Ag_2Se, but metallic silver impurities were also identified. Apart from that, it is worth noting that Ag_2Se crystallised mainly in the metastable phase (tetragonal) which can only be obtained when working with nanoscale domains.

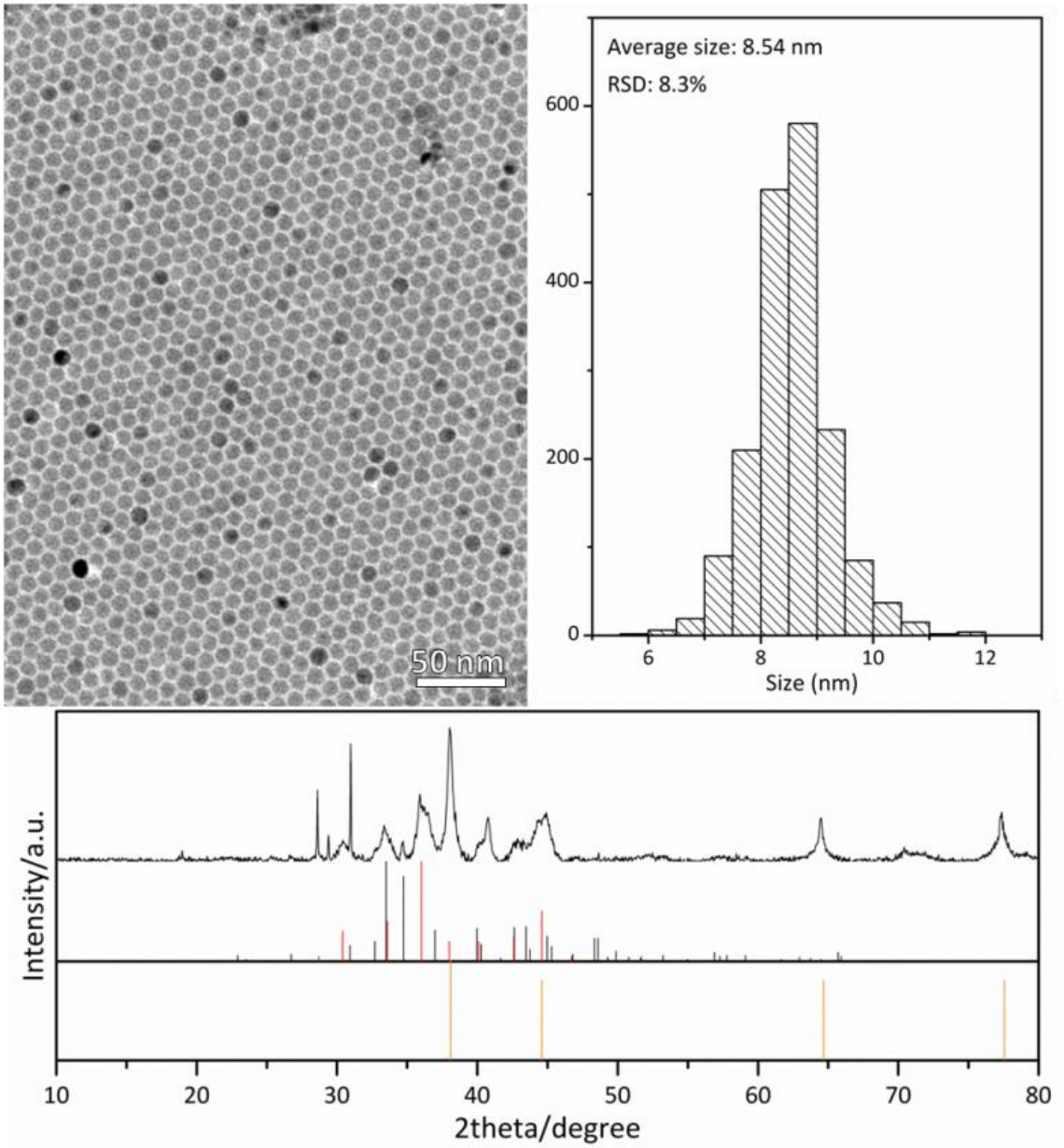

Figure 2.1: TEM image, size histogram and XRD pattern of Ag_2Se NPs. Orthorhombic Ag_2Se (JCPDS 024-1041, black), tetragonal Ag_2Se (calculated, red)[146] and cubic Ag (076-0135, orange) reference patterns.

In order to avoid the formation of metallic silver, the amount of selenium precursor was increased to have a larger excess. In this experiment, instead of using an Ag:Se ratio of 1:1, a 1:2 ratio was employed. The morphology of the NPs was similar, as can be observed in TEM image in Figure 2.2. The NPs were hexagonal in shape and around 11 nm of average diameter with a standard deviation of 4.3%. The objective of avoiding the formation of metallic silver was also accomplished, and in this case the crystallization of the orthorhombic phase (β-Ag_2Se) was favoured, as evidenced by XRD (Figure 2.2), where the peaks of the metastable tetragonal phase are hardly observed.

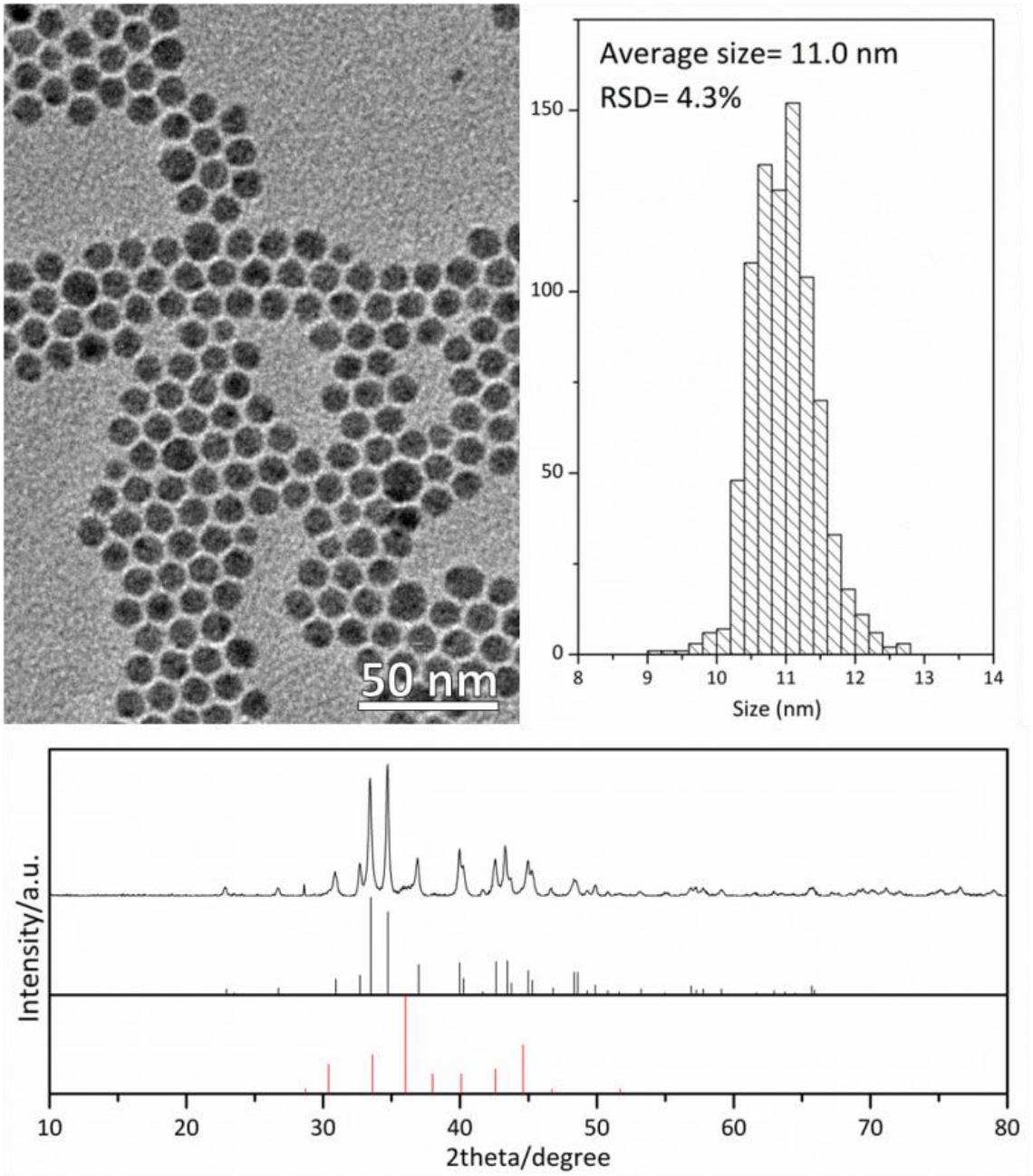

Figure 2.2: TEM image, size histogram and XRD pattern of Ag_2Se NPs (increasing the amount of Se precursor). Orthorhombic Ag_2Se (JCPDS 024-1041, black) and tetragonal Ag_2Se (calculated, red)[146] reference patterns.

This method was highly reproducible and easily scalable. In Figures 2.3 and 2.4 TEM images and XRD patterns of different synthesized batches are shown, following always the same method. The resemblance between all the samples is clear.

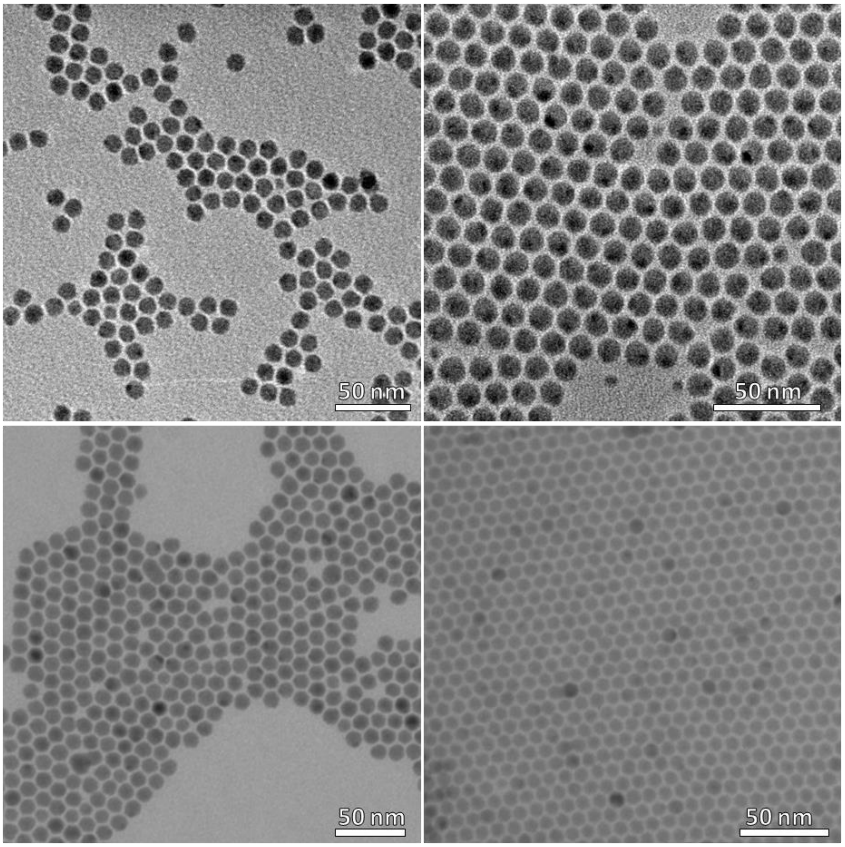

Figure 2.3: TEM images of different batches of Ag_2Se NPs.

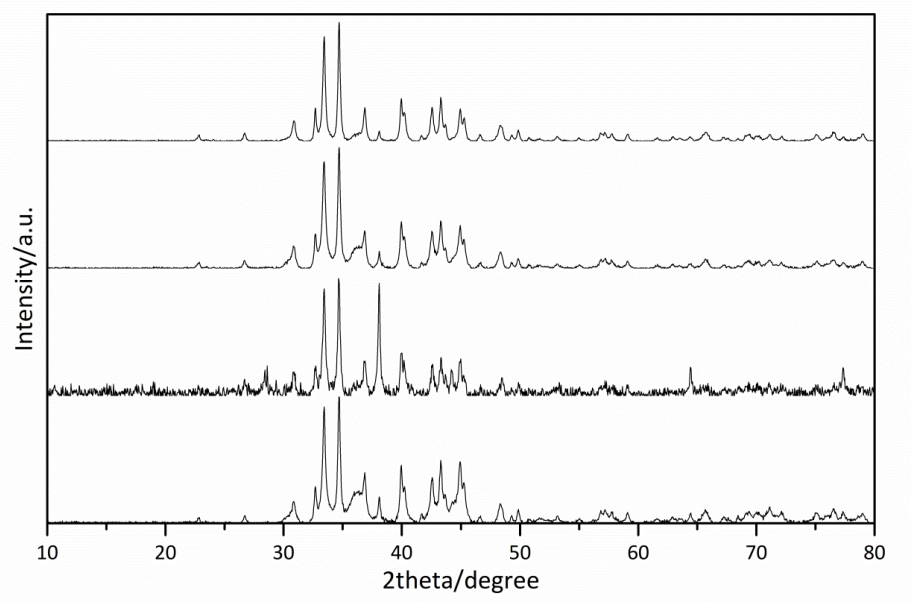

Figure 2.4: XRD patterns of different batches of Ag_2Se NPs.

The growth mechanism of the NPs was studied by analysing aliquots at different reaction times. In Figure 2.5, the morphological results are shown. The material nucleated immediately after the injection, as it was indicated for the immediate change of colour of the solution when the silver precursor was injected. This fact was confirmed by TEM, where nanoparticles could already be observed. After 5 minutes the NPs had grown uniformly and they were of 5 nm approximately. At 10 minutes of reaction, it seemed that NPs had reached the size of the final NPs. Even though at this time there were a few NPs which were larger, these NPs disappeared after 20 minutes of reaction.

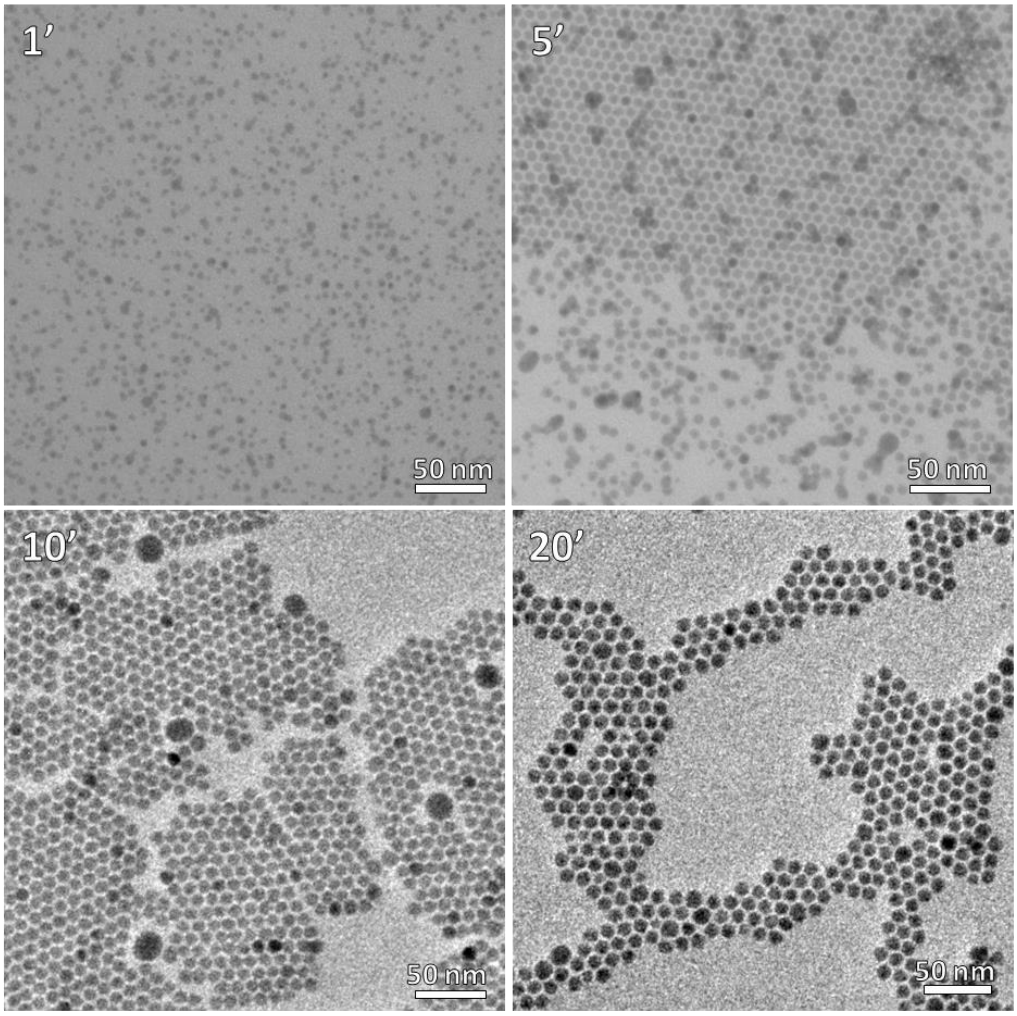

Figure 2.5: TEM images of Ag_2Se NPs extracted at different reaction times (1', 5', 10' and 20').

In some samples, the NPs of Ag_2Se contained two domains showing a clearly different contrast in TEM micrographs. So as to study this second domain, HRTEM with a FFT analysis was performed. These measurements and analyses were performed by Dr. Victor Fernández-Altable, who was working in the Laboratory of Electron Nanoscopies in the Electronics Department of the University of Barcelona, under the supervision of Dr. Sònia Estradé and Dr. Francesca Peiró. Three hypotheses were considered for the

small domain: 1) domains of the expected β-Ag_2Se with different orientations with respect to the main one, 2) domains of the metastable tetragonal Ag_2Se phase and 3) metallic Ag. The latter was the less probable hypothesis, considering that metallic silver was not observed in the XRD, but it was necessary to consider it regarding the fact that, before increasing the amount of selenium precursor in the synthesis, it was an important sub-product of the synthesis.

Figure 2.6 shows two different NPs examined and analysed by HRTEM. It can be observed that in both cases, the main domain and the small domain corresponded to β-Ag_2Se. Although, in some cases, the FFT patterns were also compatible with *fcc*-Ag, it was always with a larger error than for the Ag_2Se, which led to the rejection of the formation of the metallic domain in the synthesis. There were also other NPs (not shown in the figure) where FFT patterns did not match with β-Ag_2Se, either for the main or the small domain, or did it with errors larger than those admissible for this material. It was assumed that they were Ag_2Se NPs with the metastable tetragonal phase detected by XRD, even though it was not possible to directly verify it by this technique. The lack of crystallographic data of this metastable phase in databases and in the literature prevented the simulation of the structure and the further confirmation of the phase by FFT analyses.

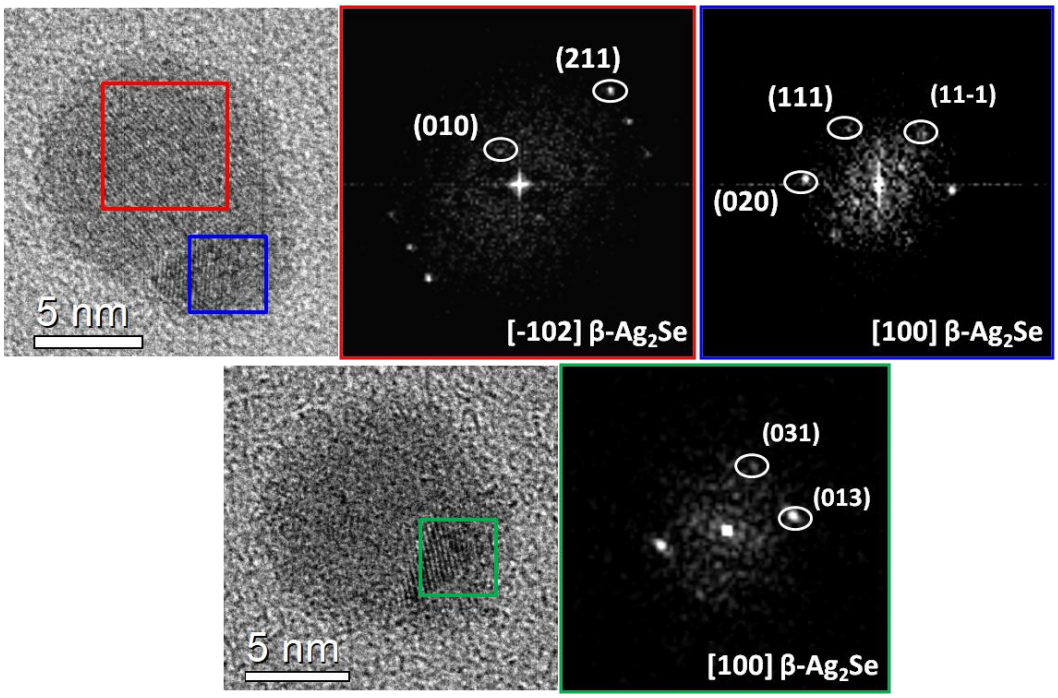

Figure 2.6: HRTEM images and corresponding indexed FFT from highlighted regions of Ag_2Se NPs.

The metastable tetragonal phase observed by XRD is only stable for a few months since it suffers a slow and gradual transition to the orthorhombic phase. This fact was proved by XRD: a Ag_2Se sample showing only the tetragonal structure was analysed 4 months later and, although the tetragonal phase could still be observed in the pattern,

its peaks suffered a significant decrease of the intensity in benefit of those of the orthorhombic β-Ag_2Se.

Ag_2Se is known to have a phase transition at 135°C from the orthorhombic β-Ag_2Se to cubic α-Ag_2Se. XRD patterns at different temperatures in vacuum conditions were acquired to see this phase transition (Figure 2.7). The initial sample was impurified with metallic silver (peaks marked with an asterisk to avoid confusion) but that did not affect to the study of the Ag_2Se phases. Basically, the phase transition was observed between 125°C, when peaks of the cubic phase appeared, and 150°C, when the transformation was complete. The phase transition is a reversible process, so when the temperature was decreased to room temperature (Figure 2.8), the orthorhombic phase was recovered between 125°C and 100°C. Having a lower phase transition temperature when going from α-Ag_2Se to β-Ag_2Se was expected according to the literature[148] and it is due to a hysteresis phenomenon. This well-known phenomenon consists in the lagging of a response when a system is exposed to a change of conditions and can affect different responses such as magnetization, electric polarization and phase transitions.

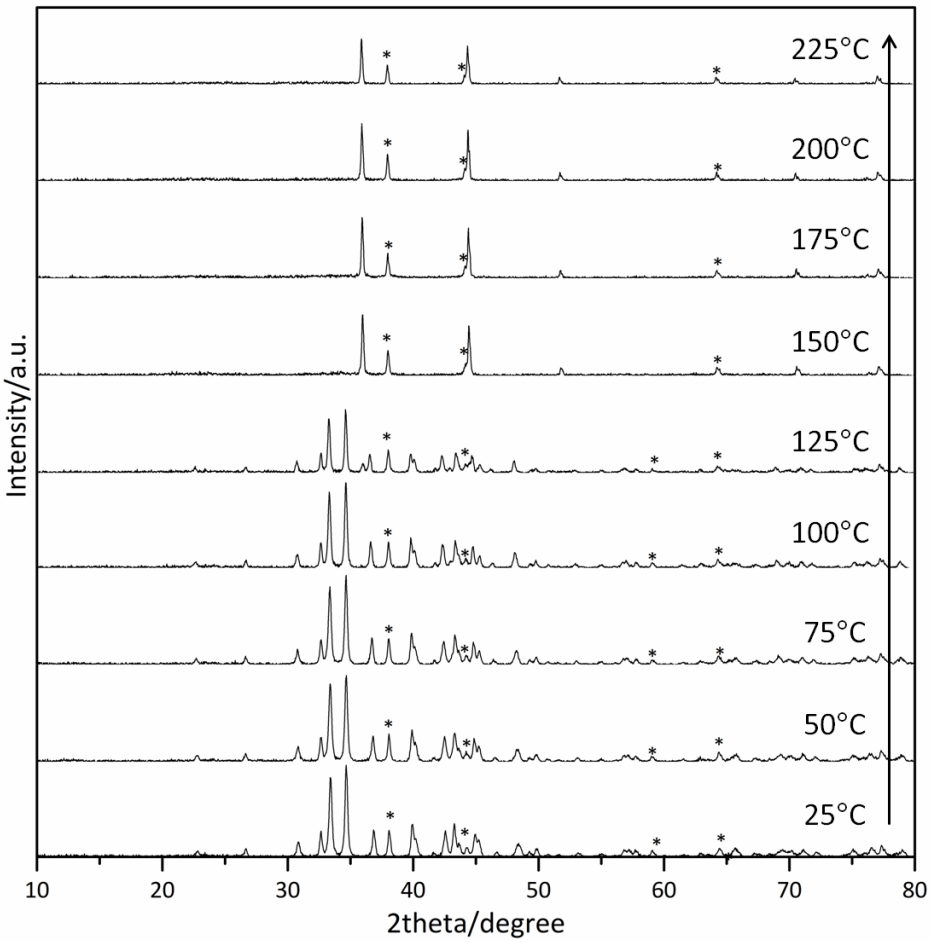

Figure 2.7: Temperature-dependent XRD patterns of heating Ag_2Se NPs. Peaks originated from metallic silver are marked with an asterisk.

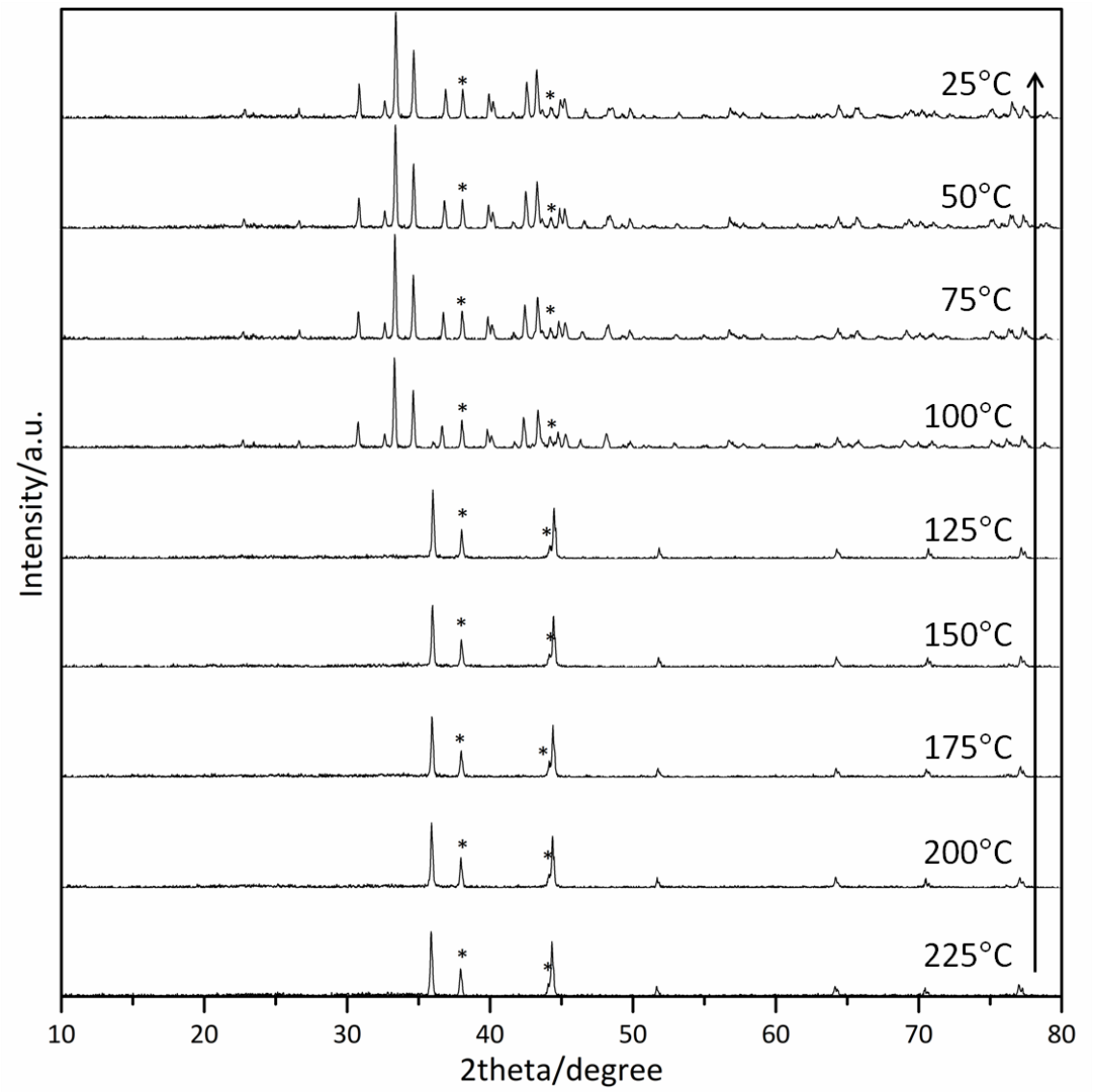

Figure 2.8: Temperature-dependent XRD patterns of cooling Ag_2Se NPs. Peaks originated from metallic silver are marked with an asterisk.

2.3 Ag-Au-Se systems: synthesis and morphological, structural and chemical characterization

As it was commented before, one of the aims of this project was to synthesise hybrid nanostructures based on silver selenide and gold. The first idea was to grow a metallic tip of gold on the surface of pre-synthesised Ag_2Se NPs. There are some examples of this kind of nanostructures with other semiconductors,[76,82,83,158–161] such as CdSe, PbSe, $Cu_{2-x}Se$, among others, in the literature.

First attempts

As a first attempt a method published by Mokari and co-workers[159] was used. Briefly, a solution of pre-synthesised NPs was mixed with a gold (III) chloride solution in toluene in the presence of an amphiphilic surfactant. The reduction potential of Au(III) is known to be high, which means that it is easy to reduce Au(III) cations to metallic Au. In this method, the surfactant, dodecylamine (DDA), apart from stabilizing the cations in the apolar solution, acts as the reducing agent. Amines have been largely used as reducing agents in gold NPs synthesis.[162–165] The amine transfers electrons to the metal ion and it is oxidized to a radical cation, which usually is the first step of a polymerization process, forming oligomeric and polymeric species.[163] Au(0) atoms subsequently nucleated heterogeneously on the surface of the semiconductor.

Even though dimer-like nanoparticles were obtained from this synthesis, the presence of chlorides in the solution caused the precipitation of Ag^+ cations, impurifying the final product.

In order to avoid the precipitation of silver cations, the strategy entailed the removal of the chlorides from the Au(III) solution. Ying and co-workers published a protocol to transfer metal cations from water to toluene.[166] In this protocol, the metal salt is dissolved in deionised water and immediately an ethanolic solution of DDA (the surfactant) is added. A cation-surfactant complex is formed and with the addition of toluene, this complex is transferred to the organic phase while most of the chlorides remain in the aqueous phase. In Figure 2.9 the procedure for this phase transfer is illustrated.

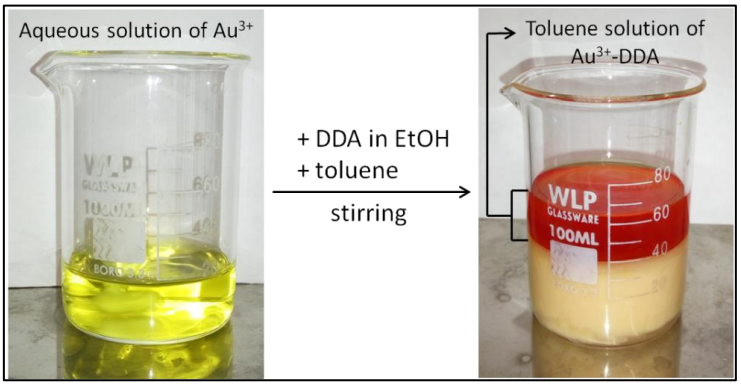

Figure 2.9: Photos of the phase transfer process of Au(III) ions from water to toluene.

After the preparation of the toluene Au(III) solution, the subsequent reaction is simple: a mixture at room temperature of the gold solution (prepared following the protocol) and a solution of pre-synthesise Ag_2Se NPs, also in toluene. In the first try on this synthesis (Ag-Au-Se_DDA1), dimer-like NPs were obtained, as can be seen in TEM micrograph of Figure 2.10. Curiously, when looking at the XRD pattern, instead of

seeing the Ag_2Se phase, a new phase was observed: the ternary phase Ag_3AuSe_2. The formation of this ternary phase is usually easy to detect thanks to its characteristic XRD reflection at 12 degree, that belongs to an interplanar distance of 7.31Å, being this value exceptionally long and hard to find in inorganic materials.

It seems that apart from growing on the surface of the NPs as a metallic domain, gold could also be reduced to Au(I), diffuse into the semiconductor crystal lattice to induce a partial cation exchange and form a different compound.

The metallic gold domain, which was clearly visible by TEM, was not observed by XRD. This fact was expected because of the small size of the domain. It is well known that in XRD the bigger the crystal size is, the narrower the peak becomes;[167,168] so, as a consequence, when the domain is too small it is hard to see it in the XRD pattern due to large widths and consequent low intensities.

With the objective of controlling the phase and chemical composition of the semiconductor domain, further studies were carried out.

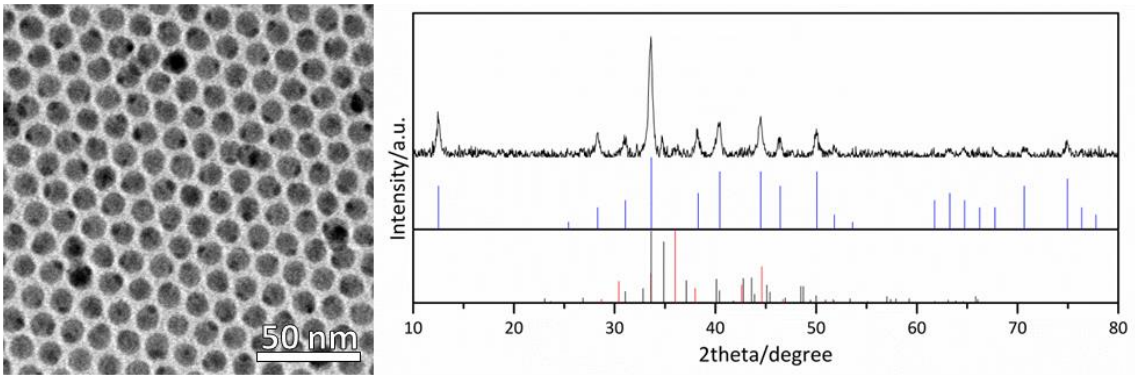

Figure 2.10: TEM micrograph and XRD pattern of Ag-Au-Se_DDA1. Cubic Ag_3AuSe_2 (JCPDS 025-0367, blue), orthorhombic Ag_2Se (JCPDS 024-1041, black) and tetragonal Ag_2Se (calculated,[146] red) reference patterns.

Study of the influence of reaction time. Synthesis of Au-Ag_2Se hybrid nanostructures

The first parameter studied was the reaction time. The conditions used in the experiments were the same as in the first attempt Ag-Au-Se_DDA1 ([Au(III)=1mM, room temperature, 1h of reaction) but reducing the reaction times to 1s (Ag-Au-Se_DDA2) and 30min (Ag-Au-Se_DDA3). In Figure 2.11 there is a comparison of the morphology and crystallography of the three samples. It can be clearly seen that although in the three cases a metallic domain was grown (there were some particles that did not have metallic domain, but almost all of them had), the shorter the reaction time was, the smaller the metallic domain grew. These results were quite

expected, with more reaction time, there was more time to reduce gold (III) ions and to grow the domain.

Regarding the crystallography, it is possible to see a clear change between the 1s sample and the 30min sample. The former was just a mixture of the two low temperature stable phases of the binary semiconductor (β-Ag_2Se and *t*-Ag_2Se), whereas the latter was almost a pure phase of the ternary semiconductor (cubic Ag_3AuSe_2). In comparison with the 1h reaction time sample, which was the sample Ag-Au-Se_DDA1, the pattern of the 30min sample was similar but with a decrease of the remaining peaks of the binary phase, which can be still seen in both samples. From this experiments it could be concluded that the reduction of Au(III) to Au(I) and its diffusion inside the structure of the semiconductor seemed to be a slower process, which requires longer times to occur.

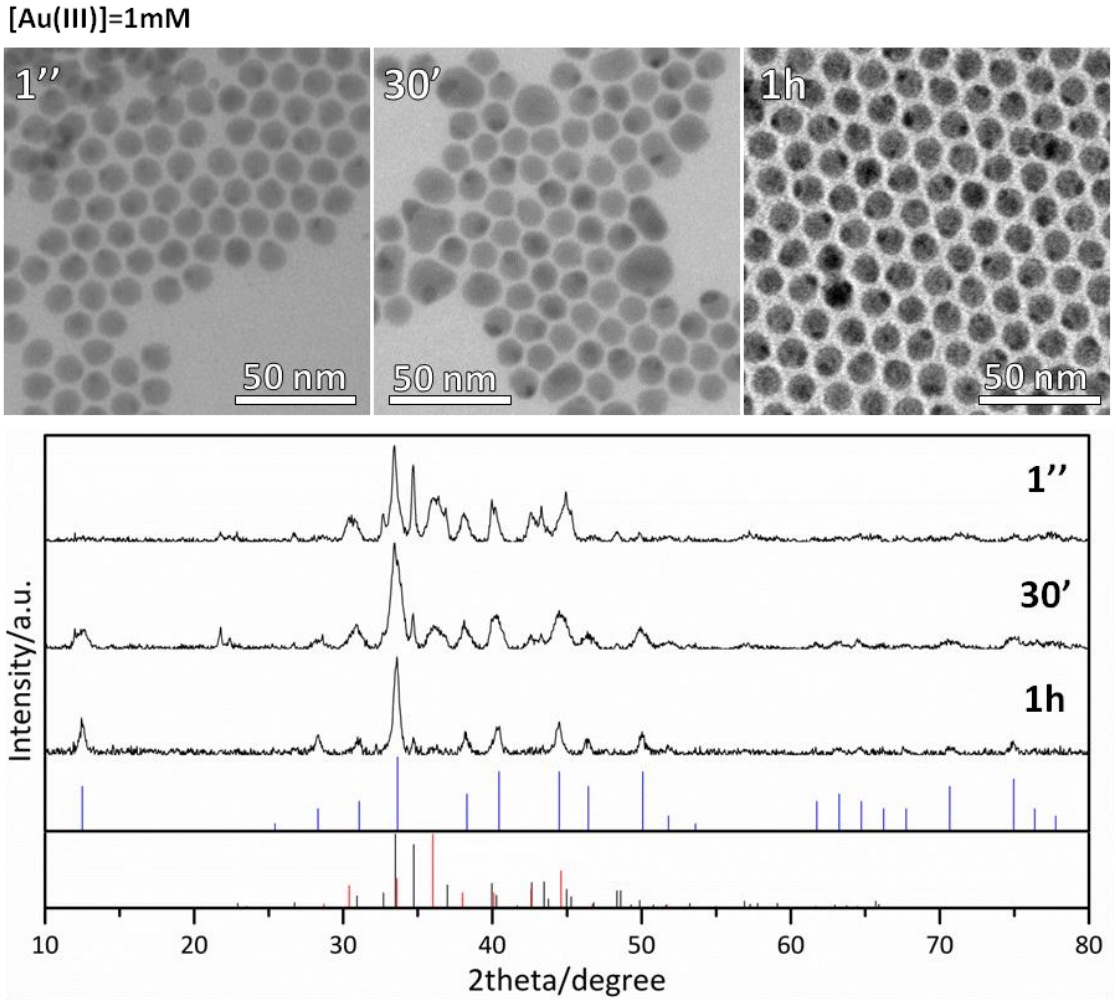

Figure 2.11: TEM micrograph and XRD patterns of Ag-Au-Se_DDA2 (1''), Ag-Au-Se_DDA3 (30') and Ag-Au-Se_DDA1 (1h). Cubic Ag_3AuSe_2 (JCPDS 025-0367, blue), orthorhombic Ag_2Se (JCPDS 024-1041, black) and tetragonal Ag_2Se (calculated,[146] red) reference patterns.

In addition, it is important to underline that hybrid Au-Ag_2Se nanostructured material was synthesised (Ag-Au-Se_DDA2) by using low reaction time (1s) and 1mM of Au(III) concentration. Nevertheless, the sample did not preserve this structure for a long time. After one year, it was measured by XRD and the results of the aged sample, shown in Figure 2.12, pointed out two important facts. Firstly, the decrease of the peak from the metastable tetragonal phase of Ag_2Se (broad peak around 37°), as expected regarding to the previous results with Ag_2Se NPs. Secondly, the appearance of the characteristic peak of the ternary material (peak at 12.5°), which indicate the gold was diffusing slowly from the metallic domain to the semiconductor domain, converting part of it to the ternary semiconductor.

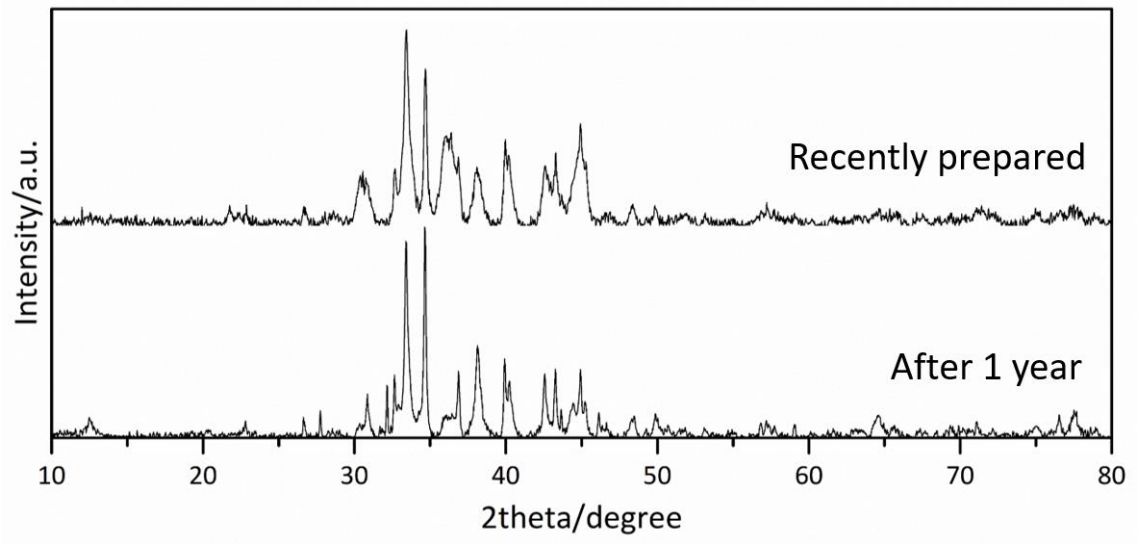

Figure 2.12: XRD patterns of Au-Ag_2Se hybrid NPs (Ag-Au-Se_DDA2) recently prepared (top) and after one year (down).

Study of the influence of concentration of Au(III) solution

The influence of the concentration of Au(III) solution was the second parameter studied. For this study just one experiment was done. The reaction time was fixed to 30' and the concentration of Au(III) was increased to 6 mM (sample Ag-Au-Se_DDA4). TEM images (Figure 2.13) clearly showed that when the concentration of gold was increased, the morphology of the particles became more homogenous, all the particles had a metallic domain and these domains were of the same size. Regarding the XRD pattern (Figure 2.13), the transformation of the semiconductor domain was not complete, a remaining peak of the orthorhombic Ag_2Se phase could be observed at 34.7°. Therefore, it seems that the increase of the concentration of gold in the solution accelerate the transformation of the binary phase to the ternary phase, even though it was not enough for the full transformation of the semiconductor domain.

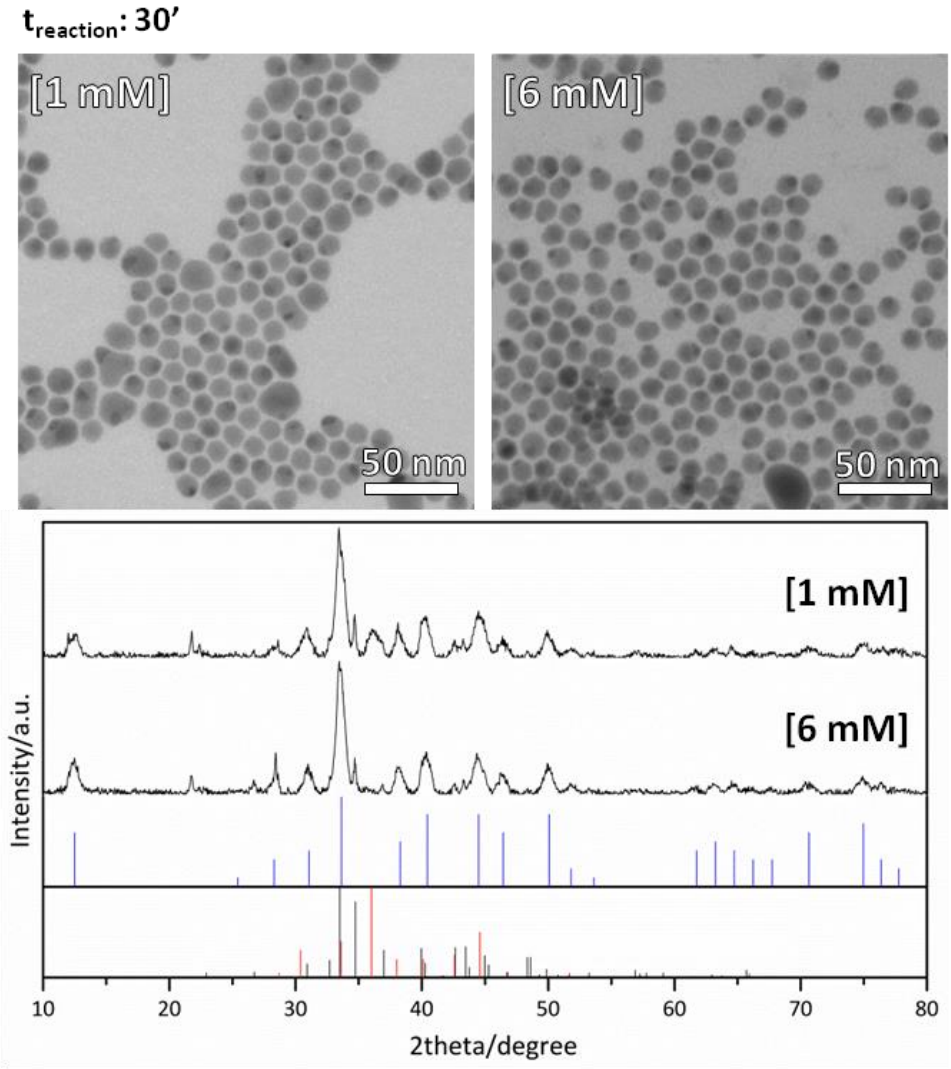

Figure 2.13: TEM images and XRD patterns of Ag-Au-Se_DDA3 (1mM) and Ag-Au-Se_DDA4 (6mM). Cubic Ag_3AuSe_2 (JCPDS 025-0367, blue), orthorhombic Ag_2Se (JCPDS 024-1041, black) and tetragonal Ag_2Se (calculated,[146] red) reference patterns.

Synthesis of hybrid Au-Ag_3AuSe_2 nanostructures

With the idea of synthesising the hybrid nanostructured material formed by metallic gold and the ternary phase Ag_3AuSe_2, a new experiment was designed having both previous studies in mind. In this synthesis (Ag-Au-Se_DDA5) the reaction time was increased to 2h and the concentration of Au(III) was maintained at 6mM. Results of this experiment are displayed in Figure 2.14. Dimer-like nanostructures were obtained and the structural transformation was complete, no remaining peaks of the binary phase could be observed in the XRD pattern.

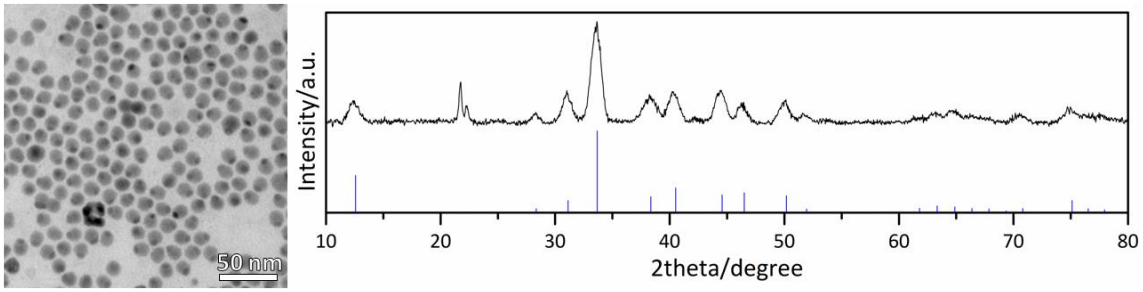

Figure 2.14: TEM image and XRD pattern of Ag-Au-Se_DDA5 (6mM, 2h of reaction time). Cubic Ag_3AuSe_2 (JCPDS 025-0367) reference pattern.

Study of the influence of the amount of DDA

Besides the study of the influence of the reaction time and the gold solution concentration, another parameter of the synthesis was changed to study its effect on the final product. One experiment (Ag-Au-Se_DDA6) increasing the amount of dodecylamine was done. The conditions for the experiments were 1h of reaction time, 6 mM of Au(III) solution and double amount of DDA in the solution. The increase of the reducing agent caused the increase in size of the metallic domain, as can be observed in TEM image of Figure 2.15. This enlargement of the gold domain allowed the observation of the characteristic reflections of cubic Au in XRD pattern, also shown in Figure 2.15, where it is possible to see the ternary semiconductor phase and the metallic phase. These nanoparticles can be considered as Janus-like NPs, as the gold domain shows an average diameter similar to that of the semiconductor section.

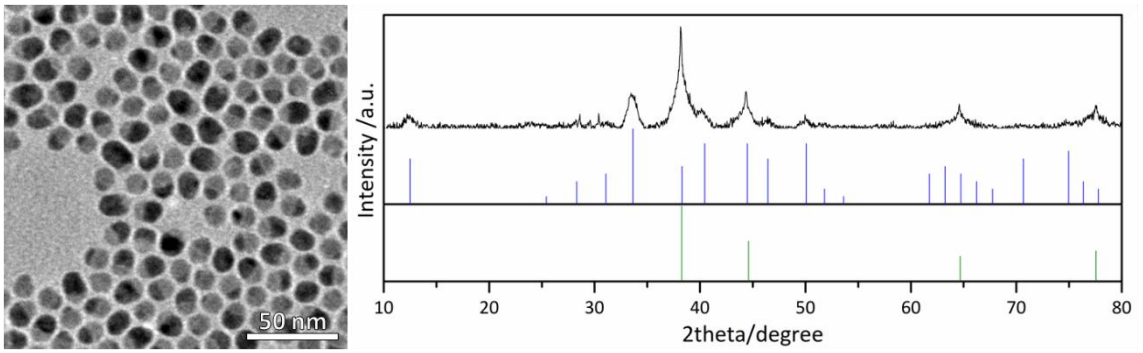

Figure 2.15: TEM micrograph and XRD pattern of Ag-Au-Se_DDA6. Cubic Ag_3AuSe_2 (JCPDS 025-0367, blue) and cubic Au (JCPDS 001-1172, green) reference patterns.

Ag-Au-Se_DDA2 (from now on Au-Ag_2Se HNPs) and Ag-Au-Se_DDA5 (from now on Au-Ag_3AuSe_2 HNPs) samples were observed by HRTEM and analysed by FFT. Moreover, HAADF-STEM and EDX techniques were used for an in-depth structural and chemical characterization. All these measurements were done by Pau Torruella and Dr. Victor Fernández-Altable, both from LENS group and under the supervision of Dr. Sònia Estradé and Dr. Francesca Peiró.

In-depth characterization of Au-Ag_2Se HNPs

HRTEM images (Figure 2.16) of Au-Ag_2Se HNPs showed the same results that were observed by low resolution TEM in Figure 2.11, the NPs had a dimer-like morphology with two different domains. The darker domain was assumed to be metallic Au, which was confirmed by the FFT analyses, where the *d*-spacing values observed in it matched clearly with *fcc* Au. The brighter domain corresponded to the binary semiconductor Ag_2Se, as it was expected. The analysis suggested the two domains were not related by any specific epitaxy, that is to say, the two crystalline lattices are randomly oriented in the nanostructures.

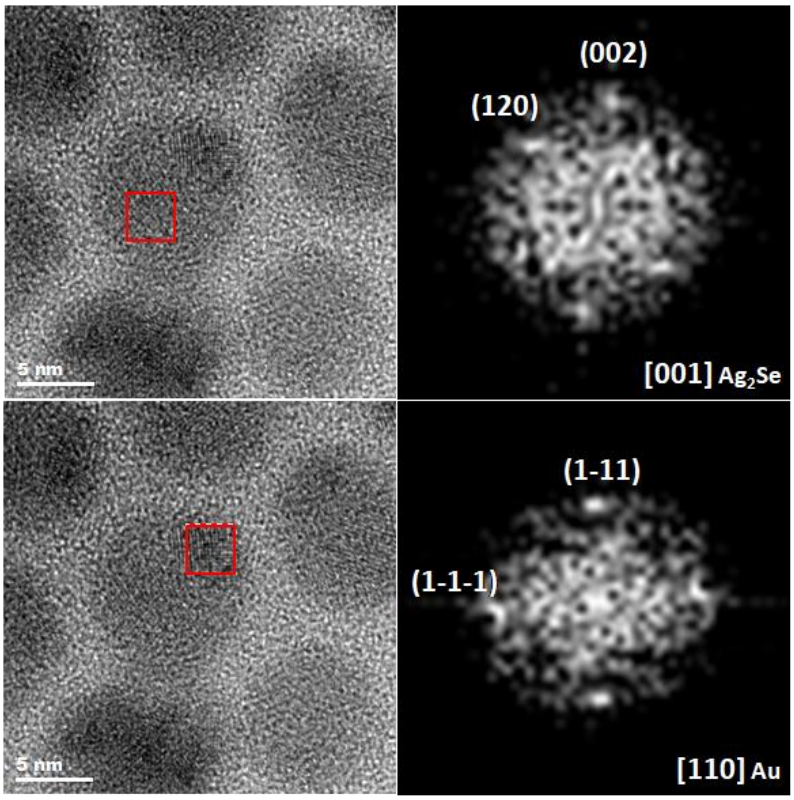

Figure 2.16: HRTEM images and indexed FFT from the corresponding highlighted regions of Au-Ag_2Se HNPs.

Figure 2.17A and C show HAADF-STEM images of two different hybrid nanoparticles of Au-Ag_2Se. A Fourier-filtered image of a region of one of these nanoparticles (Figure 2.17B) showed a good match with a simulated HAADF image of β-Ag_2Se (inset), confirming the crystalline structure of the large domain corresponded to orthorhombic Ag_2Se. EDX elemental mapping performed on the other dimeric NP (Figure 2.17D-G) showed the spatial distribution of Au, Ag and Se elements in the structure. It was clearly seen that the large domain was made, basically, of Ag and Se. The quantitative analyses confirmed the 2Ag:Se stoichiometry, which was expected for Ag_2Se. Apart from that, the analysis also suggested the gold was located almost exclusively at the small domain. Some degree of diffusion of Au(I) into the β-Ag_2Se structure cannot be totally excluded, which agrees with the fact that gold, when aging, started to diffuse to the semiconductor domain, as it has been shown in the previous section.

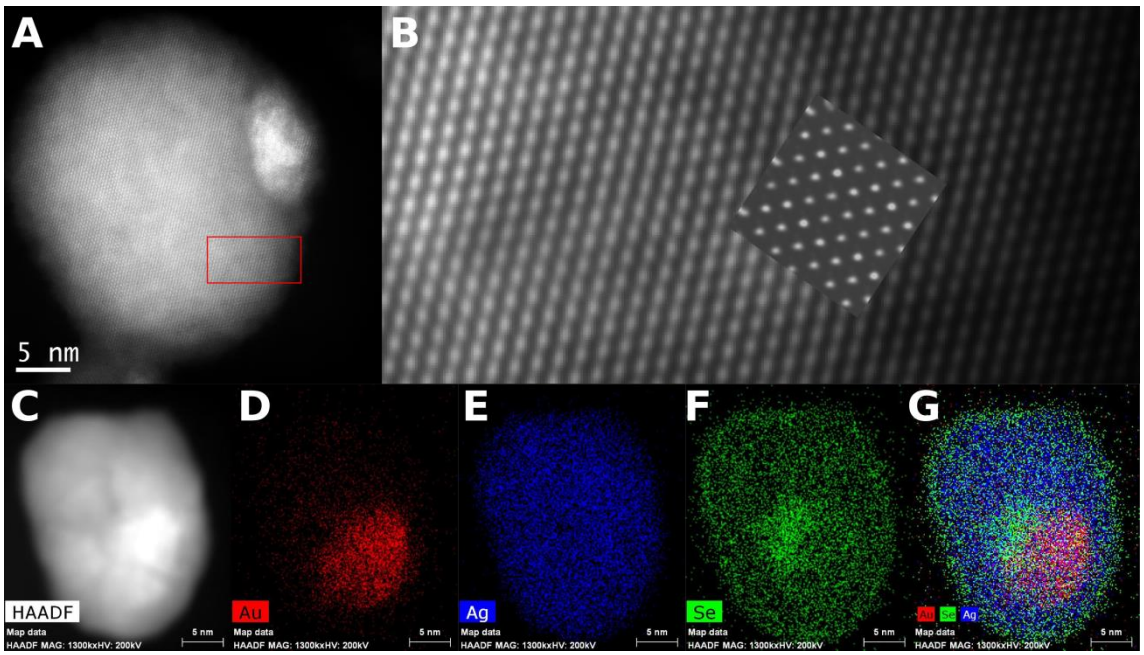

Figure 2.17: (A) HAADF-STEM image of one Au-Ag_2Se HNP. (B) Fourier-filtered image from the highlighted region in panel A. The inset is a STEM-HAADF image simulation of Ag_2Se along the [531] zone axis. (C) HAAD-STEM image of another Au-Ag_2Se HNP. (D-F) EDX elemental maps corresponding to Au (red), Ag (blue), and Se (green), respectively. (G) Panels D-F superimposed.

In-depth characterization of Au-Ag_3AuSe_2 HNPs

HRTEM image and FFT analyses displayed in Figure 2.18 (top panel) confirmed the presence of the cubic phase of Ag_3AuSe_2 in the large domain of Au-Ag_3AuSe_2 sample, which matched perfectly with the previous XRD results. In the top right panel, the most characteristic, and large, interplanar distance of the ternary compound (7.31Å) was identified, which corresponds to the XRD peak at 12.5° originating from the (110) family of planes. In the FFT analysis of the particle shown in the bottom panel, the

small domain was ratified to be metallic gold. In this material the analysis suggested the two domains did not follow any specific epitaxy, the same as for Au-Ag_2Se HNPs.

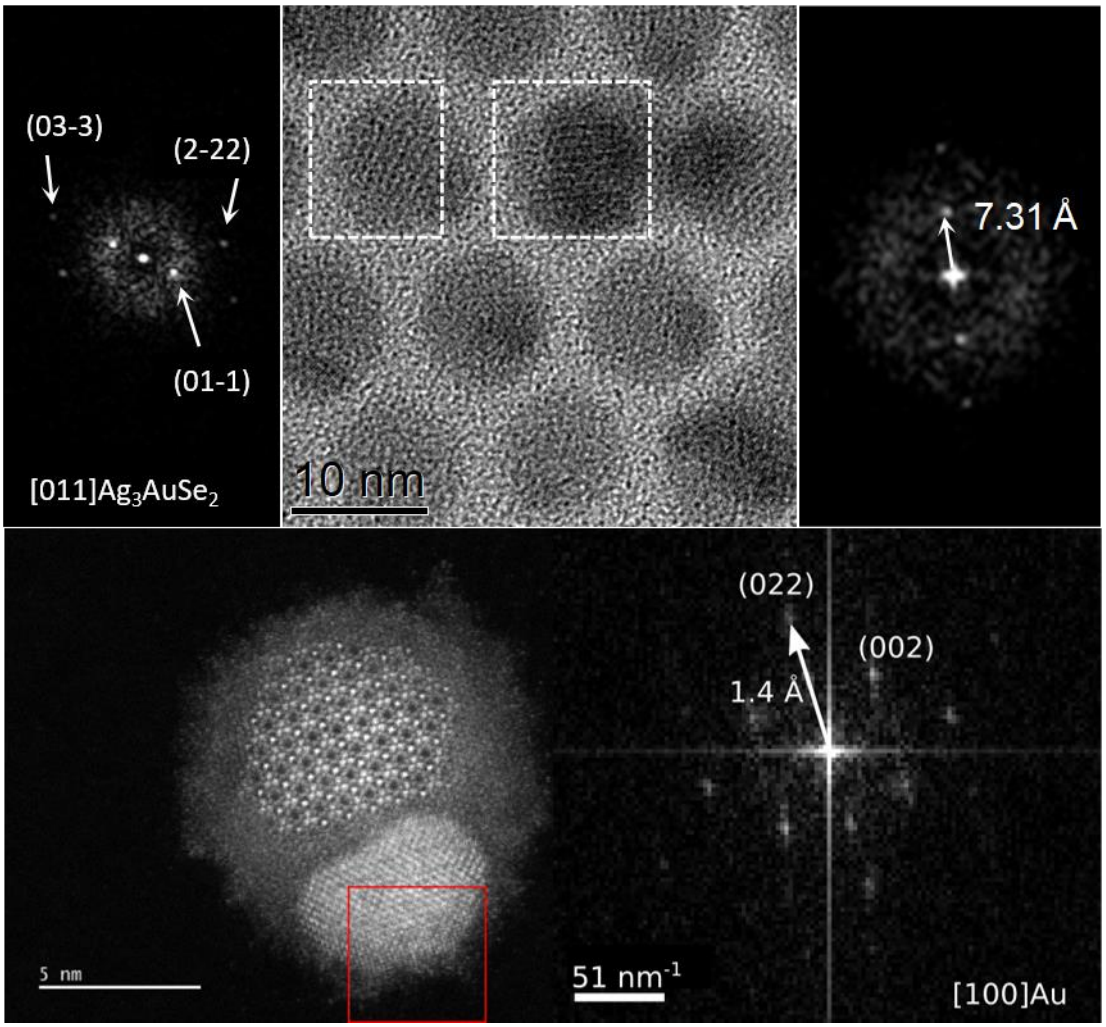

Figure 2.18: (Top panel) HRTEM image of Au-Ag_3AuSe_2 HNPs (Ag-Au-Se_DDA5) and FTT analyses of highlighted zones, confirming the cubic Ag_3AuSe_2 structure of the large domain. (Bottom panel) STEM-HAADF image of a single Au-Ag_3AuSe_2 HNP and FFT analysis of the highlighted zone, confirming the cubic Au structure of the small domain.

STEM-HAADF image simulation of Ag_3AuSe_2 (*fischesserite*) in the [111] zone axis was done (Figure 2.19B) and it was compared with the STEM-HAADF images (Figure 2.19A and C). As observed, both images follow the same structural pattern and symmetry, and one can be seen as the natural continuity of the other. Thus, it was confirmed that the initial Ag_2Se was fully transformed to Ag_3AuSe_2.

EELS of this NP (Figure 2.19D-F) was also acquired to confirm the new expected chemical distribution. The chemical mapping for Au exhibits that gold was distributed all through the particle, although a higher density was found in the region that belongs to the metallic domain. By the quantification of the spectra recorded along the semiconductor section, the Se/Au atomic ratio was obtained. It was close to 2, as

expected from the stoichiometry of the ternary semiconductor. From a different NP, additional EELS measurements were performed (Figure 2.20). In this case, chemical mappings of silver and selenium were acquired. The results indicate the homogeneous distribution of the two species in the inner core. However, the formation of an amorphous outer shell of about 1 nm thickness containing mainly Se was clearly observed. This shell could be also observed in the previous analyses (Figure 2.19). For this reason, the measured Ag/Se ratio was close to unity and consequently slightly lower than theoretical one for Ag_3AuSe_2. The origin of the selenium shell is believed to be an important factor to understand the mechanism of the reaction and it will be discussed later.

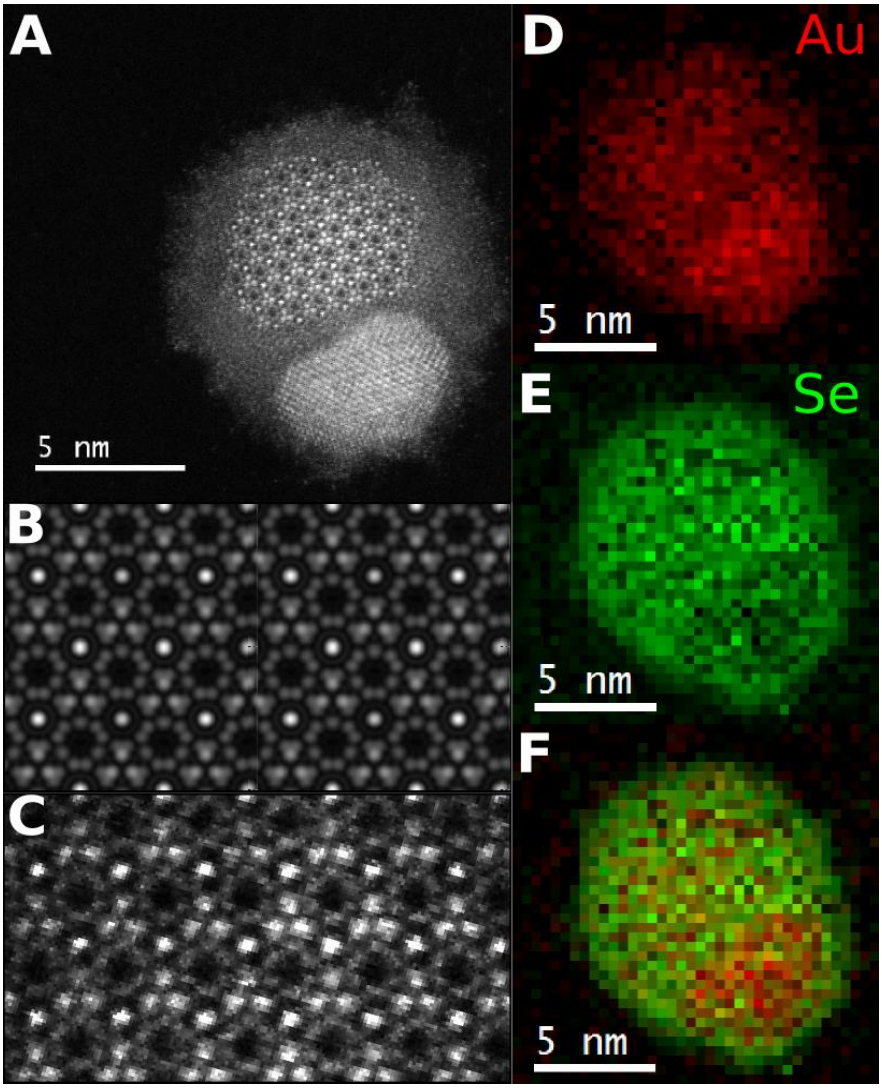

Figure 2.19: (A) STEM-HAADF image of a single Au-Ag_3AuSe_2 HNP. (B) STEM-HAADF image simulation of *fischesserite* (Ag_3AuSe_2) in the [111] zone axis. (C) Zoom of a region from panel A. The image was rotated and contrast adjusted for comparison with the simulation in panel B. (D) EELS Au signal and (E) EELS Se signal from the particle in panel A. (F) Panels D and E superpositions.

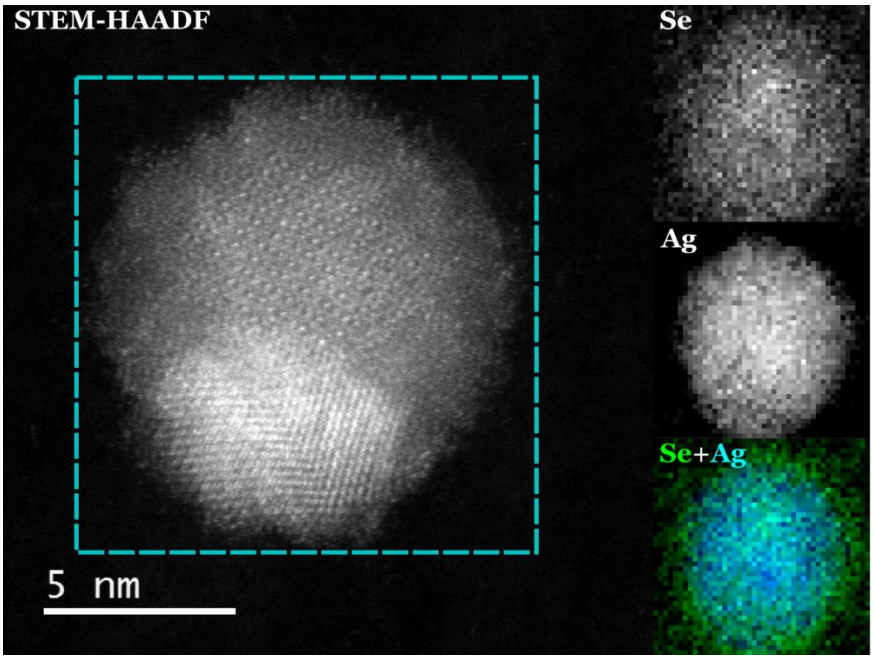

Figure 2.20: EELS quantification of a Au-Ag_3AuSe_2 HNP. The selenium and silver signals were measured on a spectrum image acquired over the highlight region in the STEM-HAADF image.

XPS characterization was also done for this sample by Dr. Jordi Llorca, from the Institut de Tècniques Energètiques i Centre de Recerca en Ciència i Enginyeria Multiescala de Barcelona in the Universitat Politècnica de Catalunya. The analyses, displayed in Figure 2.21, confirmed the presence of Ag (I) and Au(I) species in the sample with a Ag/Au ratio of 3, which was in agreement with previous results. Surprisingly, Au(0) species were not detected in the XPS measurements. Nevertheless, that could be due to the presence of the non-metallic shell, regarding the fact that this technique is surface-sensitive.

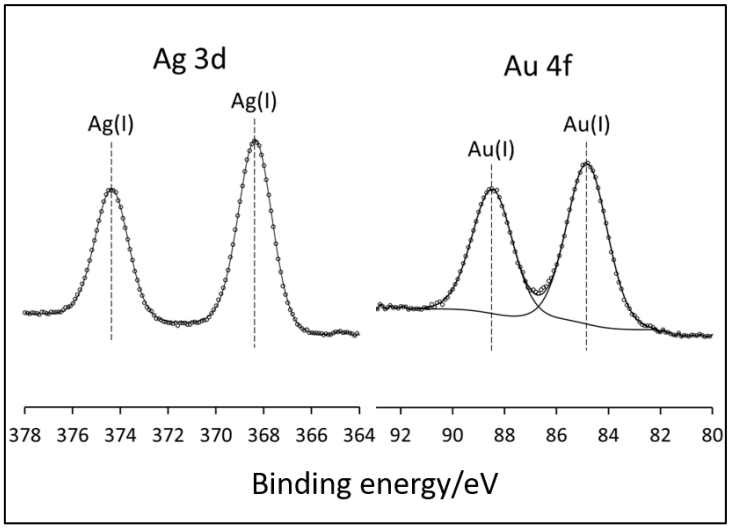

Figure 2.21: XPS spectra of Au-Ag_3AuSe_2 HNPs.

Synthesis of Ag_3AuSe_2 NPs. Influence of the surfactant nature

After the successful syntheses of hybrid Au-Ag_2Se and Au-Ag_3AuSe_2 nanostructures, the next challenge was to synthesise the nanostructured ternary semiconductor without the metallic domain. The first idea was to try to synthesise the material directly from the precursors in a hot injection method, similar to that used for the synthesis of Ag_2Se. However, none of the attempts were prosperous. Hence, it was necessary to think about another procedure.

The partial cation exchange of the procedure used for the hybrid NPs was thought to be a good option. But, avoiding the total reduction of gold and the subsequent deposition on the surface of the semiconductor was essential.

DDA, in the previous procedure, was considered to be the reducing agent of the reaction, so the strategy was to substitute this amine for another surfactant with less reducing potential, such as the tetraoctylammonium bromide (TOAB). In TEM image of this first attempt (sample Ag-Au-Se_TOAB1), displayed in Figure 2.22, it is clearly seen that when using TOAB as surfactant the formation of the metallic domain was avoided, none of the NPs observed in the TEM had a second domain, and the size and the shape of the NPs were similar to the initial Ag_2Se NPs. Nevertheless, regarding the composition of the NPs, although in the XRD pattern A in Figure 2.22 it was possible to identify the peaks from *fischesserite*, there were also more intense peaks which matched with AgBr. The silver bromide is formed upon the reaction between the bromides from the TOAB and the silver cations from the Ag_2Se NPs.

Trying to avoid the formation of this unwanted product, the Au(III) solution was washed several times before the mixture with the NPs with a mixture of H_2O/EtOH 1:1 in order to eliminate the bromides of the solution. Even though the formation of the undesirable product was visibly reduced (as can be observed in XRD pattern B in Figure 2.22, belonging to sample Ag-Au-Se_TOAB2), it was not completely avoided. It seems that bromide did not act just as the counter ion of the tetraoctylammonium cation, but it is also involved in the complexation of gold cation.

Nevertheless, the grey precipitate (of AgBr) was clearly visible in the solution and, as the final NPs were completely stable and the AgBr was not, it was easy to separate from the solution by slight centrifugation before the addition of the ethanol (needed for the purification of NPs from unreacted molecules). In Figure 2.23 TEM images and the XRD pattern of Ag_3AuSe_2 NPs (sample Ag-Au-Se_TOAB3) are shown.

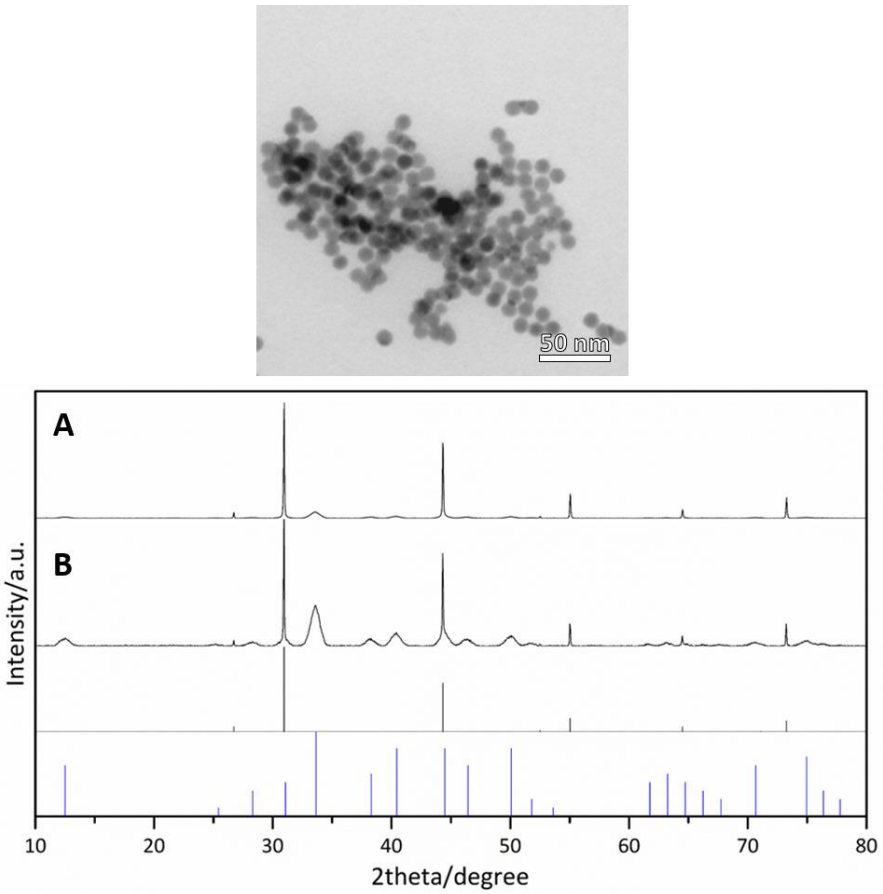

Figure 2.22: TEM micrograph of Ag-Au-Se_TOAB1 and XRD patterns of (A) Ag-Au-Se_TOAB1 and (B) Ag-Au-SE_TOAB2. Cubic AgBr (JCPDS 079-0149, black) and cubic Ag_3AuSe_2 (JCPDS 025-0367, blue) reference patterns.

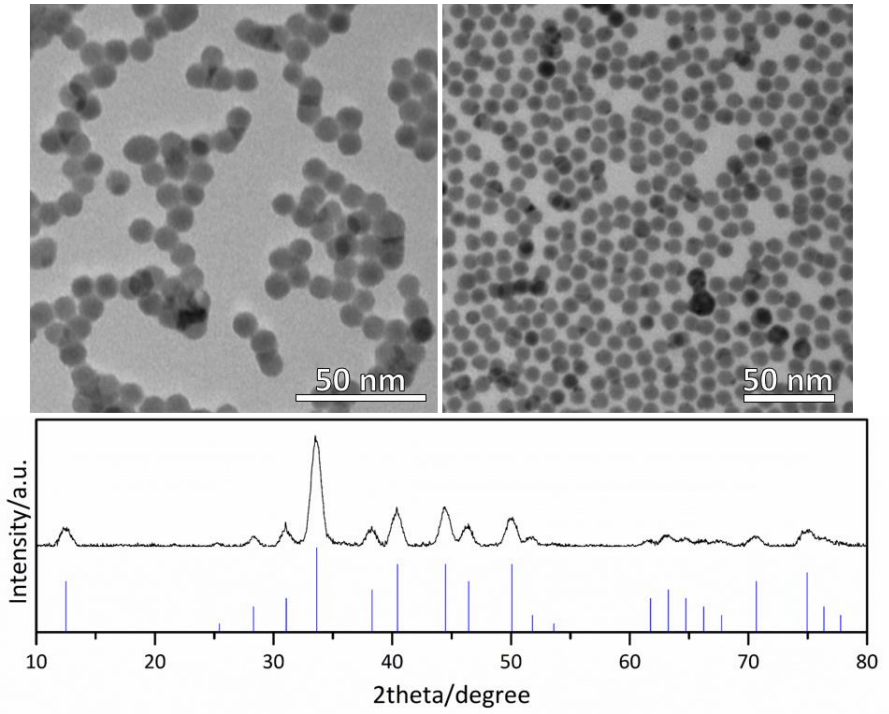

Figure 2.23: TEM images and XRD pattern of Ag-Au-Se_TOAB3. Cubic Ag_3AuSe_2 (JCPDS 025-0367) reference pattern.

In-depth characterization of Ag_3AuSe_2 NPs

These NPs (Ag-Au-Se_TOAB3) were also studied by HRTEM. The analysis showed the single-crystal character of the particles had been generally preserved after the reaction and that the interplanar distances measured corresponded to the cubic Ag_3AuSe_2 structure as further demonstrated through image simulation (Figure 2.24). Curiously, these NPs also had an amorphous shell of about 1 nm, which was clearly seen in the HRTEM image. The chemical analyses by EDX or EELS were not done for this sample, but, considering the composition of the shell in Au-Ag_3AuSe_2 HNPs, it could be assumed that this shell was also made of selenium.

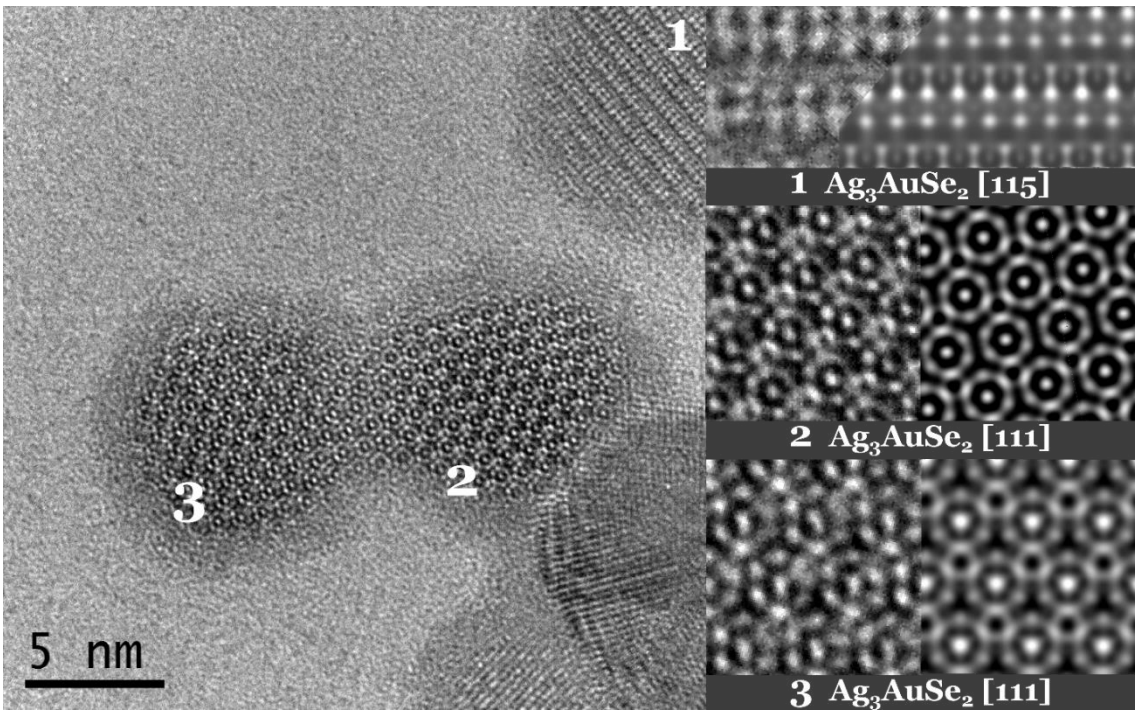

Figure 2.24: (Left) HRTEM image of Ag-Au-Se_TOAB3. (Right) Comparison between experimental and simulated images in the three different zone axes identified in the left-hand side panel.

Reaction mechanism

At the beginning, the amine from DDA (as the reducing agent) was thought to be the responsible of both Au(III) reductions, to metallic gold, as was explained in a previous section, and to Au(I). However, even without the presence of any apparent reducing agent (as it was the case of the Au(III)-TOAB), the Au(III) was reduced to Au(I), although in this case it was not reduced to metallic gold. So, clearly there was another specie that was oxidized.

The presence of the amorphous Se shell in Au-Ag_3AuSe_2 HNPs and Ag_3AuSe_2 NPs help to understand this part of the mechanism. From the fact that precursor Ag_2Se NPs did

not present the shell could be concluded that it was formed as a result of the reaction of the NPs with the Au(III) precursor, either Au(III)-DDA or Au(III)-TOAB. Nevertheless, the fact that the shell was not present in Au-Ag_2Se HNPs indicated its formation was related to the formation of the ternary material and the reduction of Au(III) to Au(I). On the basis of these evidences, Se^{2-} was deduced to be the oxidized specie when Au(III) was reduced to Au(I) and a plausible reaction mechanism for the synthesis of Ag_3AuSe_2 NPs, Au-Ag_3AuSe_2 HNPs and Au-Ag_2Se HNPs is suggested.

The mechanism has two parallel processes:

1) Reduction of Au(III) to metallic Au and growth of a second domain by the amine.

2) Formation of the ternary *fischesserite* phase by partial cation exchange. In this case, first, Au(III) cations were reduced to Au(I) by oxidizing the most external layer of Ag_2Se NPs, which act as a sacrificial shell forming elemental amorphous Se (Eq. 2.1). Secondly, the Au(I) cations diffused through the underlying β-Ag_2Se lattice (core), simultaneously exchanging one-fourth of its Ag(I) cations and leading to the formation of Ag_3AuSe_2 (Eq. 2.2).

$$[Ag_2Se]_{shell} + Au(III) \longrightarrow [Se]_{shell} + Au(I) + 2Ag(I) \quad (2.1)$$

$$2[Ag_2Se]_{core} + Au(I) \longrightarrow [Ag_3AuSe_2]_{core} + Ag(I) \quad (2.2)$$

The second process is expected to take place when using DDA and TOAB as surfactants, although the partial Au(III) to Au(I) reduction competed with the faster Au(III) to metallic Au (first process) in the first case. Both steps of the second process, Ag_2Se oxidation to Se and cation exchange, were accompanied by the release of Ag(I) cations, that precipitated with the bromides or chlorides (if there were any) of the solution.

In a few words, from pre-synthesised Ag_2Se NPs it was possible to synthesise three pure nanostructured materials: Au-Ag_2Se HNPs, Au-Ag_3AuSe_2 HNPs and Ag_3AuSe_2 NPs, just controlling the reaction time, the concentration of the gold solution and the surfactant nature of the gold solution (Scheme 2.1).

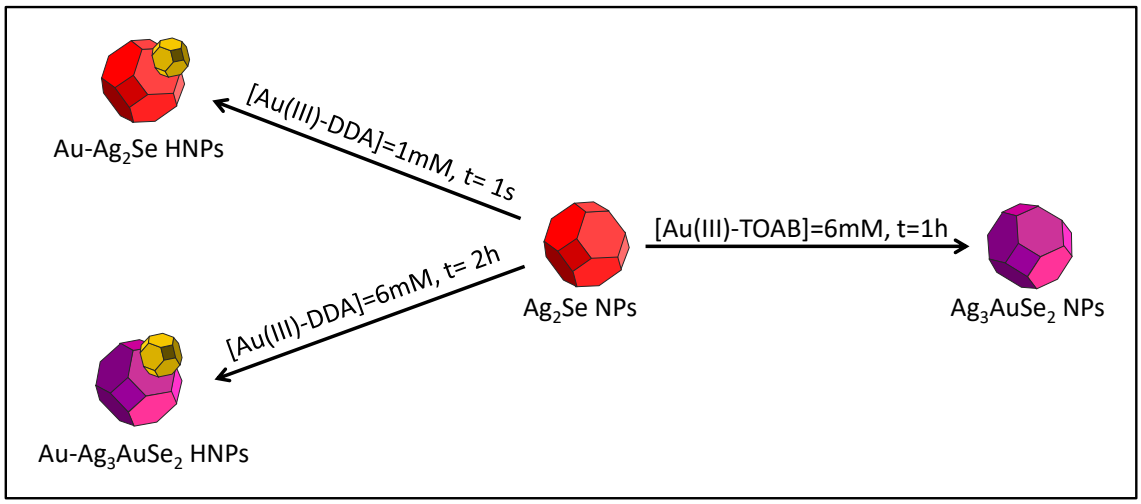

Scheme 2.1: Scheme of the results obtained for Ag-Au-Se system, playing with the surfactant nature, the concentration of Au(III) solution and the reaction time.

Alternative synthetic routes

Two different alternative methods were also tested in order to further study the synthesis of the ternary material, either to synthesise HNPs or just the ternary NPs. Both methods involve the reaction between two pre-synthesised NPs (Ag_2Se NPs and Au NPs), either in solution or in solid-state.

First of all, Au NPs had to be synthesized. In order to facilitate the reaction between the two kinds of NPs, Au NPs were synthesised with a small average diameter of 5 nm, as can be observed in TEM image in Figure 2.25. They were also characterized by Visible absorption spectroscopy, in which it was possible to see the characteristic LSPR band of this nanostructured material at *ca.* 500 nm (Figure 2.25).

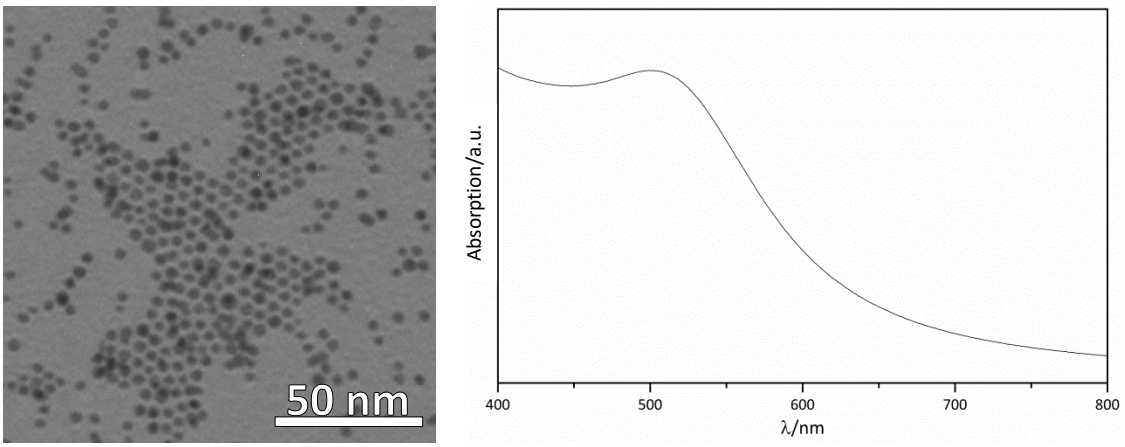

Figure 2.25: TEM micrograph and visible absorption spectrum of Au NPs.

In first place, the reaction in solution was tested. Briefly, it consisted in mixing the two solutions of NPs in toluene and letting react at room temperature in the shaker for 24 hours. Three different ratios of Ag/Au were used: 6/1, 3/1 and 1/1.

In Figure 2.26 TEM images of the three samples are shown. The addition of a larger amount of Au NPs (lower Ag/Au ratios) had two clear consequences. On the one side, a larger number of NPs with two domains in the final product. In the 6/1 ratio just half of the NPs had two domains, whereas in 1/1 ratio, almost every NP had two domains. On the other, an increase of the presence of small nanoparticles in the final solution. Although these small NPs were probably unreacted Au NPs, the fact that they are a byproduct of the reaction cannot go unnoticed and further experiments are needed in order to optimize the procedure.

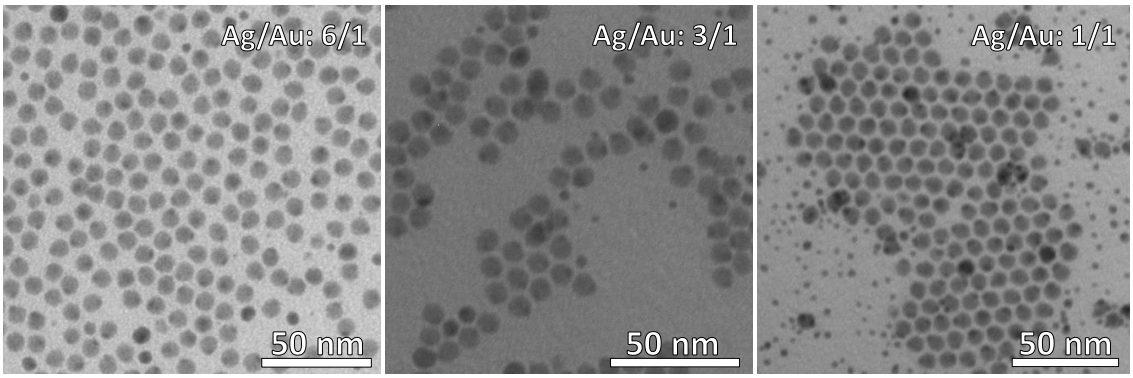

Figure 2.26: TEM images the NPs resulting from the reaction in solution with different Ag/Au ratios (6/1, 3/1 and 1/1).

With respect to the structure and composition of the materials, when using 3/1 and 1/1 ratios the transformation of Ag_2Se to Ag_3AuSe_2 was complete; there were no remaining peaks of the binary phase, while with 6/1 ratio, the conversion was partial. In addition, the XRD patterns (Figure 2.27) show the probable presence of metallic gold. Even though the peaks are broad and have low intensity because of the small size of the nanocrystals, they can be still recognized.

Regarding the mechanism of the procedure, there are no clear evidences of it. However, a possible reaction is suggested: the oxidation of metallic gold to Au(I) and the simultaneously reduction of Ag(I), from the Ag_2Se, to metallic silver. Au(I) cations would subsequently diffuse inside the structure of Ag_2Se, substituting the Ag(I) cation and forming Ag_3AuSe_2 and metallic silver would nucleate as small silver NPs. The resemblance between metallic gold and metallic silver XRD reflections difficults their distinction by XRD. Hence further in-depth characterization would be necessary to confirm this mechanism. Besides, additional experiments should be done in order to control the parameters affecting this reaction and to optimize the synthesis to obtain pure hybrid Au-Ag_3AuSe_2.

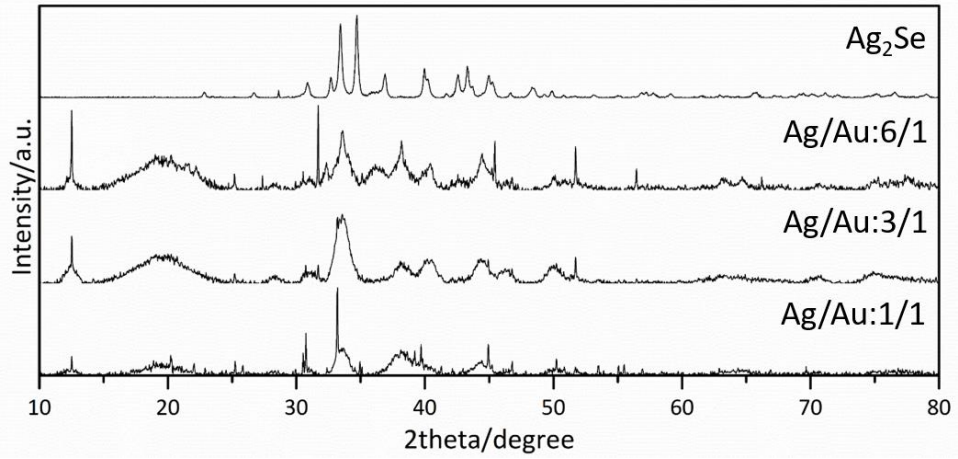

Figure 2.27: XRD patterns of NPs resulting from the reaction in solution with different Ag/Au ratios (6/1, 3/1 and 1/1).

Secondly, two experiments in solid state were carried out. These tests were done inside the powder X-Ray Diffractometer, acquiring spectra at different temperatures under vacuum conditions. In the first experiment, to guarantee the perfect mixture of the two materials (Ag_2Se NPs and Au NPs) were previously dispersed in toluene, mixed, precipitated by the addition of ethanol, centrifuged and dried. In Figure 2.28, the XRD spectrum of the sample before starting the heating is shown. It was a mixture of β-Ag_2Se, Au and Ag_3AuSe_2. The presence of the ternary material was not expected before the heating, and it was probably due to the reaction in solution during the mixture of the materials. The crystallographic evolution of the sample can be observed in XRD patterns of Figure 2.29. Basically, it seems that the two materials were not reacting: only the phase transition from β-Ag_2Se to α-Ag_2Se at 150°C (Figure 2.30) and the sintering of gold could be observed, the latter detected by the sharpening and intensification of the Au XRD reflections. In all the patterns from 450°C to 700°C and back to room temperature, the only peaks observed were those from gold, so clearly the sintering was not a reversible process.

A second experiment was carried out. In order to avoid the previous formation of Ag_3AuSe_2, the mixture of pre-synthesised NPs was done by dispersing and mixing them in ethanol, as they are not stable in this solvent, the reaction may be more difficult to take place. Additionally, the amount of gold was reduced to avoid a huge excess of this reactant, and the maximum temperature reached was decreased to 200°C to minimize the sintering of gold. XRD pattern at room temperature before the heating (Figure 2.31A) showed the mixture of the two materials (β-Ag_2Se and Au), although gold reflections were less intense, and no traces of the Ag_3AuSe_2 ternary material were detected before heating the sample. When the temperature was increased (Figure 2.31B) two different phenomena were observed: the Ag_2Se phase transition at 120°C (Figure 2.32) and the sintering of gold. When the sample was cooled and room

temperature was recovered, only the initial β-Ag_2Se structure was found in the sample, as expected from this reversible phase transition.

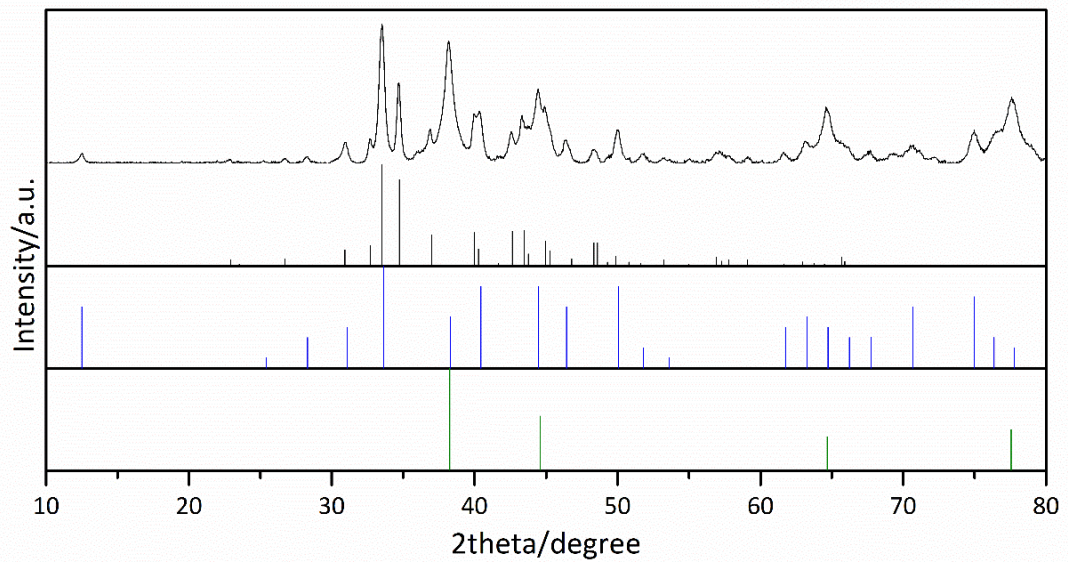

Figure 2.28: XRD pattern of mixture of Ag_2Se NPs and Au NPs before heating. Orthorhombic Ag_2Se (JCPDS 024-1041, black), cubic Ag_3AuSe_2 (JCPDS 025-0367, blue) and cubic Au (JCPDS 001-1172, green) reference patterns.

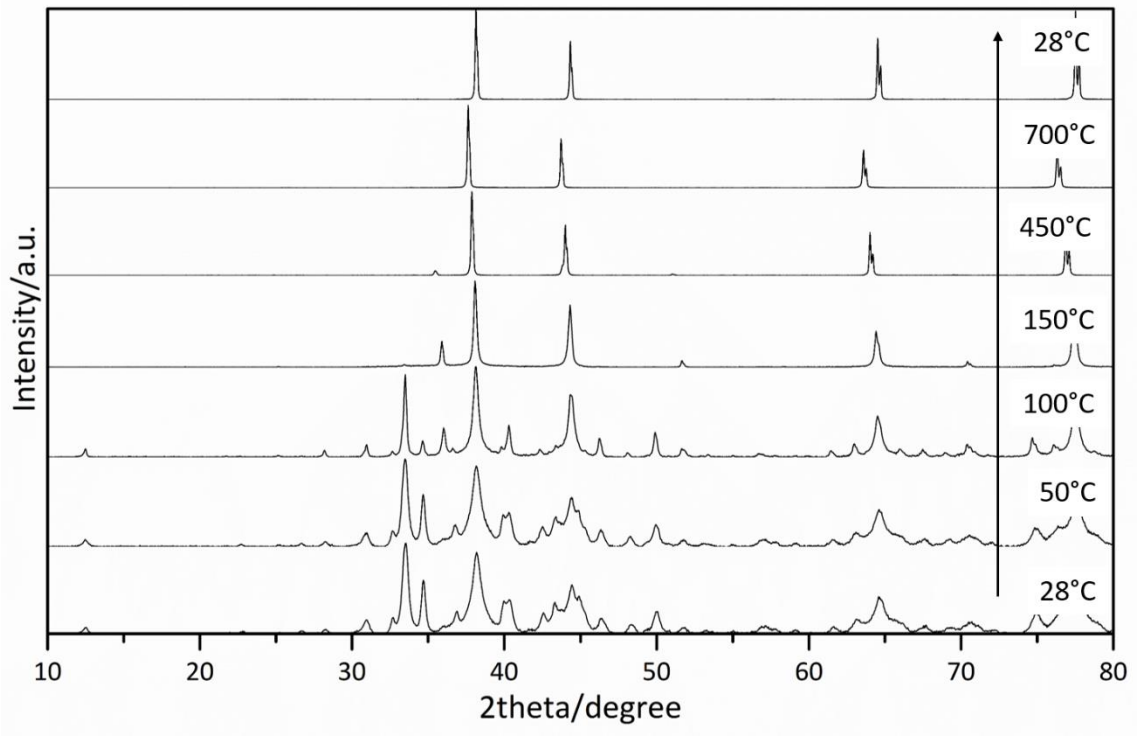

Figure 2.29: Temperature-depending XRD patterns of the solid-state experiment 1.

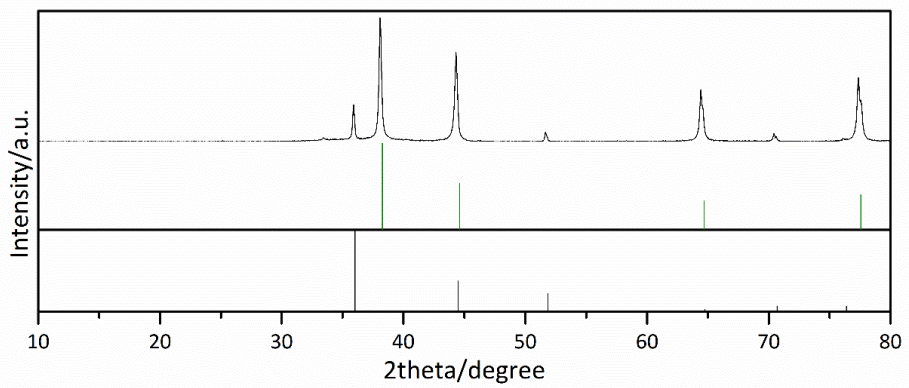

Figure 2.30: XRD pattern of solid-state experiment 1 at 150°C. Cubic Ag_2Se (JCPDS 076-0135, black) and cubic Au (JCPDS 001-1172, green) reference patterns.

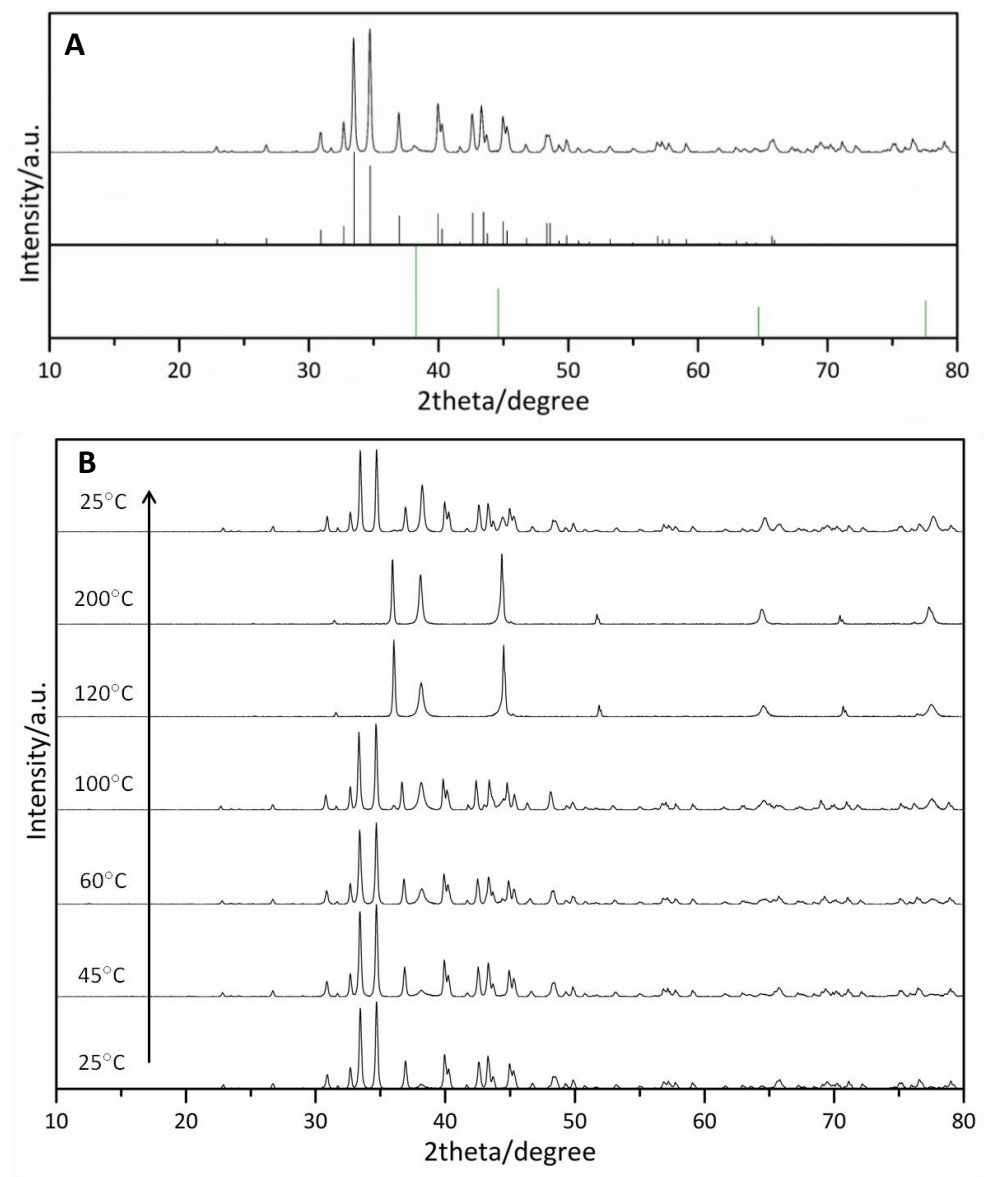

Figure 2.31: (A) XRD pattern of solid-state sample of experiment 2 before heating process. Orthorhombic Ag_2Se (JCPDS 024-1041, black) and cubic Au (JCPDS 001-1172, green) reference patterns. (B) Temperature-depending XRD patterns of the solid-state experiment 2.

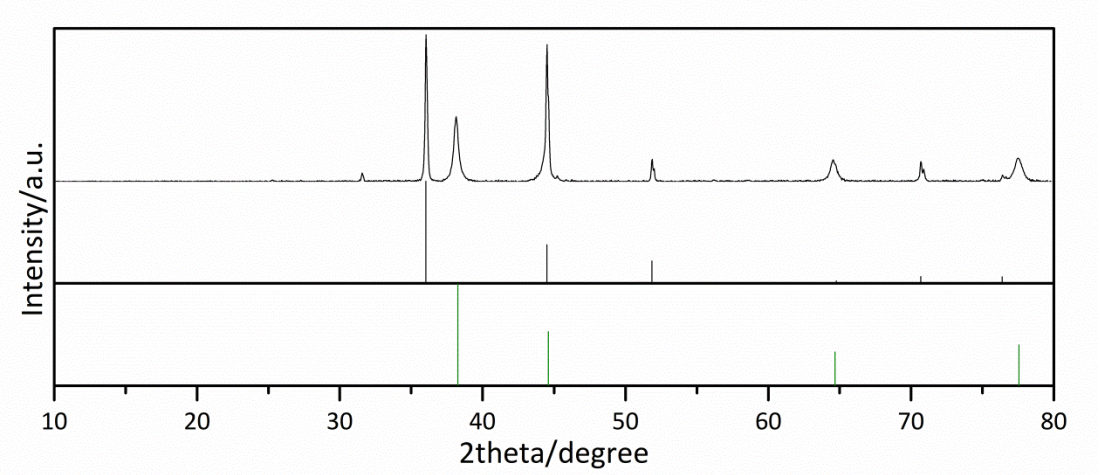

Figure 2.32: XRD pattern of solid-state experiment 2 at 120°C. Cubic Ag_2Se (JCPDS 076-0135, black) and cubic Au (JCPDS 001-1172, green) reference patterns.

Even though only a first tests were done and the characterization was not deep, these alternative experiments demonstrate that the formation of ternary Ag_3AuSe_2 from pre-synthesised Ag_2Se NPs only works in solution, either with Au(III) precursor or Au NPs as gold source. In solid state conditions the oxidation of gold is not possible, even at high temperature.

2.4 Optical characterization of Ag_2Se NPs and Ag-Au-Se systems

UV-Vis-NIR characterization of Ag_2Se NPs and Au-Ag_3AuSe_2 hybrid NPs was carried out. Both materials had a continuous absorption between 400 and 2500 nm. Bulk β-Ag_2Se is known to have a 0.15-0.18eV (6888-8265 nm) bang gap energy. When going to the nanoscale, the material might experience quantum confinement and the band gap energy, as in most of the semiconductors, can be tuned with the size or shape of the NP. Several Ag_2Se nanocrystals of 2 to 3.4 nm of average diameter exhibiting absorption features between 550 and 1000 nm have been reported.[137,139,169–173] However, when Ag_2Se NPs are larger than 6 nm are more weakly confined since they are larger than the Bohr diameter of the material, regarding to the calculations of Norris and co-workers.[147] As a consequence, their bang gap shifts to higher wavelengths.

In Vis-NIR absorption spectrum of synthesised Ag_2Se NPs (Figure 2.33) any discrete absorption feature was observed, as expected regarding the large size of the nanocrystals (11 nm).

In the case of dimer-like Au-Ag_3AuSe_2 HNPs, at 600nm approximately, a shoulder can be observed. This absorption could be due to two different factors: the LSPR of the

metallic domain or an instrinsic absorption of the ternary semiconductor material. The fact that the spectrum of Janus Au-Ag_3AuSe_2 NPs, which had a bigger metallic domain, presented a clear LSPR band supports the former. As the LSPR is a surface phenomenon, the band may shift depending on the size of the gold domain or the surroundings, so, the smaller size of the metallic domain in dimer-like Au-Ag_3AuSe_2 HNPs might be the cause of the lower intensity and the red shifting of the band feature in comparison with the one of Janus NPs. Nevertheless, the presence a broad band at the same wavelengths in the spectrum of ternary Ag_3AuSe_2 NPs indicates that the band can be considered also an intrinsic absorption of the material. The possible origin of this band is unknown since the material in its nanostructured form has not been deeply studied yet.

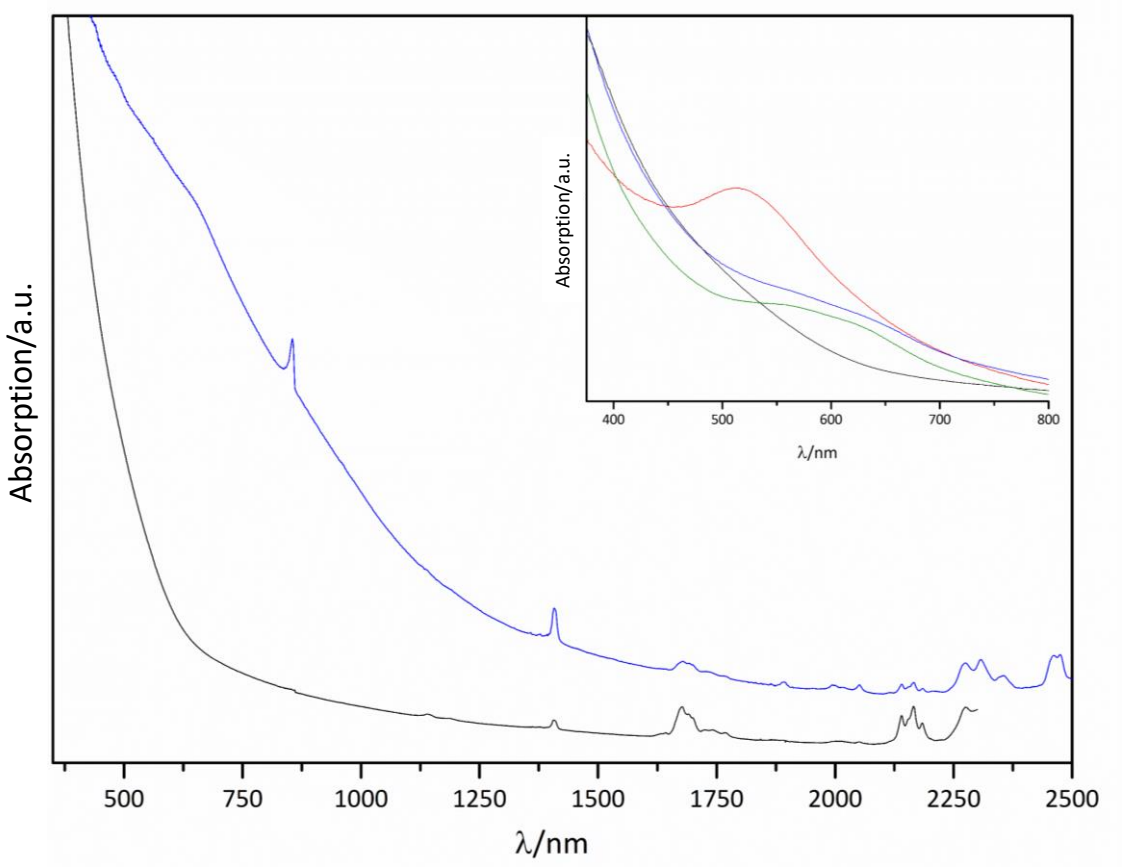

Figure 2.33: UV-Vis-NIR absorption spectra of Ag_2Se NPs (black), Au-Ag_3AuSe_2 HNPs (Ag-Au-Se_DDA5, blue), Ag_3AuSe_2 NPs (Ag-Au-Se_TOAB3, green) and Au-Ag_3AuSe_2 Janus NPs (Ag-Au-Se_DDA6, red).

2.5 Thermoelectric characterization of Ag_2Se NPs, Ag_3AuSe_2 NPs and Au-Ag_3AuSe_2 HNPs

The thermoelectric effect, also known as the Peltier-Seebeck effect, is the direct conversion of heat into electricity or viceversa.

Thomas J. Seebeck, in 1821, discovered that a needle of a compass magnet was deflected when it was in the presence of a circuit made from two dissimilar metals with junctions at different temperatures.[174] This phenomenon was due to the fact that both metals were responding differently to the temperature, creating an electric current which induced a magnetic field and deflect the magnet. The voltage developed from the temperature gradient is related to an intrinsic property of the materials called the Seebeck coefficient, which is very low for metals but quite large for semiconductors. A related effect was discovered by Peltier, in 1834, when he observed that when an electrical current was applied through a junction of two dissimilar materials, either heating or cooling could occur at the junction, depending on the direction of the current.[175]

Briefly, in that junction is happening the following: when a difference of temperature is applied to the materials, in the hot end, electron/hole pairs are created, absorbing heat in the process. Afterwards, these electrons/holes are diffusing from the hotter side to the cooler side and, once at the cold end, they recombine, rejecting some heat in the process. As it is well known, the electrical current in semiconductors is propagated by electron/hole movement, so, this movement is creating a voltage potential: the Seebeck voltage. Although just one material can be used as a thermoelectric device, the generated voltage is low, so, in order to increase it, usually many materials are connected together. The alternation of *p*-type and *n*-type materials gives more efficiency to the device, so a real device should have many pairs of *p*-*n* materials. In Figure 2.34 a schematic draw of a thermoelectric device with a pair of *p*-*n* materials is shown.

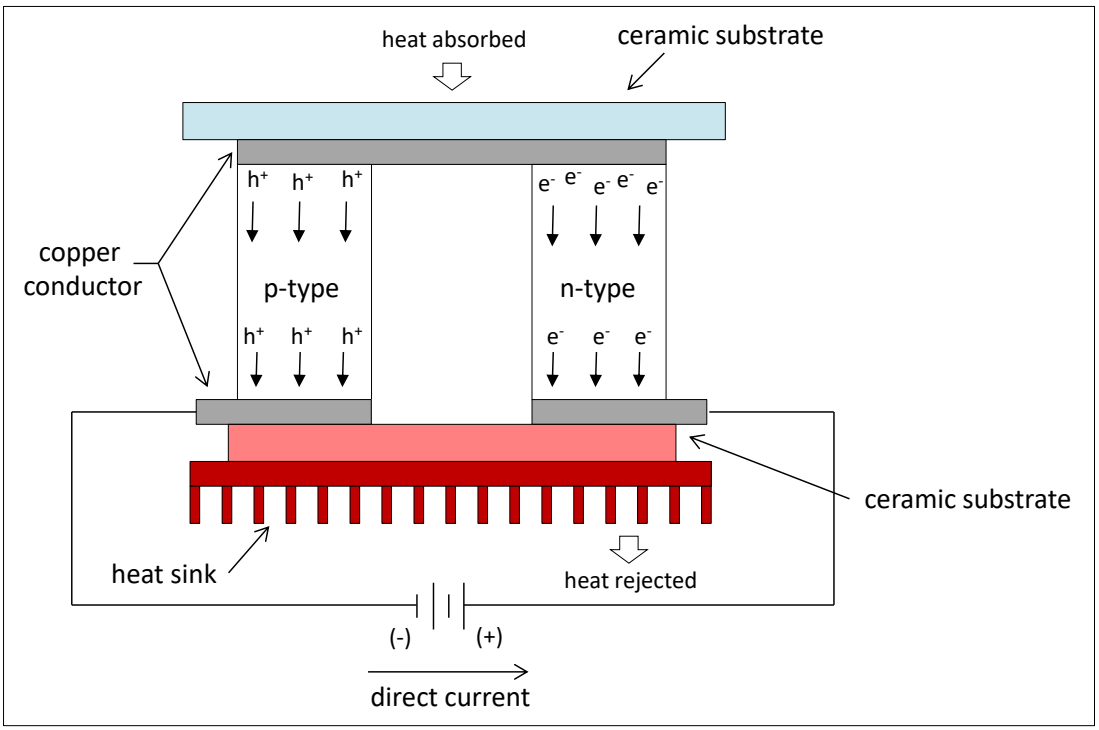

Figure 2.34: Schematic draw of a thermoelectric device.

A good thermoelectric material is expected to have some specific properties, which make it more suitable to the process. In the first place, the material needs to have a high electrical conductivity in order to have a quick movement of electrons/holes through it. In the second place, it is necessary to have a low thermal conductivity to maintain the temperature gradient between the two ends of the device and, finally, having a good Seebeck coefficient is also important. Seebeck coefficient (S) is the ratio of the voltage developed to the temperature gradient (S=ΔV/ΔT) and it is intrinsic for each material. Depending on the conduction type, the Seebeck coefficient presents different signal. When the material has a *p*-type conduction, the Seebeck coefficient has a positive value, whereas it has negative value when the material has a *n*-type conduction. The thermoelectric behaviour is measured by the figure of merit (*ZT*), whose formula includes all the parameters exposed before (Eq. 2.3).

$$ZT = \frac{S^2\sigma}{\kappa}T \qquad (2.3)$$

S is the Seebeck coefficient, σ is the electrical conductivity, κ is the thermal conductivity and T is the temperature. The improvement of thermoelectric behaviour is challenging, because all three parameters (Seebeck coefficient, electrical and thermal conductivities) are affected by the electronic properties and thus, they are all correlated. Usually when a material has a good electrical conductivity it also shows a large thermal conductivity; and the Seebeck coefficient decreases when the electrical conductivity increases. So, optimizing these properties simultaneously is necessary but it is also a hard task.[176,177]

Apart from the ability of the material to give thermoelectric performance (measured by the *ZT*), the usefulness of the material in a thermoelectric generator is another important parameter to be considered. It is measured by the Power factor, which is calculated from the Seebeck coefficient and the electrical conductivity (Eq. 2.4).

$$PF = \sigma \cdot S^2 \qquad (2.4)$$

The ability of thermoelectric materials of harvesting electricity from heat or viceversa, makes them suitable for many applications as power generators (using the sun, the human body or heat waste of different processes as heat suppliers), gas sensors, temperature sensors or water collectors.[178–180]

In the last two decades it has been shown that the nanostructuration of the materials is an effective way to enhance their thermoelectric behaviour. At the beginning, nanostructured materials were proposed because of the improvement in the Seebeck coefficient, which can be enhanced by several factors. However, the presence of multiple interfaces and their ability to scatter phonons and reduce the thermal conductivity became more important in the devices. Basically, the lattice component

of the thermal conductivity is due to the heat transported by phonons and it is low for disordered or amorphous materials, so having a huge number of interfaces which scatter phonons reduce the thermal conductivity and enhance *ZT*.[178,181–183]

Chalcogenides materials are typical thermoelectric materials. The possibility to synthesise different chalcogenide semiconductors with diverse energy band gaps over a range of temperature make them suitable for this kind of application.[184] Ag_2Se, as part of this family of materials, is well known to be a good thermoelectric semiconductor. Several publications about it can be found in the literature. Although most of these publications are focused on the bulk structure,[114,185–187] Xie and co-workers have reported satisfactory thermoelectric results for Ag_2Se nanocrystals, and they have enhanced the behaviour with a ternary Ag_4SeS nanostructured material.[115] Other groups have been working on other silver chalcogenide-based nanomaterials, such as AgCuSe,[188–190] $AgSbSe_2$,[191–193] $AgBiSe_2$,[194–196] which are also emerging as promising thermoelectric materials because of their improved ionic and electronic mobilities and ultralow thermal conductivities.

Regarding noble metal derivatives of nanocrystalline silver chalcogenides, there is very little about them. Au-Ag_3AuSe_2 hybrid nanostructured material was thought to be a good candidate in thermoelectric applications. Apart from the different crystalline and electronic structure of the semiconductor which can give a different Seebeck coefficient, the presence of a second domain could introduce an effective interface to scatter phonons and reduce the thermal conductivity. Nevertheless, the amount of metal in the structure should be maintained low to avoid a counter-productive effect, like for instance the increase of *k*.

The thermoelectric characterization was done in collaboration with Dr. Andreu Cabot. All the measurements were carried out in his laboratory in IREC (Institut de Recerca en Energia de Catalunya) by Dr. Maria Ibáñez and Dr. Doris Cadavid.

To evaluate the thermoelectric properties of the hybrid Au-Ag_3AuSe_2 nanocomposite, a pellet was made of 50% of Au-Ag_3AuSe_2 dimer-like HNPs and 50% of Ag_2Se NPs. This mixture was done to keep the total metal concentration relatively low. To use as references in the thermoelectric studies, two analogous pellets of Ag_2Se NPs and Ag_3AuSe_2 NPs were also prepared and measured.

Extra characterization of the pellet, after the annealing and consolidation process, was necessary to understand better the thermoelectric performance of the sample. The morphology and chemical composition of the Ag-Au-Se nanocomposite pellet were highly homogeneous at the micrometer scale, as it was observed by Field Emission SEM (FESEM) (Figure 2.35A and B) and EDX. However, at the nanometric scale a uniform distribution of compositional inhomegeneities were observed by HRTEM (Figure 2.35C). By FTT analyses only two phases were detected: Ag_2Se and Ag_3AuSe_2.

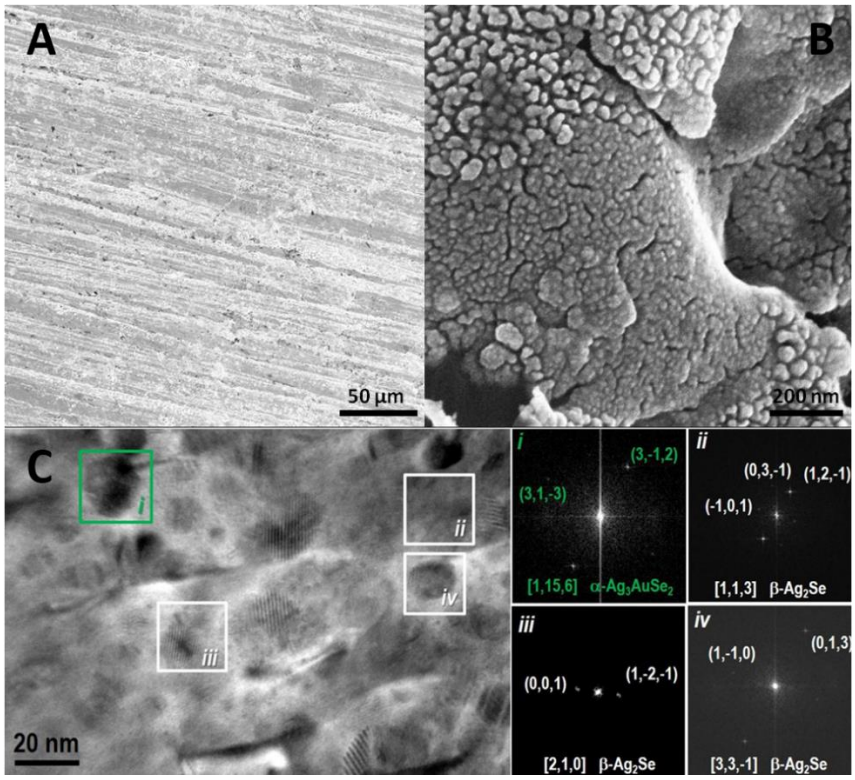

Figure 2.35: (A) and (B) FESEM images and (C) HRTEM image and FFT analysis of the Ag-Au-Se nanocomposite pellet.

Nevertheless, when a full chemical characterization of the pellet was done by X-Ray Absorption Spectroscopy (XAS) (Figure 2.36), the presence of three different phases was confirmed: Ag_2Se, Ag_3AuSe_2 and metallic Au. Hence, although it was not detected by HRTEM, the pellet contained metallic Au. XAS uses the absorption of X-Rays to determine the local geometric and electronic structure of a sample. When the energy of the X-Ray beam is similar to the binding energy of a specific core electron the absorption increases drastically, which is known as the absorption edge. The near edge region, which was the one used in this case (XANES), is sensitive to the coordination and oxidation state of the absorbing atom. The increase of the crystal size of the NPs caused by the annealing process was obvious from the XRD pattern (Figure 2.37), in which the reflections become narrower.

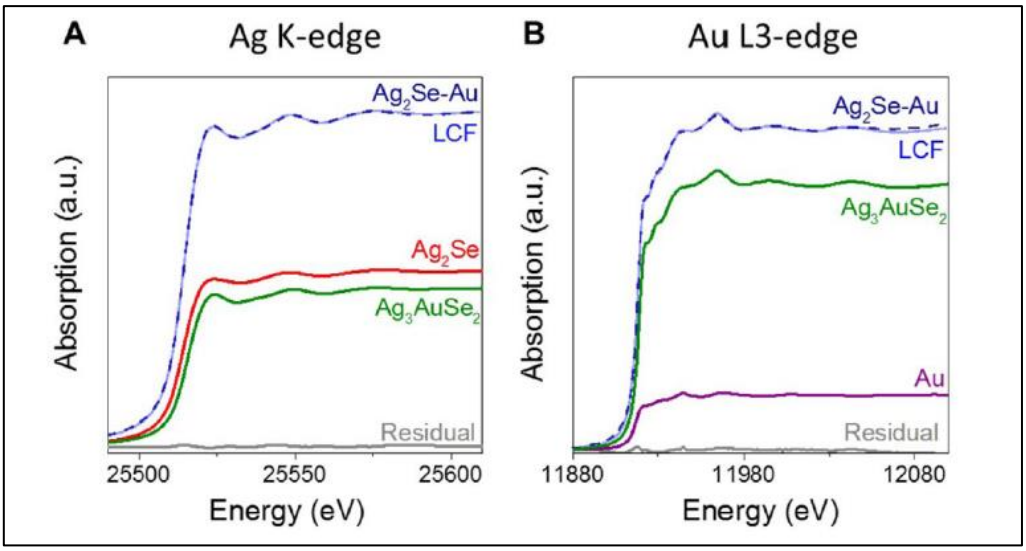

Figure 2.36: Linear combination fit of XANES of the Ag-Au-Se nanocomposite pellet at (A) Ag K-edge and (B) Au-L3. In green, the weighted Ag_3AuSe_2 spectrum, in purple, the weighted metallic Au spectrum and in red, the weighted Ag_2Se NPs spectrum, contributing to the fit of the Ag-Au-Se nanocomposite spectrum (dotted blue line).

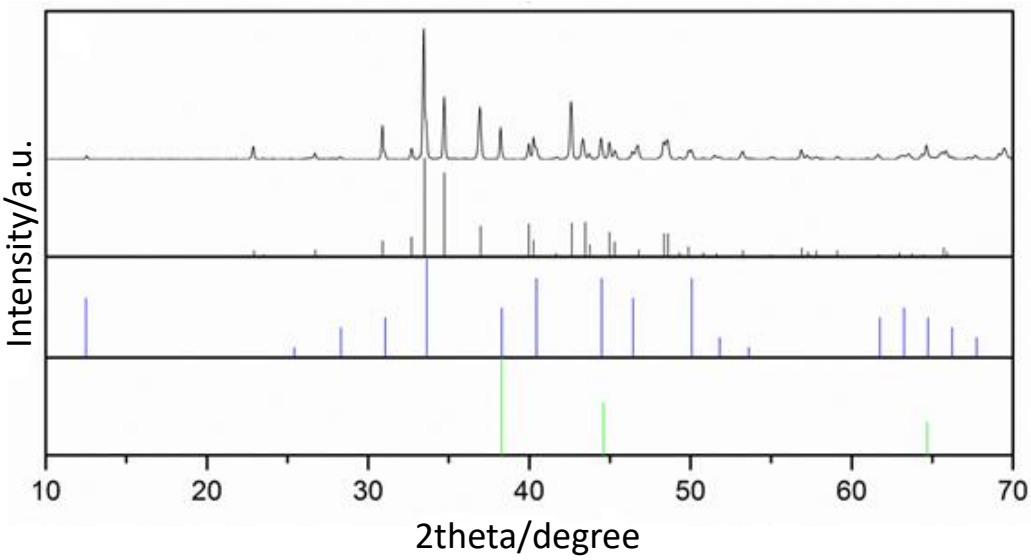

Figure 2.37: XRD pattern of Ag-Au-Se nanocomposite pellet. Orthorhombic Ag_2Se (JCPDS 024-1041, black), cubic Ag_3AuSe_2 (JCPDS 025-0367, blue) and cubic Au (JCPDS 002-1095, green) reference patterns.

Thermoelectric characterization for Ag-Au-Se nanocomposite, Ag_2Se and Ag_3AuSe_2 pellets is shown in Figures 2.38 and 2.39. The thermoelectric performance of Ag-Au-Se nanocomposite was found to be better than the performance of Ag_2Se. Both materials showed a change of the thermoelectric properties around 400 K, which was associated to the phase transition from the low temperature orthorhombic Ag_2Se to the high temperature cubic Ag_2Se. The high ionic conductivity of the cubic phase enhanced the

electrical conductivity of the materials due to the contribution of the Ag^+ charge carriers. However, this contribution was detrimental for Seebeck coefficient, as Ag^+ ions are *p*-type carriers, and Ag_2Se has *n*-type conduction.

The electrical conductivity of Ag-Au-Se nanocomposite pellet was two-fold lower than Ag_2Se, but the 50% higher Seebeck coefficient were translated to a higher power factor value. Electrical conductivity and Seebeck coefficient of ternary Ag_3AuSe_2 were also measured. The material had very high Seebeck coefficients at temperatures above 450K, but the low electrical conductivity strongly limited its power factor values.

Regarding to the thermal conductivity, the hybrid material had particularly low values because of a more efficient phonon scattering at the grain boundaries enhanced by the acoustic impedance mismatch of Ag_2Se, Ag_3AuSe_2 and Au domains. As a consequence, the thermoelectric performance of the hybrid nanocomposite was clearly better when compared to the binary material Ag_2Se. Specifically, the best thermoelectric performance for the pellet Ag-Au-Se was found to be around 390K, with a value of *ZT* of 0.88. This value is not particularly high regarding to the literature. Nowadays, values between 1 and 1.5 are usually observed, even though extraordinary values up to 2.6 has also been recorded for some materials.[178,197]

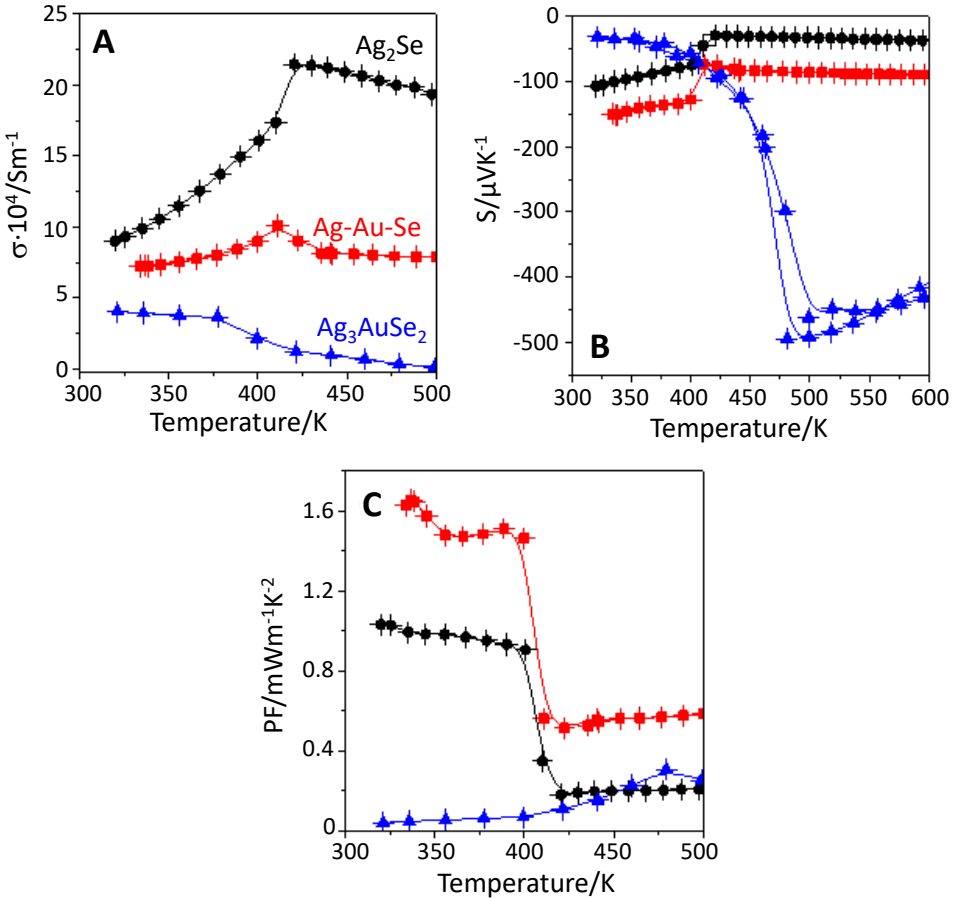

Figure 2.38: (A) Electrical conductivity, (B) Seebeck coefficient and (C) Power factor of Ag_2Se NPs (black), Ag-Au-Se nanocomposite (red) and Ag_3AuSe_2 NPs (blue).

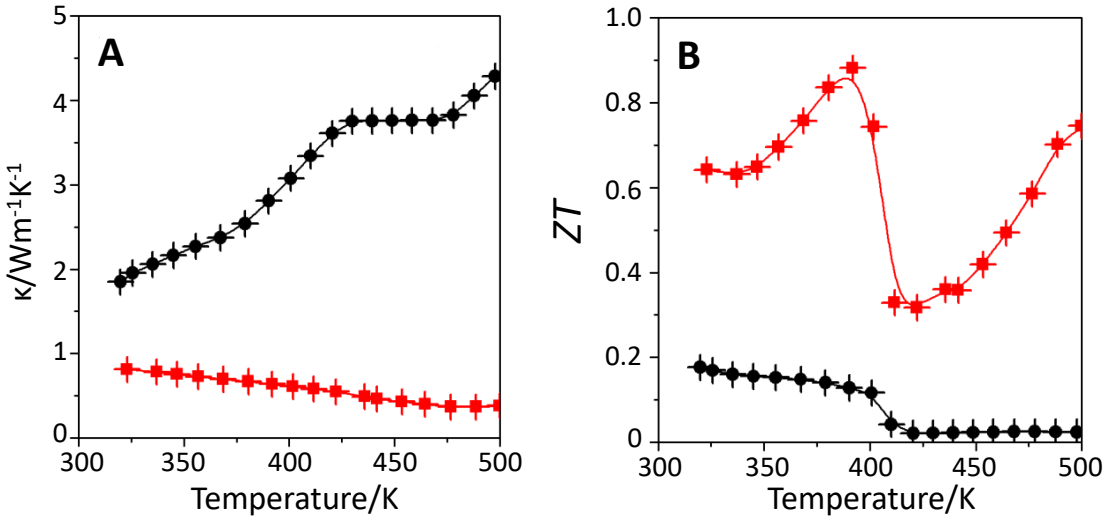

Figure 2.39: (A) Thermal conductivity and (B) figure of merit of Ag_2Se NPs (black) and Ag-Au-Se nanocomposite (red).

2.6 Application of Ag_3AuSe_2 NPs as X-Ray Computed tomography contrast agents

In addition to their possible application in thermoelectric devices, Ag_3AuSe_2 NPs were also tested as contrast agents for X-ray computed tomography. This work was done in collaboration with the group of Dr. Manuel Pernia from BIONAND (Andalusian Centre for Nanomedicine and Biotechnology) and Universidad de Sevilla.

Computed tomography (CT) is a diagnostic tool which provides 3D images with high spatial resolution, based on X-Ray intensity attenuation by the interaction with an object. Basically, a CT image is created from the series of attenuation profiles/projections acquired by rotating an X-ray source around an object with a detector positioned directly opposite to the radiation source (Figure 2.40). Usually, the scans are taken at small angular increments during the rotation around the object.

In general, materials which possess higher density (ρ) or high atomic number (Z) tend to absorb better X-Ray, so their X-ray absorption coefficient (μ) is higher. In equation 2.5 the relationship between these parameters is expressed:

$$\mu = \frac{\rho Z^4}{AE^3} \qquad (2.5)$$

where A is the atomic mass and E is the X-ray energy.

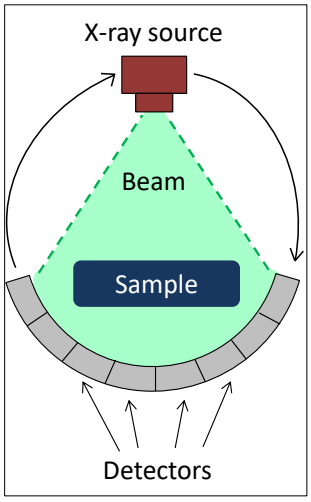

Figure 2.40: Schematic drawing of a CT system.

Apart from that, when the X-ray energy is equal or slightly greater than the binding energy of K-shell electrons of the atom (electrons from the shell closest to the nuclei of the atom), there is a large increase of the absorption coefficient. As a consequence, atoms of high atomic number have a higher contrast of the attenuation of the X-ray.

Although most of body tissues can exhibit contrast, it is difficult to image and identify the interface between two adjacent tissues or image soft tissues in contact with blood or other physiological fluids. Therefore, the use of contrast agents is necessary to enhance sensitivity and contrast and to have a better visualization of the tissue of interest. Besides, they can provide specific biochemical information of a tissue. In order to have a higher X-ray attenuation, the contrast agents usually are high atomic elements as iodine, barium and bismuth.

Specifically, nowadays the most used compounds as contrast agents are barium sulphate suspensions and iodinated molecules. Nevertheless, these contrast agents show, also, important drawbacks, such as short circulation times with rapid renal clearance, side toxicity effects due to the necessity of high doses, and inefficient X-ray attenuation. Other compounds are being studied in order to overcome these limitations. Even though some studies about lanthanides chelates have been done, nanostructured materials have attracted more interest. NPs can carry a high payload, which make possible to reduce the dose of contrast agent required and, can be functionalized to increase the blood circulation times and to endow target specificity and bioavailability. In addition, the fact that they do not diffuse in extravascular space and undergo rapid renal clearance, allows longer time window for imaging and enhanced image contrast using lower doses.

For this application, lipid-based structures, such as liposomes, emulsions, micelles or lipoproteins, and solid core NPs such as metal, metal alloy or metal salt, are the most frequently investigated nanocomposites.

Au NPs have been the most studied as CT contrast agents, due to its high atomic number, which enhances significantly the X-ray attenuation, its excellent biocompatibility and the ease of surface modification. Moreover, the method to control the size, shape and morphology of NPs is well stablished and different properties can be achieved with this material. Other heavy metal elements, like iodine, bismuth, bromine, tantalum, platinum, ytterbium, yttrium, gadolinium, and tungsten are also being studied.

The Ag-Au-Se ternary system described in this chapter could be a good candidate as a contrast agent. Apart from having a high atomic number, the presence of silver and selenium in the material could provide different properties that could be used, for instance, in the field of antibiotic resistance.

Dr. Manuel Pernia's group has demonstrated that coating small NPs, about 6 nm, with 3 kDa PEG-OH molecules resulted in optimal stealth properties and increased blood circulation times, thus turning these NPs into potential contrast agents for molecular imaging or tumour targeting. Besides, the hydrophilicity of the ligand ensures the stability of the nanoparticles in different media, such as water, physiological solution and plasma and minimize plasma proteins' absorption to avoid rapid clearance by mononuclear phagocytic system.

The material tested as a contrast agent for CT was the ternary semiconductor material: the Ag_3AuSe_2 NPs. Firstly, to transfer the nanomaterial from organic solvents to water, a ligand exchange was done. The oleylamine, placed in the surface of the NPs, was replaced by the modular ligand DHLA-PEGn-OH (Scheme 2.2). The dithiol terminal group was strongly anchored to the nanoparticle and the PEGylated chain of 3kDa ensured the solubility of the material in water or polar media.

TEM images (Figure 2.41) show that NPs maintained the colloidal distribution after the ligand exchange, agreeing with Dynamic Light Scattering (DLS), which showed the absence of aggregates, even after one week. DLS is a technique that determines the size distribution of small particles in suspension by analysing the scattering of the light when it interacts with the particles in solution. The negative values of *Z*-potential allow NPs to reduce uncontrolled aggregation in plasma.

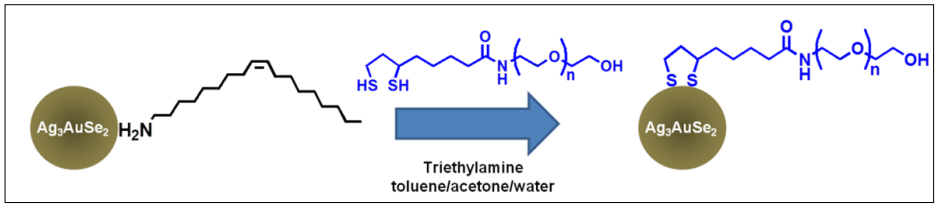

Scheme 2.2: Scheme of the functionalization of Ag_3AuSe_2 nanoparticles with DHLA-PEGn-OH.

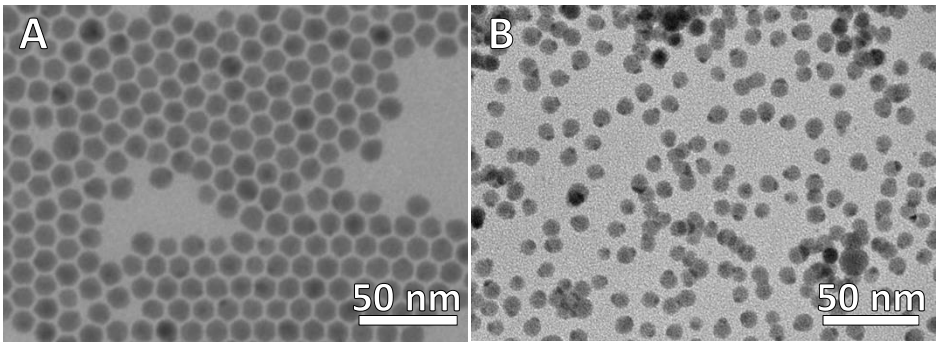

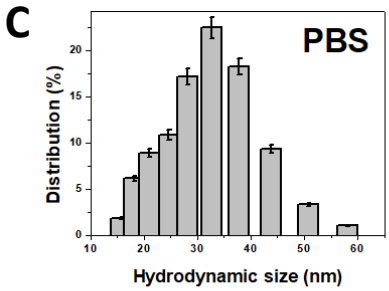

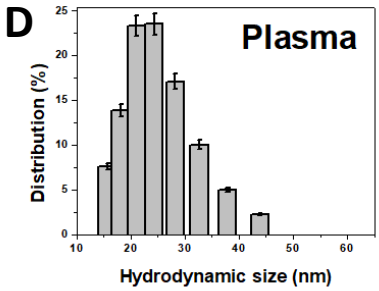

Solvent	DLS (nm)	PDI	ζ (mV)
PBS	30.6 ± 9.4	0.28	-7.6

Solvent	DLS (nm)	PDI	ζ (mV)
Plasma	25.4 ± 0.7	0.64	-6.3

Figure 2.41: TEM images of Ag_3AuSe_2 NPs before (A) and after (B) the functionalization with DHLA-PEGn-OH. Histograms of DLS sizes in PBS (C) and plasma (D). Table of average hydrodynamic diameters and *Z*-potential of the NPs.

The presence of the dithiol PEGylated at the NPs surface was confirmed by Fourier-Transform Infrared (FTIR) spectroscopy and ^{1}H- Nuclear Magnetic Resonance (Figure 2.42).

The potential of the material as CT contrast agents was confirmed by X-ray attenuation measurements (Figure 2.43A). The slope of ternary NPs, which is 3.2 HU mM^{-1} [Au], was higher than iohexol (2.69 HU mM^{-1} [I]), which is a commonly used clinical contrast agent.

The cellular biocompatibility of the PEGylated Ag-Au-Se nanoparticles was also evaluated. As the presence of silver cations in the nanoparticle could lead to severe toxicity problems, the *in vitro* cytotoxicity of the nanoparticles was evaluated using the

C6 rat glioma as a working model. The cultured cells were exposed to an increasing concentration of the PEGylated Ag-Au-Se nanoparticles from 0.5 μg mL^{-1} to 500 μg mL^{-1} for 24h. As can be observed in Figure 2.43B, cell viability is 100% even at high concentration of 50 μg mL^{-1}, with a calculated median lethal dose (LD_{50}) of 296 μg mL^{-1}. It seems that the ligand shell protects the inorganic surface from the external medium, avoiding possible leaching of cations from the ternary material.

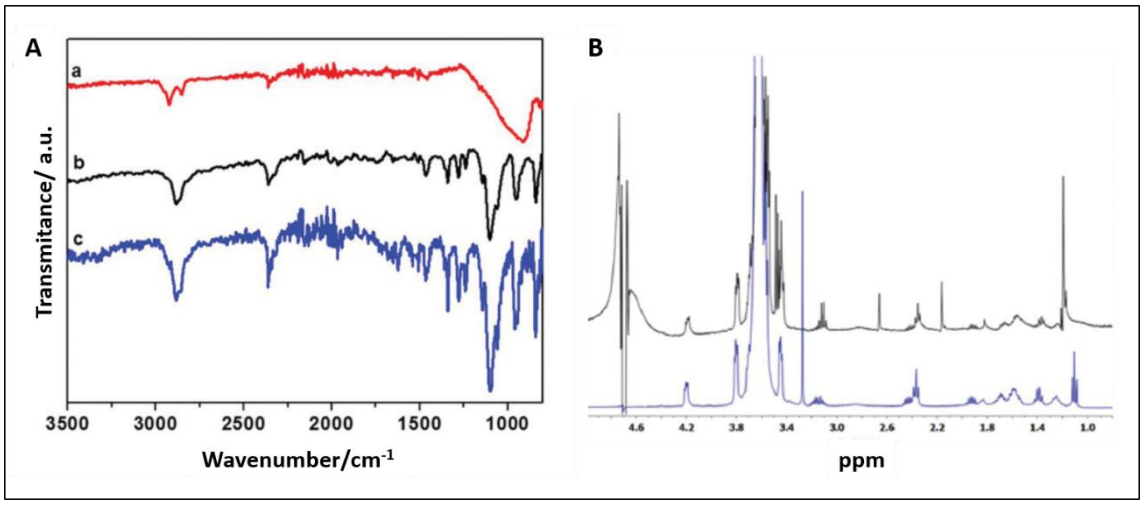

Figure 2.42: (A) FTIR spectra of the ligand DHLA-PEGnOH (blue) and the Ag_3AuSe_2 NPs before (red) and after (black) the functionalization. (B) ^1H NMR spectra of ligand DHLA-PEGnOH (blue) and the NPs after the functionalization (black).

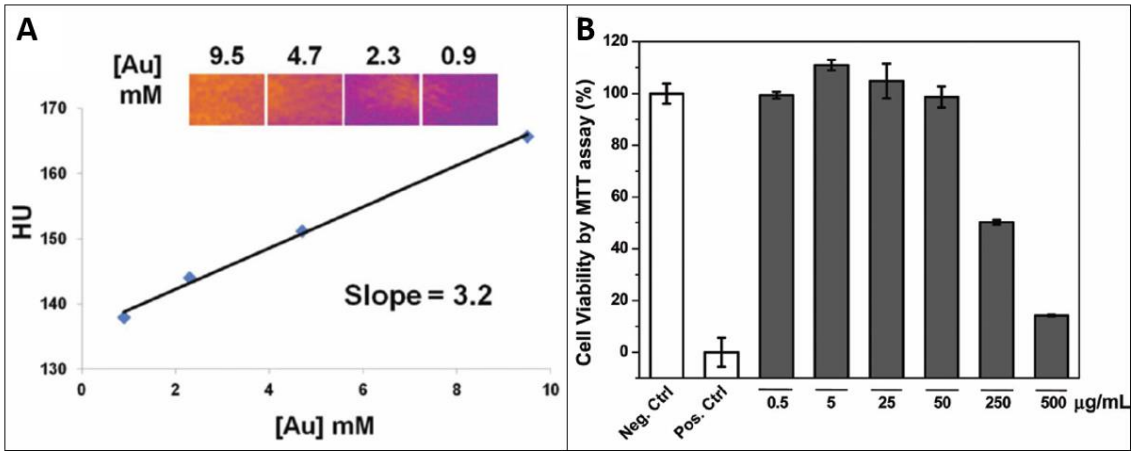

Figure 2.43: (A) X-Ray attenuation intensity measurement, by linear relationships between CT values and concentrations. (B) Cytotoxicity effects of PEGylated ternary Ag_3AuSe_2 NPs by the MTT assay of C6 cells treated for 24 h at different concentrations.

After the *in vitro* characterization of the PEGylated ternary NPs, *in vivo* studies of biodistribution and bioavailability of the NPs to evaluate their potential as CT contrast agents were performed. 10 mg of NPs per kg of balb/c mouse was inoculated into the tail vein and the *in vivo* accumulation of the injected NPs were followed and quantified by CT in different organs at 1, 24, 48, 72 and 168h.

In the liver and the bladder, even though the increase of the contrast shown after 1h confirmed the accumulation of NPs at these organs, the maximum concentration was after 24h, with a ΔHounsfield units of 9.1±0.5 and 15.7±1.5 respectively. At 168h the NPs were totally excreted from them. The presence of the NPs in the bladder, which is governed by a glomerular filtration of 6-8 nm, could be explained by the shrinkage or partial degradation of the organic coating on the NPs, as already described by the group of Dr. Manuel Pernia.

Concerning to the kidneys, there were no accumulation of NPs at any time, as expected, since the hydrodynamic diameter of the NPs were below the size for the effective retention in the corpuscles of the kidney cortex. However, the presence of the NPs on urine demonstrate the partial excretion of the material through these organs.

Samples of blood plasma were analysed at 1h and 24h to determine the lifetime of the circulating PEGylated NPs in the bloodstream. There was a high concentration of NPs after 1h and there were still present after 24h, but at very low concentration, indicating that NPs are being efficiently cleared from the bloodstream at this point.

Histology proved the fact that there were no significant alterations in the tissues exposed to the NPs. Moreover, mice exposed to NPs did not show any weight loss after one week, compared to the control group, which show the absence of toxic effects.

These results showed that PEGylated Ag_3AuSe_2 NPs exhibited good contrast in CT with low toxicity effects. They had long blood circulation times with minimal mononuclear phagocyte system retention. This behaviour is ideal for most clinical applications and it has great potential for *in vivo* molecular imaging.

2.7 Experimental part

Chemicals

Silver chloride (AgCl, 99.9%), selenium powder (Se, 99.99%), tri-n-octylphosphine oxide (TOPO, 99%), and tri-n-octylphosphine (TOP, 97%) were obtained from Strem Chemicals. Gold (III) chloride trihydrate ($HAuCl_4 \cdot 3H_2O$, ≥99.9%), oleylamine (OLAm, 70%), dodecylamine (DDA, 98%), tetraoctylammmonium bromide (TOAB, 98%) and toluene (99.9%) were purchased from Sigma-Aldrich. Ethanol (EtOH, 96% v/v) was obtained from Panreac. Butanol (BuOH, 99.9%) was obtained from Alfa Aesar. All the reagents and solvents were used without further purification.

Synthesis of Ag_2Se NPs

The synthesis of Ag_2Se NPs was adapted from that published by Sahu and co-workers.[147] Briefly, 7.8 g TOPO and 6.6 mL OLAm were degassed under vacuum at 120°C for 30 min. Meanwhile, two precursor solutions were prepared in the glovebox: 474 mg (6 mmol) Se were dissolved in 6 mL TOP and 572 mg (4 mmol) AgCl were dissolved in 4 mL TOP. Under N_2 atmosphere, the temperature was raised to 180°C and the TOP-Se solution was injected. Once the temperature was recovered, the AgCl-TOP precursor solution was injected. After 20 min of reaction, the heating was stopped and the solution was let cool naturally. Once at 50°C 5 mL of BuOH was added to the reaction flask to avoid solidification of the solvent. Finally, the solution was washed three times with EtOH, centrifuging 4 min 4500 rpm and re-dispersing with 4 mL toluene.

Phase transfer of Au(III) ions from water to toluene

The phase transfer of Au(III) ions from water to toluene was based on that reported by Ying and co-workers[166] as follows: 40 mg (0.1 mmol) $HAuCl_4 \cdot 3H_2O$ were dissolved in 100 mL desionized water and mixed with 1.61 g (8.6 mmol) DDA dissolved in 100 mL EtOH. After 3 min of stirring, 100 mL toluene was added to the solution and the stirring was kept for 3 more min. Finally, the toluene phase was separated and washed twice with 50 mL of H_2O/EtOH 1:1 mixture to avoid the precipitation of silver chlorides in further reactions with Ag_2Se NPs. This solution is stable for 3-4 days. The preparation of more concentrated Au(III) solutions was adapted from the procedure above using proportionally increased amounts of $HAuCl_4 \cdot 3H_2O$ and DDA.

The preparation of 6 mM Au(III)-TOAB stock solution was adapted from the protocol described in the previous paragraph by using 1.5 g of TOAB (2.7 mmol) instead of DDA and 240 mg (0.6 mmol) of $HAuCl_4 \cdot 3H_2O$ instead of only 40 mg.

Synthesis of dimer-like Au-Ag_2Se/Au-Ag_3AuSe_2 NPs

180 µL Ag_2Se NPs solution (3.6 µM) were mixed with 3 mL of toluene solution of Au(III)-DDA 1 mM and shaked during 1h at room temperature. After this time, the final solution was washed once with EtOH and re-dispersed with toluene. Time of reaction and concentration of Au(III) toluene solution were modified following the conditions of Table 2.1.

Table 2.1: Reaction conditions of samples Ag-Au-Se_DDA.

Sample	[Au(III)-DDA]	Reaction time
Ag-Au-Se_DDA1	1 mM	1h
Ag-Au-Se_DDA2	1 mM	1 second
Ag-Au-Se_DDA3	1 mM	30 minutes
Ag-Au-Se_DDA4	6 mM	30 minutes
Ag-Au-Se_DDA5	6 mM	2h
Ag-Au-Se_DDA6*	6 mM	1h

*In this sample, before the mixing of Au(III)-DDA solution and Ag_2Se NPs solution, 0.29 g DDA were added to the Au(III)-DDA solution.

Synthesis of Ag_3AuSe_2 NPs

A solution of 180 µL of Ag_2Se NPs (3.6 µM) was mixed with 2 mL of a 6 mM Au(III)-TOAB stock solution in toluene and shaken for 1h. After this time, the final solution was washed once with EtOH and the NPs redispersed in toluene.

Functionalization of ternary NPs for Computed Tomography characterization

The functionalization of the ternary NPs was performed following the protocol previously published.[198,199] Briefly, in a separating funnel was added a solution of 1.0 mL of ternary nanoparticles (10 g L−1 of metal), 1.0 mL of the corresponding dihydrolipoic acid-PEGn-OH with a concentration of 0.1 M in $CHCl_3$ and 50 µL of triethylamine. The mixture was shaken gently and diluted with 5 mL of toluene, 5 mL of Milli-Q water and 10 mL of acetone. Then, the ternary nanoparticles were transferred into the aqueous phase. After that, the aqueous phase was collected in a round-bottom flask and the residual organic solvents were rota-evaporated. Then, the dihydrolipoic acid derived ternary NPs were purified in centrifuge filters with a molecular weight cut-off of 30 kDa, at 4500 rpm for 20 min. In each centrifugation, the functionalized ternary NPs were re-suspended with Milli-Q water. The purification step was repeated several times until the filtered solution was clear. Then, the dihydrolipoic acid derived ternary NPs were re-suspended in PBS buffer. Finally, to ensure highly

stable monodispersed ternary nanoparticles, the solution was centrifuged at 1500 rpm for 5 min.

Characterization Methods

Transmission Electron Microscopy (TEM): samples were prepared for observation by transmission electron microscopy (TEM) by dilution in toluene followed by sonication. A droplet of the solution was then poured in holey carbon covered copper TEM grids. The sintered pellets used in the thermoelectric measurements were thinned to electron transparency using the focused ion beam in situ lift-out technique. A Hitachi H800MT conventional TEM equipped with Bioscan Gatan camera and tungsten filament, operating at an accelerating voltage of 200 kV and 3 µm spot size, was used for the morphological study of all synthesized nanostructures. Images were recorded with Digital Micrograph v.1.82.80 software. Further TEM and high-resolution (HR)TEM images of Ag_2Se, Ag_3AuSe_2, Au−Ag_2Se, and Au−Ag_3AuSe_2 NPs and pellets were acquired in a Jeol JEM 2100 equipped with a LaB6 source and with a Jeol JEM 2010F equipped with a FEG gun, both operated at 200 kV. High-angle annular dark-field (HAADF) and energy-dispersive X-ray spectroscopy (EDX) measurements for Au−Ag_2Se NPs were performed in a probe corrected FEI Titan3 instrument, equipped with an X-FEG source and a Bruker EDX analyzer. HAADF and electron energy loss spectroscopy (EELS) measurements for Au−Ag_3AuSe_2 NPs were performed in a probe corrected JEOL ARM-200 equipped with a cold-FEG source and a Quantum GIF EELS spectrometer. HAADF and HRTEM image simulations were carried out using the TEMSIM open source image simulation software. Crystal cells for simulation were built using the Rhodius software.

Absorbance Spectroscopy: A Cary 100 Scan 388 Varian UV−vis spectrophotometer was used with quartz cuvettes for optical characterization. The instrument was commanded with Varian UV v.3.33. Near infrared (NIR) spectra were recorded using a Spectrophotometer UV-Visible-NIR lambda-19 from Perkin Elmer with an own software program.

X-ray Diffraction: XRD patterns were acquired with a PANalytical X'Pert Pro MPD Alpha1 diffractometer operating in θ/2θ geometry at 45 kV, 40 mA, and λ= 1.5406 Å (Cu Kα1). Thin layers of the samples were prepared by drop casting and evaporation of the solvent on a monocrystalline Si holder of 15 mm diameter and 0.15 mm height. Scans in the range 2θ = 4−100° were run at a step size of 2θ = 0.017° and 100 s per step.

Temperature-dependent X-Ray Diffraction: for the temperature-dependent XRD the sample was place in an Al_2O_3 substrate and warmed up in a High Temperature Camera (HTK-1200N, Antoon Par) from 28°C to 600°C in vacuum conditions ($5{\cdot}10^{-3}$ mBar) with a 10°C/min slope. A PANalytical X'Pert PRO MPD power diffractometer, with a radius

of 240 millimeters, operating in a Bragg-Brentano geometry with a variable automatic divergence slit was used. X-Ray beam of 45 kV, 40 mA and λ=1.5418 Å (Cu Kα1). Scans in the range of 2θ = 10−80° were run at a step size of 2θ = 0.017° and 50 s per step.

All XRD data were treated with X'Pert HighScore Plus software.

X-ray photoelectron spectroscopy: XPS was performed on a SPECS system equipped with an Al anode XR50 source operating at 150 W and a Phoibos 150 MCD-9 detector. The pass energy of the hemispherical analyser was set at 25 eV, and the energy step was set at 0.1 eV. The binding energy (BE) values referred to the C 1s peak at 284.8 eV.

Field emission scanning electron microscopy: FESEM images were recorded on a Zeiss Neon40 scanning electron microscope Crossbeam Station equipped with a field emission electron source operating at 5 kV.

Inductively Coupled Plasma-Atomic Emission Spectroscopy: The composition and concentration of the NPs solutions were determined by ICP-AES. The measurements were carried out by an Optima3200 RL PerkinElmer spectrometer. For these measurements, 50 µL of each of the solutions was precipitated in MeOH and redispersed in $CHCl_3$. The solution was evaporated in an oven overnight at 90 °C. Before the vial was sealed, 2.5 mL of HNO_3 and 0.7 mL of H_2O_2 were added to the precipitate and then heated to 90 °C for 72 h. The resulting solution was transferred to a 25 mL volumetric flask and diluted with Milli-Q water.

X-ray absorption spectroscopy: XAS measurements were carried out at the X10DA (SuperXAS) beamline at the Swiss Light Source, Villigen, Switzerland, which operated with a ring current of approximately 400 mA in top-up mode. The polychromatic radiation from the superbend magnet, with a magnetic field of 2.9 T and critical energy of 11.9 keV, was monochromatized using a channel cut Si(311) crystal monochromator. Spectra were collected on pressed pellets optimized to 1 absorption length at the Ag K-edge (25 515 eV), respectively, at the Au L3-edge (11 919 eV) in transmission mode by using 15 cm long Ar filled ionization chambers at the Ag K-edge and N_2 filled ionization chambers at the L3 edge. The beamline energy axis was calibrated with an Ag or Au reference foil, respectively. Measurements were performed at ambient conditions. XAS spectra were treated with the iFeffit software suite. The XAS spectra were normalized and background-corrected. At this stage, the spectra were ready for performing linear combination fitting (LCF).

Thermoelectric Characterization. Electric Properties. The pressed samples were polished and maintained the disk-shape morphology. Final pellets had a 10 mm diameter and were approximately 1 mm thick. The Seebeck coefficient was measured using a static DC method. Electrical resistivity data were obtained by a standard fourprobe method. Both the Seebeck coefficient and the electrical resistivity were

simultaneously measured with accuracies better than 1% in an LSR-3 LINSEIS system from room temperature to 850 K, under helium atmosphere. Samples were held between two alumel electrodes and two probe thermocouples with spring-loaded pressure contacts. A resistive heater on the lower electrode created temperature differentials in the sample to determine the Seebeck coefficient.

Thermal Properties. An XFA 600 Xenon Flash Apparatus was used to determine the thermal diffusivities of all samples with an accuracy of about 6%. Total thermal conductivity (κ) was calculated using the relation $\kappa = DC_p\rho$, where D is the thermal diffusivity, Cp is the heat capacity, and ρ is the mass density of the pellet. The ρ values were calculated using the Archimedes method. The specific heat (Cp) of the samples was measured using a differential scanning calorimeter DSC 204 F1 Phoenix from NETZSCH.

Dynamic Light Scattering: The size distribution and zeta potential measurements of the dihydrolipoic acid derived ternary nanoparticles were performed on a Zetasizer Nano ZS90 (Malvern, USA). The nanoparticles were dispersed in Milli-Q water at a concentration of 50 mg L−1 of metal. The nanoparticle diameters were also measured in blood plasma by processing the animal blood after 1 h of ternary nanoparticles injection. The measurements were done on a cell type: a ZEN0118-low volume disposable sizing cuvette, setting 3.068 as the refractive index with 173° backscatter (NIBS default) as an angle of detection. The measurement duration was set as automatic and three as the number of measurements. Analysis model general purpose (normal resolution) was chosen.

Fourier-Transform Infrared Spectroscopy: FTIR spectra were recorded with a FTIR-4100 Jasco using a single reflection ATR accessory (MIRacle ATR, PIKE Technologies) coupled to a liquid nitrogen cooled mercury cadmium telluride (MCT) detector. All spectra were recorded in the 4000 to 800 cm^{-1} range at 4 cm^{-1} resolution and accumulating 50 scans. Dihydrolipoic acid derived ligands were deposited as solid products and ternary nanoparticles were prepared by drop casting of a highly concentrated nanoparticle solution onto a microscope slide (Thermo Scientific).

Proton Nuclear Magnetic Resonance: the ^1H NMR spectra were recorded on an NMR Bruker Ascend™ 400 MHz spectrometer. The spectra were measured either in $CDCl_3$ or D_2O.

Thermogravimetric analysis: TGA was carried out by using a METTLER TOLEDO model TGA/ DSC 1 in the temperature range of 30–800 °C at a heating rate of 10 °C min−1 under a N2 flow (50 mL min−1).

Cytotoxicity assays: C6 rat glioma cells were cultured in Dulbecco's Modified Eagle Medium (DMEM) supplemented with 2 mM L-glutamine, 10% fetal bovine serum (FBS)

and 1% penicillin/streptomycin at 37 °C in an incubator under a humidified atmosphere containing 5% CO_2. In order to perform the cytotoxicity assays, the C6 cells were plated at a density of 1 × 104 cells per well in a 96-well plate at 37 °C under a 5% CO2 atmosphere (200 µL per well, number of repetitions = 5). After 24 h of culture, the medium in the wells was replaced with fresh medium containing the PEGylated ternary NPs with varying concentrations from 0.5 µg mL−1 to 500 µg mL−1. After 24 h, the medium was removed, and 200 µL of fresh medium with MTT (0.5 mg mL−1) was added to each well. After 2 h of incubation at 37 °C and 5% CO_2 the medium was removed and the formazan crystals were solubilized with 200 µL of DMSO, and the solution was vigorously mixed to dissolve the reacted dye. Two controls were performed in order to evaluate properly the cytotoxicity: as a negative control, unexposed cells to PEGylated nanocomposites were used, and as a positive control, the cells were exposed to Triton X-100 (1% v/v) for 15 min previous to the MTT procedure. The absorbance of each well was read on a microplate reader (Dynatech MR 7000 instruments) at 550 nm.

The relative cell viability (%) and its error related to control wells containing cell culture medium without nanoparticles were calculated by the equations 2.6 and 2.7.

$$Relative\ Cell\ Viability\ (RCV)(\%) = \frac{[Abs]_{test}}{[Abs]_{control}} \cdot 100 \qquad (2.6)$$

$$Error\ (\%) = RCV_{test} \cdot \sqrt{\left(\frac{[\sigma]_{test}}{[Abs]_{test}}\right)^2 + \left(\frac{[\sigma]_{control}}{[Abs]_{control}}\right)^2} \qquad (2.7)$$

where σ is the standard deviation.

In vitro and in vivo X-ray: In vivo mice experiments were performed in accordance with the ethical guidelines from the Andalusian government. Male Balb/c mice (n = 3) with ca. 22 g in weight, provided by Janvier Labs were used. Animals were anesthetized with 1% isoflurane, the tail vein was cannulated and then the animals were placed in the X-ray scanner. The functionalized nanoparticles were administered intravenously via tail vein at a concentration of 10 mg nanoparticles per kg.

The CT images were acquired using a Bruker Albira small animal CT system. The X-ray focal spot size (Nominal) used was 35 µm and the energy used was 45 kVp, working at 400 µA. Values are Hounsfield units with the adjusted scale to see differences between soft tissues (leaving the bones overexposed) in 1000 images. Histological analysis of the major organs.

Histological analysis of the major organs: After one week post injection of the ternary NPs, the mice were sacrificed and the major organs were extracted. Histology of the

major organs was determined by light microscopy. The tissues were fixed in 4% formaldehyde (Panreac, pH 7 buffered) for 48 h, changing the 4% formaldehyde after 24 h. Then, the samples were dehydrated through graded ethanol, and embedded in paraffin (temperature 56 °C for 2 h under stirring and vacuum). At this point, the haematoxylin and eosin staining was performed: Haematoxylin and Eosin (H&E): the paraffin-embedded samples were sectioned at 7 μm thickness and then were deparaffinized, rehydrated and stained with H&E, and then dehydrated in ascending concentrations of ethanol, cleared in xylene and mounted on commercial glass slides.

Chapter 3 Ag-Au-S system

3.1 Introduction

Silver sulphide is the other material of the silver chalcogenide family that has been studied in this thesis, together with its ternary and hybrid nanostructured materials with gold. As it was commented in the previous section, it is a narrow band gap semiconductor, with a band gap energy of 0.9eV.

This binary material and HgS are the only sulphides with semiconducting properties which have three polymorphic structures. α-Ag_2S, a monoclinic phase, also known as *acanthite*, is stable at low temperature, below 177°C. Between, 177 and 586°C, silver sulphide exists in a body centred cubic phase, *argentite* (β-Ag_2S), which shows superionic conductivity. Beyond 586°C, the material is transformed to a face centred cubic structure, the γ-Ag_2S.[200]

In relation to its ternary system with gold, it offers some variations in comparison to its analogous of selenium that makes it more interesting for study. Basically, it is presented in two different ternary materials with different stoichiometries. On the one side, the analogous of the ternary Ag_3AuSe_2 compound: Ag_3AuS_2, which has a tetragonal crystalline structure. On the other, a gold-richer material: AgAuS with a monoclinic phase. Both materials have a phase transition to a cubic phase, at 185°C and 307°C respectively.[156] The mineral with the formula Ag_3AuS_2 is known as *Uytenbogaardite* and it was first defined by Barton and co-workers in 1978.[201] Six years later, in 1984, AgAuS was reported as the new mineral *Petrovskaite* by Nestrenko and co-workers. Some characteristics of these materials have been studied in the bulk: thermodynamic properties,[202] heat capacity[203] and electronic structure.[204] Moreover they attracted the interest of geologists[205] and crystallographists.[206–208]

On the nanoscale there are also a few publications. In most of them, their synthesis is based on the sulfurization of a pre-synthesised metallic nanostructure made of gold or an alloy of silver and gold.[157,209–211] Yang and co-workers worked with silver sulphide NPs and they mixed them with gold NPs or Au(III)-DDA complex, similar procedures of

those done in this project, but they did not describe the presence of ternary materials in any case.[212–214]

3.2 Ag_2S NPs: Synthesis and morphological and structural characterization

The first step of this part of the project was to synthesise silver sulphide NPs. The literature is full of different methods to synthesise this material:[215] by decomposition of a semi-stable precursor containing both Ag and S (such as Ag-DDT[216] or Ag(SCOPh)[217]); by a simple reaction between $AgNO_3$ and S powder in oleylamine,[218] by cation exchange,[102] or by a reaction at room temperature of Ag NPs or a solution of Ag(I) cations with elemental sulphur in toluene,[219] just to cite a few examples. Nevertheless, the intention of the project was to have a general method for synthesising silver chalcogenide NPs. On account of this, the first procedure tested was the same used for the synthesis of Ag_2Se NPs but using sulphur instead of selenium.

After several attempts on this synthesis, including some small changes in the procedure (increasing and decreasing the injection/reaction temperature and changing the solvent for octadecylamine) the result was not good. In all cases metallic silver NPs were obtained, instead of silver sulphide NPs. Sulphur was not reacting, probably because it was not available in the solution: from the Pearson's Hard Soft Acid Base Theory, it is well known that the affinity between phosphorous (from the trioctylphosphine) and sulphur is strong, both are soft Lewis acid/base, and as a result they have a strong coordinating bond, which can be difficult to break. Therefore, the solution may be to change the coordinating agent to one with an atom which is a harder Pearson base. For example, nitrogen. Oleylamine, as it was already a surfactant of the original reaction, would be the perfect candidate.

NPs obtained through this method (just substituting the trioctylphosphine for oleylamine in the sulphur precursor), from now on Method A, gave satisfactory results. TEM images in Figure 3.1 show the evolution with time of the synthesised NPs (Ag_2S_A1). It was clear that NPs nucleated and grew very quickly, in 2 minutes there were already NPs in the solution, but they were small and presented high polydispersity in terms of size. With time, the NPs suffered Ostwald ripening and the sample became monodisperse after 10-20 minutes of reaction. The final NPs were of 12nm of diameter.

Apart from that, in TEM images of long reaction time it is clearly seen that NPs were not separated between them, they were forming a net of fused nanoparticles. Even though the material did not seem to be nanostructured, the sample in solution was in good condition, as it will be shown in subsequent experiments. This effect was most

likely attributable to an interaction between the electron beam of the microscope and the material.

As it was reflected in the XRD pattern of synthesised NPs (Figure 3.2), their crystalline structure matched perfectly with a monoclinic phase of Ag_2S, which was the expected phase for this material at low temperatures.

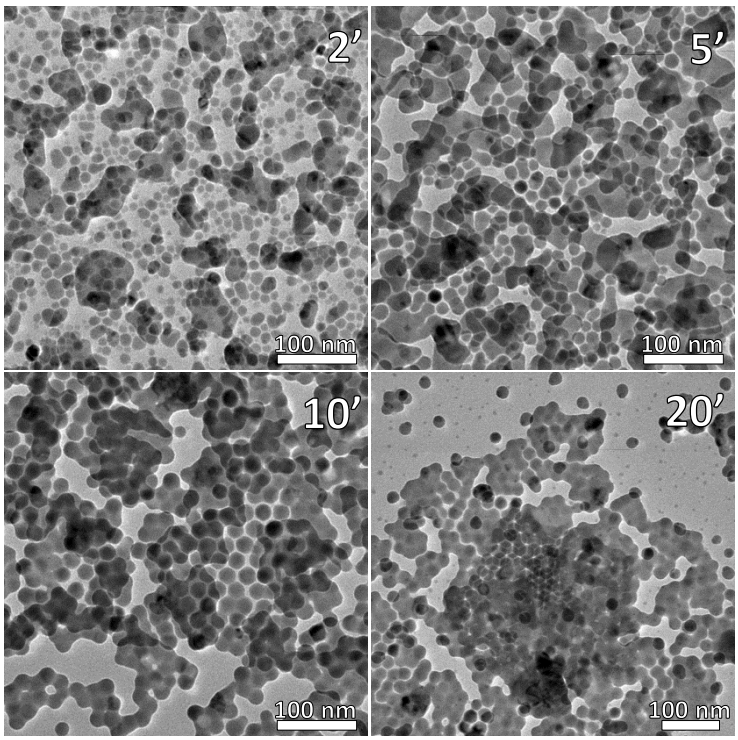

Figure 3.1: TEM images of Ag_2S_A1 NPs extracted at different times of reaction (2', 5', 10' and 20').

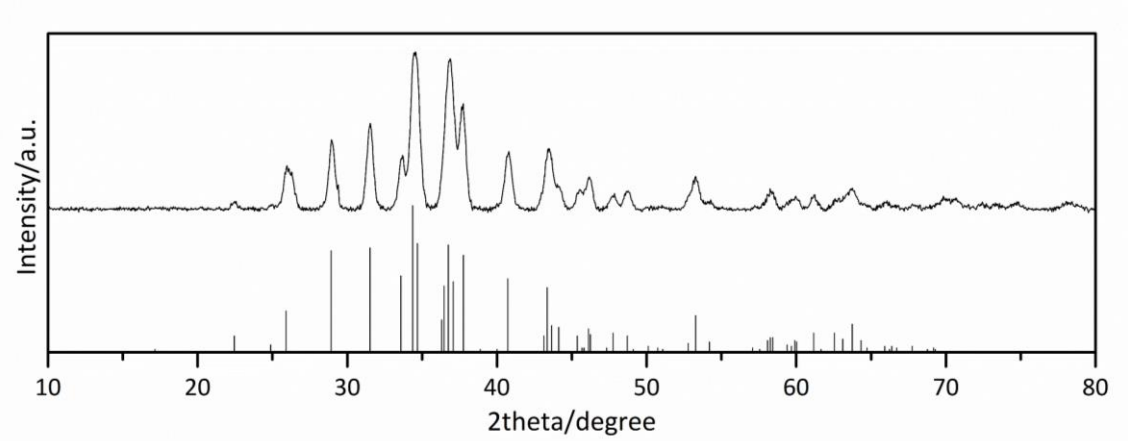

Figure 3.2: XRD pattern of Ag_2S_A1 NPs and monoclinic Ag_2S reference pattern (JCPDS 024-0715).

Despite method A gave good results in the first attempts, when a scale-up was tried, it resulted a non-reproducible method. As can be observed in Figure 3.3, the monodispersity of the sample was lost. NPs of these two different attempts gave a

polydisperse sample. And in other attempts, impurified NPs with metallic silver were obtained.

With the aim of having an easy scale-up and a reproducible synthesis of Ag_2S NPs, the next step was changing the solvent to a less polar solvent, using octadecene instead of trioctylphosphine oxide: Method B. Apart from the polarity change, the toxic phosphines are avoided, becoming a more environmentally-friendly procedure. In this method the first tests were promising as well, as can be seen in TEM image and XRD pattern in Figure 3.4. But, it was also difficult to control the reproducibility, depending on the synthesis less monodisperse NPs were formed (Figure 3.5).

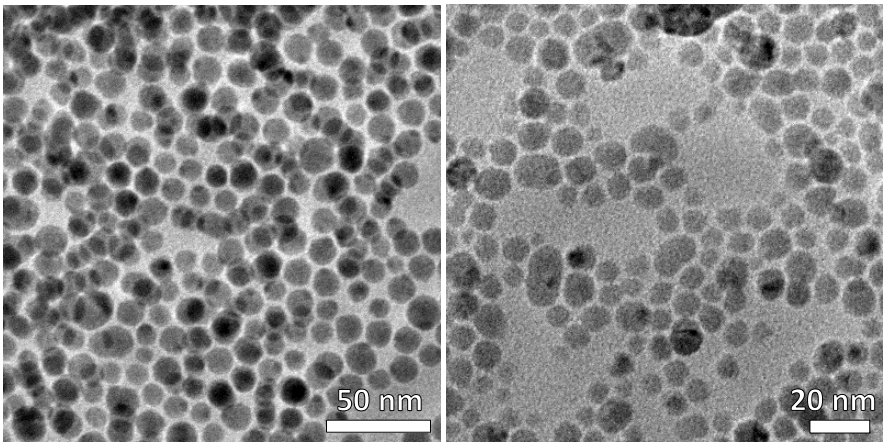

Figure 3.3: TEM images of two different sample synthesised by scaling-up method A.

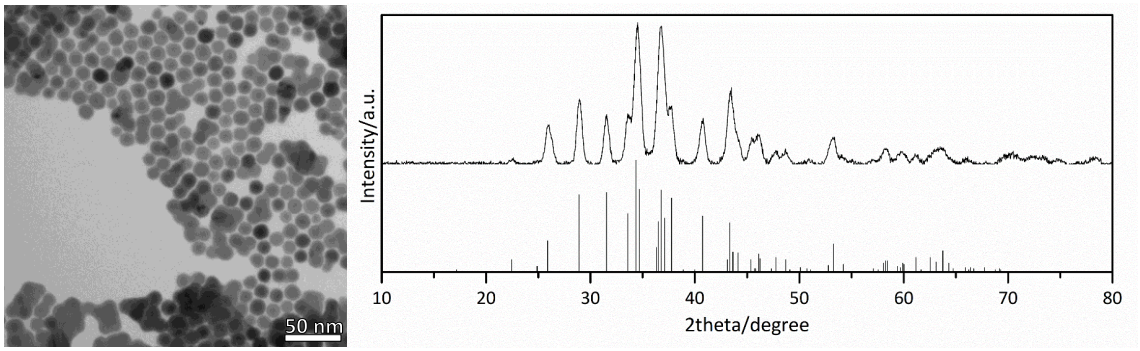

Figure 3.4: TEM image and XRD pattern of Ag_2S NPs synthesised by method B and monoclinic Ag_2S reference pattern (JCPDS 024-0715).

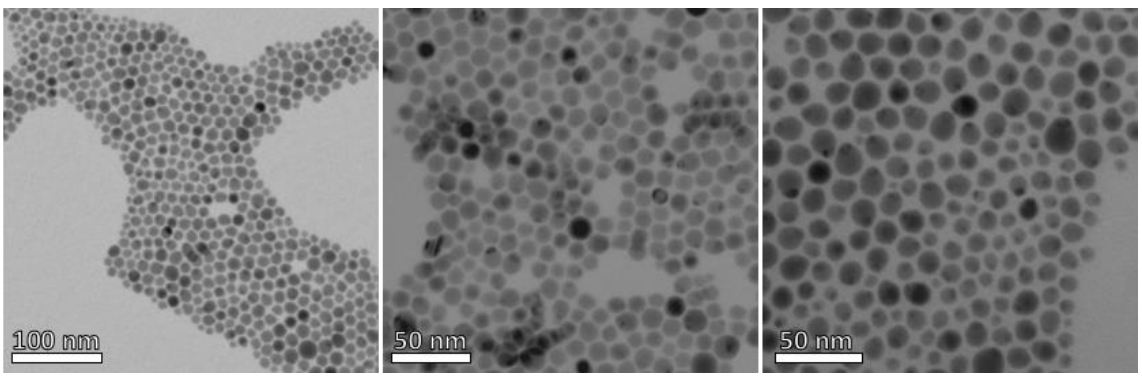

Figure 3.5: TEM images of different attempts of method B.

Finally, a completely different method was used (Method C). In this case, the procedure was directly extracted from the literature.[220] In the paper, Wang and co-workers synthesized Ag_2S-CdS matchstick-like hybrid nanostructures and only the first step of the procedure (the synthesis of Ag_2S NPs) was used. This procedure is a heat-up method which uses oleylamine as solvent and surfactant and $AgNO_3$ and sulphur as metallic reactants. Even though this method was completely different from the one used for Ag_2Se NPs synthesis, it offered a good scale up and high reproducibility.

NPs obtained in three different batches were clearly similar but, in comparison with the good samples obtained from method A and B, they were not all spherical and the monodispersity was lower (Figure 3.6). XRD pattern, displayed in the same figure, showed the NPs presented the monoclinic phase of Ag_2S. The sharp peaks at small angles (between 10 and 22 degree) do not belong to the material. Small angles indicate large crystallographic distances and, in this case, can be associated with oleylamine, which remained in the solution after the washing process of the nanoparticles and may have crystallized during the deposition of the sample to the XRD substrate.

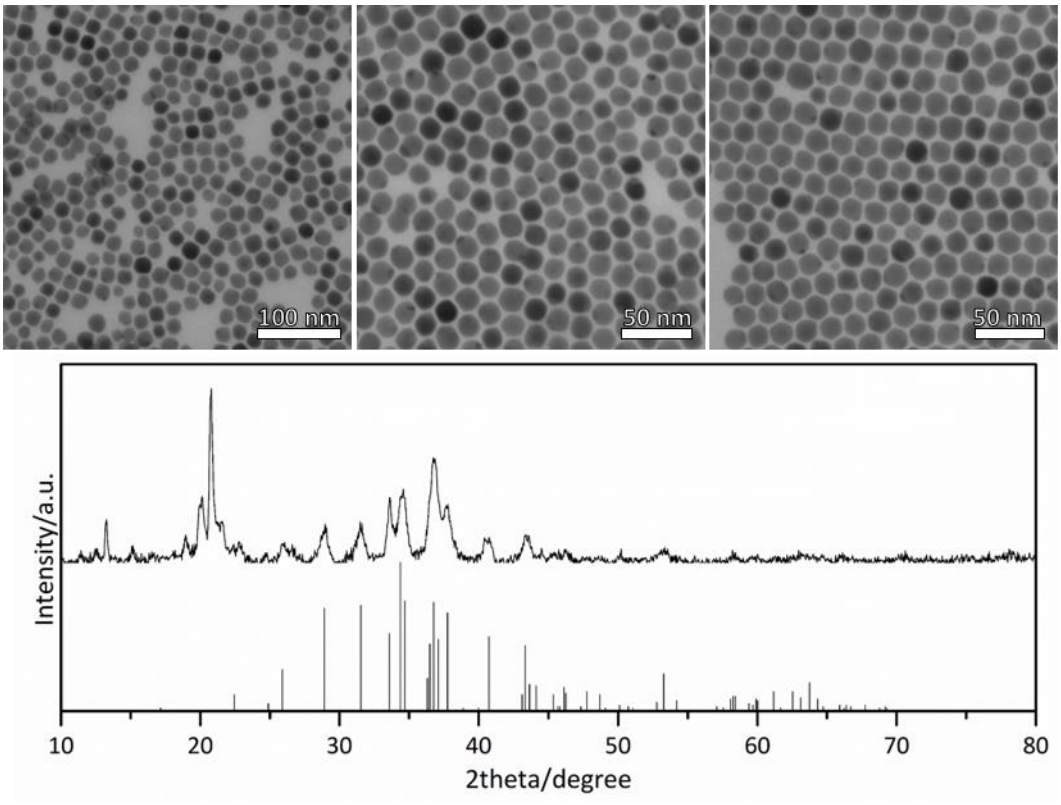

Figure 3.6: TEM images of three different samples synthesised by method C and XRD patterns of one of the samples and monoclinic Ag_2S reference pattern (JCPDS 024-0715).

In some nanoparticles, two different domains are clearly visible. There are two possible explanations for this fact. On the one hand, the two domains are of Ag_2S and

the NPs are not single crystals; which would be the same that happened in some of the Ag_2Se NPs. On the other, the second domain could be a small tip of metallic silver, which might grow during the synthesis.

Ag_2S NPs, specifically the sample Ag_2S_B2, was observed by HRTEM and FTT analysis were done. These measurements and analyses were done by Pau Torruella. In this study, most of nanoparticles were found to consist in *acanthite* (Figure 3.7A), the monoclinic phase of Ag_2S, which perfectly matched with the XRD results. However, there were also some nanoparticles (Figure 3.7B), in lower frequency, which matched with a cubic phase of Ag_2S (which is stable at high temperatures). Apart from that, some of the NPs, presented two domains, as it was highlighted in the previous paragraph. In this case, the second domain was of metallic silver (Figure 3.7).

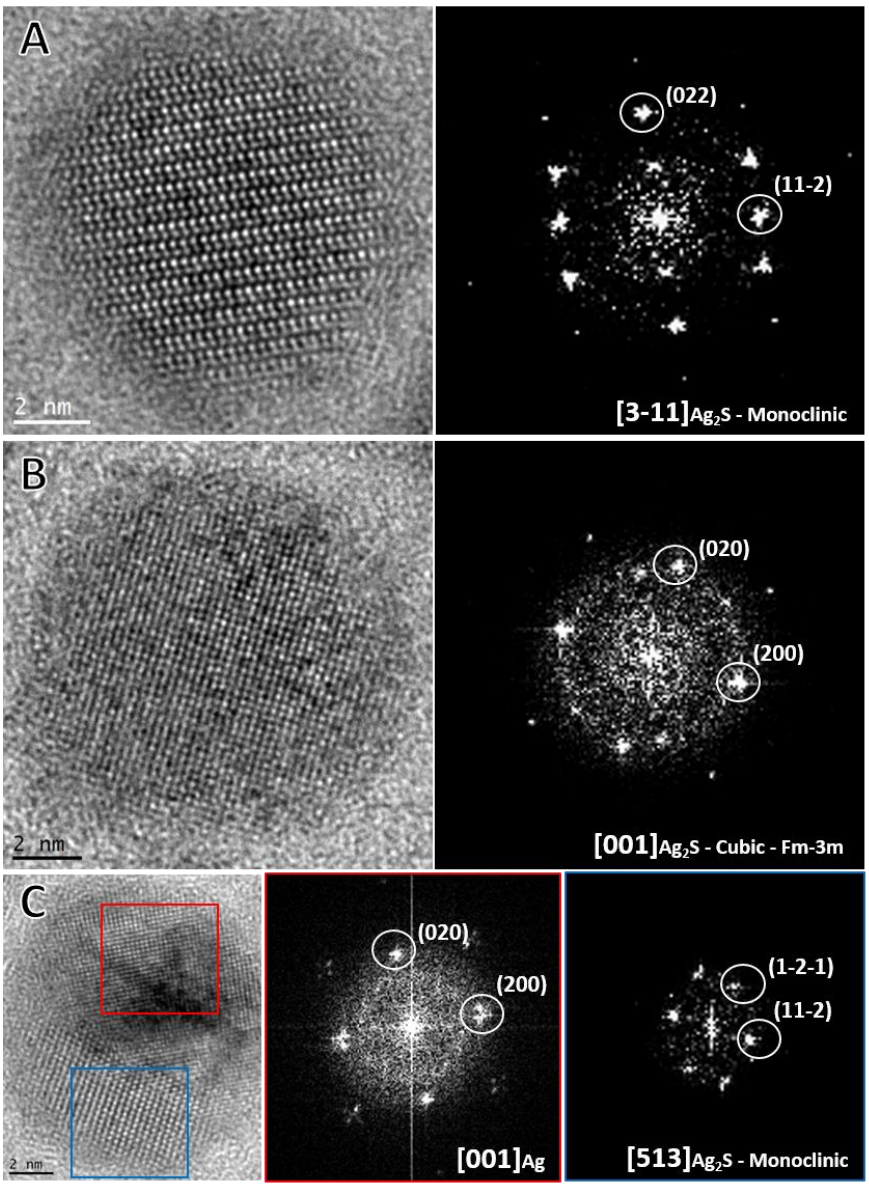

Figure 3.7: HRTEM images and corresponding indexed FFT. (A) Monoclinic Ag_2S NP (B) Cubic Ag_2S NP (C) dimer-like Ag-Ag_2S HNP.

3.3 Ag_2S nanorods: synthesis and morphological and structural characterization

To expand the study to different shapes, Ag_2S nanorods (NRs) were synthesised. This part of the project was done with the help of Albert Vidal, a master student of the group.

The Ag_2S NRs synthesis was adapted from the method published by Son and co-workers in 2007.[221] The main change done to the synthesis was the decrease of the reaction time in order to synthesise shorter NRs. As it can be observed in TEM image (Figure 3.8), the sample was highly monodisperse with short rods of 50nm length and 10nm width. XRD showed the crystalline phase was the same as in the spherical samples: the monoclinic phase of Ag_2S.

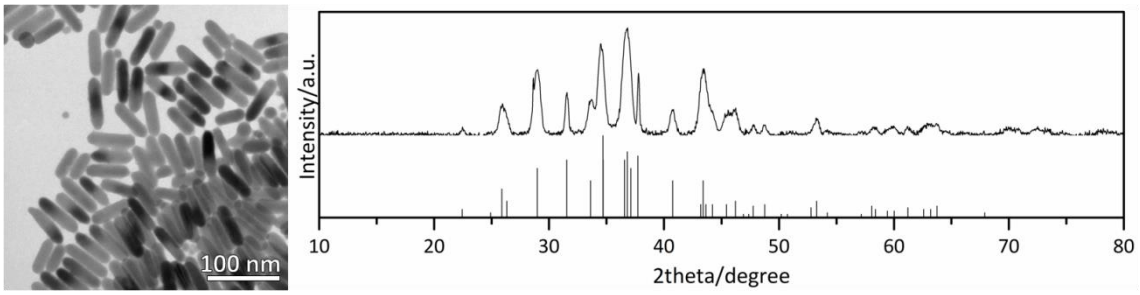

Figure 3.8: TEM image and XRD pattern of Ag_2S NRs and monoclinic Ag_2S (JCPDS 014-0072) reference pattern.

In addition, the sample was observed by HRTEM and FFT analyses were carried out (Figure 3.9). The results matched perfectly with the previous characterization done by low resolution TEM and XRD.

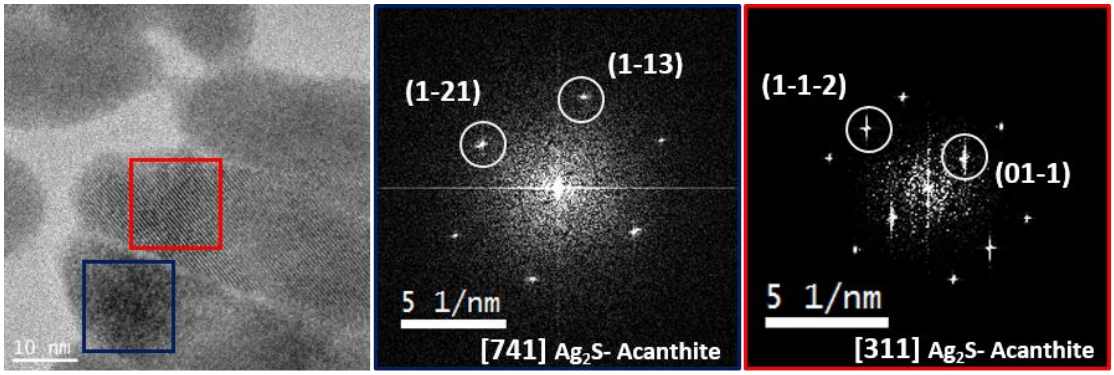

Figure 3.9: HRTEM image with indexed FFT from the corresponding highlighted regions of Ag_2S NRs.

3.4. Ag-Au-S systems: synthesis and morphological and structural characterization

Similar to the procedure used in Ag-Au-Se systems, the first step of the synthesis was the preparation of Au(III) cationic solution in toluene, by the phase transfer protocol[166] using DDA or TOAB as transfer agents. Subsequently, this solution was mixed with the solution of pre-synthesised Ag_2S NPs or NRs to let them react at different conditions in order to study the evolution of the system.

Use of TOAB as phase transfer agent

First, the aim was to synthesise the nanostructured ternary semiconductors, without any metallic domain. Following the example of Ag-Au-Se systems, TOAB was used as phase transfer agent with the idea of avoiding the total reduction of Au(III) to metallic gold.

As it was said before, the interesting part of this system is the fact that it has two different ternary semiconductors, with different stoichiometries: Ag_3AuS_2 (tetragonal phase) and AgAuS (monoclinic phase). So, in order to synthesise both phases separately two different parameters were studied: Ag:Au ratio and reaction time.

Study of the influence of Ag:Au ratio

The first parameter studied was the Ag:Au ratio, keeping the reaction time constant (24h). As a general trend, it was clearly observed that it was possible to control the partial cation exchange depending on this parameter. Apart from that, proper experimental conditions could not be found in order to avoid the formation of metallic gold tip or tips on the surface of the nanoparticles, in contrast with the Ag-Au-Se system, in which it was possible to isolate the ternary nanostructured material without metallic decoration.

When the Ag:Au ratio was 5:1 (Sample Ag-Au-S_TOAB1), as can be observed in Figure 3.10, the product was a dimer-like structure which, regarding to XRD, was a mixture of the original material, Ag_2S, and Ag_3AuS_2. The amount of gold was not enough to transform completely all the material. The small size of the gold domain prevented its observation by XRD, due to the large widths and consequent low intensities.

When the ratio was increased to 3:1 (Sample Ag-Au-S_TOAB2), as is shown in the TEM image (Figure 3.11) the morphology of the material was the same, showing the only presence of dimers, but the XRD showed that the original Ag_2S lattice was completely

transformed to Ag_3AuS_2 (tetragonal structure), and no remaining peaks of monoclinic Ag_2S were detected.

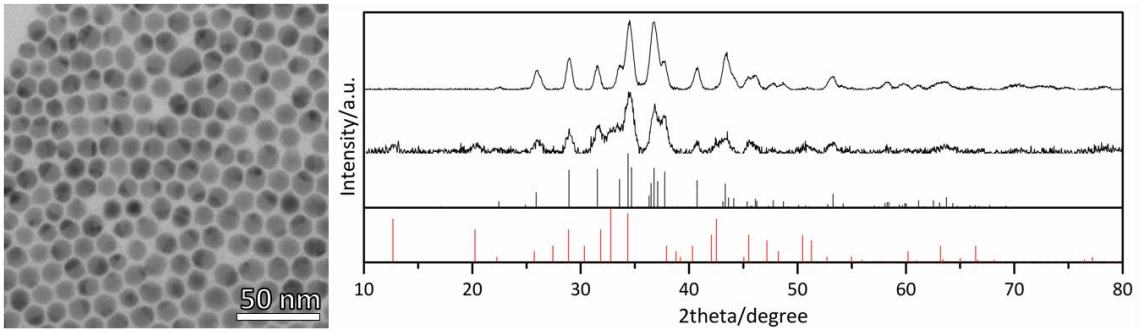

Figure 3.10: TEM image of Ag-Au-S_TOAB1 NPs. XRD patterns of Ag_2S NPs (top) and Ag-Au-S_TOAB1 NPs (bottom). Monoclinic Ag_2S (JCPDS 024-0715, black) and tetragonal Ag_3AuS_2 (JCPDS 020-0461, red) reference patterns.

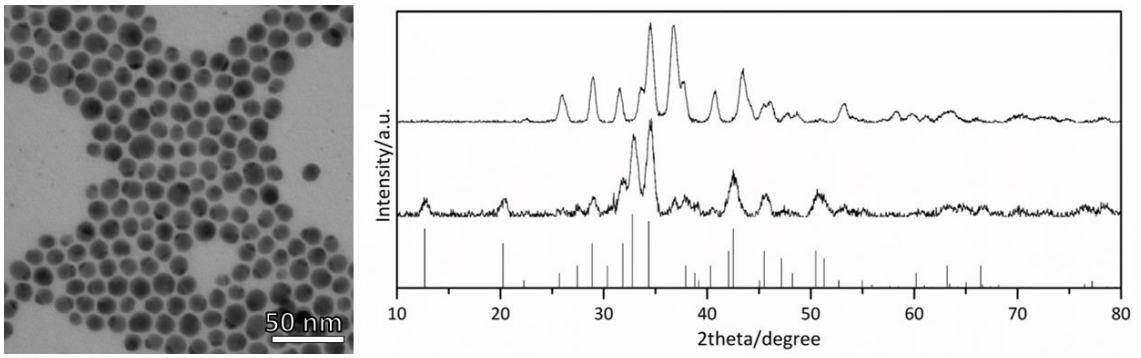

Figure 3.11: TEM image of Ag-Au-S_TOAB2 NPs and XRD patterns of Ag_2S NPs (top) and Ag-Au-S_TOAB2 NPs (bottom). Tetragonal Ag_3AuS_2 (JCPDS 020-0461) reference pattern.

If the ratio was increased to 1:1 (Sample Ag-Au-S_TOAB3) Ag_2S was also completely transformed, but in this case, to the other ternary stoichiometry, the monoclinic AgAuS. The morphology of the nanomaterial was also slightly different, instead of having just one, each semiconductor nanoparticle had multiple and smaller domains of metallic gold (Figure 3.12).

Finally, an excess of gold was used in the last two experiments. In sample Ag-Au-S_TOAB4 the ratio was 1:5 and XRD pattern showed that a complete cation exchange to Au_2S was practically done, there was a mixture of cubic Au_2S with some traces of AgAuS. Also, the morphology of the particles had changed: the NPs were nearly cubic with multiple domains of metallic gold on the surface (Figure 3.13).

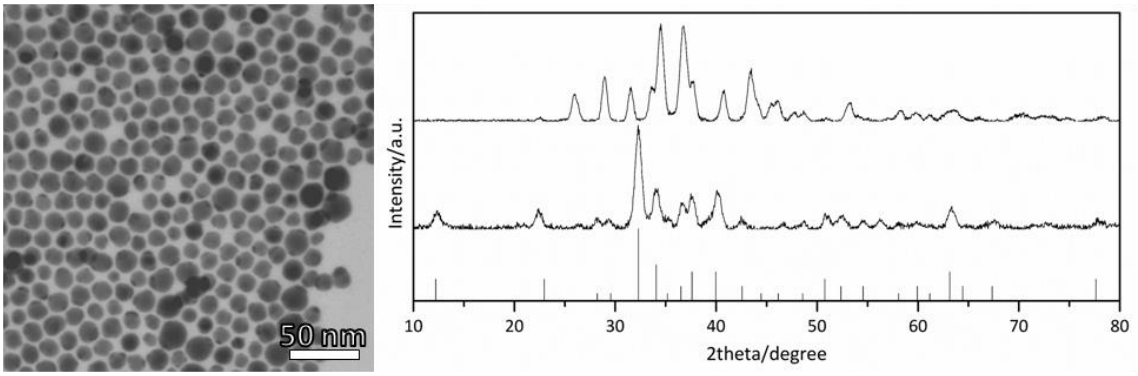

Figure 3.12: TEM image of Ag-Au-S_TOAB3 NPs and XRD patterns of Ag_2S NPs (top) and Ag-Au-S_TOAB3 NPs (bottom). Monoclinic AgAuS (JCPDS 038-0396) reference pattern.

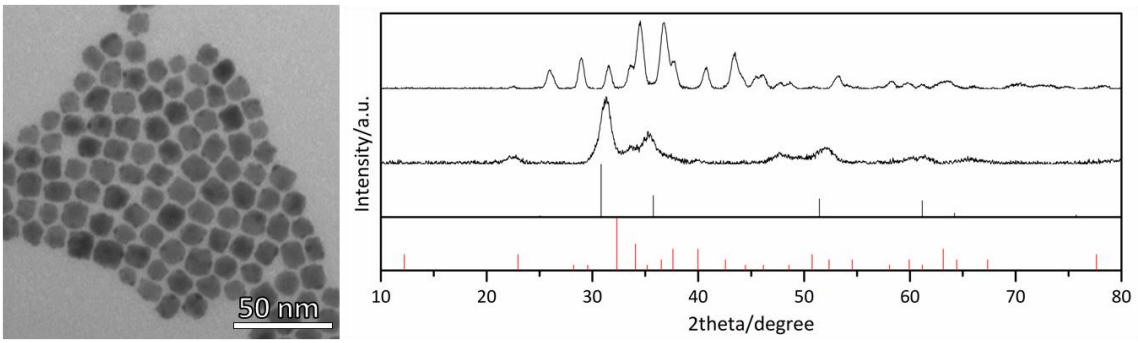

Figure 3.13: TEM image of Ag-Au-S_TOAB4 NPs and XRD patterns of Ag_2S NPs (top) and Ag-Au-S_TOAB4 NPs (bottom). Cubic Au_2S (JCPDS 085-1997, black) and monoclinic AgAuS (JCPDS 038-0396, red) reference patterns.

Au_2S is a *p*-type semiconductor that crystallizes in a cubic phase, which is considered metastable and usually decomposes under both inert atmosphere and air conditions at temperatures above 420K.[222,223] Its direct bandgap energy values are controversial with theoretical estimations from 1.3 to 2.6eV.[224] Even though its preparation often leads to amorphous solids, some exceptions, in the nanoscale, have been reported.[225,226] In addition, when it combinates with other materials it has been suggested as an interesting light harvesting, catalytic, biosensing or therapeutic component.[227–232]

When the excess of gold was even higher, 1:10 (Sample Ag-Au-S_TOAB5), the XRD pattern was similar to the previous one, but with a lower amount of AgAuS, and thus the sample was composed by almost pure Au_2S. However, the most surprising result was the morphology of the NPs, as can be seen in TEM image (Figure 3.14). They were cubic and hollow. The formation of a hole in the nanoparticle could be due to the Kirkendall Effect, which will be described later.

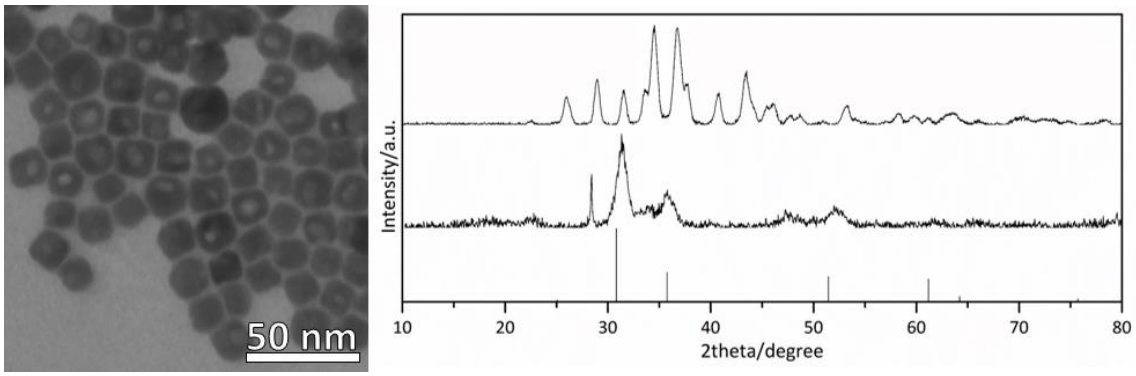

Figure 3.14: TEM image of Au-Ag-S_TOAB5 NPs and XRD patterns of Ag_2S NPs (top) and Ag-Au-S_TOAB5 NPs (bottom). Cubic Au_2S (JCPDS 085-1997) reference pattern.

This last experiment was also done with the Ag_2S NRs, to test if the results depended of the shape. The result is shown in Figure 3.15, confirming the formation of hollow NRs. XRD of this sample was not done, because hollow NRs were not stable on solution and it was impossible to separate successfully the AgBr, which was impurifying the sample. As it was reported in Chapter 2, AgBr was formed upon the reaction between the bromides from the TOAB and the silver cations from the Ag_2S NPs/NRs. In former samples, the AgBr precipitate was previously separated by centrifugation, before the cleaning step, taking advantage of the stability of the NPs in toluene. Nevertheless, FTT analyses of the sample, which will be shown and discussed in the following section, confirmed the nature of the sample: a mixture of Au_2S and AgAuS.

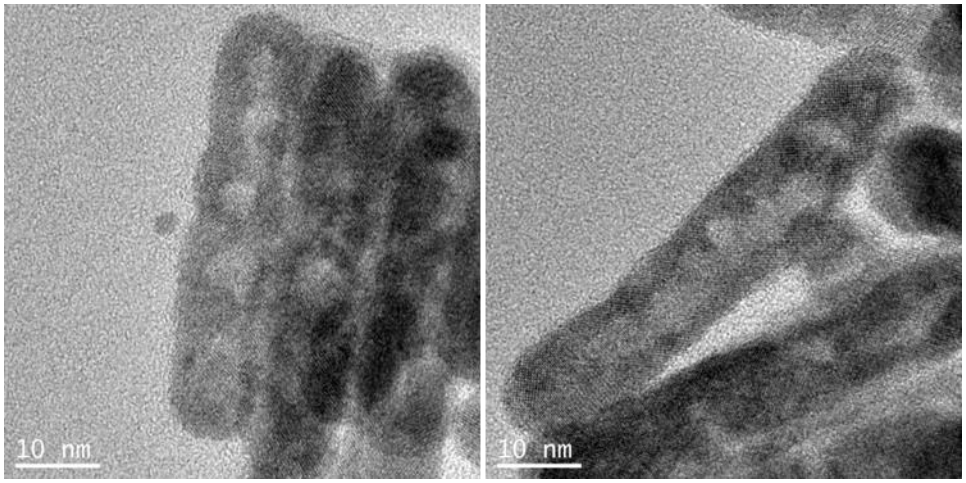

Figure 3.15: HRTEM images of hollow nanorods.

The Kirkendall effect is a phenomenon described in 1947 by Ernest Kirkendall and A. Smigelskas. After some experiments they proved the theory that atomic diffusion between two metals for the formation of an alloy occurs through vacancy exchange, instead of by direct interchange of atoms or ring mechanism. As a consequence, when the diffusion rate of the two metals is unequal, this is to say that the outward diffusion

of atoms A is much faster than inward diffusion of atoms B, a diffusion of vacancies is necessary to balance the diffusivity difference and when these vacancies supersaturate, they coalescence into a void (Figure 3.16A).[233] In metallurgy or in macroscopic materials, the formation of Kirkendall voids is not beneficial because these voids affect the mechanical properties, making them more fragile. However, in the nanoscale, it allows the formation of controlled hollow NPs[234–237] (Figure 3.16B), which can be promising in many applications such as in nanoreactors,[238] energy conversion[239] and biomedicine,[240] among others.[241]

Prof. Alivisatos' group published the first reference in this field in 2004 with the synthesis of hollow nanostructures of cobalt oxides/chalcogenides from solid nanoparticles of metallic cobalt.[242] After them, many groups have centred their research in this kind of reactions, using different metallic nanoparticles and oxidizing them to synthesise a wide variety of hollow nanostructured materials.[243–245]

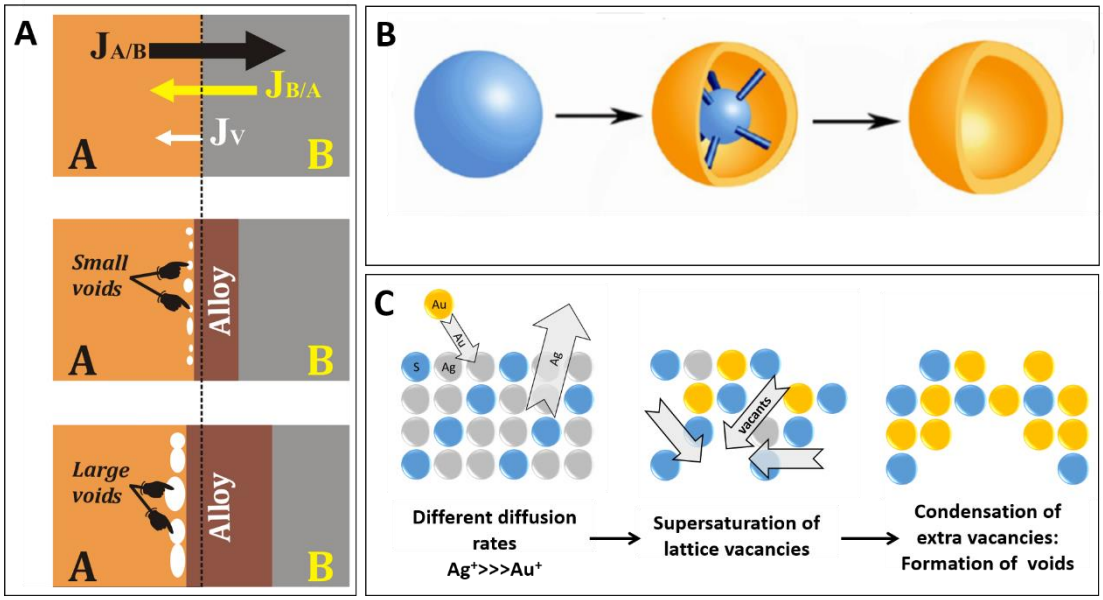

Figure 3.16: Schematic illustration of (A) the different stages occurring during the formation of voids at the interface of two different metals (A and B) as a consequence of Kirkendall Effect (Extracted from Ref. 236) (B) nanoscale Kirkendall Effect for the formation of hollow NPs (Extracted from Ref. 235) and (C) the mechanism of formation of Ag-Au-S_TOAB5 hollow NPs.

The Kirkendall effect was also observed in cation diffusion,[246,247] so it can be a reasonable explanation for the formation of hollow nanoparticles in Ag-Au-S_TOAB5 experiment (Figure 3.16C). However, the fact that this phenomenon was only observed in the last experiment implies there should be an extra factor that increased the diffusion rate of silver cations or decreased the one of gold cations in this specific experiment, as so to provoke the Kirkendall effect. In all the experiments, the undesirable product AgBr was obtained as a result of the reaction between the Ag^+ emitted by the cation exchange and the bromides from the gold solution. The increase

of the amount gold is directly related to the amount of bromides in the solution and this big excess of bromides might be responsible of the displacement of the equilibrium of precipitation, increasing the outward diffusion rate of silver cations, provoking an important difference between the two velocities and leading to the Kirkendall effect.

In depth characterization of Au-Ag_3AuS_2 HNPs, Au-AgAuS HNPs and hollow Ag_2S nanostructures

Au-Ag_3AuS_2 HNPs (Ag-Au-S_TOAB2), Au-AgAuS HNPs (Ag-Au-S_TOAB3) and hollow Au_2S NPs (Ag-Au-S_TOAB5) were observed by high-resolution TEM and analysed by FTT and EDX. All these measurements were done by Pau Torruella.

HRTEM image of dimer-like Au-Ag_3AuS_2 HNPs (Figure 3.17) reflect the same results that have been shown in TEM images in previous section. The small domain, which was darker, was thought to be gold. The other domain, which was brighter, was supposed to be Ag_3AuS_2. STEM-HAADF images (Figure 3.18) were also consistent with these hypotheses, the smaller domain is brighter than the larger domain, indicating it is composed by heavier elements. These surmises were proved by FTT analyses (Figure 3.17), where the results of both domains clearly matched with the expected materials.

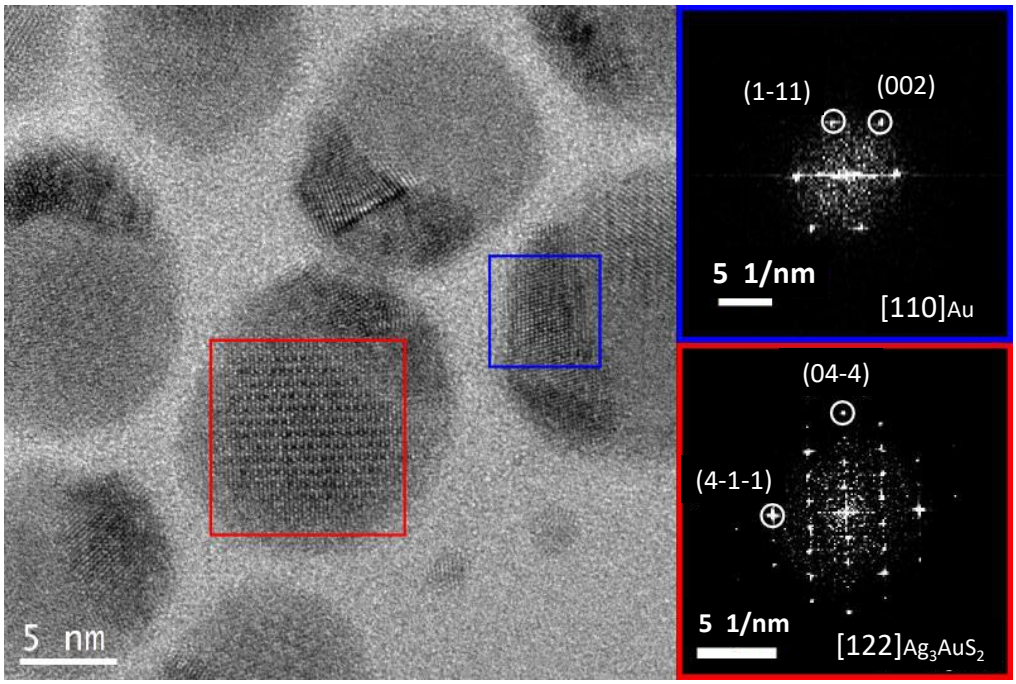

Figure 3.17: HRTEM image of Au-Ag_3AuS_2 HNPs and corresponding FFTs from the highlighted regions.

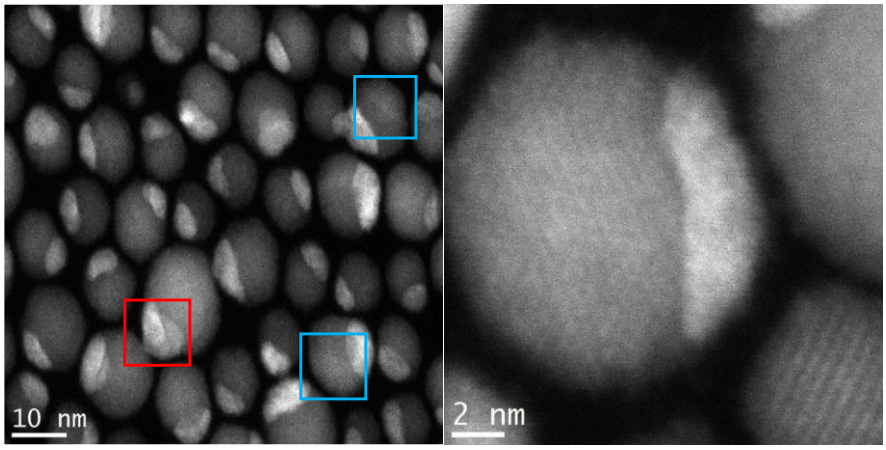

Figure 3.18: STEM-HAADF images of Au-Ag_3AuS_2 HNPs. In the left image, defects in gold domains are highlighted in red and defects in Ag_3AuS_2 are highlighted in blue.

Moreover, in STEM-HAADF images, in the highlighted areas, it is possible to see that some nanoparticles have defects in the gold (in red) and in the Ag_3AuS_2 (in blue) crystals. Apart from that, in the left image, the darker contrast in the barrier between the two domains is an indication of the lack of epitaxy between them.

HRTEM images and FTTs analyses of Au-AgAuS (Figure 3.19) were also consistent with previous TEM and XRD results. Most HNPs had more than one gold domain and the semiconductor domain was mainly AgAuS. Nevertheless, it was found by FTT analyses (blue region) that there were remains of Ag_3AuS_2, which gave an idea of the mechanism of the reaction. The formation of AgAuS was not a direct process, it had an intermediate step: the formation of Ag_3AuS_2. This fact was also consistent with the results of the experiment Ag-Au-S_TOAB3.1, that will be reported in the following section, in which the reaction time was decreased and the second transformation, to AgAuS, was not complete.

STEM-HAADF images of Au-AgAuS HNPs are shown in Figure 3.20. As it was mentioned before, these images are useful to identify nanostructures with multiple domains. Red arrow in the left image shows a nanoparticle with more than one domain of gold. Also, it is possible to see the boundary between the gold domain and the semiconductor domain (blue arrow in the right image) and some defects in the semiconductor crystals (green arrow in the right image shows a planar defect). Although these defects were also seen in Au-Ag_3AuS_2 HNPs, they were more frequent in Au-AgAuS HNPs, most likely due to the more advanced cation exchange suffered.

Besides, EDX analyses of these two samples were carried out. Different punctual spectra and averaged scans from wider areas were acquired for each sample. The spectra were quantified, and the average results showed the mean composition of Ag-Au-S crystals of each sample. Whereas sample Ag-Au-S_TOAB2 had 75±2% of silver and 25±2% of gold, sample Ag-Au-S_TOAB3 had 54±2% of silver and 46±2% of gold. These

results agreed perfectly with the stoichiometry of the two ternary materials. Figure 3.21 shows the averaged spectra for both samples.

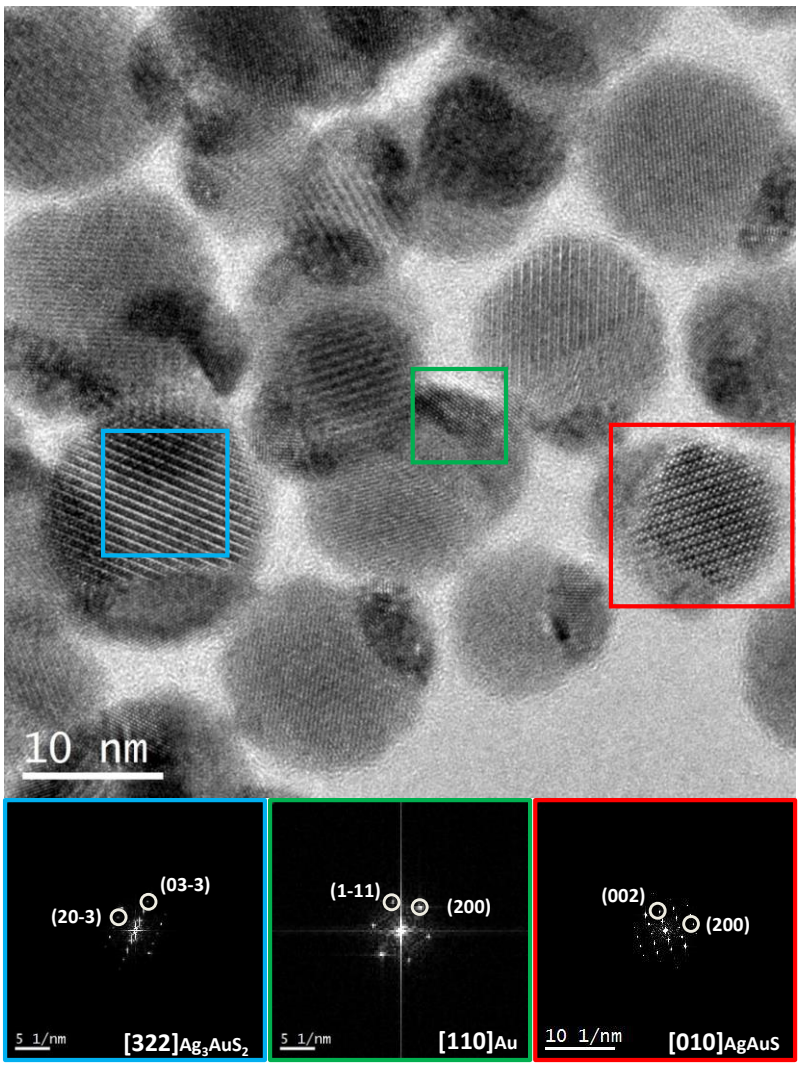

Figure 3.19: HRTEM image of Au-AgAuS HNPs and corresponding FFTs analyses from the highlighted regions.

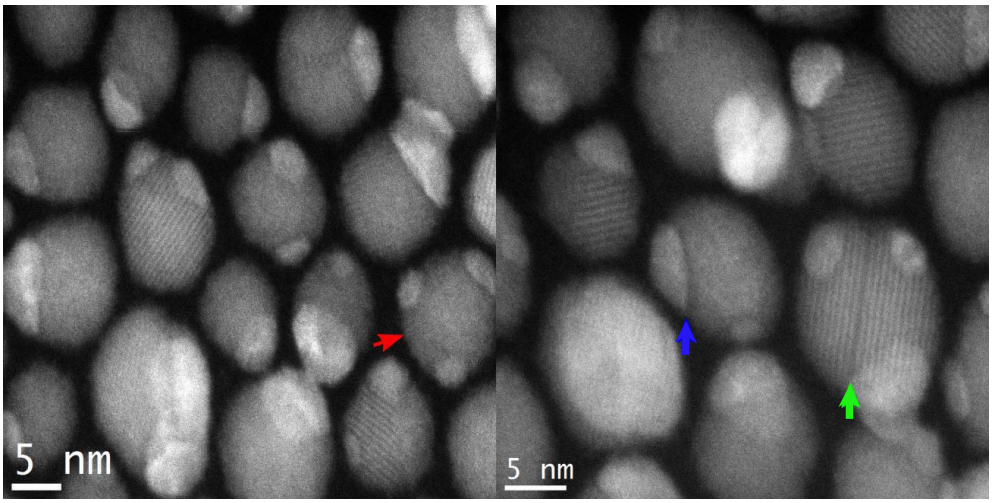

Figure 3.20: STEM-HAADF images of Au-AgAuS HNPs.

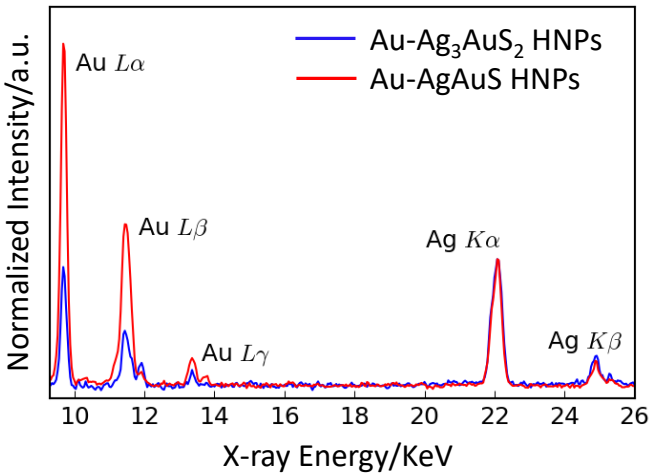

Figure 3.21: Averaged EDX spectra for Au-Ag_3AuS_2 HNPs and Au-AgAuS HNPs, each normalized by the Ag K_α peak.

Hollow Au_2S NPs and NRs were also studied by HRTEM and FFT analyses. The results agreed with the conclusions extracted from the XRD of the hollow Au_2S NPs. However, some minor portions of the monoclinic AgAuS were also identified (Figure 3.22).

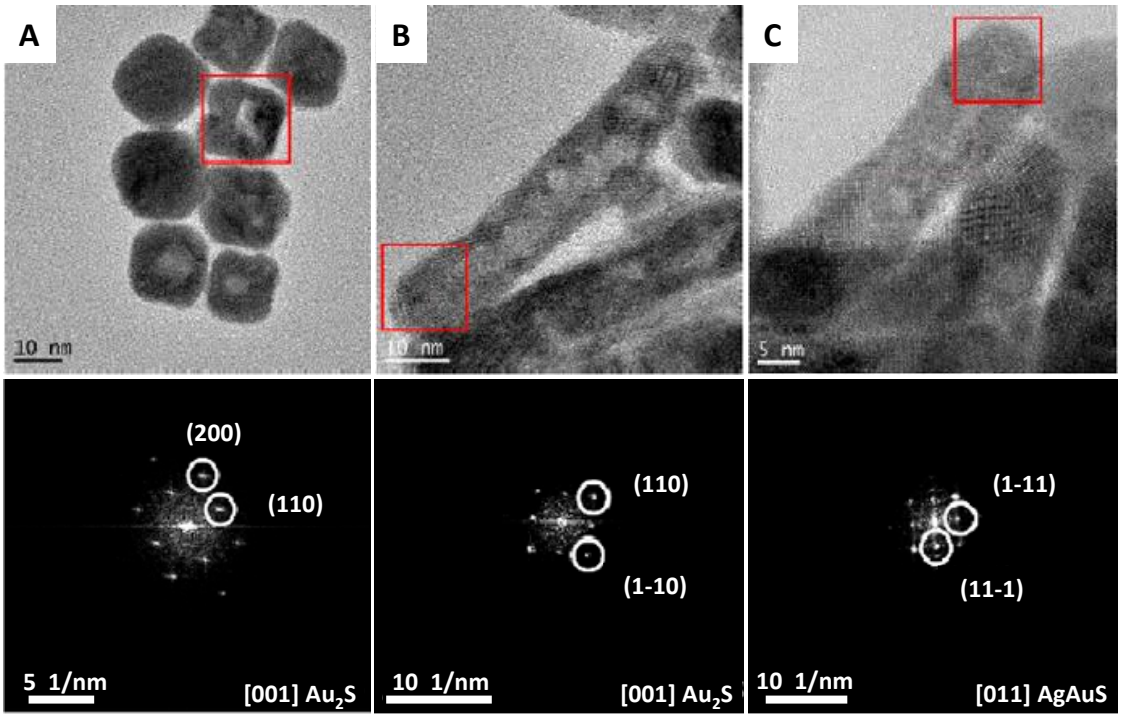

Figure 3.22: (A) HRTEM image of spherical hollow Au_2S NPs and indexed FFT from the highlighted region. (B and C) HRTEM images of hollow Au_2S NRs and indexed FFT from the highlighted regions.

In summary, when TOAB is used as surfactant, the variation of Ag:Au ratio allowed the control of the degree of cation exchange and thus, the semiconductor stoichiometry of

the final product, being possible to isolate both ternary semiconductors (Ag_3AuS_2 and AgAuS) and the binary gold sulphide (Scheme 3.1).

HRTEM images of hybrid nanosystems show the presence of an amorphous shell, which was assumed to be elemental sulphur, regarding the previous results with Ag-Au-Se systems (Chapter 2). Hence, the chalcogenide (S^{2-} specie) is thought to be the reducing agent of the synthesis. However, in this case, despite the use of a non-reducing surfactant, the formation of metallic gold domains in the surface of the nanoparticles could not be avoided in most cases. The general trend of chalcogens is that the reducing character increases when going down in the group. So, selenides should be more reductants than sulphides. Nevertheless, the high affinity of sulphides and gold is well known, and the reduction of Au(III) could be significantly enhanced, in these systems, for the possibility of the formation of Au(I)-S(-II) and Au(0)-S(-II) bonds, which have been reported to be highly thermodynamically favoured.

Curiously, hollow Au_2S NPs do not present the metallic domain. The difference between the outward and inward rates of Au(I) and Ag(I) during the cationic exchange, which induce the formation of the void, as a consequence of the Kirkendall effect, might also avoid the further reduction of gold and the subsequent deposition on the semiconductor surface.

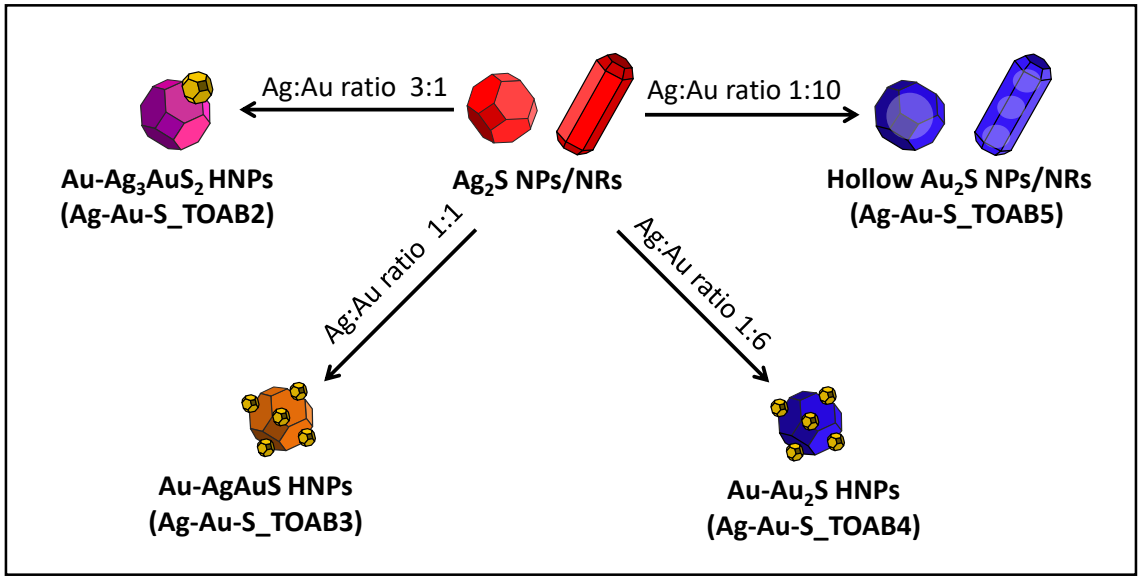

Scheme 3.1: Scheme of the results obtained playing with different ratios Ag:Au, using TOAB as surfactant and long reaction times (24h).

Study of the influence of reaction time

Another parameter that could be important for the control of the final product might be the reaction time. Two simple experiments were done in this direction: the reaction time, which in the previous experiments was 24h, was decreased to 30 minutes in

experiments Ag-Au-S_TOAB2 (Ag:Au ratio of 3:1, the new sample will be Ag-Au-S_TOAB2.1) and 3 (Ag:Au ratio of 1:1, new sample will be Ag-Au-S_TOAB3.1). In both experiments, as it can be checked in XRD patterns of Figure 3.23B and D, the reactions were not complete at short times. In sample Ag-Au-S_TOAB2.1, there were a mixture of Ag_3AuS_2 and Ag_2S instead of just the ternary semiconductor. Whereas in sample Ag-Au-S_TOAB3.1 there were a mixture of the two ternary materials (Ag_3AuS_2 and AgAuS). TEM images of the samples (Figure 3.23A and C) show the dimer-like nanostructures with a metallic domain and a semiconductor domain, even though, the morphology and the aggregation of the nanostructures was not as good as in the previous experiments. The use of a different batch of pre-synthesised Ag_2S NPs in these syntheses might be the cause of these differences between these samples and the previous ones.

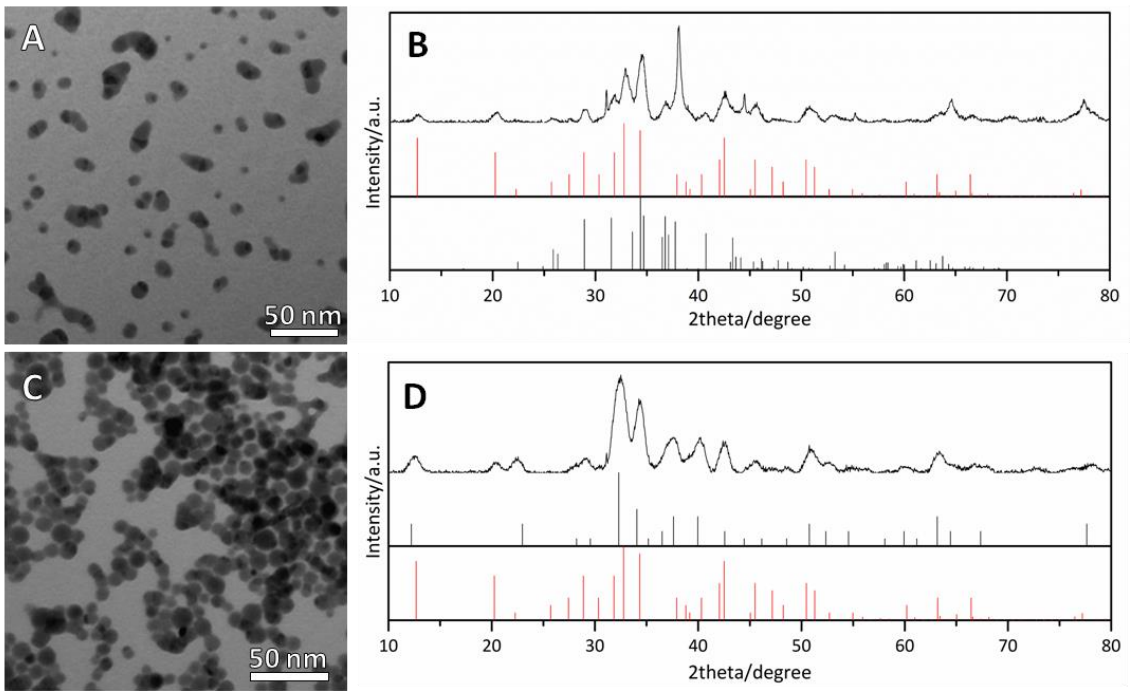

Figure 3.23: TEM images of (A) Ag-Au-S_TOAB2.1 and (C) Ag-Au-S_TOAB3.1. (B) XRD pattern of Ag-Au-S_TOAB2.1 and tetragonal Ag_3AuS_2 (JCPDS 020-0461, red) and monoclinic Ag_2S (JCPDS 014-0072, black) reference patterns. (D) XRD pattern of Ag-Au-S_TOAB3.1 and monoclinic AgAuS (038-0396, black) and tetragonal Ag_3AuS_2 (red) reference patterns.

Use of DDA as phase transfer agent

In order to further study the Ag-Au-S system, TOAB was substituted by DDA as the phase transfer agent. Since in the previous section it was demonstrated that the final product was not related to the shape of the pre-synthesised Ag_2S nanomaterial, in this section, spherical and rod-like nanostructures will be presented indistinctively and just the reaction parameters (reaction time and Ag:Au ratio) and the composition of the samples will be discussed.

The first idea was to synthesise a hybrid nanoparticle which had the metallic domain but that maintained the binary semiconductor. The recreation of the conditions used in selenium systems was a successful experiment (Ag-Au-S_DDA1). Briefly, the conditions used were low reaction time (1s) and intermediate gold concentration (3 mM). As it is easily observed in the TEM image (Figure 3.24) the morphology of the NPs was dimeric. In the XRD pattern it is possible to see that the binary phase of the pre-synthesised NPs was preserved during the reaction.

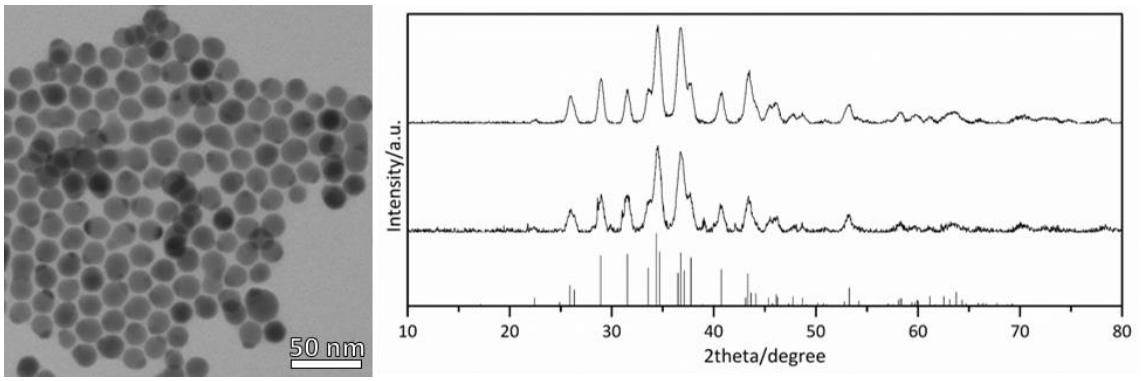

Figure 3.24: TEM image of Ag-Au-S_DDA1 and XRD patterns of Ag_2S NPs (top) and Ag-Au-S_DDA1 (bottom) and monoclinic Ag_2S (JCPDS 014-0072) reference pattern.

When the reaction time was increased to 30 minutes and the concentration of gold solution was maintained at 3 mM (Ag-Au-S_DDA2), the diffusion of gold in the binary structure could not be avoided. The XRD pattern (Figure 3.25) showed the mixture of Ag_2S and Ag_3AuS_2. However, the morphology of the nanostructures was maintained, as it can be observed in TEM image.

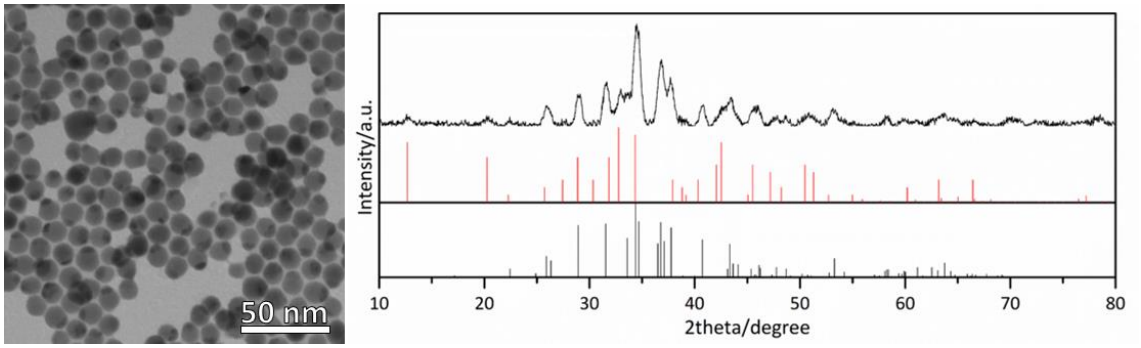

Figure 3.25: TEM image and XRD patterns of Ag-Au-S_DDA2 and monoclinic Ag_2S (JCPDS 014-0072, black) and tetragonal Ag_3AuS_2 (JCPDS 020-0461, red) reference patterns.

Two experiments, with Ag:Au ratios of 3:1 and 1:1 keeping the long reaction time (24h) were done. In Ag-Au-S_DDA3 (Ag:Au ratio of 3:1), there were two kinds of morphologies (Figure 3.26): some nanorods with a big metallic tip, others with more

than one, but smaller. Despite of the different morphology, the XRD pattern showed all the sample were of Ag_3AuS_2.

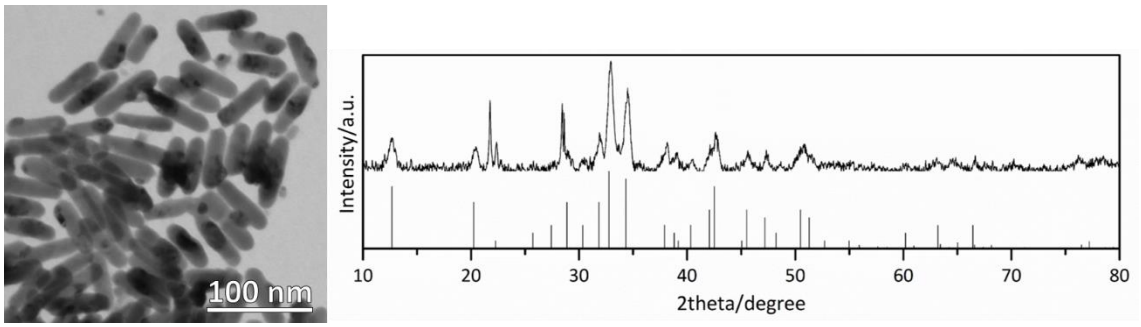

Figure 3.26: TEM image and XRD pattern of Ag-Au-S_DDA3 and tetragonal Ag_3AuS_2 (JCPDS 020-0461) reference pattern.

When using the Ag:Au ratio of 1:1 (sample Ag-Au-S_DDA4), the morphology was practically the same as in the previous sample, but the ternary semiconductor was different (Figure 3.27). The higher amount of gold allowed a higher cation exchange to obtain the monoclinic phase AgAuS.

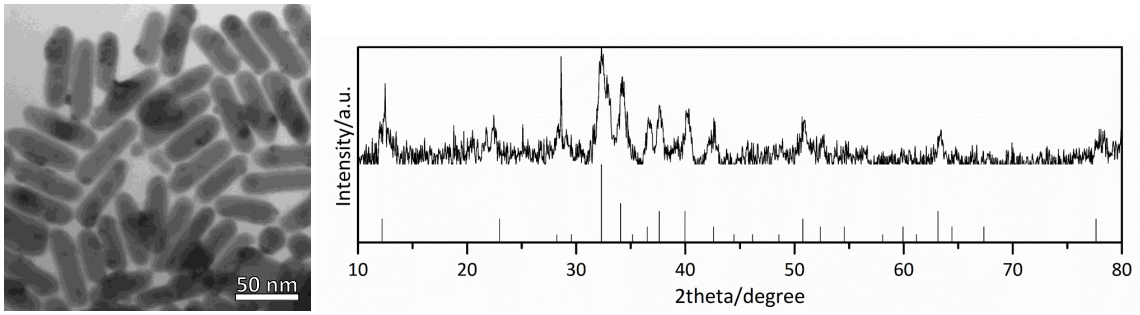

Figure 3.27: TEM image and XRD pattern of Ag-Au-S_DDA4 and monoclinic AgAuS (JCPDS 038-0396) reference pattern.

Finally, a last experiment (Ag-Au-S_DDA5) was done increasing the amount of gold complex to a big excess (Ag:Au ratio 1:10, 24 h). The intention was to imitate the experiment of hollow NPs to test if it was possible to obtain this kind of nanostructures using this surfactant. In this case, hollow nanostructures were not formed. As it is possible to see in TEM image (Figure 3.28) the sample was composed of spherical nanoparticles with metallic tips on the surface. However, it was not just the morphology, but also the crystalline phase was different: with DDA, a complete cation exchange to have Au_2S was not achieved and the exchange stops at the AgAuS phase, as it can be checked in the XRD pattern.

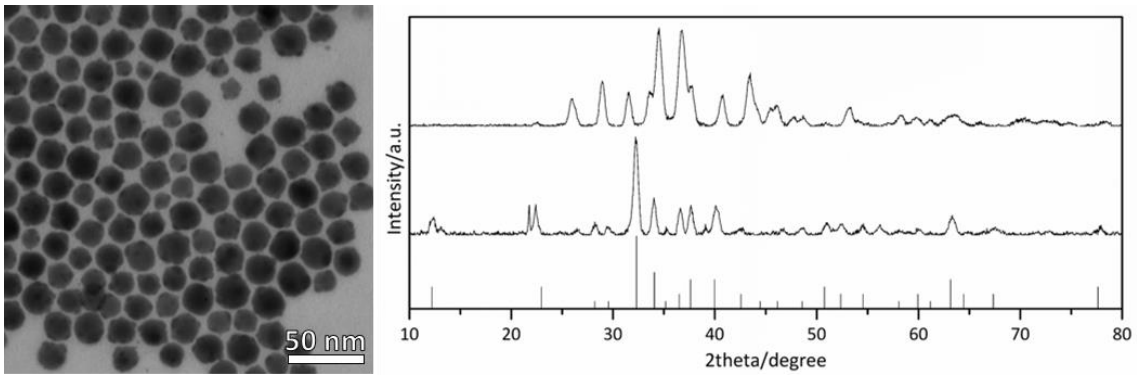

Figure 3.28: TEM image of Ag-Au-S_DDA3 and XRD patterns of Ag_2S NPs (top) and Ag-Au-S_DDA5 (bottom) and monoclinic AgAuS (JCPDS 038-0396) reference pattern.

At the same Ag:Au ratios, the presence of a more reducing surfactant in the gold complex allowed a faster reduction of gold and, accordingly, a faster growth of the metallic tip, letting the possibility to obtain, when working at short reaction time, a dimer-like nanostructure which preserved the binary phase of the semiconductor. When the ratio of Ag:Au or the time was increased, the metallic tip also grows quicker and bigger, as it was proved in experiments 4 and 5, and gold started to diffuse inside the semiconductor. In addition, and probably due to the absence of bromide in the solution, Ag^+ cations do not precipitate and, as a consequence, their outward diffusion rate was slower and no Kirkendall effect occurred in these conditions. So, it was not possible to have the complete cation exchange nor to obtain hollow nanostructures (Scheme 3.2).

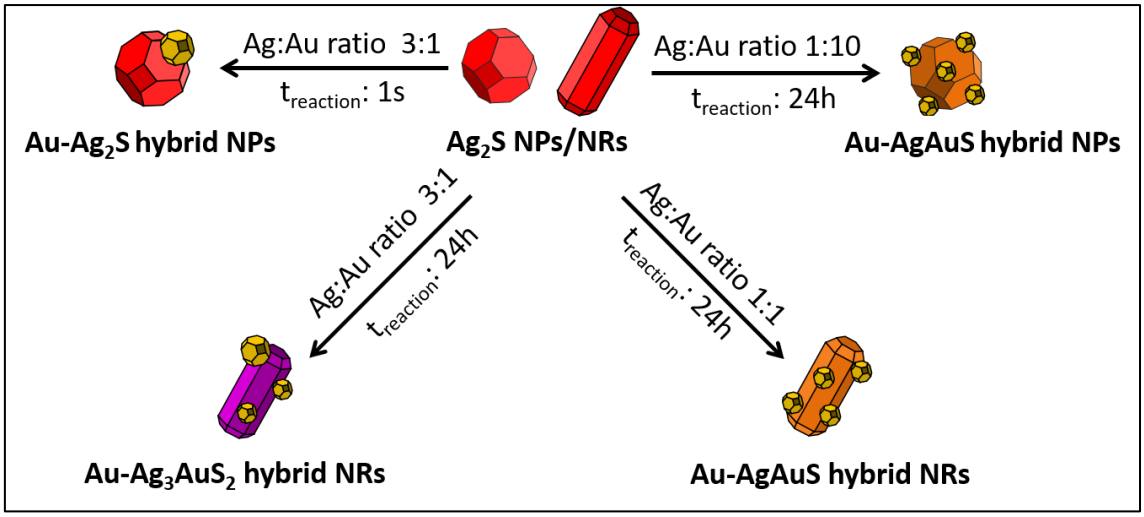

Scheme 3.2: Scheme of the obtained results when using DDA as surfactant.

3.5 Optical characterization of Ag_2S NPs, Au-Ag_3AuS_2 HNPs and Au-AgAuS HNPs

UV-Vis-NIR absorption spectroscopy of Ag_2S NPs, Au-Ag_3AuS_2 HNPs and Au-AgAuS HNPs was done (Figure 3.29). The spectrum of Ag_2S NPs (black line) showed a featureless absorption, nearly zero at high wavelengths and that started to increase at 1000nm. Bulk Ag_2S has a band gap energy of 0.9-1.1 eV (1380-1130nm), however, it is possible to tune this bang gap, to lower, by reducing the size of the nanoparticle, as a consequence of the quantum confinement.[216,248] Synthesised Ag_2S NPs did not show a bang gap peak. Since the nanoparticles were large, it is possible there is no quantum confinement and, as a result, they just present the continuous absorption, which is more typical of bulk semiconductors. The absorption spectrum of hollow Au_2S NPs is similar to the Ag_2S NPs, they also show a continuous absorption, which starts increasing at 700 nm.

The absorbance spectra of Au-Ag_3AuS_2 HNPs (blue line) and Au-AgAuS HNPs (red line) did neither show a band gap absorption peak. The broad band around 600 nm in both spectra, is probably the plasmonic resonance of metallic gold domains. Nevertheless, the possibility to have a contribution of an intrinsic absorption of the ternary compounds, as was observed in Ag_3AuSe_2 NPs, could not be fully discarded.

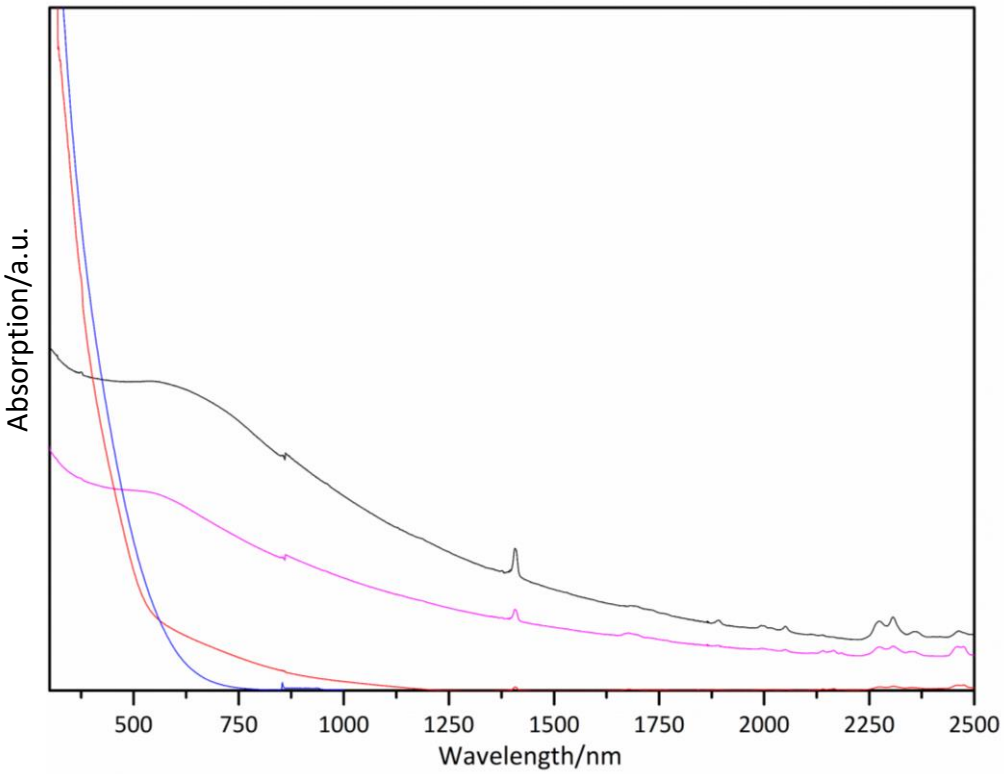

Figure 3.29: UV-Vis-NIR absorption spectra of Ag_2S NPs (red), Au-Ag_3AuS_2 HNPs (sample Ag-Au-S_TOAB2, black), Au-AgAuS HNPs (sample Ag-Au-S_TOAB3, pink) and hollow Au_2S NPs (sample Ag-Au-S_TOAB5, blue)

3.6 Water transference of Ag_2S NPs and Ag-Au-S nanostructures

Ag_2S and Ag-Au-S nanostructures synthesised in this thesis were hydrophobic. As the nanoparticles were surrounded by an amphiphilic surfactant, they were stable in apolar solvents such as toluene, hexane, chloroform, among others. However, many applications, usually catalytic or biomedical applications, need the nanoparticles to be dispersed in water or hydrophilic solvents such as ethanol.

Trying to explore a potential application for the NPs, their catalytic performance in two different reactions was tested: the reduction of nitrophenol to aminophenol and the degradation of the dye methylene blue, being both easy to follow by UV-Vis absorption spectroscopy. Both reactions take place in aqueous media. So, the first step was to transfer the nanostructures to water.

A published method was adapted for this water transference. Liu and co-workers did a ligand replacement of a hydrophobic surfactant (mostly oleylamine with the possible presence of trioctylphosphine) to a hydrophilic ligand (4-mercaptobenzoic acid).[249] Since deprotonated 4-mercaptobenzoic acid is negatively charged, it is stable in polar solvents such as water. It was possible to easily transfer the binary and ternary Ag-Au-S systems to water without losing their morphology, as it is shown in comparative TEM images in Figure 3.30.

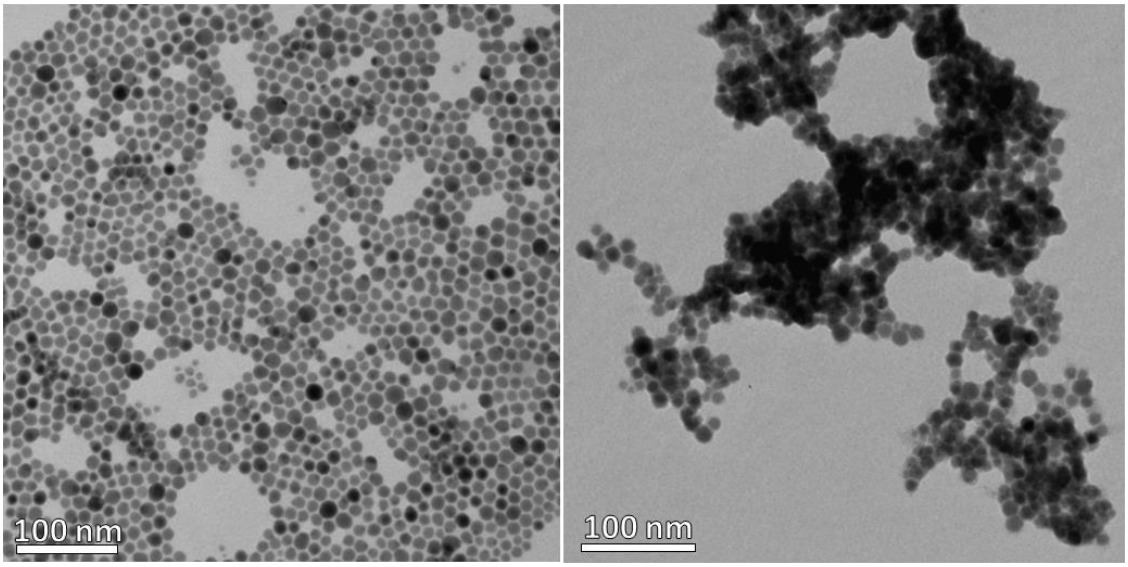

Figure 3.30: TEM images of (A) Ag_2S NPs in toluene (B) Ag_2S NPs in water.

Unfortunately, the results of catalytic experiments cannot be shown considering neither of the reactions worked properly. Regarding to the reaction of reduction of nitrophenol, the “catalysts”, which should have been the synthesised nanostructures, were destroyed. The sodium borohydride, which was the reducing agent of the reaction and it was essential, reduced the nanoparticles to metallic silver. With respect

to the degradation of methylene blue, the reaction did not work, the methylene blue remained in the solution, without being reduced, after hours of reaction.

3.7 Experimental part

Chemicals

Silver chloride (AgCl, 99.9%), sulphur powder (S, 99.99%) and tri-n-octylphosphine (TOP, 97%) were obtained from Strem Chemicals. Silver nitrate ($AgNO_3$, ≥99%), gold (III) chloride trihydrate ($HAuCl_4 \cdot 3H_2O$, ≥99.9%), 1-octadecene (ODE, 90%), oleylamine (OLAm, 70%), dodecylamine (DDA, 98%), tetraoctylammonium bromide (TOAB, 98%), 4-mercaptobenzoic acid (99%), toluene (99.9%) and tetrahydrofuran (THF, 99.9%) were purchased from Sigma-Aldrich. Ethanol (EtOH, 96% v/v) was obtained from Panreac. All the reagents and solvents were used without further purification.

Synthesis of Ag_2S NPs

For the synthesis of Ag_2S NPs three methods were used.

Method A: The first method was adapted from that used for the synthesis of Ag_2Se NPs. Briefly, 1.95g TOPO and 1.65 mL OLAm were disposed in a three-neck flask and degassed under vacuum at 120°C for 30 minutes. Meanwhile, two precursor solutions were prepared in the glovebox: 1 mL OLAm-S and 1 mL AgCl-TOP. After degassing, and under N_2 atmosphere, the temperature was raised to 180°C and the OLAm-S solution was injected. Once the temperature was recovered, the AgCl-TOP precursor solution was injected. Immediately after the silver precursor injection the colour of the solution changed from clear orange to dark brown. After 20 minutes of reaction, the heating was stopped, and the solution was let cool down naturally. Subsequently, the NPs were collected adding EtOH, centrifuging 4 minutes at 4500 rpm and re-dispersing them in 1 mL toluene. This last step was repeated three times. The final solution was usually stable and dark brown.

S-OLAm precursor solution was prepared dissolving 64 mg S (2 mmol) in 1 mL OLAm, it was necessary to heat intensely the solution with a heat gun in order to dissolve completely the sulphur. The solution was dark orange and transparent. AgCl-TOP was taken from the stock solution prepared for the synthesis of Ag_2Se. This was prepared as follows: 3.6 g (25 mmol) AgCl were dissolved in 25 mL TOP. The solution needed to be heated in a hot plate until complete dissolution of the solid. It is important the heating was gently and with continued magnetic stirring to avoid the reduction of Ag(I) to metallic silver. Additionally, this solution is light sensitive, so, it was indispensable to

protect it from the light, covering the vial with aluminium foil. The final solution was transparent and pale yellow.

Method B: Same procedure used in A, substituting the solvent of the reaction, using 2.5 mL of octadecene instead of TOPO.

Method C: This method was published by Wang and co-workers as part of a more complex nanostructure.[220] 17 mg $AgNO_3$ (0.1 mmol), 8 mg S (0.25 mmol) and 8 mL OLAm were placed in a three-neck flask and were purge three times by vacuum-N_2 cycles. Under N_2 atmosphere, the system was heated to 160^{o}C and let it react for 20 minutes at this temperature. The colour of the solution was changing slowly from orange to dark brown. After this time, the heating was removed, and the solution was let cool down naturally. Once the solution was at room temperature, NPs were precipitated by the addition of EtOH and centrifugation (4 minutes at 4500 rpm), finally the precipitate was dispersed in toluene. In order to maintain the stability of these NPs it was important to wash them just one time.

Synthesis of Ag_2S Nanorods

The synthesis of silver sulphide nanorods was adapted from the procedure published by Son and co-workers.[221] Briefly, under inert atmosphere, sulphur precursor solution was prepared dissolving 50 mg S (1.56 mmol) in 7 mL OLAm, slightly heating was necessary for the complete dissolution of the solid. This solution was injected to a three-neck flask under nitrogen and temperature was raised to 100°C. Once this temperature was reached, silver precursor was injected and the mixture reacted for 2 minutes at this temperature. After this time, the heating mantle was removed and the solution was let cool down naturally. The mixture was extracted to a vial with 2 mL of toluene and, 2 mL of ethanol were added to destabilize the dispersion and precipitate the nanoparticles. After 3 minutes of centrifugation at 4500 rpm, supernatant was discarded and the precipitate was re-dispersed in toluene.

Silver precursor solution was prepared dissolving 50 mg $AgNO_3$ (0.29 mmol) in 2 mL OLAm at temperature above 200°C. Heating the solution was important, because having metallic silver instead of Ag(I) was essential for obtaining elongated nanostructures.

Phase transfer of Au(III) cations from water to toluene

For the phase transfer of Au(III) cations from water to toluene the same procedure described in the experimental part of chapter two was used. It was based on the protocol reported by Yang and co-workers.[166]

For the preparation of 6 mM Au(III)-DDA stock solution, 25 mL of Au(III) cations 6 mM aqueous solution (60 mg (0.15 mmol) $HAuCl_4 \cdot 3H_2O$ dissolved in 25 mL of deionized water) were mixed with an ethanolic solution of dodecylamine (2.4 g (13 mmol) DDA in 25 mL EtOH). The aqueous solution, which was transparent and orange, became translucid after the mixture with the ethanolic solution. After 3 minutes of stirring, 25 mL of toluene were added to the solution, and the stirring was kept for 3 more minutes. After the separation of the two phases (aqueous phase which contains basically chloride anions, and organic phase with the Au(III)-DDA complex) the toluene phase was extracted and washed three times with 10 mL of H_2O/EtOH 1:1 mixture to avoid the precipitation of silver chloride in further reactions with silver sulphide NPs.

The preparation of more diluted solutions, specifically the 3 mM solution, was done using proportional amounts of $HAuCl_4 \cdot 3H_2O$ (30 mg) and DDA (0.6 g).

The preparation of 6 mM Au(III)-TOAB stock solution was also adapted from this protocol, using 187.5 mg (0.34 mmol) of TOAB instead of DDA.

Synthesis of Ag-Au-S hybrid nanostructures

For the synthesis of complex nanostructures made of Ag, Au and S a simple reaction at room temperature was used in all cases. The procedure consisted in the mixture of the pre-synthesised Ag_2S nanoparticles (0.6 µM) with the Au(III)-TOAB/DDA solution. Three conditions were changed: surfactant, reaction time and Ag:Au rate.

In Table 3.1 there is a compiling of the conditions used in each experiment. All the experiments were done at room temperature and shaken mechanically and 300 µL of pre-synthesised Ag_2S NPs solution were used.

Table 3.1: Conditions used in the synthesis of Ag-Au-Se nanostructures.

Sample Ag-Au-S	Shape Ag_2S	Au(III)-complex concentration	Volume (mL) Au-complex	Ag:Au ratio	Reaction time
TOAB 1	NPs	Au-TOAB 6mM	0.3	~ 5:1	24h
TOAB 2	NPs	Au-TOAB 6mM	0.6	~ 3:1	24h
TOAB 3	NPs	Au-TOAB 6mM	1.2	~ 1:1	24h
TOAB 4	NPs	Au-TOAB 6mM	8.1	~ 1:5	24h
TOAB 5	NPs/NRs	Au-TOAB 6mM	16.2	~ 1:10	24h
TOAB 2.1	NPs	Au-TOAB 6mM	0.6	~ 3:1	30 min
TOAB 3.1	NPs	Au-TOAB 6mM	1.2	~ 1:1	30 min
DDA 1	NPs	Au-DDA 3mM	0.6	~5:1	1s

DDA2	NPs	Au-DDA 3mM	0.6	~5:1	30 min
DDA3	NRs	Au-DDA 6mM	0.6	~1:3	24h
DDA4	NRs	Au-DDA 6mM	1.2	~1:1	24h
DDA5	NPs	Au-DDA 6mM	16.2	~10:1	24h

Water transference of Ag_2S and Ag-Au-S nanosystems

The transference of synthesised nanomaterials from hydrophobic solvents (toluene) to hydrophilic solvents (water) was done following the procedure published by Tan and co-workers.[249] The amount of 4-mercaptobenzoic acid was adapted to have a more stable solution.

40 mg 4-mercaptobenzoic acid were dissolved in 5 mL of THF and the solution was heated to 50°C, a solution of 5 mg of nanoparticles dispersed in THF was added and the system was kept at this temperature for 5 hours. It was important to use a condenser to avoid the evaporation of the solvent. After the ligand exchange, 0.5 mL of NaOH 0.5M was added to the solution to destabilize the nanoparticles and the solution was centrifuged 3 minutes at 4500 rpm. The supernatant was discarded and the solid was re-dispersed in water.

Characterization Methods

Transmission Electron Microscopy (TEM). Samples were prepared for observation by dilution in toluene followed by sonication. A droplet of the solution was then poured in holey carbon covered copper TEM grids. A JEOL 2000 FX II conventional TEM operating an accelerating voltage of 80 kV was used.

X-ray Diffraction (XRD). The patterns were acquired with a PANanalytical X'Pert Pro MPD Alpha1 diffractometer operating in θ/ 2θ geometry at 45 kV, 40 mA, and λ = 1.5406 Å (Cu Kα1). Thin layers of the samples were prepared by drop casting and evaporation of the solvent on a monocrystalline Si holder of 15 mm diameter and 0.15 mm height. Scans in the range 2θ = 4−100° were run at a step size of 2θ = 0.017° and 100 s per step. The data were treated with X'Pert HighScore Plus software.

High Resolution TEM, Electron Diffraction and High Angular Annular Dark Field imaging. HRTEM, Electron diffraction and HAADF imaging were performed in a Jeol 2010F operating at 200 kV equipped with a FEG gun and a GIF spectrometer.

Vis−NIR Absorption Spectroscopy. Vis−NIR absorption spectra of all samples were recorded in toluene solution on a PerkinElmer LAMBDA 950 spectrophotometer.

Chapter 4 Ag-Cu-S system

4.1 Introduction

Another family of ternary materials which have stand out in the last few years for their interesting conductivity properties are silver copper chalcogenides. The high mobility of Ag^+ and Cu^+ at high temperature give them a mixed ionic electronic conduction in superionic phases. AgCuS, AgCuSe and AgCuTe are polymorphous semiconductors that exhibit phase transitions as function of temperature that lead to transitions between *p* and *n* type conduction in their charge transport, which makes them appropriate to be applied as thermoelectric or photovoltaic materials, diode or transistor devices.[188,189,250–255]

Silver copper sulphide system, as well as the previous silver gold sulphide system, has two stable compounds with different stoichiometries: Ag_3CuS_2 (mineral *Jalpaite*) and AgCuS (mineral *Stromeyerite*).

Ag_3CuS_2 was first identified in 1858 by C. Breithaupt.[256] Several publications studied its phase transitions; it has a tetragonal crystallographic phase at room temperature which undergoes to a body-centred cubic phase at 112°C in the first transition, and to a face-centred cubic phase, in the second phase transition at 300°C.[257–259] It has been studied as an ammonia sensor,[260] as a photocatalyst[261] and as an absorber material for solar cells.[254,262]

Concerning AgCuS, it crystallizes in an orthorhombic phase (β), which is stable until 93°C, when it goes through a first phase transition to an hexagonal phase (α) and at 166°C, it undergoes to a cubic phase (γ) in the second transition.[252,253,263–265] This material was basically studied for thermoelectric devices.

Silver copper sulphides have been prepared, in the bulk, by a solid state or hydrothermal reaction between the elements Ag, Cu and S. Regarding its nanometric structuration, three different methods have been published. Biswas and co-workers synthesised free capped AgCuS nanocrystals (from 40 nm to 120 nm) by a bottom up

wet chemical method.[252] Zhang and co-workers and Dorfs and co-workers did the synthesis via cation exchange from Ag_2S NPs[266] and $Cu_{2-x}S$ NPs,[267] respectively. Qian and co-workers synthesised Ag_3CuS_2 nanorods by a hydrothermal route.[268]

This chapter is centred in the synthesis of Ag-Cu-S ternary nanostructures using a hot injection method with the objective of achieving an average diameter of the nanoparticles below 40 nm by a direct method.

4.2 Study of the influence of copper precursors

The idea was to employ a method based on the one described for the synthesis of Ag_2S NPs in Chapter 3. As a reminder, the synthesis was done using octadecene as solvent, oleylamine as surfactant, and AgCl-tryoctylphosphine and S-oleylamine as precursors. The reaction temperature was 180°C and the reaction time, 20 minutes. The addition of a copper precursor was essential to obtain ternary Ag-Cu-S materials so, different Cu(I) and Cu(II) salts were tested, including copper halides, copper (II) acetylacetonate, copper (II) nitrate and copper (II) sulphide. In all the experiments a Ag:Cu rate of 1:1 was used. Even though Ag-Cu-S ternary phases were obtained in most experiments, the samples were impurified with other products such as Ag_2S, Cu_2S and metallic Ag. Only with CuCl, CuI, $Cu(NO_3)_2$ and $CuCl_2$ solely ternary phases were synthesised. Below, the results obtained with each reactant are described.

Copper (I) chloride

The first approach consisted in the use of reactants with a copper oxidation state of 1, to avoid the necessity of having an extra redox reaction in the system. When CuCl was used with a Ag:Cu ratio of 1:1, hexagonal NPs with an average diameter of 13.6 nm and a standard deviation of 25% were obtained. TEM micrograph, histogram and XRD pattern of the sample, from now on Ag-Cu-S_A, are displayed in Figure 4.2 and 4.2. XRD showed the formation of two different phases: $(Ag, Cu)_2S$ and AgCuS.

$(Ag, Cu)_2S$ was discovered by Djurle in 1958.[257] This material was named as *Mckinstryite* in 1966[269] and it crystallises in an orthorhombic phase, the same as AgCuS. The exact formula of the compound is not clear, that is why in most references is written as $(Ag,Cu)_2S$, but Djurle suggested the formula $Ag_{1.2}Cu_{0.8}S$. An apparent dimensional relationship between the cell of $(Ag, Cu)_2S$ and AgCuS was noted.[269,270]

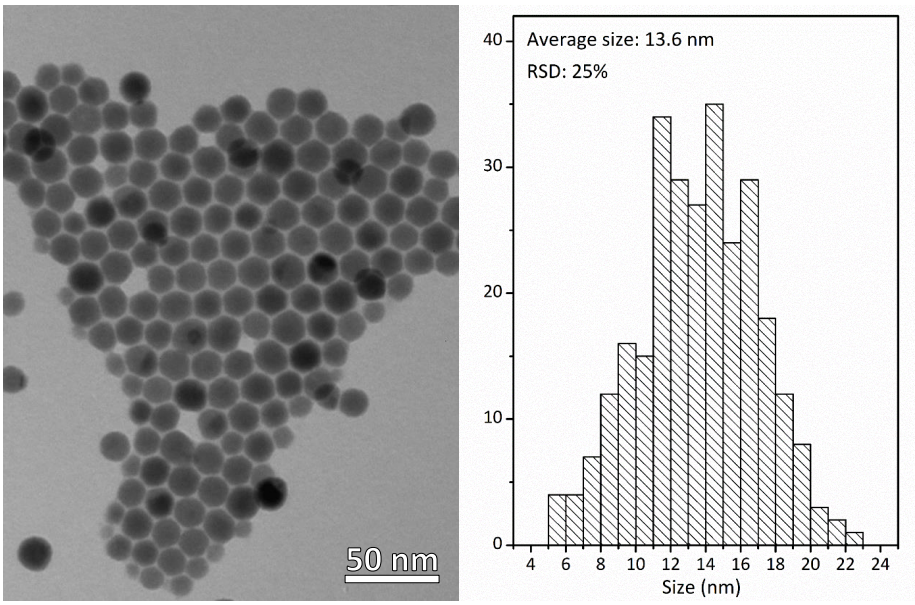

Figure 4.1: TEM micrograph and size histogram of Ag-Cu-S_A NPs (synthesised using CuCl).

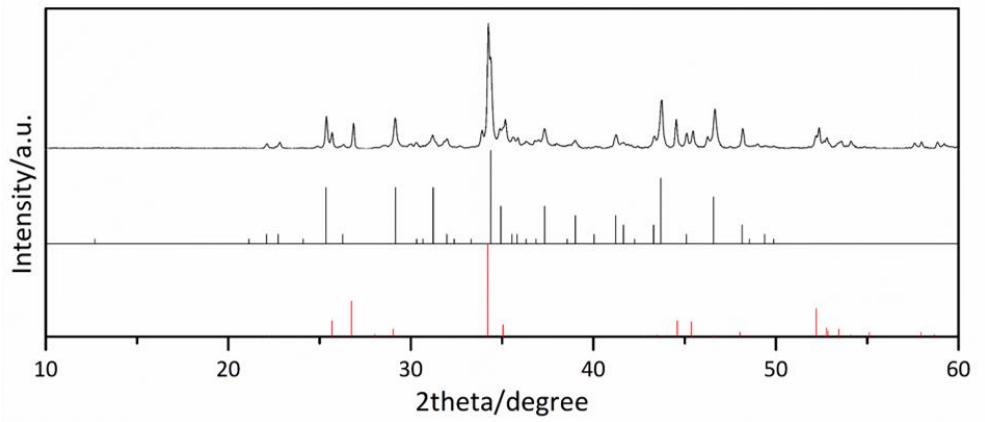

Figure 4.2: XRD pattern of Ag-Cu-S_A NPs (synthesised using CuCl). Orthorhombic $(Ag, Cu)_2S$ (JCPDS 019-0406, black) and orthorhombic AgCuS (JCPDS 075-0890, red) reference patterns.

Copper (I) iodide

When CuI was used as copper precursor instead of CuCl, as can be observed in the TEM micrograph in Figure 4.3, the NPs (sample Ag-Cu-S_B) lost the hexagonal shape and became more spherical, even though they were not perfect spheres. Besides this, the NPs were slightly bigger, with an average size of 18.4 nm, but more monodisperse, with a standard deviation of 13%.

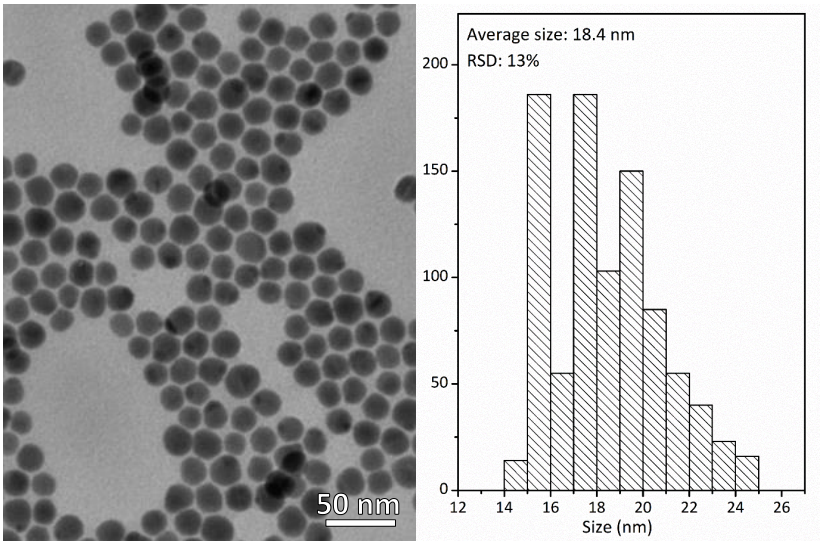

Figure 4.3: TEM image and size histogram of Ag-Cu-S_B NPs (synthesised using CuI).

Regarding the structural phases found in the sample, these were similar to the previous sample (using CuCl), showing a mixture of AgCuS and $(Ag, Cu)_2S$, although the proportion of AgCuS was larger, since their peaks in the XRD pattern increased in intensity (Figure 4.4).

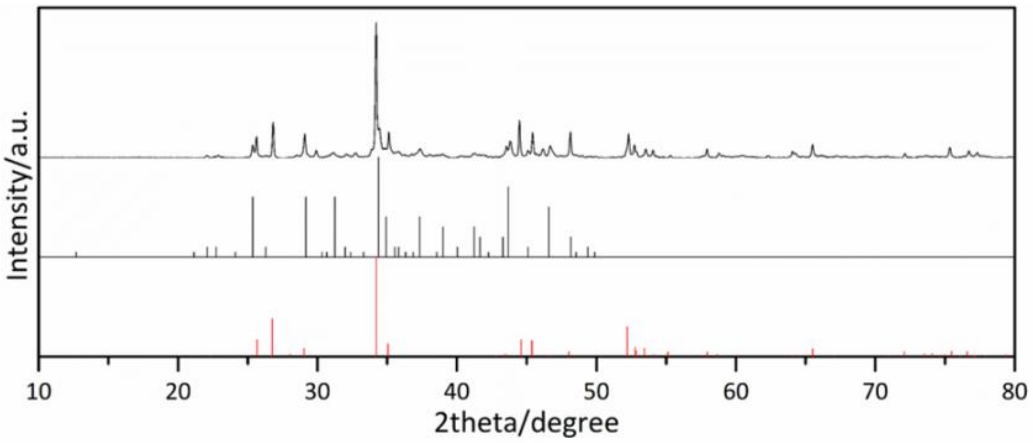

Figure 4.4: XRD pattern of Ag-Cu-S_B NPs (synthesised using CuI). Orthorhombic $(Ag, Cu)_2S$ (JCPDS 019-0406, black) and orthorhombic AgCuS (JCPDS 075-0890, red) reference patterns.

$Cu(NO_3)_2$

Apart from the Cu(I) precursor salts, Cu(II) compounds were also checked. Two of them gave proper results: copper (II) nitrate and copper (II) chloride. When the former was used (sample Ag-Cu-S_C), as can be seen in TEM image of Figure 4.5, the NPs were faceted but with an irregular shape and about 20-25. XRD, shown in Figure 4.6, confirmed there was a mixture of orthorhombic AgCuS and $(Ag,Cu)_2S$, a similar result

to the previous synthesis, even though the XRD reflections of this sample were broader and it was harder to do the assignation.

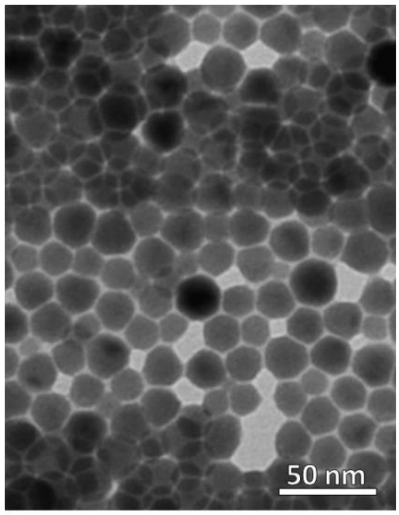

Figure 4.5: TEM micrograph of Ag-Cu-S_C NPs (synthesised using $Cu(NO_3)_2$).

This broadening of XRD reflections was not related to the decrease of NPs size since they were clearly larger than previous samples. It may be due to a high concentration of defects, which is to say that the sample has lower crystallinity.

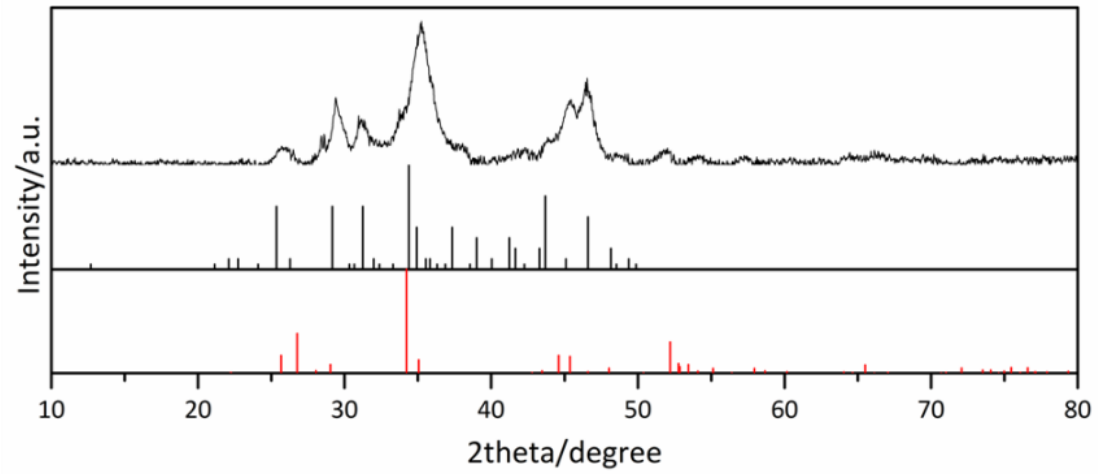

Figure 4.6: XRD pattern of Ag-Cu-S_C NPs (synthesised using $Cu(NO_3)_2$). Orthorhombic AgCuS (JCPDS 075-0890, red) and orthorhombic $(Ag,Cu)_2S$ (JCPDS 019-0406, black) reference patterns.

Copper (II) chloride

Finally, when the Cu(II) salt with chloride counterion was used (sample Ag-Cu-S_D), also faceted irregular shaped NPs were obtained with an average size of 20.8 nm and a standard deviation of 12.3%, as can be observed in TEM image of Figure 4.7. XRD pattern, shown in the same figure, had also broad reflections which indicate an

apparent low crystallinity. The fact that samples synthesised from a Cu(II) precursor (samples C and D) presented higher number of defects in the structure in comparison with samples synthesised from a Cu(I) source (samples A and B) pointed out a possible connection between the copper oxidation of the precursor and the crystallinity of the sample. The use of Cu(II) might induce a partial oxidation of the Cu(I) of the ternary material, creating vacancies and, as a consequence, defects.

Additionally, for the first time, XRD showed the presence of the tetragonal Ag_3CuS_2, even though it was together with the orthorhombic $(Ag,Cu)_2S$. Some extra experiments, basically changing the Ag:Cu ratio, were done with this copper precursor in order to favour the formation of Ag_3CuS_2. Even though the proportion of this silver-rich phase could be increased significantly in these experiments, the multiple impurities that were obtained made unachievable to isolate it.

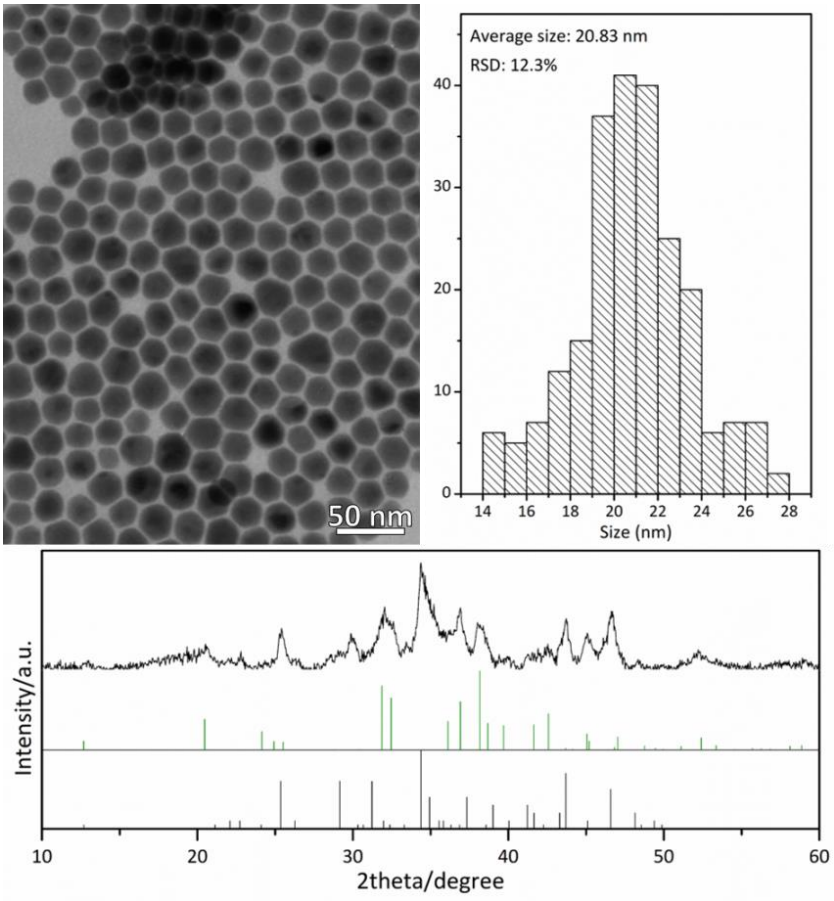

Figure 4.7: TEM image, size histogram and XRD pattern of Ag-Cu-S_D NPs (synthesised using $CuCl_2$ as copper precursor). Orthorhombic (Ag, Cu)$_2$S (JCPDS 019-0406, black) and tetragonal Ag_3CuS_2 (JCPDS 079-2271, green) reference patterns.

4.3 Study of reaction mechanism with different copper precursors

To understand the mechanism of the reaction, a study by XRD and TEM at different times was done using CuCl, $CuCl_2$ and CuI as copper precursors. Interestingly, the three precursors took different mechanisms.

Copper (I) chloride

Figure 4.8 shows the TEM images of different aliquots of the reaction done using CuCl as copper precursor. First aliquots (taken after the injection and after 1 minute of reaction) are not displayed because no particles were observed in them. The morphological characterization did not give relevant information, for the moment. As can be observed, from minute 5 to the end of the reaction, the NPs had similar size and shape. It seems that they were gaining monodispersity with time.

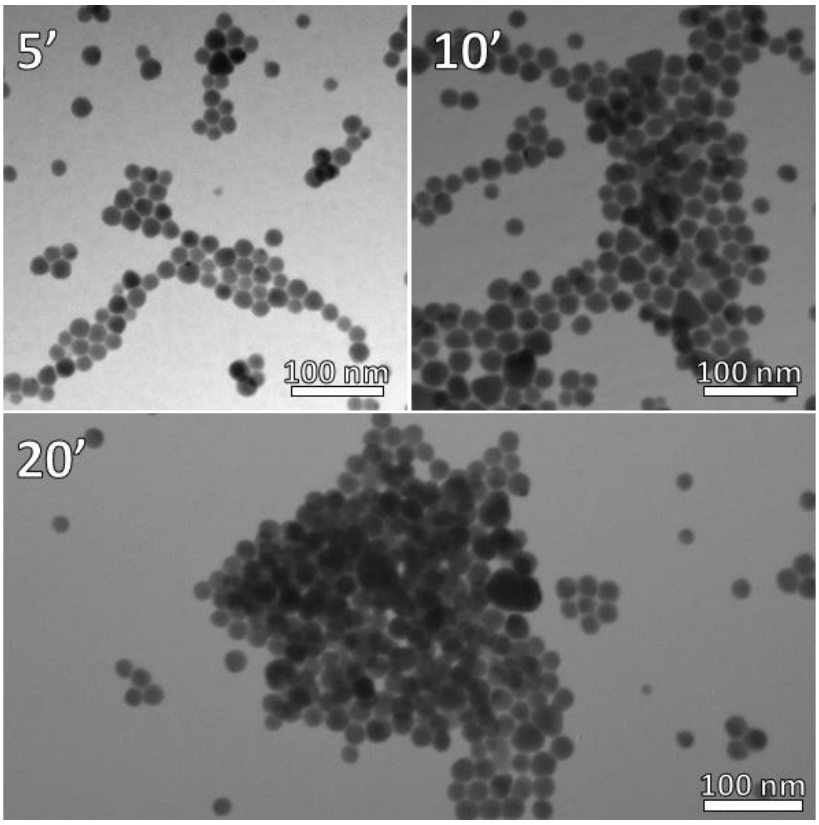

Figure 4.8: TEM images of Ag-Cu-S_A NPs (synthesised using CuCl) extracted at different reaction times (5', 10' and 20').

All XRD patterns of the different aliquots are exhibited in Figure 4.9 and 4.10. XRD pattern of the aliquot extracted right after the injection of the metallic precursors showed the immediate formation of monoclinic Ag_2S. There were some peaks which

did not exactly match with this monoclinic phase, but they did with other phases of silver sulphide, such as Ag_8S. These nanoparticles of Ag_2S reacted quickly with Cu(I) cation to form ternary compounds, which can be observed after one minute of reaction. At this stage of the synthesis, a mixture of Ag_3CuS_2 and $(Ag,Cu)_2S$ was observed clearly.

After 5 minutes of reaction, only peaks of $(Ag, Cu)_2S$ phase were detected. So, it seems that the Ag_3CuS_2 (formed as a first stage of the reaction) carries on with the reaction with copper to be transformed to $(Ag,Cu)_2S$. These results suggest that although in the initial reaction (Ag-Cu-S_A) only AgCuS could be obtained, there is also a possibility to isolate Ag_3CuS_2 by tuning both reaction time and amount of CuCl in the reaction medium.

From minute 5 to the end of the reaction (minute 20) the phase did not change. This was consistent with the fact that the material was not suffering big morphological changes.

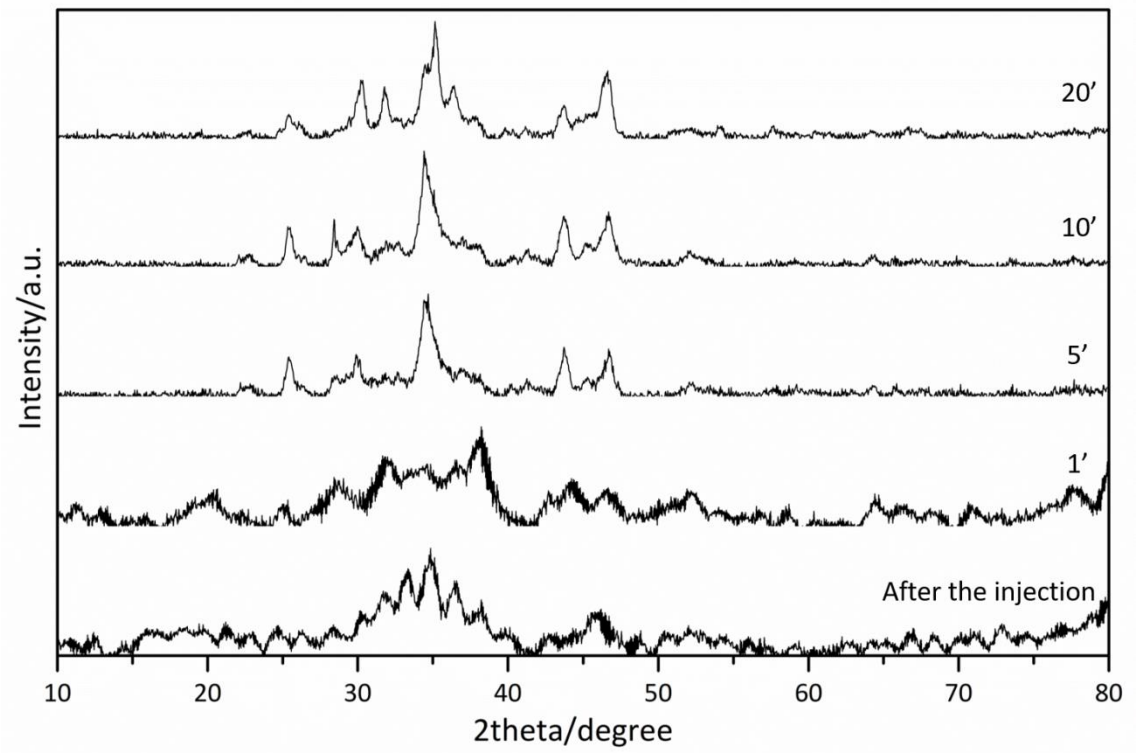

Figure 4.9: XRD patterns of Ag-Cu-S NPs_A (synthesised using CuCl as copper precursor) extracted at different reaction times (after the injection, 1', 5', 10' and 20').

Thus, it seems that the silver precursor is more reactive than the copper precursor and it reacts quicker with the sulphur to form Ag_2S. Afterwards, the silver sulphide reacts with the copper precursor, suffering a partial cation exchange that leads to the formation of the mixture of ternary materials.

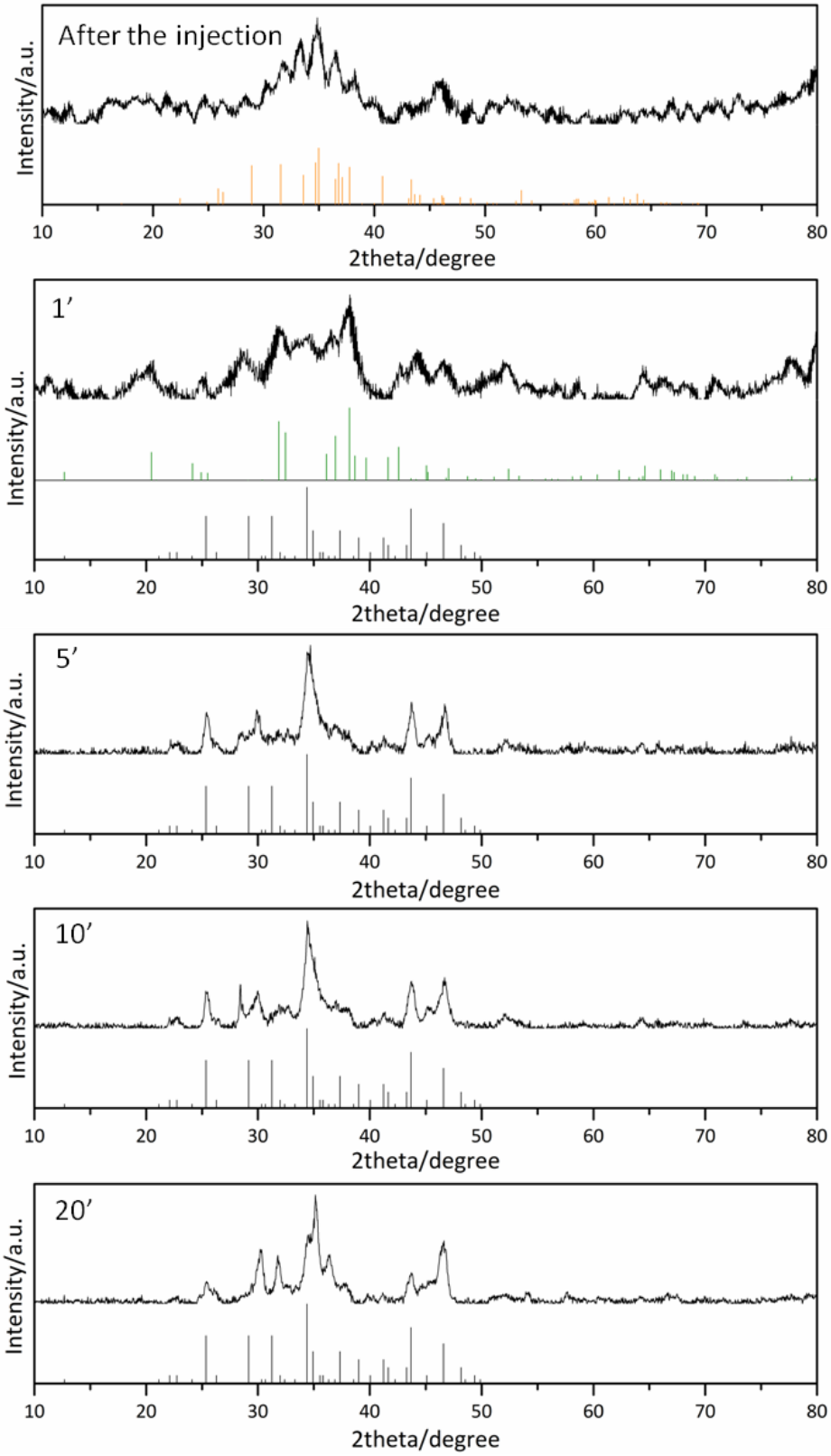

Figure 4.10: XRD patterns of Ag-Cu-S_A NPs (synthesised using CuCl) extracted at different reaction times (after the injection, 1', 5', 10' and 20'). Monoclinic Ag_2S (JCPDS 024-0715, orange), tetragonal Ag_3CuS_2 (JCPDS 079-2271, green) and orthorhombic $(Ag,Cu)_2S$ (JCPDS 019-0406, black) reference patterns.

This mechanism is similar to the synthesis published by Wang and co-workers, in which they synthesise AgCuS nanocrystals via cation exchange using pre-synthesised Ag_2S NPs and $CuCl_2$ as copper precursor.[266] The fact that the Ag_3CuS_2, seen after 1 minute of reaction, disappeared after 5 minutes of reaction to be converted in $(Ag,Cu)_2S$ suggests the idea that copper (I) ions are entering the structure slowly, forming, in first place, the Ag_3CuS_2 and then, with the introduction of more cations, the $(Ag,Cu)_2S$ or AgCuS (Scheme 4.1).

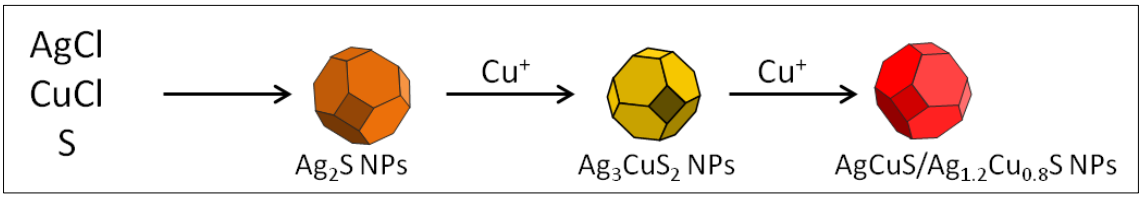

Scheme 4.1: Scheme of the reaction mechanism for the synthesis of Ag-Cu-S NPs when CuCl was used as copper precursor.

Copper (II) chloride

The reaction mechanism when using $CuCl_2$ as copper precursor was also studied. In Figure 4.11, TEM images of the aliquots extracted at different times are displayed. Images of the sample after the injection are not shown because, similar to the previous experiments, no particles were observed. At the beginning of the reaction, two kinds of NPs were observed. With time, they were becoming more homogeneous. However, the final sample was not as monodisperse as the previous and analogous Ag-Cu-S_D. This could be due to the fact that the reaction had been disturbed constantly to extract the aliquots and that could cause some changes in it.

Regarding to the crystallographic evolution of the sample, XRD patterns are displayed in Figure 4.12 and 4.13. After the injection, Ag_2S was quickly formed and after one minute of reaction it was completely transformed to Ag_3CuS_2 and AgCuS. Apart from the ternary compounds, it was possible to observe extra peaks from a phase of a copper sulphide (Cu_8S_5). The composition of the sample did not suffer considerable changes during the reaction. After 20 minutes, the mixture of compounds was the same as after one minute of reaction. Curiously, in the XRD pattern of the 10 minutes-aliquot the extra peaks of the copper sulphide phase cannot be observed. However, as it appeared again at the final product, it was assumed that the copper sulphide should be also in 10' sample. It is possible that it was eliminated during the washing procedure or that the sample was not well mixed and in the extraction of the aliquot, this byproduct was not taken.

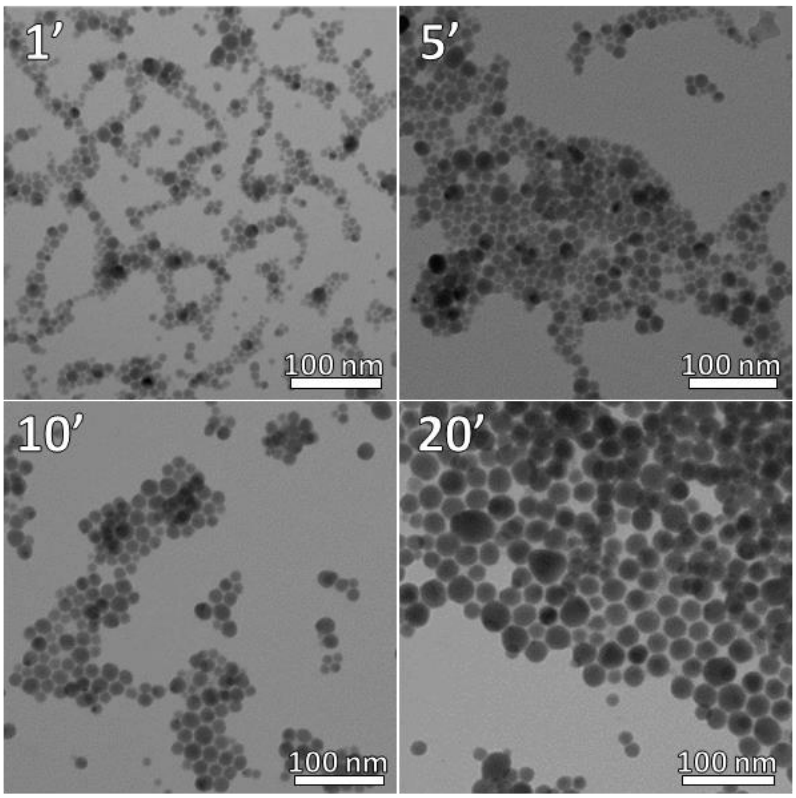

Figure 4.11: TEM images of Ag-Cu-S_D NPs (synthesised $CuCl_2$) extracted at different reaction times (1', 5', 10' and 20').

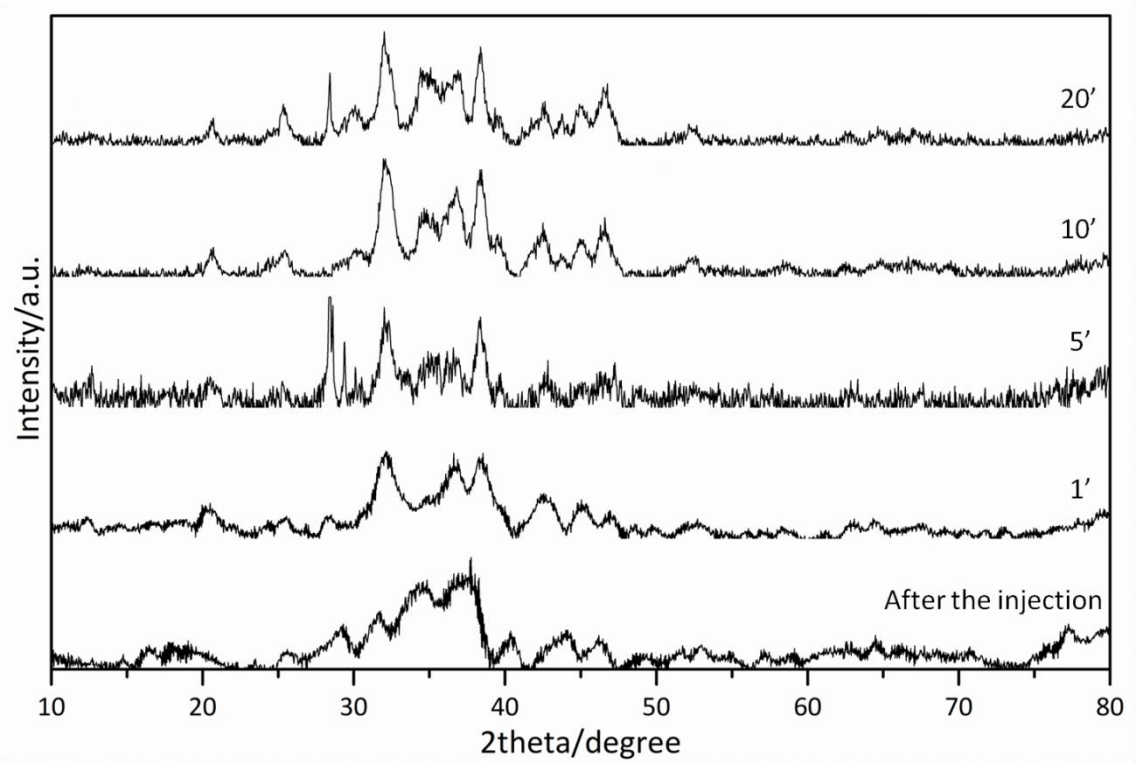

Figure 4.12: XRD patterns of Ag-Cu-S_D NPs (synthesised using $CuCl_2$) extracted at different reaction times (after the injection, 1', 5', 10' and 20').

At 30° there is a broad peak which at first sight does not seem to match to any of the phases. However, Ag_3CuS_2 presents two reflections in this range, which have low intensity and are not visible in the reference plot. Sometimes, depending on the synthesis, different crystallographic planes are exposed or overgrown and, therefore, the relative intensity of peaks can change.

Both mechanisms, with CuCl and $CuCl_2$, are similar. At the first moment, Ag_2S was formed, to quickly react with copper ions and to transform to the ternary materials. In the CuCl experiment, a two-step partial cation exchange reaction was suggested (Scheme 4.1), first to Ag_3CuS_2, and second to $(Ag,Cu)_2S$. Curiously, in the case of $CuCl_2$, at the end of the reaction, the phase Ag_3CuS_2 remains in the system. As the mechanism is assumed to be the same, there might be some unknown factor blocking the total transformation of Ag_3CuS_2 to $(Ag,Cu)_2S$ or AgCuS. The unexpected formation of copper sulphide (Cu_8S_5) binary NPs could be related to this issue because it decreases the amount of copper available in the reaction medium and the transformation could not be completed (Scheme 4.2).

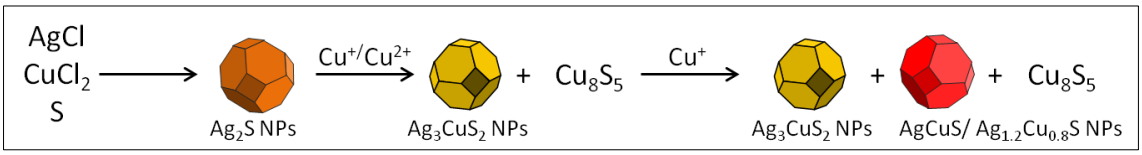

Scheme 4.2: Scheme of the reaction mechanism for the synthesis of Ag-Cu-S NPs when $CuCl_2$ is used as copper precursor.

In fact, the presence of the Ag_3CuS_2 was observed previously in Ag-Cu-S_D sample. Although at first sight, the presence of copper sulphide was not detected in the XRD in Figure 4.7, it could not be totally discarded, as it seems to be related to the presence of Ag_3CuS_2. The broad peak around 28.5° could be due to this material. In that sample, the amount of Cu_8S_5 was smaller, and that would be consistent with the fact that there was also less amount of Ag_3CuS_2.

Cu_8S_5 is a copper sulphide, also known as *Geerite*, which is composed by S^{2-} ions and a mixture of Cu(I) and Cu(II) cations. Its rhombohedral crystallographic structure was studied, for the first time, by Goble in 1985.[271] The fact that part of the copper ions of the sulphur are Cu(II) ions makes difficult their formation when working with CuCl, whereas it is favoured when the copper precursor is $CuCl_2$.

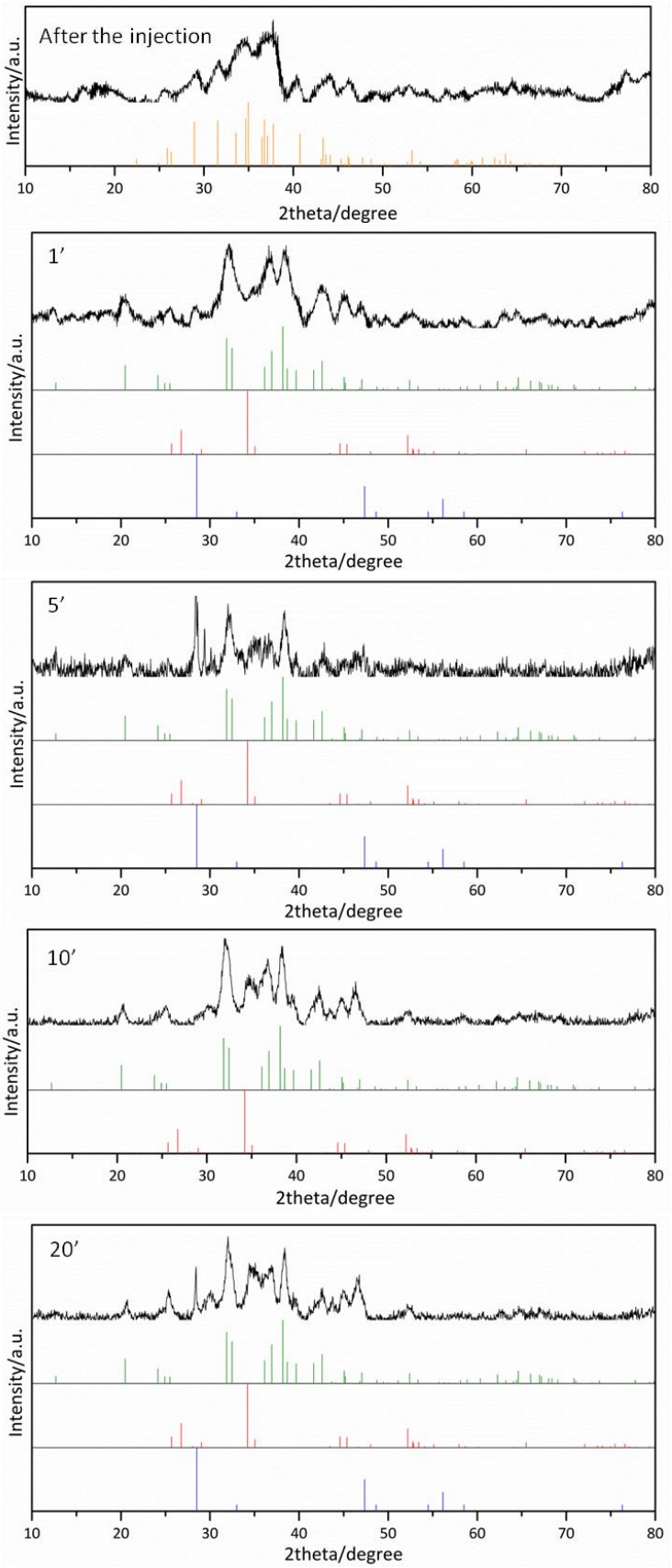

Figure 4.13: XRD patterns of Ag-Cu-S_D NPs (synthesised using $CuCl_2$) extracted at different reaction times (after the injection, 1', 5', 10' and 20'). Monoclinic Ag_2S (JCPDS 024-0715, orange), tetragonal Ag_3CuS_2 (JCPDS 079-2271, green), orthorhombic AgCuS (JCPDS 075-0890, red) and rhombohedral Cu_8S_5 (JCPDS 033-0491, blue) reference patterns.

Copper (I) iodide

Finally, the reaction mechanism when using CuI as copper precursor was studied. Figure 4.14-16 show the XRD patterns of all the aliquots.

XRD pattern of the aliquot extracted after the injection of the metallic precursors show a mixture of two different phases of AgI (cubic and hexagonal) and cubic Cu_2S. After one minute, the Cu_2S remains in the solution but, the silver iodide had reacted with sulphur to form the monoclinic Ag_2S. At 3 minutes of reaction the two binary sulphides had reacted between them and the ternary $(Ag,Cu)_2S$ was detected, together with metallic silver. XRD patterns of minutes 6 and 10 were similar to the one of the 3 minutes-aliquote, but the final sample, after 20 minutes of reaction, shows the vanishing of the metallic silver peaks, leading to orthorhombic and stoichiometric AgCuS.

The high affinity between silver and iodide and its low solubility product leads to the formation of AgI in the first place, instead of Ag_2S, and the consequent formation of copper sulphide. However, in less than one minute, the bonding between silver and iodide was broken to obtain the silver sulphide. In this mechanism instead of having a partial cation exchange, there was a direct reaction between the two binary sulphides to synthesise directly the orthorhombic ternary material AgCuS or $(Ag,Cu)_2S$ (Scheme 4.3).

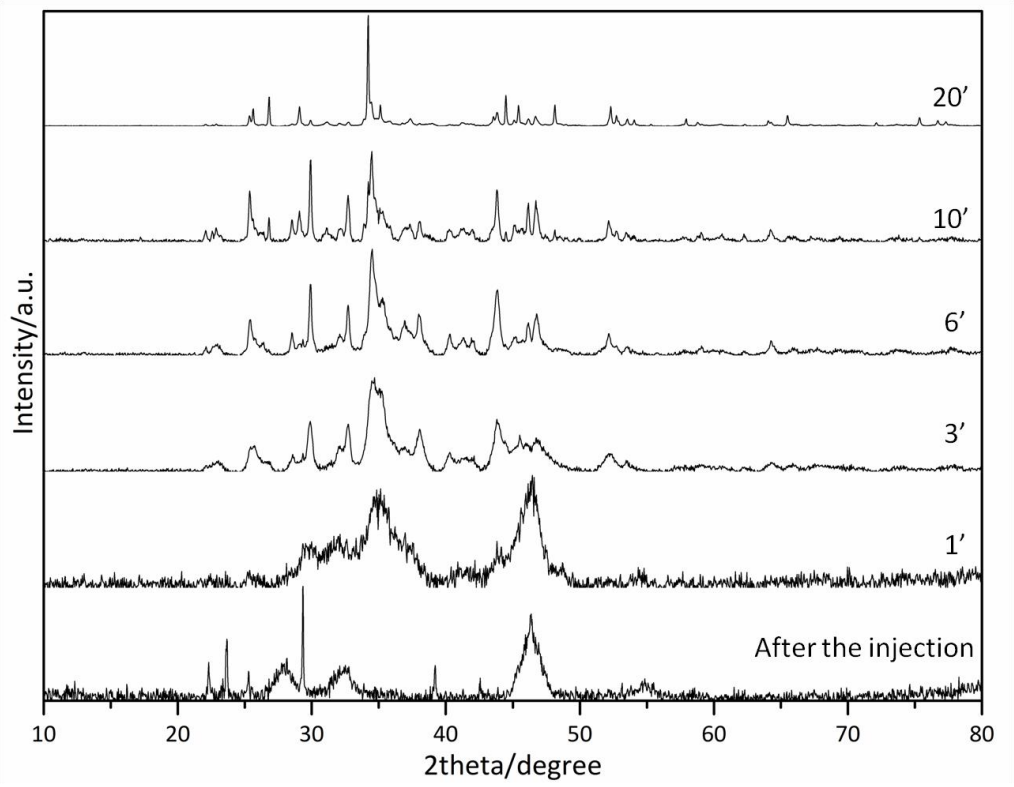

Figure 4.14: XRD patterns of Ag-Cu-S_B NPs (synthesised using CuI as copper precursor) extracted at different reaction times (after the injection, 1', 3', 6', 10' and 20').

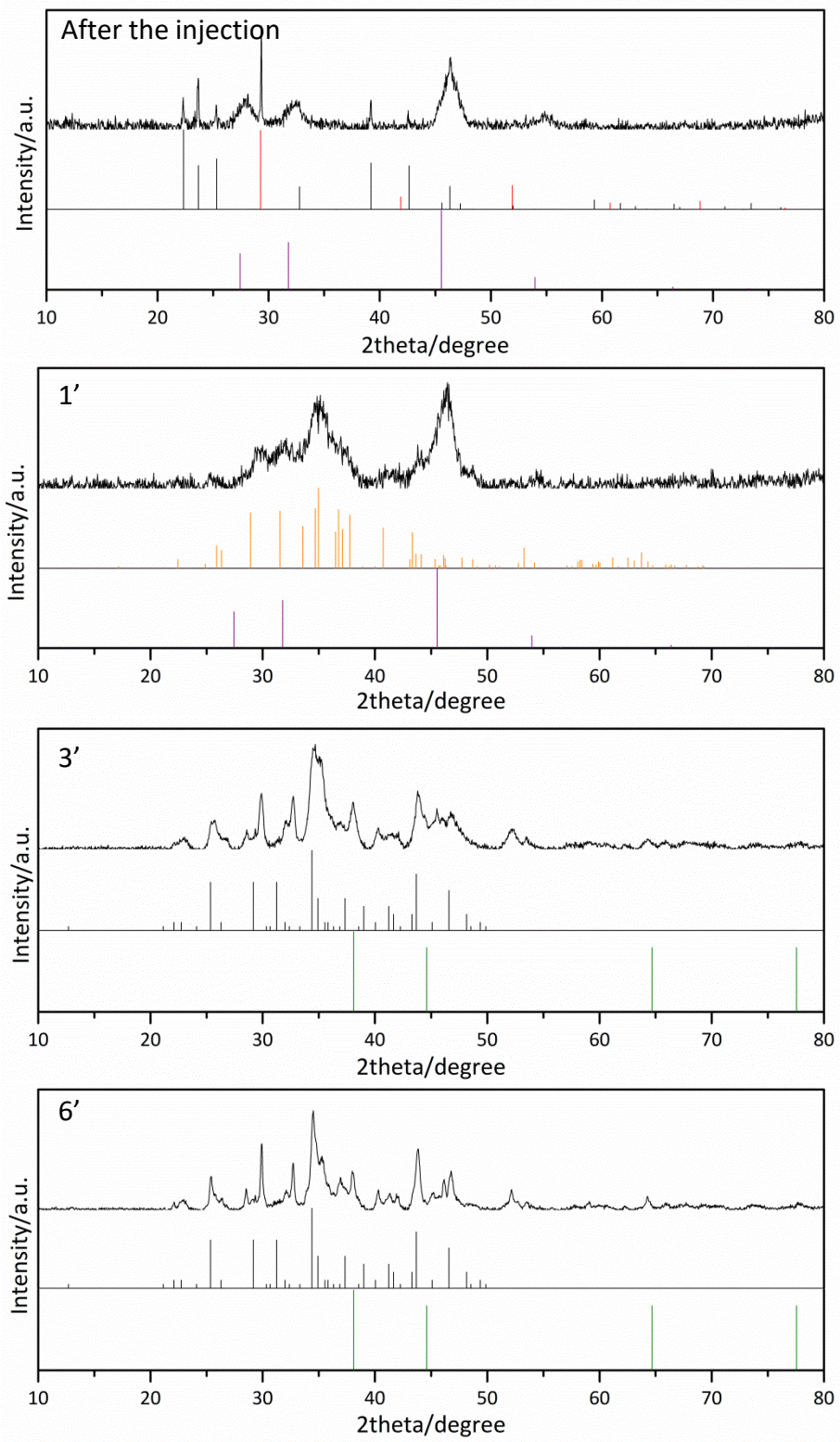

Figure 4.15: XRD patterns of Ag-Cu-S_B NPs extracted at different reaction times (after the injection, 1', 3’ and 6’). Cubic AgI (JCPDS 089-2781, black), hexagonal AgI (JCPDS 078-1614, red), cubic Cu_2S (JCPDS 084-1770, purple), monoclinic Ag_2S (JCPDS 024-0715, orange), orthorhombic $(Ag,Cu)_2S$ (JCPDS 019-0406, black), cubic Ag (JCPDS 003-0921, green) and orthorhombic AgCuS (JCPDS 075-0890, red) reference patterns.

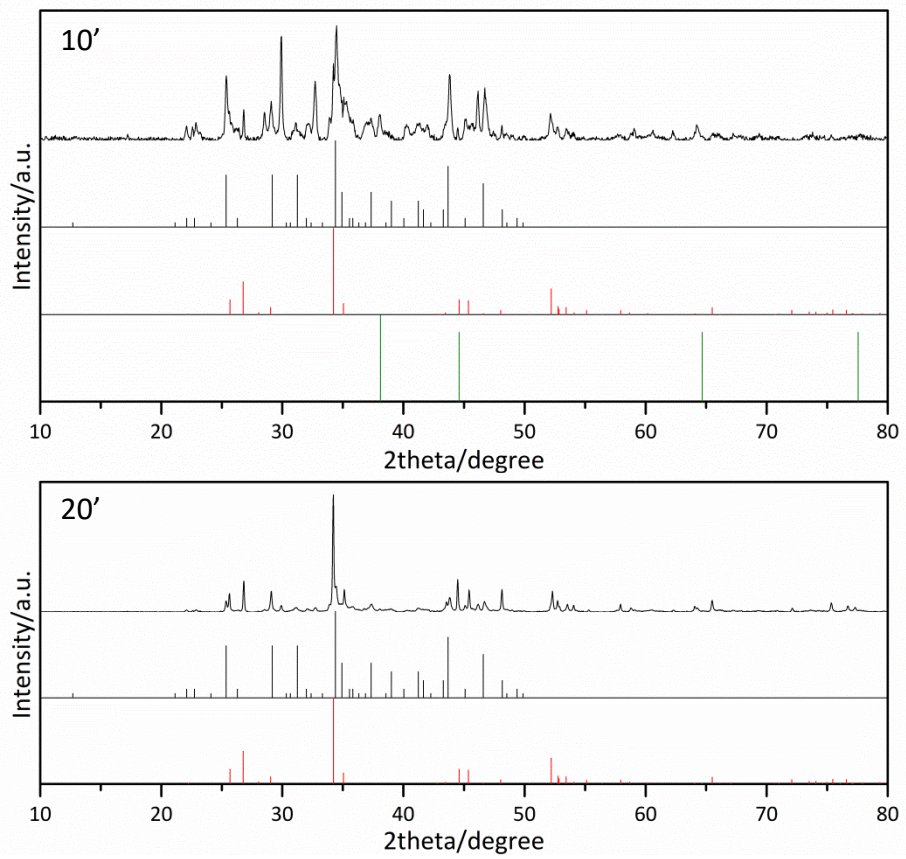

Figure 4.16: XRD patterns of Ag-Cu-S_B NPs extracted at different reaction times (10' and 20'). Orthorhombic $(Ag,Cu)_2S$ (JCPDS 019-0406, black), cubic Ag (JCPDS 003-0921, green) and orthorhombic AgCuS (JCPDS 075-0890, red) reference patterns.

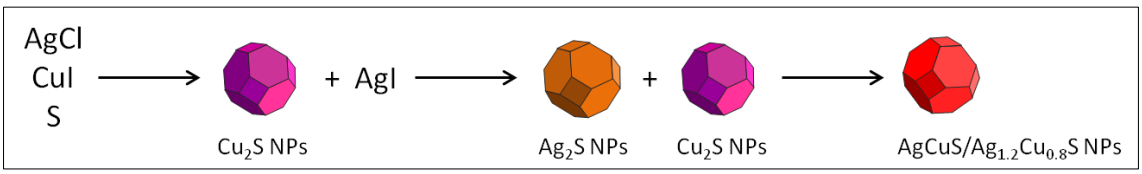

Scheme 4.3: Scheme of the reaction mechanism for the synthesis of Ag-Cu-S NPs when CuI is used as copper precursor.

The morphological study by TEM for this sample was also done, the results are shown in Figure 4.17.

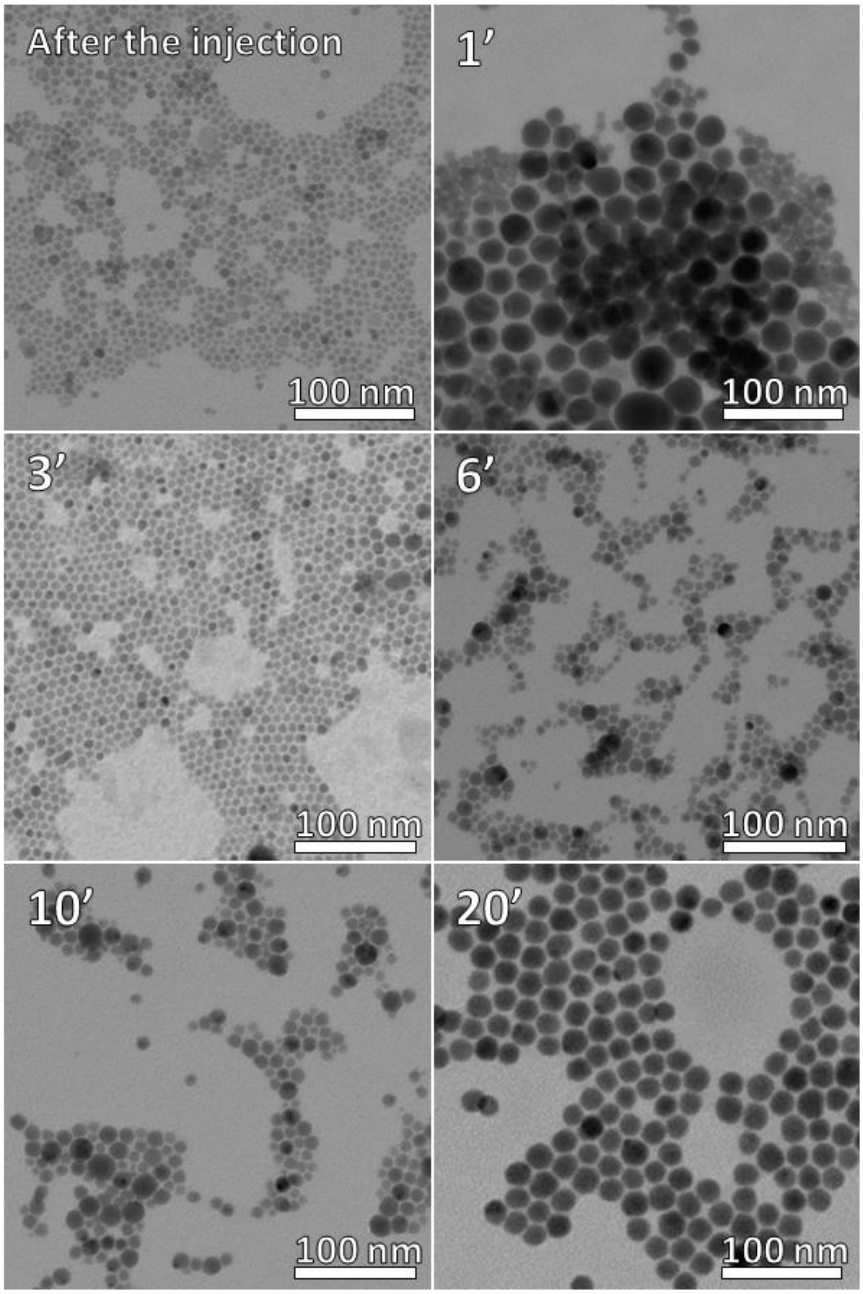

Figure 4.17: TEM images of Ag-Cu-S_B NPs (synthesised CuI) extracted at different reaction times (after the injection, 1', 3', 6', 10' and 20').

After the injection small NPs of *ca.* 5-6 nm of diameter were observed. AgI presented sharp peaks in the XRD, which indicate a large microcrystalline size, whereas the peaks of Cu_2S were broad, indicating the small size of the material. Hence, it was assumed that the NPs observed in the TEM image, were made of Cu_2S, and the AgI was not observed due probably to its low colloidal stability in solution. After 1 minute, another kind of NPs appeared in the solution. These NPs were bigger, with a diameter of 25 nm, approximately, which is consistent with the synthesis of Ag_2S NPs at this stage of the reaction. Next aliquots showed the homogenisation of the sample, demonstrating

the reaction between the two binary sulphide NPs to synthesise the ternary material $(Ag,Cu)_2S$.

4.4 Study of temperature dependent phase transitions of AgCuS NPs

Silver copper sulphides are known to exhibit phase transitions depending on the temperature, so one of the samples, specifically the Ag-Cu-S_D, was analysed by XRD at different temperatures and under vacuum in order to study these phase transitions. Figure 4.18 show the temperature dependant XRD for the heating from 28°C to 500°C.

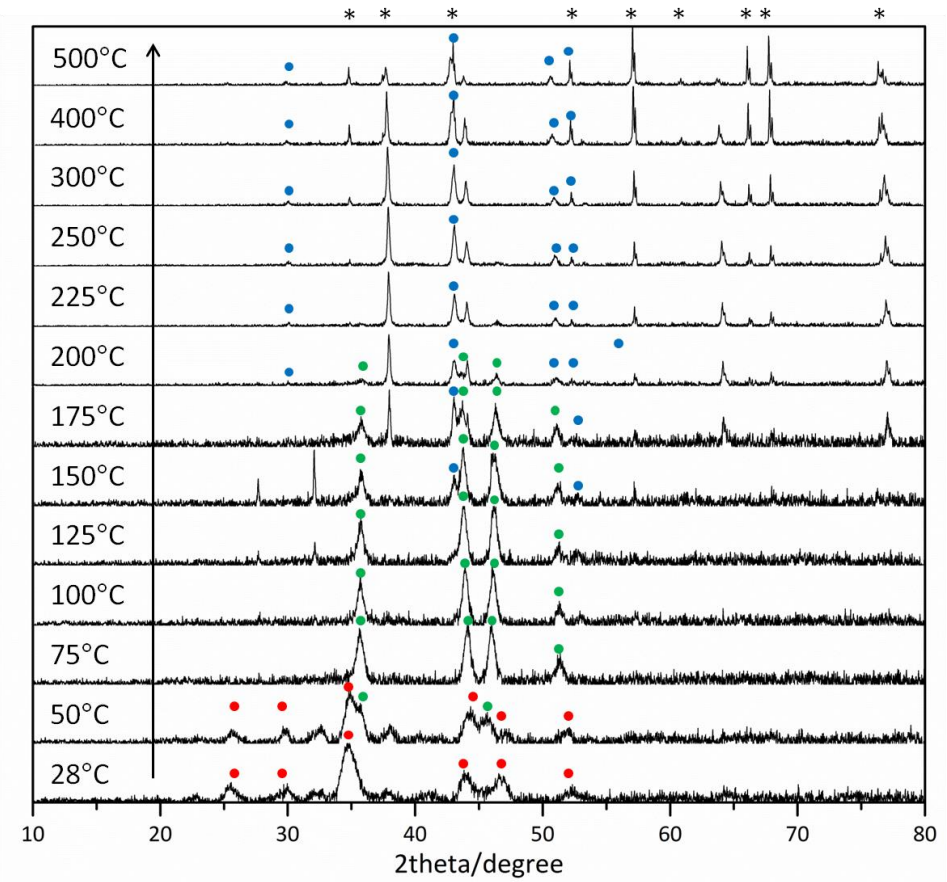

Figure 4.18: Temperature-dependent XRD patterns of heating Ag-Cu-S_D NPs. Orthorhombic AgCuS peaks, marked by red dots. Hexagonal $Ag_{0.93}Cu_{1.07}S$ peaks, marked by green dots. Cubic $Ag_{1.2}Cu_{0.8}S$ peaks, marked by blue dots. Extra peaks from Al_2O_3 substrate, marked by asterisks.

The sample at room temperature (Figure 4.19) presented a similar XRD pattern than the previous samples synthesised using the same copper precursor ($CuCl_2$). Mainly, it was composed by orthorhombic AgCuS (peaks marked by red dots in Figure 4.18) with a small presence of Ag_3CuS_2. In this sample the presence of copper sulphide (Cu_8S_2) was not clear. However, as it was discussed in the study of the reaction mechanism for this synthesis, it should not be discarded.

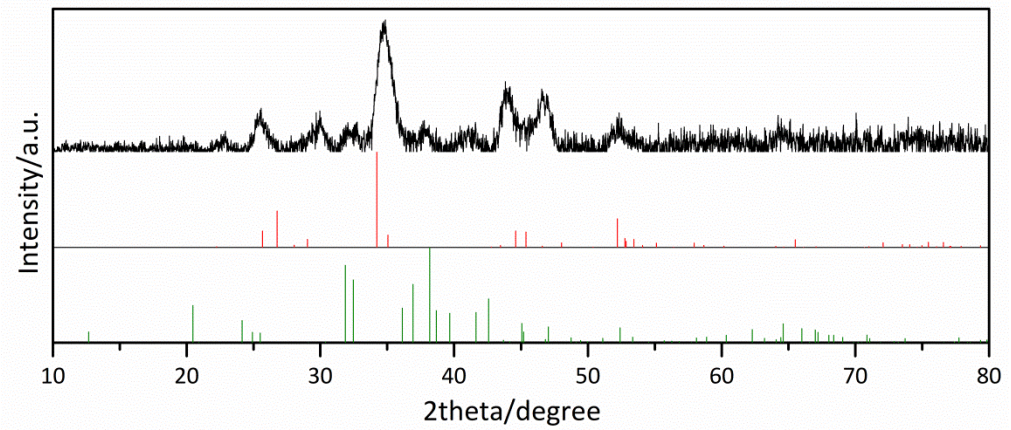

Figure 4.19: XRD pattern of Ag-Cu-S_D system at 28°C. Orthorhombic AgCuS (JCPDS 075-0890, red) and Ag_3CuS_2 (JCPDS 079-2271, green) reference patterns.

When the sample was heated, a first phase transition from the orthorhombic phase to the hexagonal phase was observed between 50 and 75°C. At 50°C it was possible to observe the appearance of the hexagonal phase peaks (marked by green dots in Figure 4.18) and at 75°C the transition was complete (Figure 4.20).

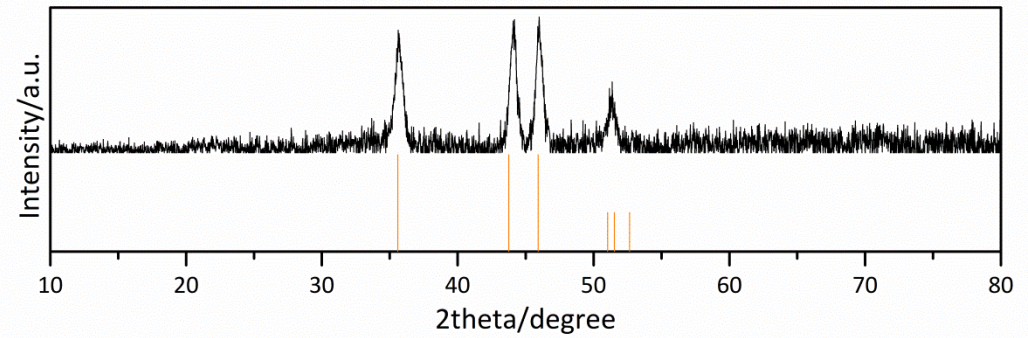

Figure 4.20: XRD pattern of Ag-Cu-S_D system at 75°C. Hexagonal $Ag_{0.93}Cu_{1.07}S$ (JCPDS 012-0151, orange) reference pattern.

Interestingly, at 125°C two small peaks appeared at 27.7° and 32° and they became more intense when the sample was heated to 150°C (Figure 4.21). These peaks could be assigned to a cubic copper sulphide phase with the formula $Cu_{7.2}S_4$. Two possible origins of this compound can be discussed. On the one side, the segregation of this phase as a result of the heating of AgCuS. However, in the literature, there is no reference of the segregation of copper sulphide compounds when orthorhombic AgCuS is heated.[252,253,264,265] On the other side, as a result of the phase transition of a copper sulphide compound, present in the sample from the beginning, as was suggested by the reaction mechanism study. Although there are no references about this phase transition, it is a possibility that should be considered. Besides, the increase of temperature may have induced the Cu_xS_y small crystals to sinterise, increasing their size, and as a consequence, increasing the intensity of their XRD reflections.

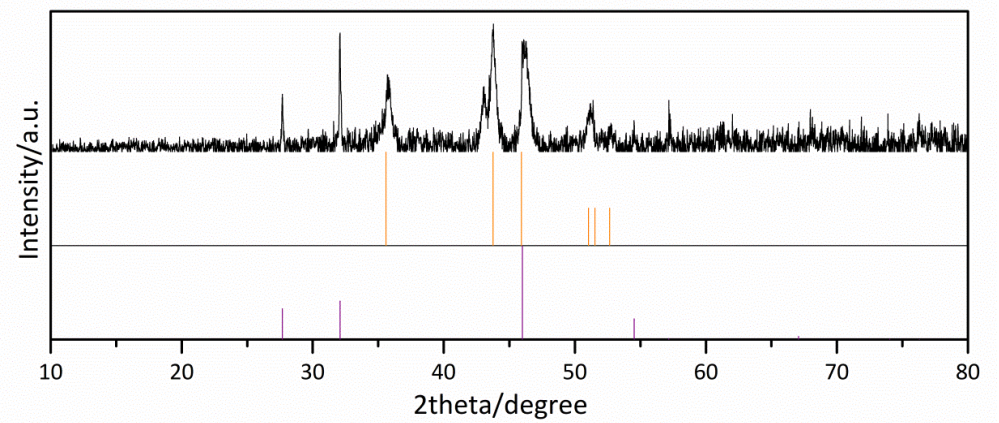

Figure 4.21: XRD pattern of Ag-Cu-S_D system at 150°C. Hexagonal $Ag_{0.93}Cu_{1.07}S$ (JCPDS 012-0151, orange) and cubic $Cu_{7.2}S_4$ (JCPDS 072-1966, purple) reference patterns.

This copper sulphide phase disappeared at 175°C, when the second phase transition of the ternary material, from hexagonal phase to cubic phase, was starting. Apart from the ternary Ag-Cu-S phases, at this temperature, extra peaks from rhombohedral Al_2O_3 could be also observed. These signals came from the substrate, which was exposed when the pellet cracked as a consequence of the change of volume associated to the phase transition. Even though these peaks were not interfering the measurements, they appeared in all the patterns from this moment. Finally, at 225°C the transition to the cubic phase was complete (Figure 4.22). The peaks at 45° and at 65° could not be unambiguously assigned.

When the sample was cooled down (Figure 4.23) the reversibility of the phase transitions was proved. The material went from the cubic phase to the hexagonal phase, between 200°C and 150°C, and from the hexagonal to the orthorhombic between 100°C and 50°C.

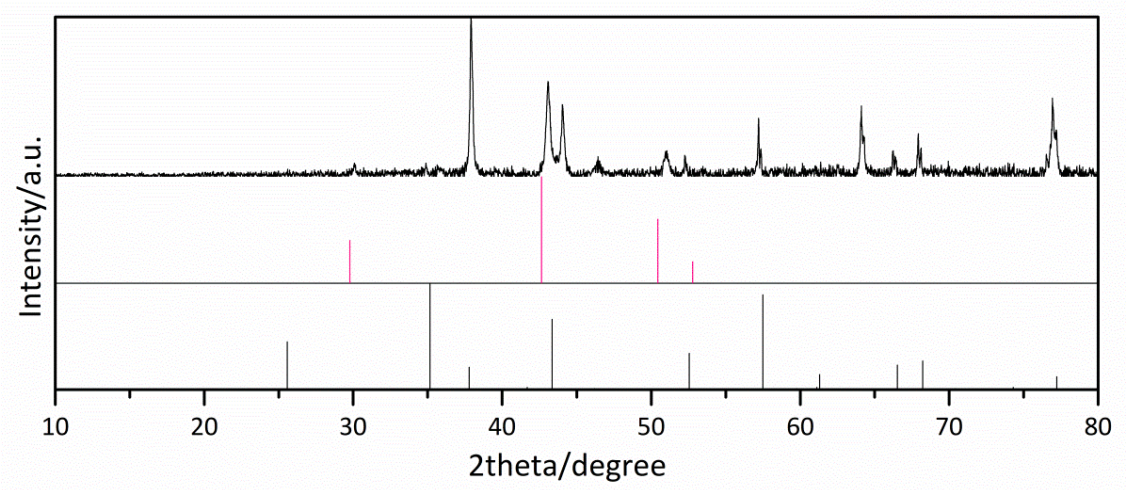

Figure 4.22: XRD pattern of Ag-Cu-S_D system at 225°C. Cubic $Ag_{1.2}Cu_{0.8}S$ (JCPDS 012-0154, pink) and rhombohedral Al_2O_3 (JCPDS 046-1212, black) reference patterns.

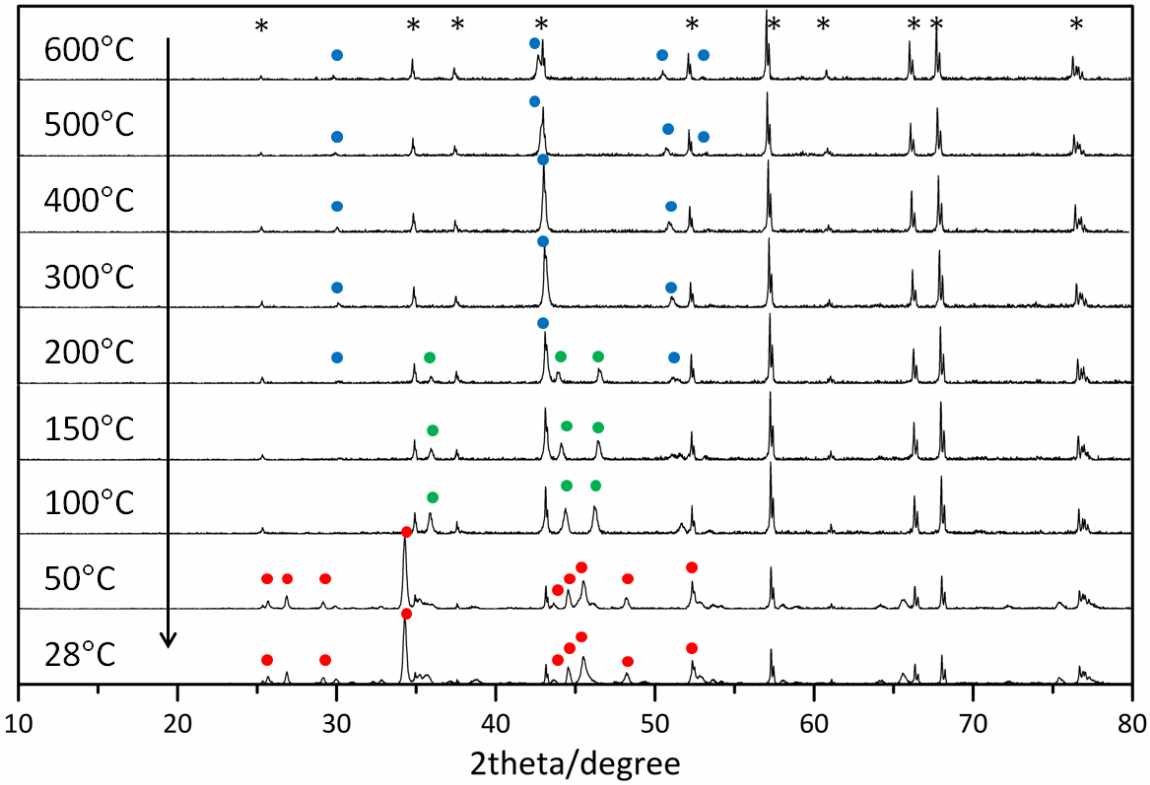

Figure 4.23: Temperature-dependent XRD patterns of cooling Ag-Cu-S_D NPs. Orthorhombic AgCuS peaks, marked by red dots. Hexagonal $Ag_{0.93}Cu_{1.07}S$ peaks, marked by green dots. Cubic $Ag_{1.2}Cu_{0.8}S$ peaks, marked by blue dots. Extra peaks from Al_2O_3 substrate, marked by asterisks.

In the cooling process, the peaks from the copper sulphide phase (cubic $Cu_{7.2}S_4$) were not detected, leading to the theory that the copper sulphide is reacting at high temperature, probably with the remaining Ag_3CuS_2 to give AgCuS. XRD pattern at room temperature after the cooling down (Figure 4.24) did not show the peaks from Ag_3CuS_2, which were observed in the original sample.

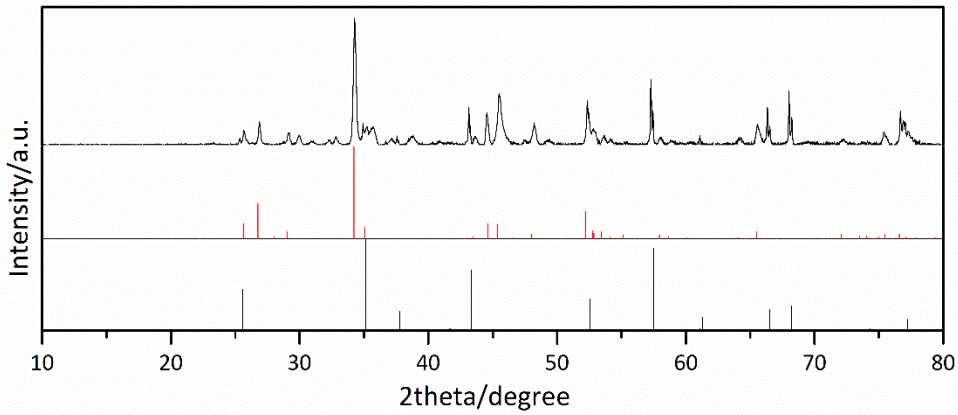

Figure 4.24: XRD pattern of Ag-Cu-S_D system at 28°C, after cooling down the sample. Orthorhombic AgCuS (JCPDS 075-0890, red) and rhombohedral Al_2O_3 (JCPDS 046-1212, black) reference patterns.

In summary, the known phase transitions (orthorhombic to hexagonal, hexagonal to cubic) were clearly observed by temperature-dependant XRD. However, the transition phase temperatures were slightly different regarding to the ones reported for the bulk material. The first phase transition temperature, from orthorhombic to hexagonal phase, was between 50 and 75°C, slightly lower than the 93°C of the bulk, whereas the second phase transition temperature, from hexagonal to cubic phase, was slightly higher, it was between 175 and 200°, instead of being around 166°C. The apparition of minority phases of Ag_3CuS_2 and $Cu_{7.2}S_4$ at pre-heated sample and at 125°C, respectively, needs also to be pointed out, even though these phases disappeared during the treatment and were not detected at the end.

4.5 Thermoelectric characterization of AgCuS NPs

Thermoelectric properties of synthesised AgCuS NPs were studied by Dr. Andreu Cabot's group in IREC. Preliminary measurements of electrical conductivity, Seebeck coefficient and thermal conductivity were done (Figure 4.25) and power factor and figure of merit were calculated (Figure 4.26).

The electrical conductivity was significantly affected by the temperature dependant phase transitions. It showed a sharp decrease after the phase transition to the hexagonal phase and a continuous increase during the second phase transition to the cubic phase. The Seebeck coefficient had also important changes at different temperatures. It smoothly increases to 250 μvK^{-1} from room temperature to 400K, then, it decreases to a value lower than 100 μvK^{-1} and finally, with the second phase transition (between 475 and 500K) it sharply increases to values of 300 μvK^{-1}. Bulk AgCuS is known to have a *p-n-p* type conduction switching during the orthorhombic to hexagonal phase transition, perceived by a change of the signal of the Seebeck coefficient (negative values imply *n*-type conduction and positive values, *p*-type conduction).[253,265] However, when the material is nanostructurated, as was reported by Biswas and co-workers[252] and it was observed in the measured sample, this switching disappears. They reported that the absence of Cu-S bond vibration during the first phase transition, proved by Raman Spectroscopy measurements, and the higher electronic band gap of the nanostructured material, compared to its bulk counterpart, disfavour the formation of a semimetallic intermediate electronic state which was the responsible, in the bulk structure, of the *p-n-p* type conduction switching. In addition, the localized nature of silver vacancies in the nanostructured material, also disfavours the macroscopic movement of Ag/Cu during the transition, which was also responsible of the *p-n-p* type conduction switching.[253]

Regarding to thermal conductivity, the material shows low values, which decrease with the raise of the temperature. Low thermal conductivity is suitable in thermoelectric devices to maintain the temperature gradient. Nevertheless, the power factor and figure of merit, calculated from these parameters, are low, which means that, although the material present thermoelectric properties, they are not prominent. The Seebeck coefficient and thermal conductivity values are acceptable for this kind of devices, but the notably low values of the electrical conductivity (the values of electrical conductivity of Au-Ag-Se nanocomposite in Chapter 2 were of 7-10 $S \cdot m^{-1}$) are clearly detrimental for the thermoelectric response of the material.

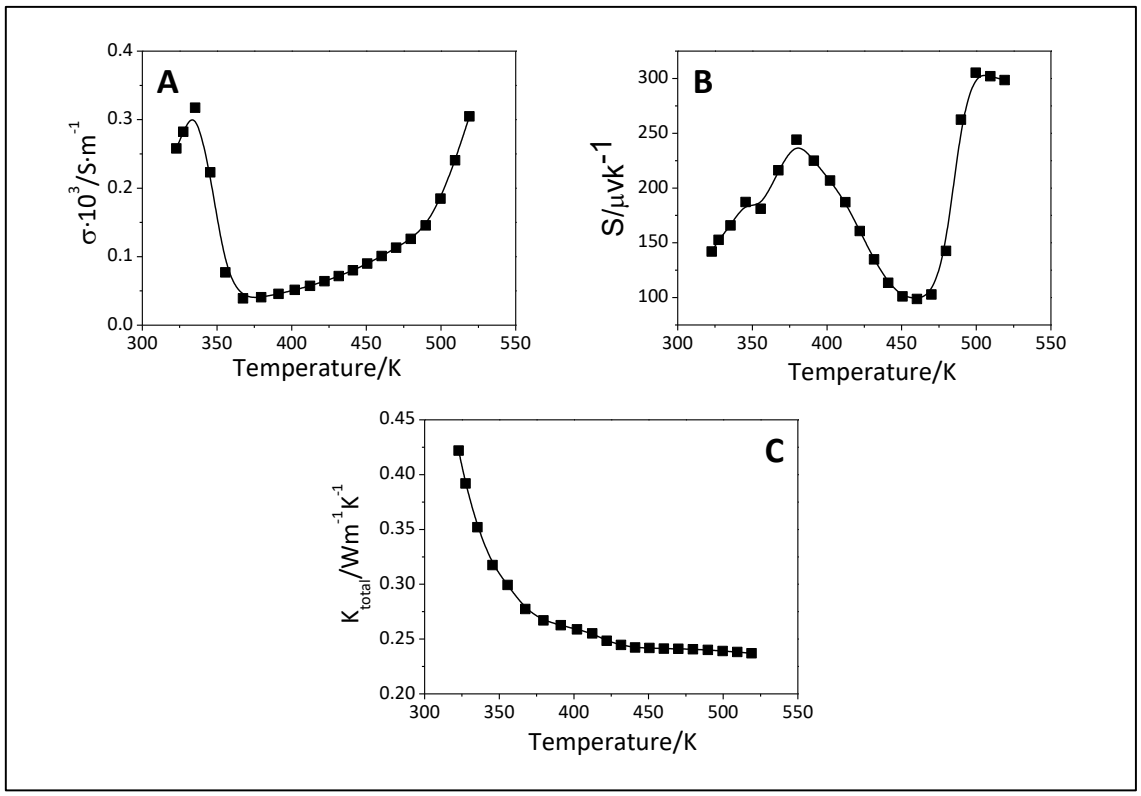

Figure 4.25: (A) Electrical conductivity, (B) Seebeck coefficient and (C) thermal conductivity of Ag-Cu-S_D NPs.

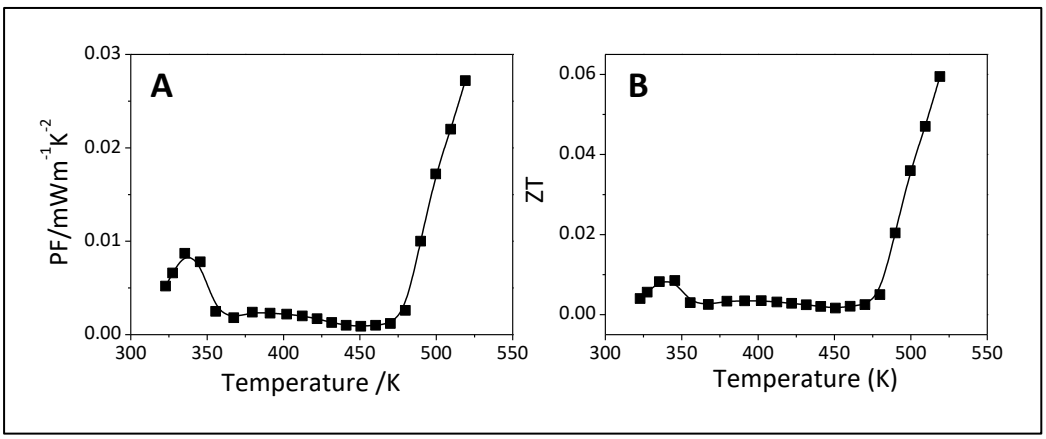

Figure 4.26: (A) Power factor and (B) Figure of merit of Ag-Cu-S_D NPs.

4.6 Experimental part

Chemicals

Silver chloride (AgCl, 99.9%), copper (I) chloride (CuCl, 99.999%-Cu), sulphur powder (S, 99.99%) and tri-n-octylphosphine (TOP, 97%) were obtained from Strem Chemicals. Copper (I) iodide (CuI, ≥ 99.5%), copper (II) nitrate ($Ag(NO_3)_2$, ≥99%), 1-octadecene (ODE, 90%), oleylamine (OLAm, 70%) and toluene (99.9%) were purchased from Sigma-Aldrich. Copper (II) chloride ($CuCl_2$, 99%) ethanol (EtOH, 96% v/v) were obtained from Panreac. All the reagents and solvents were used without further purification.

Synthesis Ag-Cu-S NPs_A

This procedure was based on method B used for the synthesis of Ag_2S NPs in Chapter 3. Briefly, 2.5 mL ODE and 1.65 mL OLAm were disposed in a three-neck flask and degassed under vacuum at 120°C for 30 minutes. Meanwhile, three precursor solutions were prepared in the glovebox: OLAm-S, AgCl-TOP and CuCl-OLAm precursor solutions. After degassing, and under N_2 atmosphere, the temperature was raised to 180°C and the OLAm-S solution was injected. Once the temperature was recovered, the AgCl-TOP and CuCl-OLAm solutions were injected. Immediately after the metallic precursor injections the colour of the solution changed from clear orange to dark brown. After 20 minutes of reaction, the heating was stopped, and the solution was let cool down naturally. Subsequently, the NPs were collected adding EtOH, centrifuging 4 minutes at 4500 rpm and re-dispersing them in 1 mL toluene. This last step was repeated three times.

S-OLAm precursor solution was prepared dissolving 64 mg S (2 mmol) in 1 mL OLAm, it was necessary to heat intensely the solution with a heat gun in order to dissolve completely the sulphur. The solution was dark orange and transparent.

AgCl-TOP was taken from the stock solution prepared for the synthesis of Ag_2Se. This was prepared as follows: 3.6 g (25 mmol) AgCl were dissolved in 25 mL TOP. The solution needed to be heated in a hot plate until complete dissolution of the solid. It is important the heating was gently and with continued magnetic stirring to avoid the reduction of Ag(I) to metallic silver. Additionally, this solution is light sensitive, so, it was indispensable to protect it from the light, covering the vial with aluminium foil. The final solution was transparent and pale yellow. CuCl-OLAm was prepared dissolving 49.5mg (0.5mmol) CuCl in 3 mL ODE and 0.5 mL OLAm. Gently heating was also necessary for the complete dissolution of CuCl. The injection was done when the solution was hot to avoid the precipitation of the salt.

Synthesis Ag-Cu-S NPs_B, C and D

For synthesis of these three samples, the same procedure as for Ag-Cu-S_A NPs synthesis was used, but substituting the CuCl for another salt of Cu. In the case of Ag-Cu-Se NPs_B it was substituted for 95 mg (0.5mmol) of CuI. For the synthesis of Ag-Cu-Se NPs_C 148 mg (0.5 mmol) of $Cu(NO_3)_2$ were used. Finally, for the synthesis of Ag-Cu-S_D, 85 mg (0.5 mmol) of $CuCl_2 \cdot H_2O$ were used.

Characterization methods

Transmission Electron Microscopy (TEM): Ag-Cu-S ternary NPs were prepared for observation by TEM by dilution in toluene followed by sonication. A droplet of the solution was then poured in holey carbon covered copper TEM grids. A JEOL 2000 FX II conventional TEM operating at an accelerating voltage of 80kV was used.

X-ray diffraction: XRD patterns were acquired with a PANalytical X'Pert Pro MPD Alpha1 diffractometer operating in θ/2θ geometry at 45 kV, 40 mA, and λ= 1.5406 Å (Cu Kα1). Thin layers of the samples were prepared by drop casting and evaporation of the solvent on a monocrystalline Si flat substrate. Scans in the range 2θ = 4−100° were run at a step size of 2θ = 0.017° and 100 s per step.

Temperature-dependent X-Ray Diffraction: for the temperature-dependent XRD the sample was place in a Al_2O_3 substrate and warmed up in a High Temperature Camera (HTK-1200N, Antoon Par) from 28°C to 600°C in vacuum conditions ($5 \cdot 10^{-3}$ mBar) with a 10°C/min slope. A PANalytical X'Pert PRO MPD power diffractometer, with a radius of 240 millimeters, operating in a Bragg-Brentano geometry with a variable automatic divergence slit was used. X-Ray beam of 45 kV, 40 mA and λ=1.5418 Å (Cu Kα1). Scans in the range of 2θ = 10−80° were run at a step size of 2θ = 0.017° and 50 s per step.

All XRD data were treated with X'Pert HighScore Plus software.

Thermoelectric Characterization. Electric properties. The NPs mixture was washed by multiple precipitation and redispersion steps and dried under vacuum to obtain a dark grey nanopowder. To remove completely the residual organic ligands, NPs were heated at 450°C for 1h under an argon flow. The annealed powder was ground and hot-pressed under an Ar atmosphere at 40 mPa and 300°C during 5 min. The Seebeck coefficient was measured using a static DC method. Electrical resistivity data were obtained by a standard four-probe method. Both the Seebeck coefficient and the electrical resistivity were simultaneously measured with accuracies better than 1% in a LSR-3 LINSEIS system from room temperature to 850 K, under helium atmosphere. Samples were held between two alumel electrodes and two probe thermocouples with

spring-loaded pressure contacts. A resistive heater on the lower electrode created temperature differentials in the sample to determine the Seebeck coefficient.

Thermal Properties. An XFA 600 Xenon Flash Apparatus was used to determine the thermal diffusivities of all samples with an accuracy of about 6%. Total thermal conductivity (κ) was calculated using the relation $\kappa = DC_p\rho$, where D is the thermal diffusivity, C_p is the heat capacity, and ρ is the mass density of the pellet. The ρ values were calculated using the Archimedes method. The specific heat (C_p) of the samples was measured using a differential scanning calorimeter DSC 204 F1 Phoenix from NETZSCH.

Chapter 5 Cu-Pt-Se system

5.1 Introduction

Nanostructured $Cu_{2-x}S$ was the first no noble-metal material in which a LSPR in the near infrared region was detected in 2009.[272] Since then, many other nanostructured semiconductors or conducting metal oxides were proved to also present a LSPR.[273–278] Actually, as LSPR relies on the interaction between light and free charge carriers, it has been demonstrated that any nanostructured semiconductor can have surface plasmonic resonance if it has appreciable free carrier concentrations.[279] Whereas metal NPs have high density of free electrons, in the case of semiconductors or metal oxide nanocrystals the free charge carriers can be extra electrons in the conduction band or extra holes in the valence band, and they usually come from doping.

There are two types of doping: extrinsic and intrinsic. Extrinsically doped semiconductors get the free carriers from the impurities/defects generated by the introduction of a dopant atom. Whereas, in intrinsically doped semiconductors, also known as "self-doped" semiconductors, the free carriers come from the vacancies generated by the variation of the oxidation state of one of the elements of the material, for instance, copper-deficient copper chalcogenides[279–283] or oxygen-deficient metal oxides.[284–286]

One of the most important advantages of plasmonic semiconductors is the fact that the LSPR can be easily tuned from the visible range to the infrared range not only with the size and shape of the nanoparticles, but with the composition of the material, the concentration of the doping or the nature of the surfactant. In addition, they present LSPR even when the NPs are smaller than 2-3 nm, in comparison with the noble metal NPs, which do not have LSPR at these smaller sizes. All these advantages increase exponentially the applications for this kind of materials. Photothermal therapy, computed tomography, thermal photovoltaics, catalysis, sensors[287] are some of the applications of LSPR semiconductors that have emerged in last years.

$Cu_{2-x}Se$ is one of the semiconductors that presents LSPR due to a "self-doping": extra holes are created in the structure when copper (I) is oxidized to copper (II). Many

groups have studied this material.[281,283,288] It is well known that it presents a LSPR at the near infrared region, which can be tuned from 900 nm to 1600 nm. Apart from the strategies commented in the previous paragraph for tuning the LSPR, the growth of a second domain in the semiconductor nanocrystal can also modify the optical response of the material as well as it can originate an hybrid nanomaterial with combined properties. Several studies have been done with Au-$Cu_{2-x}Se$ hybrid nanocrystals in which the LSPR of the $Cu_{2-x}Se$ NPs was modified slightly with the presence of the metallic domain and dual plasmonic HNPs have been synthesised.[161,267,289,290] The combination of the two plasmonic responses in one material can be interesting for different applications such as deep tissue imaging[161] or photothermal therapies.[290]

Nanostructured systems presenting any form of Pt (single atoms, small clusters of Pt or Pt nanoparticles) are particularly interesting due to their catalytic properties. The possibility of combining Pt with a plasmonic semiconductor, such as $Cu_{2-x}Se$, might confer the opportunity of exploring a new ternary system with promising properties. For instance, two groups have made a first incursion in the field. Dorf and co-workers have reported a synthesis of a PtCu-$Cu_{2-x}Se$ hybrid nanomaterial from pre-synthesised $Cu_{2-x}Se$ NPs[291] and Schaark and co-workers developed a synthesis for Pt-$Cu_{2-x}Se$ HNPs by cation exchange from Pt-MnSe HNPs.[292]

This chapter is centred in the development of a procedure that allows the study of the formation of Pt-Cu-Se ternary phases. The synthesis entailed the reaction between a platinum molecular precursor and pre-synthesised $Cu_{2-x}Se$ NPs at high temperature.

5.2 $Cu_{2-x}Se$ NPs: synthesis and morphological and structural characterization

$Cu_{2-x}Se$ NPs were synthesised following a published method from Kriegel and co-workers.[283] It was a hot injection method under air-free conditions, in which octadecene (ODE) was used as solvent and oleylamine as surfactant. Copper (I) chloride and elemental selenium were the precursors, that decomposed at 310°C leading to the nucleation and growth of the desired material.

The material crystallised in the cubic phase of Cu_2Se, also known as the mineral *berzelianite*, as could be observed by XRD (Figure 5.1). A small shift of the XRD peaks to higher angles could be clearly observed. The oxidation of Cu(I) cations cause the decrease of the lattice parameters of the cell and, as a consequence, a shift of the XRD reflections. The connection between the shift of XRD peaks and the degree of oxidation was studied by Kriegel and co-workers in 2012.[283] TEM image of synthesised $Cu_{2-x}Se$ NPs (Figure 5.2) showed the NPs are spherical and about 13.9 nm of diameter with a standard deviation of 15.1%.

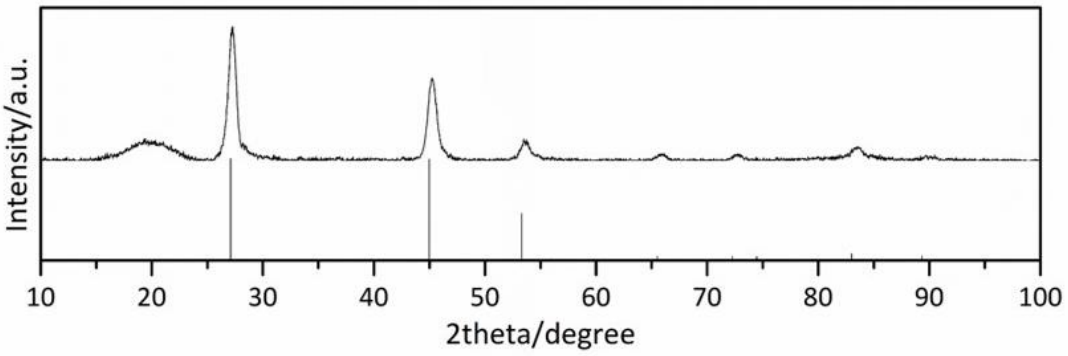

Figure 5.1: XRD pattern of $Cu_{2-x}Se$ NPs. Cubic Cu_2Se (JCPDS 088-2043) reference pattern.

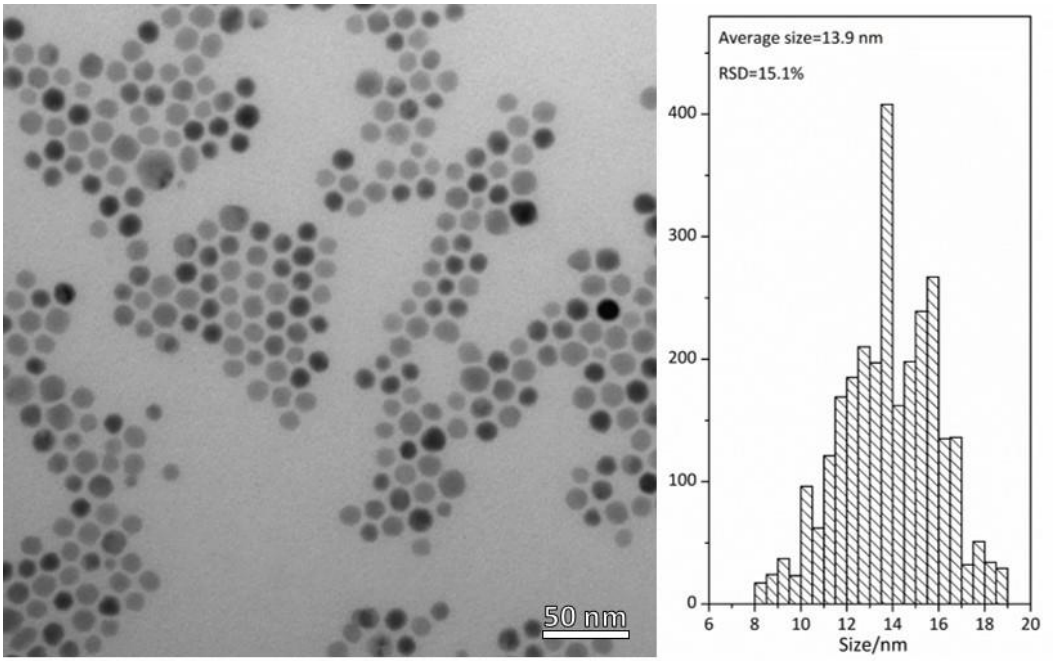

Figure 5.2: TEM micrograph and size histogram of $Cu_{2-x}Se$ NPs

5.3 Pt-Cu-Se systems: synthesis and morphological and structural characterization

Subsequent reactions of $Cu_{2-x}Se$ NPs and platinum molecular precursor based on platinum acetylacetonate caused gradual and noticeable changes in the initial sample, depending on the Pt:Cu molar ratios used in the synthesis. Four different experiments were done with different Pt:Cu molar ratios, starting from 0.1 and up to a value of 1.6, in order to study the influence of this parameter in the final product.

When the Pt:Cu molar ratio was low (0.1, sample Pt-Cu-Se_1) the NPs lost their sphericity and became more faceted, as can be observed in the TEM micrograph in Figure 5.3. Besides, some of them presented a second domain. XRD of the sample showed the presence of $Cu_{2-x}Se$ and the appearance of several new peaks. Some of

these peaks could be assigned to a phase of PtCu. However, some others could not be attributed to any known crystallographic phase. Consequently, further analyses of the sample were considered essential to study its composition. HRTEM and STEM-EDS analyses were performed and they will be shown and discussed in the next section.

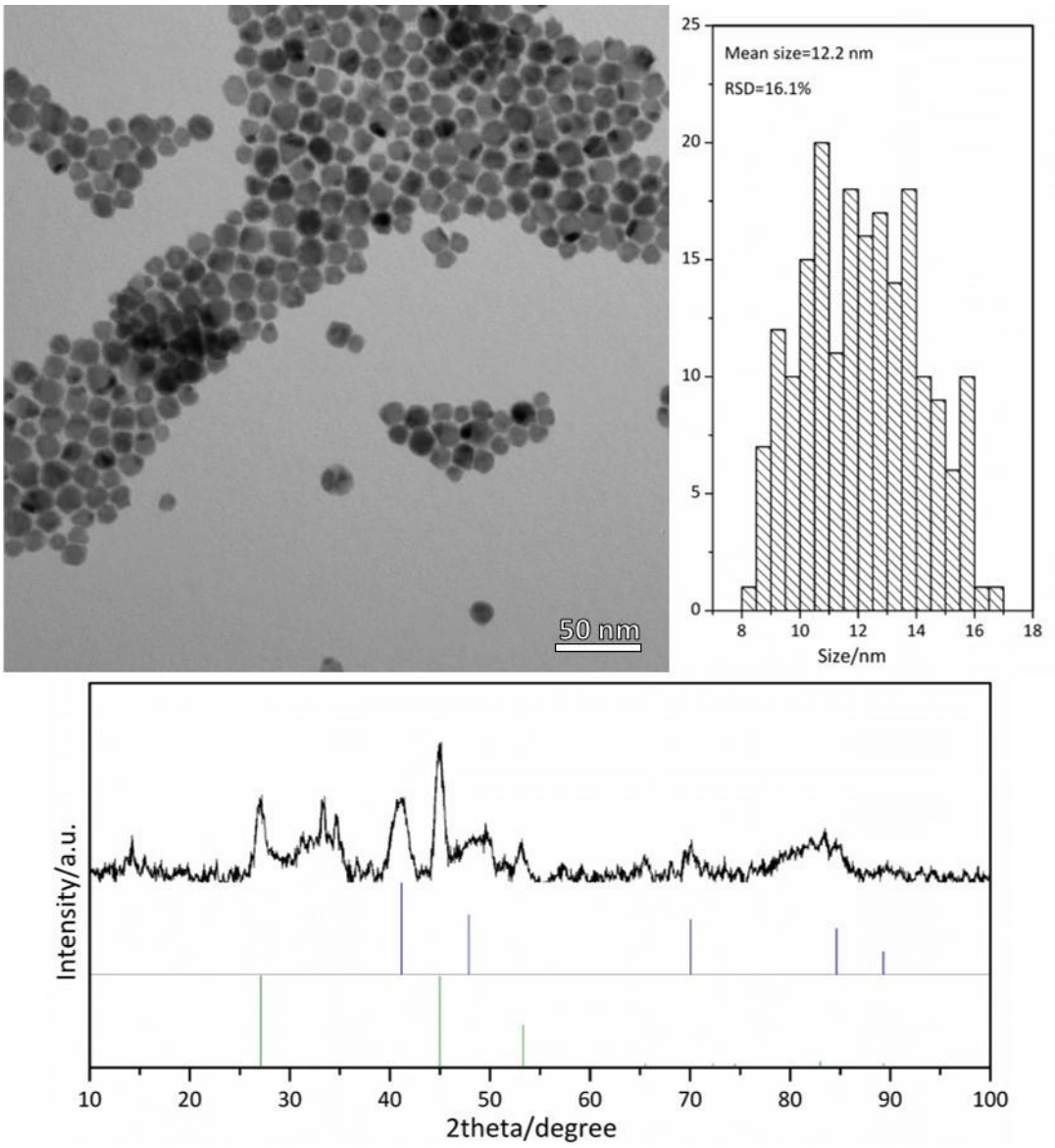

Figure 5.3: TEM image, size histogram and XRD pattern of Pt-Cu-Se_1 NPs. Cubic Cu_2Se (green, JCPDS 088-2043) and cubic CuPt (blue, JCPDS 048-1549) reference patterns.

While Pt:Cu molar ratio was doubled to 0.2 (sample Pt-Cu-Se_2) the morphology of the obtained nanomaterial was similar to the previous one with one difference: it had a larger number of particles with an extra domain, as could be observed by TEM (Figure 5.4). Regarding to the crystallographic characterization (XRD), the differences were more significant, the peaks from $Cu_{2-x}Se$ had almost completely disappeared whereas

the new peaks had become increasingly important. So, it seemed that new phases were appearing at the expense of the sacrifice of copper selenide.

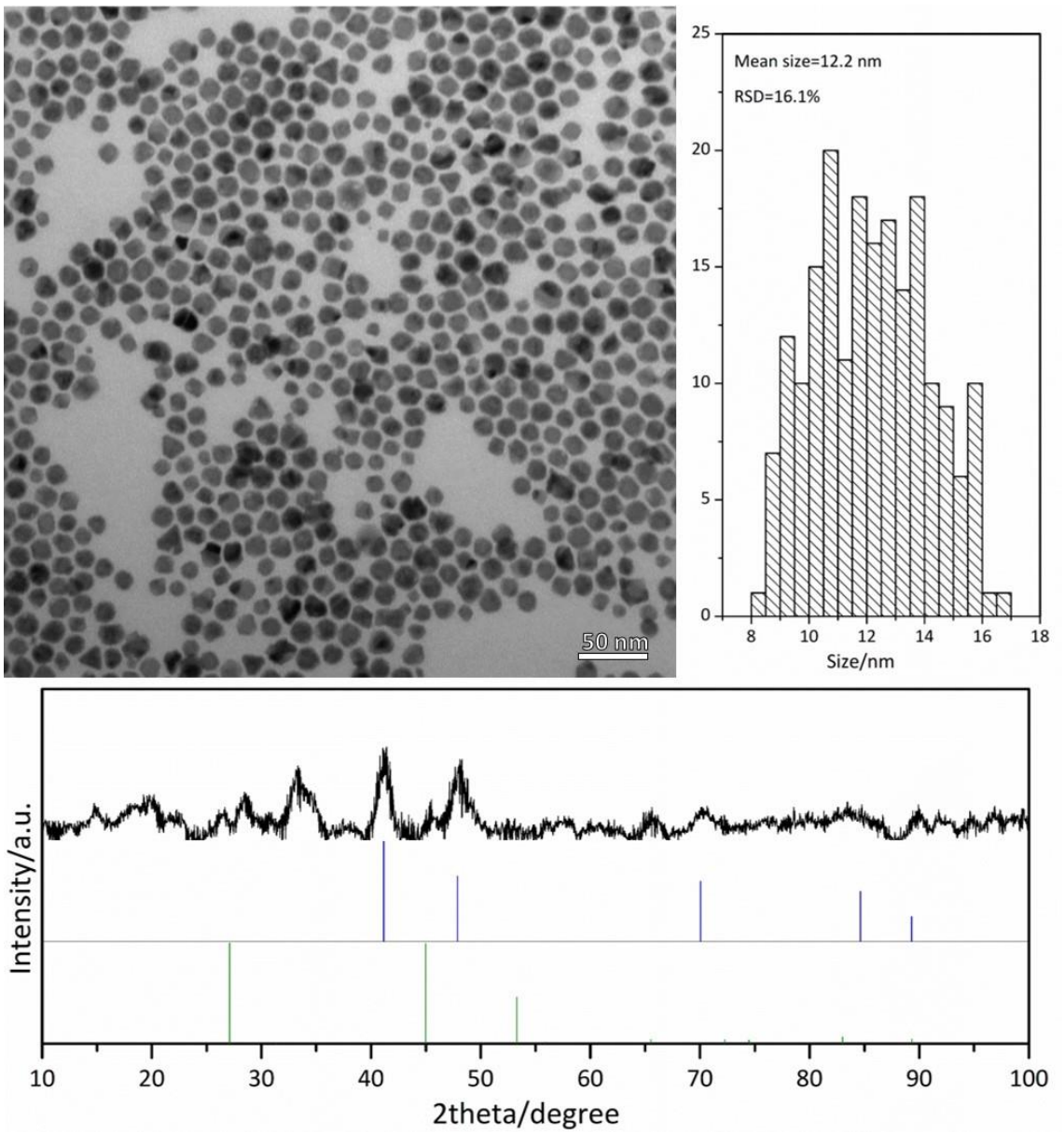

Figure 5.4: TEM image, size histogram and XRD pattern of Pt-Cu-Se_2 NPs. Cubic Cu_2Se (green, JCPDS 088-2043) and cubic CuPt (blue, JCPDS 048-1549) reference patterns.

With the addition of more platinum, to achieve a Pt:Cu molar ratio of 0.65 (sample Pt-Cu-Se_3), the shape of the nanoparticles suffered a significant alteration. TEM image (Figure 5.5) showed that, in this case, the particles exhibit stronger faceting, leading to heterogeneous nanostructures composed by more than one domain in the same particle. Curiously, the XRD pattern was resembling to the pattern from sample Pt-Cu-Se_2. Even though the sample looked so different, it seemed that the composition was not as dissimilar as could be expected.

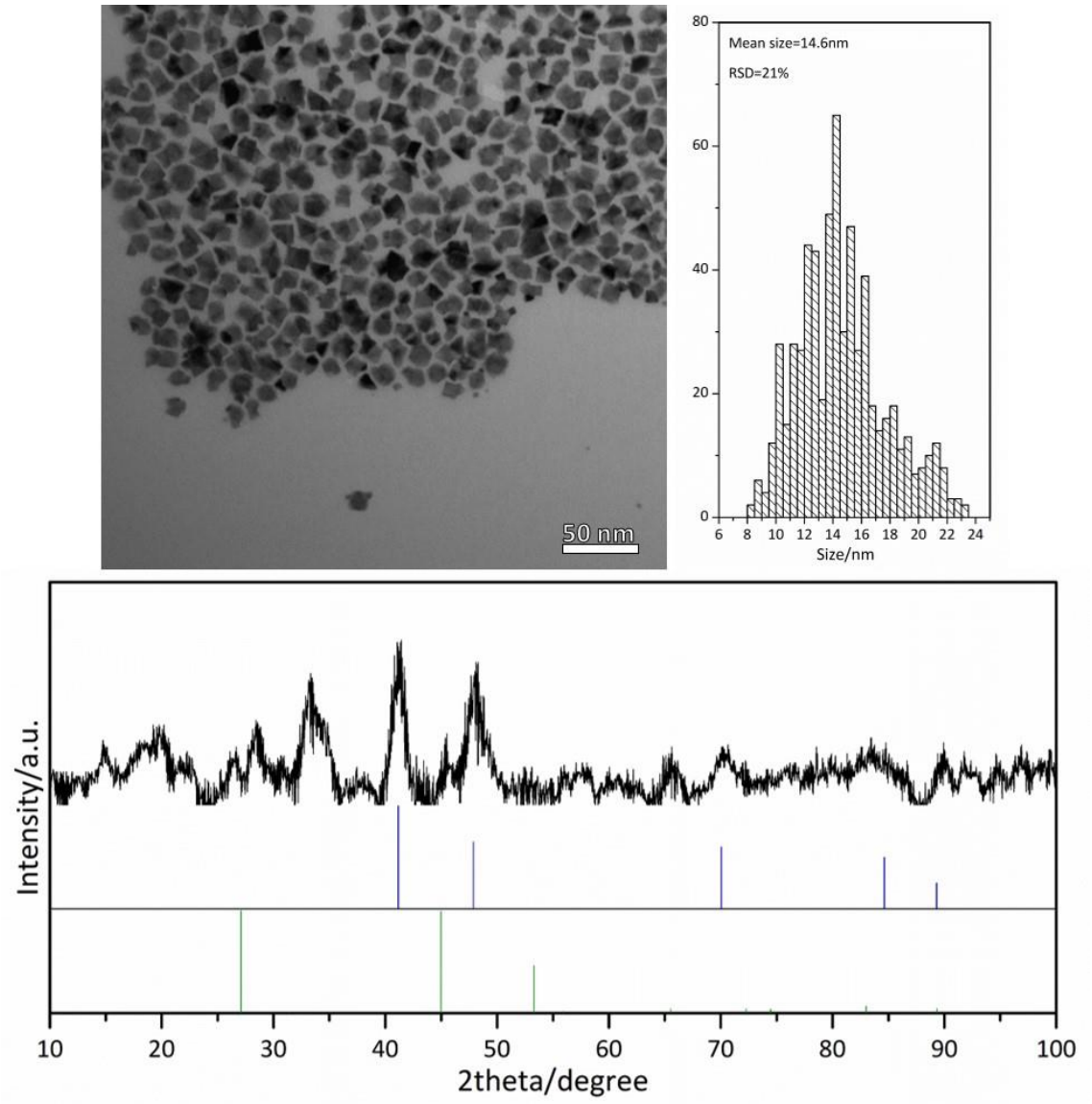

Figure 5.5: TEM image, size histogram and XRD pattern of Pt-Cu-Se_3 NPs. Cubic Cu_2Se (green, JCPDS 088-2043) and cubic CuPt (blue, JCPDS 048-1549) reference patterns.

Finally, when the Pt:Cu ratio reached 1.6 (sample Pt-Cu-Se_4), totally different nanostructures were obtained. In the TEM image (Figure 5.6) nanostar-shaped nanoparticles were found. At the first sight, little non-uniform domains, which seemed to constitute a shell surrounding the pre-synthesised $Cu_{2-x}Se$ NPs, were tentatively attributed to be small metallic Pt nanoparticles grown on the surface of the semiconductor NP. Concerning the crystallographic characterization (XRD), only reflections that could be attributed to metallic platinum were perceived.

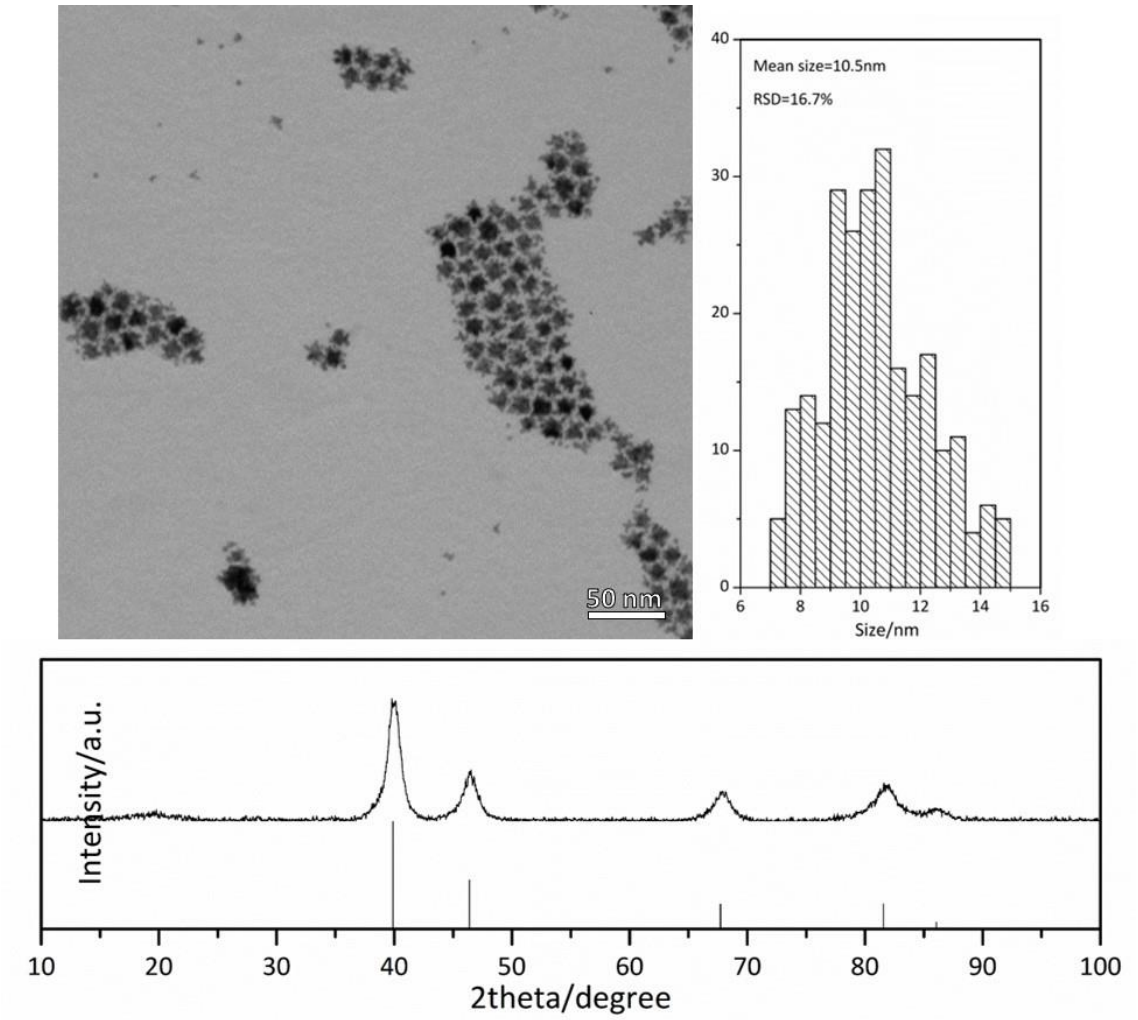

Figure 5.6: TEM image, size histogram and XRD pattern of Pt-Cu-Se_4 NPs. Cubic Pt (JCPDS 087-0640) reference pattern.

The morphological and crystallographic characterization showed the evolution of $Cu_{2-x}Se$ NPs when reacting with the platinum molecular precursor. It seems that precursor NPs had suffered some changes after the reaction. However, the basic characterization done until this point was not enough to elucidate the nature of these new nanomaterials. So, as it was commented before, additional characterization was fulfilled.

5.4 In-depth characterization of Pt-Cu-Se nanostructured systems

The additional characterization, by HRTEM and STEM-EDS, was done by Dr. Andrea Falqui's group, from the King Abdullah University of Science and Technology, in Saudi Arabia.

Figure 5. ***7*** shows the STEM-HAADF images and EDS elemental maps of samples Pt-Cu-Se_1-4.

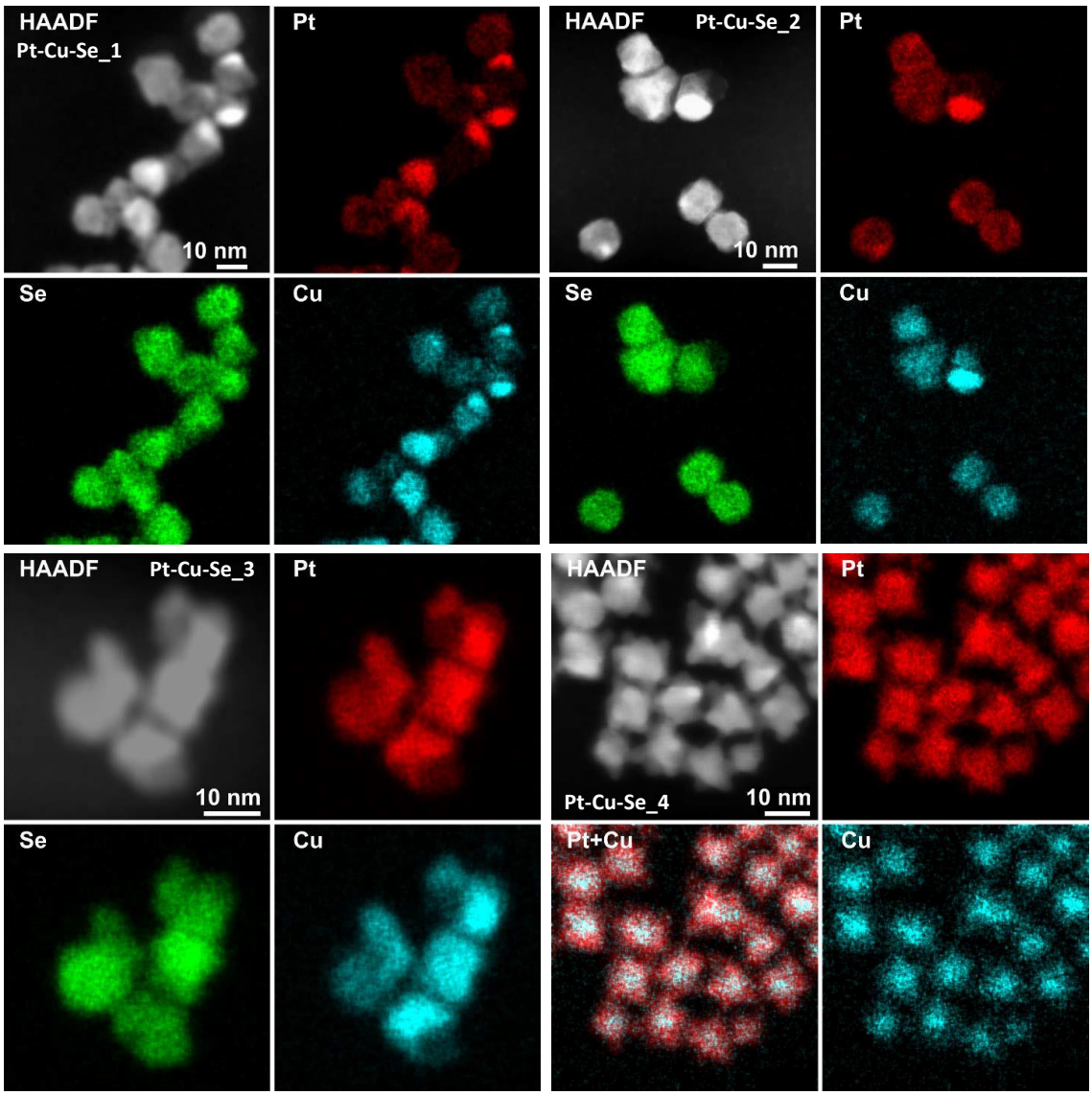

Figure 5. 7: STEM-HAADF images and EDS elemental maps of samples Pt-Cu-Se 1-4.

Two different domains were clearly seen in samples 1 and 2, as it was already observed by low resolution TEM. The brighter domain, which seemed to have a more metallic character and it was only in a few particles, was made of platinum, selenium and copper. The other domain, which was more abundant, was mainly composed by selenium and copper. Even though copper was present in both domains, the main part of it was found in the more metallic domain.

Apart from that, a slight presence of platinum can be also observed in the larger domain. As the amount of Pt was increasing in the reaction, the incursion of Pt was becoming more considerable at the same time that the metallic domain was disappearing, to get a more homogeneous morphology in sample 3.

Finally, when a higher Pt:Cu ratio was used, in sample Pt-Cu-Se_4, the material evolved to a core-shell nanostructuration, which, curiously has no trace of selenium. The core-shell nanoparticles were formed by a platinum shell and a copper-containing core.

Comprehensively, the reaction between platinum and pre-synthesised $Cu_{2-x}Se$ NPs led to four different hybrid and ternary samples depending on the Pt:Cu ratio. As the amount of platinum was increasing, this element was diffusing inside the Cu-Se semiconductor nanostructure, forming ternary structures with Cu and Se and favouring the formation of a pure metallic CuPt alloy after expelling Se from the NPs at high Pt loads.

Quantitative elemental analyses were also conducted on the EDS elemental maps to identify the different phases of the nanomaterials and to calculate the chemical composition of the whole NP. The results of these calculations, also done by the group of Dr. Andrea Falqui, are compiled in Table 5.1.

Table 5.1: STEM-EDS elemental characterisations. *indicates a minor phase; Full NP indicates the averaged composition of the whole NPs constituted by different phases.

Pt-Cu-Se_1	**Phase A**	**Phase A***	**Phase B**	**Phase B***	**Full NP**
Cu	31	26	21	35	47
Se	21	29	64	53	47
Pt	48	45	24	12	26
Pt-Cu-Se_2					
Cu	14	-	13	-	13
Se	43	-	56	-	58
Pt	43	-	31	-	29
Pt-Cu-Se_3					
Cu	36	-	14	-	29
Se	5	-	47	-	23
Pt	59	-	39	-	48
Pt-Cu-Se_4	**Core**		**Shell**		
Cu	12	-	4	-	7
Se	-	-	-	-	-
Pt	88	-	96	-	93

The quantitative analyses indicate that all samples, as was already suggested by TEM, were, at least, composed by two different phases. Phase A corresponded to the more metallic domain, with a higher proportion of copper and platinum. With the increase

of the amount of platinum in the reaction, the general trend of this domain was to slightly increase the amount of platinum and to decrease the amounts of copper and selenium, to became, at the end, a Pt-rich core of CuPt alloy.

Phase B matched with the semiconductor phase, which was, at the beginning, rich in Se. Similar to the trend of Phase A, with the increase of Pt in the synthesis, the proportion of this element in the phase becomes higher, while the amounts of Se and Cu decrease until full disappearance at the end. Sample 2 does not strictly follow the general trend in all cases, maybe due to inhomogeneities in the sample. Sample 1 seems to be the most disordered sample, with the presence of two additional minor phases with slightly different chemical composition.

Concerning the whole system (Full NP column in Table 5.1), it was observed that with the increment of the amount of platinum in the reaction, there was an increment of the average amount of platinum in the whole NP and a reduction of the selenium down to the complete expulsion of it. The amount of copper was also reduced with the presence of platinum, but without achieving total removal.

In addition to this elemental characterization, structural analyses of the precursor $Cu_{2-x}Se$ NPs and Pt-Cu-Se nanomaterials were carried out according to the planar and angular relationships occurring between diffraction spots in the 2D-FFTs (numerical diffractograms) and the corresponding lattice parameters were calculated for each orientation. HRTEM images with the different phases are shown in Figure 5.8.

All the 2D-FFT patterns analysed were compatible with the formation of face centred cubic (*fcc*) structures with different lattice parameters depending on the domain. The calculated lattice parameters are compiled in Table 5.2.

Table 5.2: HRTEM-based lattice parameters. *indicates a minor phase

	Phase A	**Phase A***	**Phase B**	**Phase B***
Pt-Cu-Se_1	4.0 Å	3.0 Å	6.0 Å	5.3 Å
Pt-Cu-Se_2	4.0 Å	-	5.4 Å	-
Pt-Cu-Se_3	4.0 Å	-	5.5 Å	-
Pt-Cu-Se_4	4.0 Å	-	-	-

Even though the composition was changing, phase A presented a lattice parameter of 4.0 Å which was consistent in all samples, while lattice parameter of phase B varying depending on the sample from 5.4 to 6.0 Å, being again sample 2 in disagreement of the trend. More in detail, Pt-Cu-Se_1 was characterised by highly disordered polycrystalline NPs, which had two main structural phases and two minor structural phases in agreement with the previous compositional analysis. Pt-Cu-Se 2 and 3 resulted less disordered, with just two different phases each, and they progressively

revert from polycrystalline NPs to heterostructured NPs. Finally, Pt-Cu-Se_4 showed the formation of a single phase, with a lattice parameter of 4 Å which could have two different compositions: the Pt shell and the Cu-containing core.

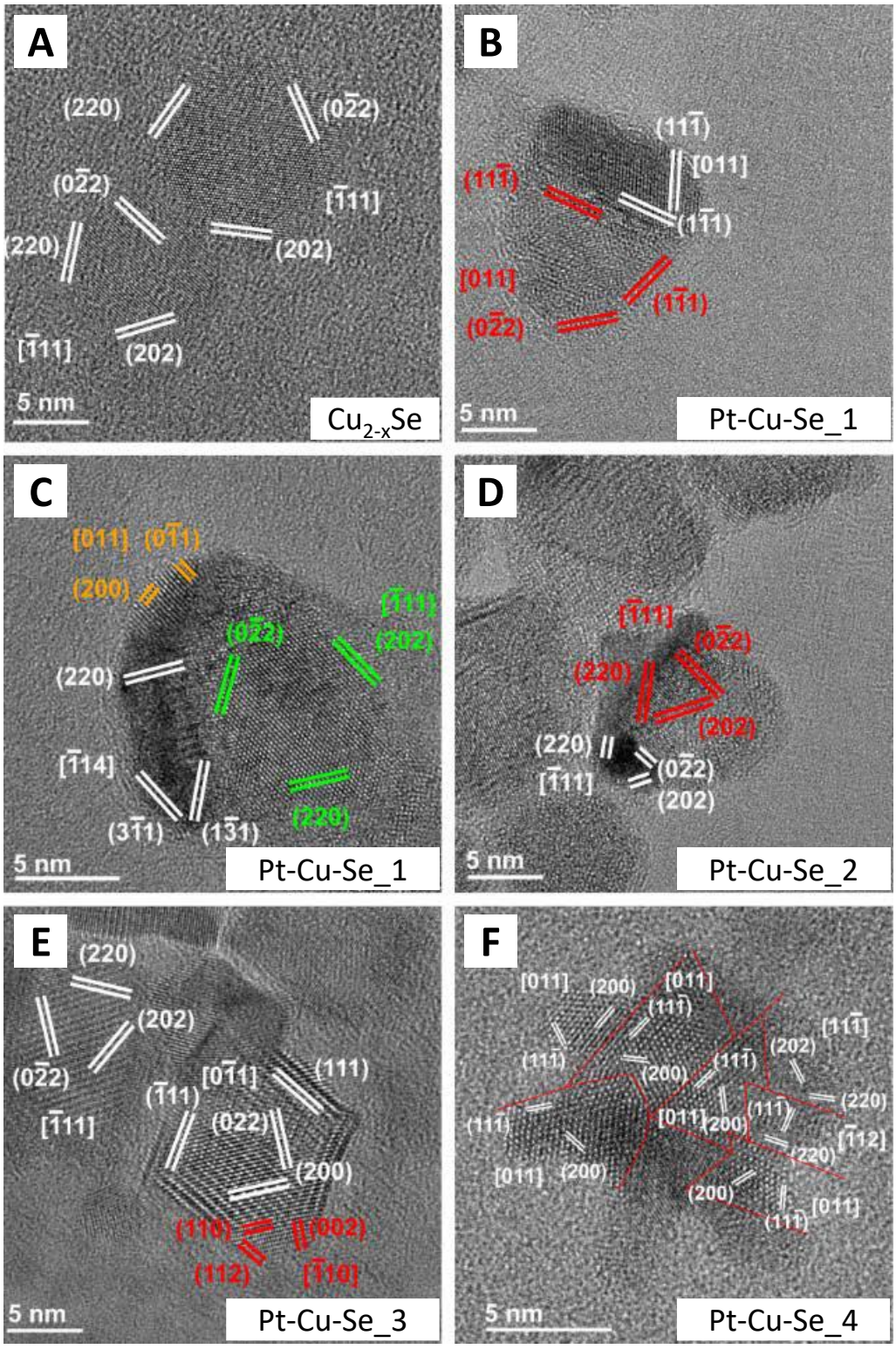

Figure 5.8: HRTEM images of representative NPs of A) $Cu_{2-x}Se$, B) and C) Pt-Cu-Se_1, D) Pt-Cu-Se_2, E) Pt-Cu-Se_3 and F) Pt-Cu-Se_4. Different phases in panels in panels B-E are depicted in false colours as indicated: Phase A (main) in white, Phase B (main) in red, Phase A (minor) in green and Phase B (Minor) in orange.

XPS measurements of samples $Cu_{2-x}Se$, Pt-Cu-Se_1, 2 and 4 were done by Dr. Jordi Llorca. Unfortunately, it was not possible to measure sample Pt-Cu-Se_3. Briefly, the results show the presence of Pt, Cu and Se in samples Pt-Cu-Se 1 and 2. The fact that part of these platinum showed a certain degree of oxidation supported the idea of the nanomaterials being formed by ternary structures. Regarding to Pt-Cu-Se_4 sample, only platinum was detected, which was expected considering that copper was only located at the core of the nanomaterial and XPS is a surface-sensitive technique.

5.5 Optical characterization of $Cu_{2-x}Se$ NPs and Pt-Cu-Se nanostructured systems

Optical characterization of samples was also done. Vis-NIR absorption spectroscopy is shown in Figure 5.9**:** Vis-NIR absorbance spectra of Cu2-xSe and Pt-Cu-Se_1-4 samples.. $Cu_{2-x}Se$ NPs showed the well-known LSPR band centred at 976 nm. It had been seen and commented that the growth of a metallic domain in the nanostructure could change or damp the plasmonic response of copper chalcogenides. However, in this case, the introduction of platinum inside the structure to form ternary phases instead of the growth of a metallic domain, seemed to damp completely the LSPR, leading to a flat absorption in NIR range.

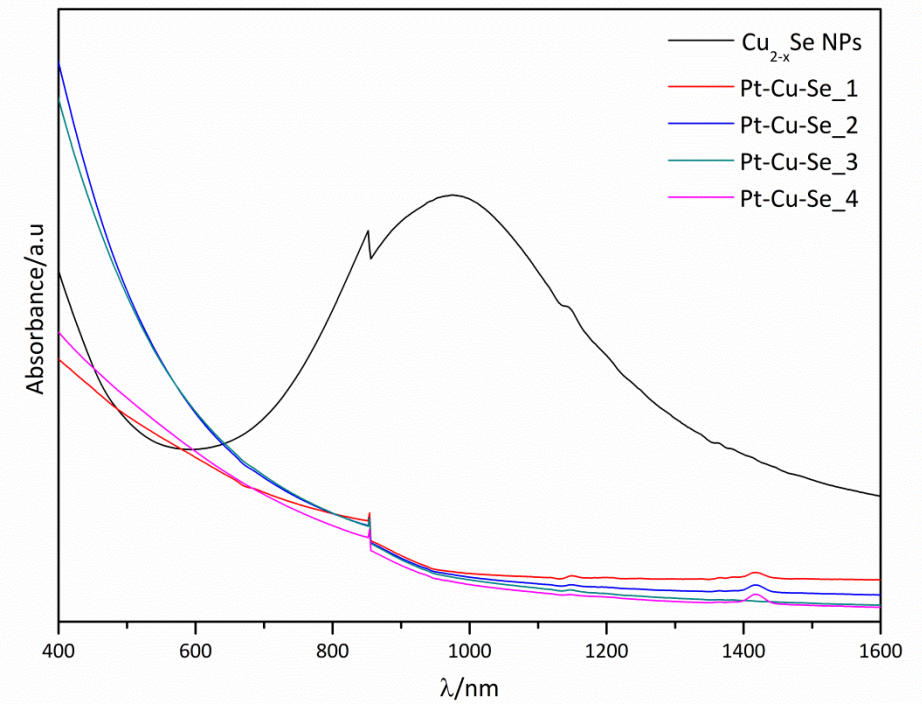

Figure 5.9: Vis-NIR absorbance spectra of $Cu_{2-x}Se$ and Pt-Cu-Se_1-4 samples.

In summary, the reaction between pre-synthesised $Cu_{2-x}Se$ NPs and a Pt(II) precursor in a hydrophobic medium and at high temperature led to the formation of ternary

materials made of Pt, Cu and Se, in which it was possible to change the composition depending on the ratio Pt:Cu used in the synthesis. Two main phases, one Se-rich and other Pt-rich, were found and deeply characterised. The increment of the amount of platinum in the reaction led to a higher proportion of this element within the crystal lattice, with a decrease of the total amount of selenium, until the total disappearance of the latter in the nanostructures of the last sample. These changes cause the total damping of the plasmonic resonance of the copper selenide nanostructures.

5.6 Experimental part

Chemicals

Copper (I) chloride (CuCl, 99.999%-Cu), platinum (II) acetylacetonate ($Pt(acac)_2$, 98%) and selenium powder (Se, 99.99%) were obtained from Strem Chemicals. Oleylamine (OLAm, 70%), 1-octadecene (ODE, 90%), oleic acid (≥99%), 2-propanol (≥99.9%) and toluene (99.9%) were purchased from Sigma-Aldrich. All the reagents and solvents were used without further purification, except for the ODE and OLAm which had been previously degassed under vacuum for 3h at 120°C.

Synthesis of $Cu_{2-x}Se$ NPs

The synthesis of $Cu_{2-x}Se$ NPs was carried out following a method published by Kriegel and co-workers.[283] Briefly, 47.4 mg (0.6 mmol) Se, 4.5 mL ODE and 3 mL OLAm were degassed in a three-neck flask for 1h at 120°C under vacuum. Meanwhile, Cu precursor solution was prepared in the glovebox: 49.5 mg (0.5 mmol) CuCl were dissolved in 1.5 mL ODE and 1 mL OLAm, the solution was slightly heated to achieve the complete dissolution of the solid. Under N_2 atmosphere, the temperature of the system was raised to 310°C and the Cu precursor solution was injected. After 20 min of reaction, the heating was stopped, and the solution was let cool down naturally. The final solution was washed once with 2-propanol, centrifuging 4 min 4500 rpm and re-dispersing the precipitate with ODE.

Synthesis of Pt-Cu-Se nanocomposites

The synthesis of Pt-Cu-Se nanocomposites were based on the method developed by Chao and co-workers for the synthesis of metallic platinum nanocubes[43] but using a solution of pre-synthesised $Cu_{2-x}Se$ NPs instead of the catalyst $Fe(CO)_5$. Specifically, 5 mg of $Pt(acac)_2$ (0.013 mmol), 1.25 mL ODE, 125 µL OLAm and 125µL OLAc were degassed in a three-neck flask for 30 minutes at 120°C under vacuum. Once under N_2,

a $Cu_{2-x}Se$ NPs solution ([Cu]=80 mM) in toluene was injected and the temperature of the system was raised to 200°C slowly. Once at Sremoved, and the solution was let cool down naturally. The final solution was washed once with 2-propanol, centrifuging 4 min 4500 rpm and the precipitate was redispersed in toluene.

The exact amounts of $Cu_{2-x}Se$ injected in each sample are shown in Table 5.3.

Table 5.3: Volumes of $Cu_{2-x}Se$ solution used in each synthesis of Pt-Cu-Se.

Sample	Volume of $Cu_{2-x}Se$ solution injected	Pt:Cu ratio
Pt-Cu-Se_A	1.5 mL	0.1
Pt-Cu-Se_B	0.75 mL	0.2
Pt-Cu-Se_C	0.25 mL	0.65
Pt-Cu-Se_D	0.1 mL	1.6

Characterization Methods

$Cu_{2-x}Se$ and Pt-Cu-Se ternary NPs were prepared for observation by transmission electron microscopy (TEM) by dilution in toluene followed by sonication. A droplet of the solution was then poured in holey carbon covered copper TEM grids. A JEOL 2000 FX II conventional TEM operating at an accelerating voltage of 80kV was used.

X-ray diffraction (XRD) patterns were acquired with a PANalytical X'Pert Pro MPD Alpha1 diffractometer operating in θ/2θ geometry at 45 kV, 40 mA, and λ= 1.5406 Å (Cu Kα1). Thin layers of the samples were prepared by drop casting and evaporation of the solvent on a monocrystalline Si flat substrate. Scans in the range 2θ = 4−100° were run at a step size of 2θ = 0.017° and 100 s per step. The data were treated with X'Pert HighScore Plus software.

X-ray photoelectron spectroscopy (XPS) was performed on a SPECS system equipped with an Al anode XR50 source operating at 150 W and a Phoibos 150 MCD-9 detector. The pass energy of the hemispherical analyzer was set at 25 eV, and the energy step was set at 0.1 eV. The binding energy (BE) values referred to the C 1s peak at 284.8 eV.

The composition and concentration of $Cu_{2-x}Se$ NPs solution was determined by inductively coupled plasma-atomic emission spectroscopy (ICP-AES). The measurements were carried out by an Optima 3200 RL PerkinElmer spectrometer. For these measurements, 50 µL of each of the solutions was precipitated in MeOH and redispersed in $CHCl_3$. The solution was evaporated in an oven overnight at 90 °C.

Before the vial was sealed, 2.5 mL of aqua regia and 0.7 mL of H_2O_2 were added to the precipitate and then heated to 90 °C for 72 h. The resulting solution was transferred to a 25 mL volumetric flask and diluted with Milli-Q water.

High Resolution TEM (HRTEM) structural analysis was performed by a CS-image corrected FEI Titan working at 300 kV. STEM-EDS elemental mapping was performed on a double spherical corrected FEI Titan Themis cubed microscope equipped with a SuperX EDS spectrometer with 0.7 srad collection angle and working at 80 kV. Both instruments were equipped with an ultra-bright Schottky (FEI X-FEG) electron source. The lower voltage used for EDS mapping was chosen to maximize the X-Ray signal production and to minimize the possibility of beam damage on the samples, thus improving the S/N ratio during the collection of elemental maps. The elemental maps were also used to perform quantitative analysis and assess the composition of the NPs and of the different phases constituting them. Obviously, given the intrinsic 2-Dimensional nature of TEM related techniques, where 3-Dimensional objects are observed and analyzed according to their 2-D projections, and the irregular shape and distribution of the phases composing the NPs, the quantification conducted on different Regions Of Interest (ROIs) is forcibly the convolution of all the different phases comprised in each ROI. Then, the results of the quantification will be averaged among the phases within the ROI but mostly driven by the main phase (*i.e.*, the most present phase within the ROI)

The structural characterization was conducted by 2-Dimensional Fast Fourier Transform (2D-FFT) analysis. The diffraction peaks of the 2D diffractograms could not be attributed to any known crystal phases in the case of the ternary NPs, thus a “blind” approach was used: at first the planar and angular relationships occurring between diffraction spots in the 2D-FFTs (numerical diffractograms) were calculated in order to verify the kind of crystal lattice formed and its orientation within the NPs, then the lattice parameters were calculated from the diffraction spots of each orientation. This two-step procedure led to lattice parameters that were self-consistent within each 2D-FFT diffractogram, while also resulting in different lattice parameters for each ternary sample. Finally, the structural data were successfully put in relation with the different phases observed by EDS mapping.

X-ray photoelectron spectroscopy (XPS) was performed on a SPECS system equipped with an Al anode XR50 source operating at 150 W and a Phoibos 150 MCD-9 detector. The pass energy of the hemispherical analyzer was set at 25 eV, and the energy step was set at 0.1 eV. The binding energy (BE) values referred to the C 1s peak at 284.8 eV.

UV-Vis-NIR absorption spectra of all samples were recorded in toluene solution on a Perkin Elmer LAMBDA 950 spectrophotometer.

Chapter 6
Inorganic NP-Au(I) metallogelator system

6.1 Introduction

Hybrid materials science is a huge field that comprehends all the materials composed by two or more different compounds in the same structure. Two different blocks can be distinguished regarding to the nature of the domains. On the one side, the inorganic-inorganic hybrid materials,[61,63,65,293,294] which include, among others, the metal-semiconductor hybrid structures that have been studied in previous chapters. On the other, the organic-inorganic hybrid materials.

Organic-inorganic hybrid materials are known to be the combination of an organic component and an inorganic material at the nanoscale. In mother nature, several examples of this kind of structures can be easily found: crustacean carapaces, mollusc shells, bones and teeth tissues, etc. Their proper and combined properties, i.e. good thermal, mechanical and chemical stabilities, hydrophobia, colour, permeability, density…, have attracted the attention of humans since long time ago, finding the first examples of this kind of materials used in Egyptian inks, green bodies of China ceramics, prehistoric frescos, among others. Between 1940 and 1960 they started to be considered in industry and science and the importance of this kind of material has not stopped growing since then.[295–298]

Three important parts can be distinguished in this kind of materials: the inorganic part (usually are metal oxides, metal-oxo polymers, phosphates, carbonates, chalcogenides), the organic part (molecules or polymers) and the hybrid interphase. Depending on the interphase, the inorganic-organic hybrid materials have been classified in two classes: 1) *Class I* materials, in which the interphase is formed by weak bonds (Van der Waals, hydrogen bonds, metallophilic interactions) and, 2) *Class II* materials, which has the two parts linked by a strong orbital overlap (covalent bonds).

Metal-organic frameworks (MOFs) are probably the most renowned type of inorganic-organic hybrid materials due to the high versatility of composition, structure and

properties that offer, that make them suitable in many applications such as gas storage, catalysis, gas purification, drug delivery, among others.[299–305]

Nevertheless, many other types of inorganic-organic hybrid materials (hybrid hydrogels, NPs embedded in soft materials, quantum dots with molecular linkers…) have been studied and applied in different fields such as protective and decorative coatings, energy applications (solar cells, hybrid flexible batteries), health care and cosmetics, construction.[306–308]

To give an example, some groups have been working on the embedding of NPs on soft materials such as polymer thin films, liquid crystals, hydrogels or self-assembled monolayers.[309–314] In some cases, these soft materials have been used for the in-situ synthesis of the nanoparticles. Besides, their noncovalent supramolecular interactions can be used to control the organization of NPs.

This chapter is centred in the synthesis of inorganic-organic hybrid nanocomposites originated by the spontaneous supramolecular assembly of noble metal NPs and a highly fluorescent low molecular weight Au(I) metallogelator. All the work was done in collaboration with Dr. Elisabet Aguiló, from the group of Dr. Laura Rodríguez of the Inorganic Chemistry Section of the Inorganic and Organic Chemistry Department of the University of Barcelona.

Noble metal NPs, as plasmonic nanostructures, have gained importance in last years due to their interesting optical properties that make them suitable for many applications, including visible-light absorbers and exciton-dissociation enhancers in photovoltaic[315–317] and photocatalytic devices.[46,50] In order to enhance the light harvesting an active material such as polymers or small organic molecules can be linked to the metallic NPs forming an inorganic-organic hybrid material. The study of the interphase between the materials is essential to ease charge-carrier percolation through the composite and consequently maximize the energy conversion or photocatalytic activity.

[Au(4-pyridylethynyl)(DAPTA)], for which DAPTA is 3,7-diacetyl-1,3,7-triaza-5-phosphabicyclo [3.3.1]nonane, from now on called complex 1 for simplicity, is a luminescent gold(I) alkynyl phosphine complex synthesised by the group of Dr. Laura Rodríguez (structure shown in Figure 6.1A). This complex is a metallogelator, which means that is a low molecular weight gelator formed by the coordination of organic ligands to metallic ions. Usually, these compounds spontaneously self-assemble through a combination of noncovalent interactions, which results in the formation of filaments or aggregated structures. Besides, the presence of the metal ion offers the possibility to establish, in some cases, metallophilic intermolecular interactions. The strength of these interactions is comparable to that of the hydrogen bond and can be a possible driving force for the formation of supramolecular structures.[318–320]

Complex 1 has been deeply studied by the group of Dr. Laura Rodríguez.[321] When the complex is dissolved in water, it goes through a gelation process with the formation of entangled fibres that could be easily observed by optical microscopy and SEM (Figure 6.1C and D). This aggregation process is thought to be due to the π-π stacking of the C≡C-pyridine units, combined with aurophilic intermolecular interactions between Au(I) atoms. Both, the complex 1 and the hydrogel have strong luminescent properties (Figure 6.1B, E and F).

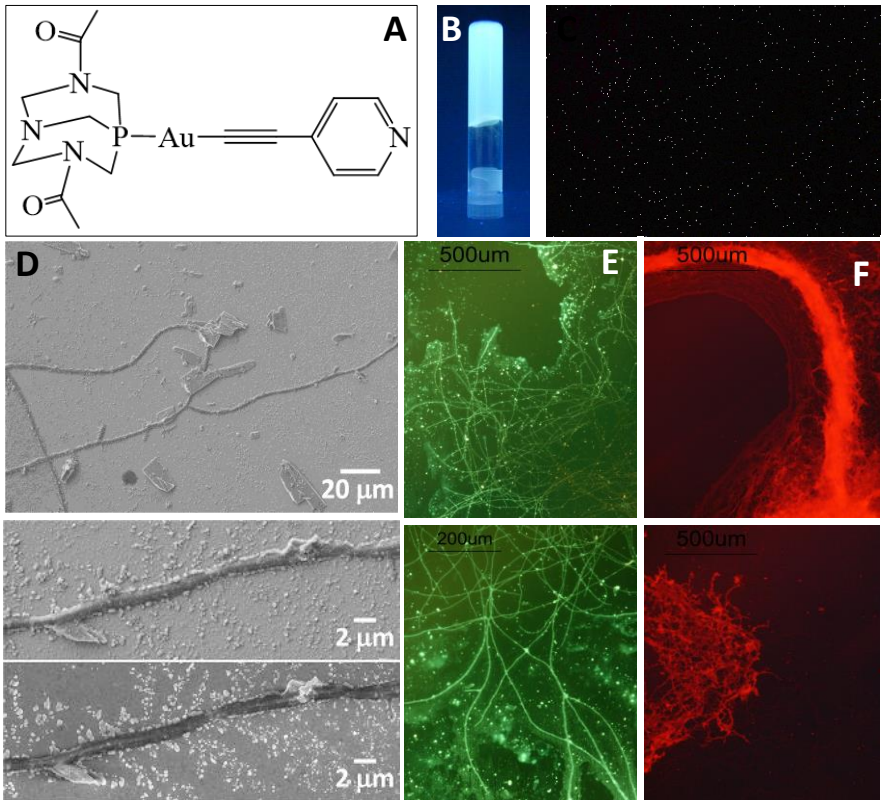

Figure 6.1: (A) Molecular structure of complex 1. (B) Complex 1 hydrogel under Ultraviolet light. (C) Optical microscopy and (D) SEM images of complex 1 fibres. (D) Fluorescent microscopy images took with a 395-440 nm filter (E) and with a 510-560 nm filter of complex 1 fibres.

Although metallophilic interactions have been studied in solid-state molecule-based crystalline systems[322,323] and in solution,[324,325] their use for anchoring a complex with metal-based nanoparticles has not been widely explored. Hence the idea of this part of the project was to try to take advantage of these metallophilic interactions to "functionalize" noble metal nanoparticles with complex 1.

6.2 Au-complex 1 nanocomposite: synthesis, morphological characterization and study of its stability

The synthesis of the nanocomposite (NCP) of gold NPs and complex 1 was done by a simple mixture at room temperature of the two components in chloroform and a consecutive separation of the NCP by centrifugation.

Gold NPs were previously synthesised by a heat-up method adapted from the literature[72] and, as can be observed in the TEM image in Figure 6.2A, they were spherical with a diameter of 15nm. After the reaction between complex 1 and gold NPs, the size and shape of the original NPs were preserved, as can be seen in Figure 6.2B. However, whereas the original gold NPs were hydrophobic and could just be dispersed in apolar solvents such as toluene, chloroform or hexane, the Au-complex 1 NCP was stable in polar solvents like water, ethanol or methanol (Figure 6.3). Apart from that, there was also a considerable change of colour between the two nanomaterials solutions, hydrophobic gold NP solution (in toluene) had its typical red colour, while the hydrophilic nanocomposite solution (in water) was blue.

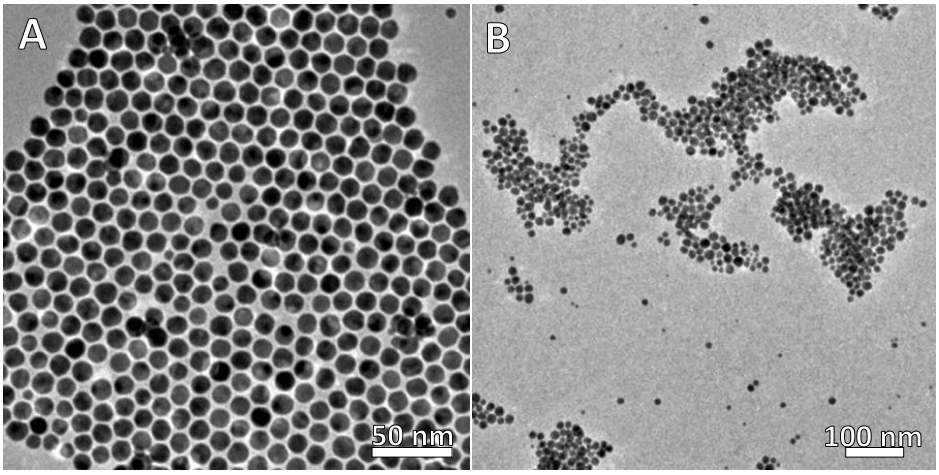

Figure 6.2: TEM images of (A) hydrophobic Au-OLAm NPs and (B) hydrophilic Au-complex 1 NCP.

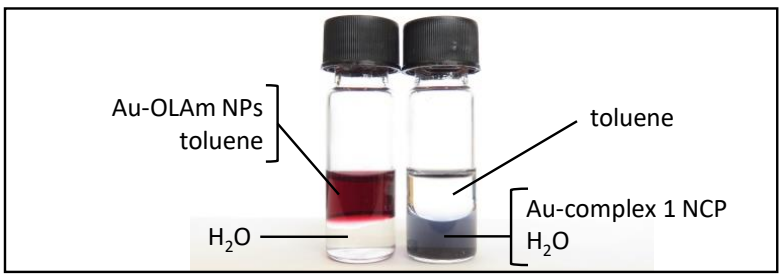

Figure 6.3: Solubility of the initial hydrophobic Au-OLAm NPs and the final hydrophilic Au-complex 1 NCP.

Complex 1, in presence of water, formed long fibres as a result of the gelation process, as was commented in a previous section. FESEM was done to study the influence of the NPs in the natural gelation process of complex 1. As can be observed in Figure 6.4A, the NCP was constituted by aggregates of metallic NPs surrounded by a light contrasted shell. In SEM, the brighter the contrast is, the heavier the element is. Hence, the shell has a lower atomic weight, which suggested it could be made of organic matter. The presence of a polydisperse distribution of stable aggregates with a size range of 75 to 200 nm was also pointed out by DLS measurements (Figure 6.4B).

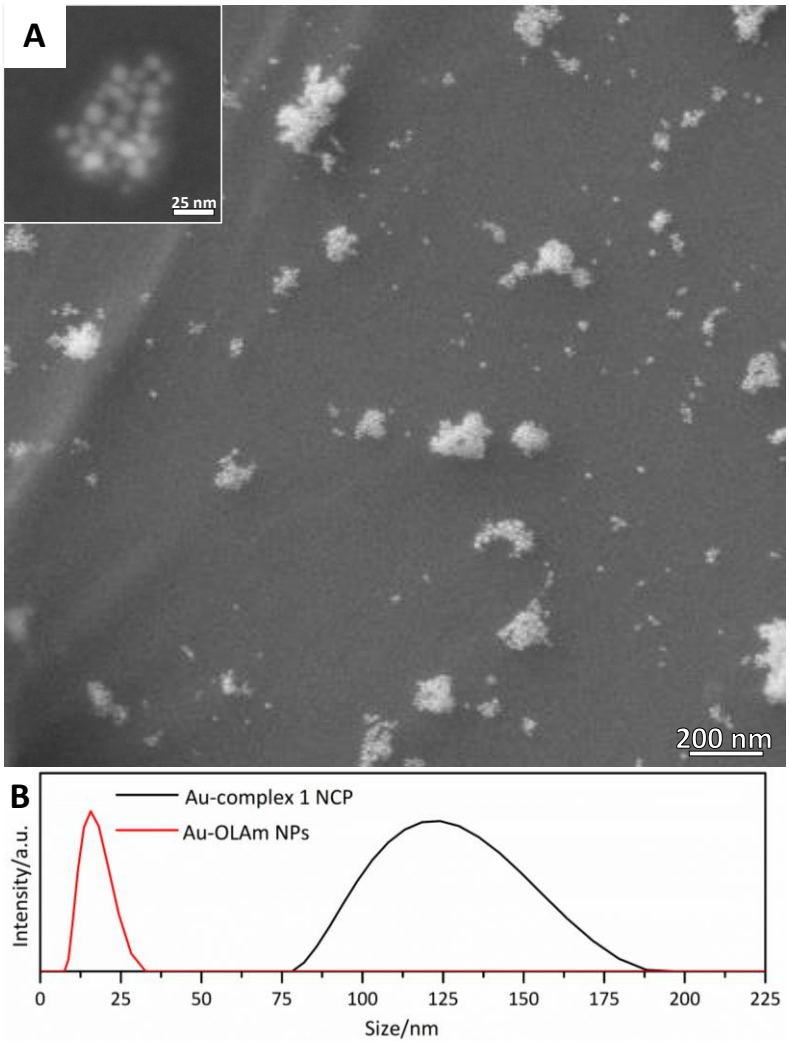

Figure 6.4: (A) FESEM micrographs of Au-complex 1 NCP. (B) DLS measurements of hydrophobic Au-OLAm NPs (red) and hydrophilic Au-complex 1 NCP (black).

When different molar ratios of complex 1/gold NP were used (ranging from 20000 to 100000), no significant changes were observed, apart from the higher size dispersion, shown by DLS (Figure 6.5A), which could not be unequivocally linked to the change of ratios. The shape of the aggregates or the possibility of having extra amount of

complex 1, which might have gone through the gelation process itself, could cover up the results.

The stability of the aggregates in front of temperature (Figure 6.5B), time and pH were also studied by DLS (Figure 6.6). Basically, the measurements confirmed the high stability of the system at different temperatures (between 25 and 50°C), at different pH (ranging from 4 to 9) and for long periods of time (at least 12 months), since in any case DLS measurements suffered severe changes.

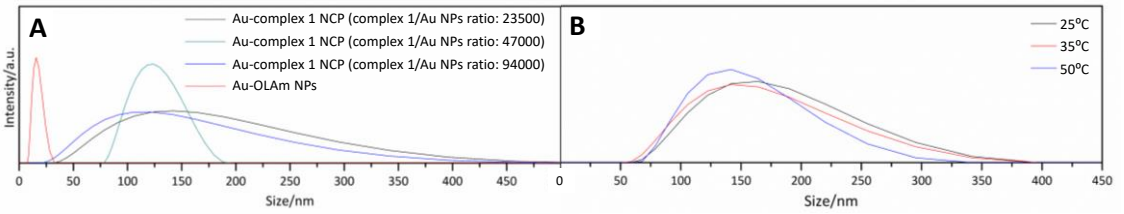

Figure 6.5: DLS measurements of Au-complex 1 NCPs synthesised (A) with different [Au/complex 1] molar ratios and (B) at different temperatures.

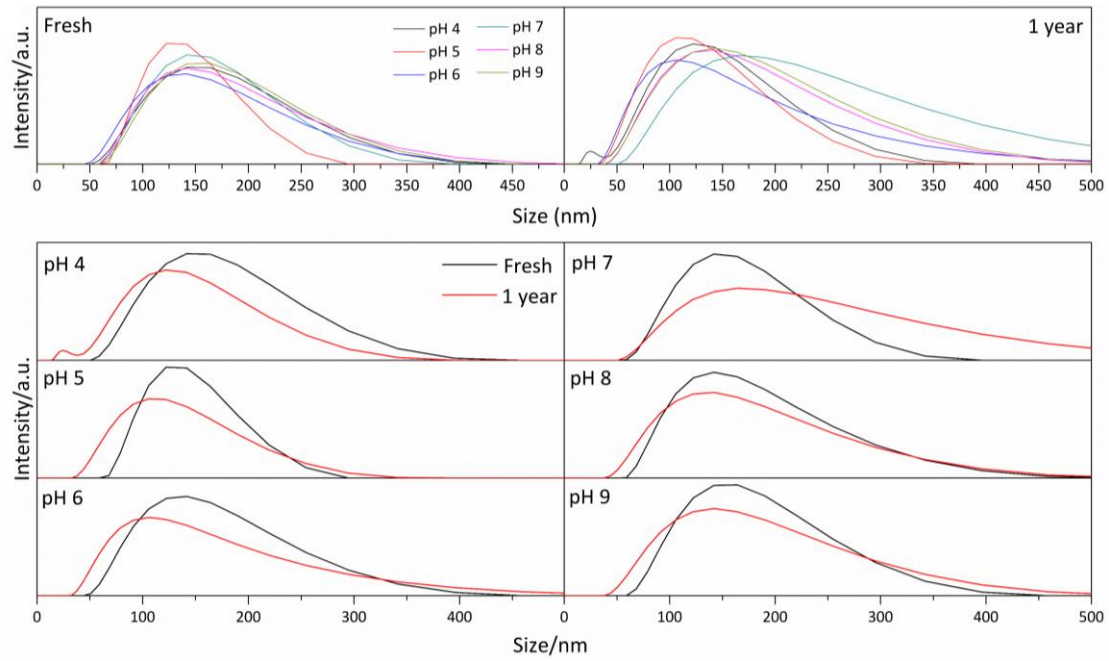

Figure 6.6: DLS measurements of Au-complex 1 NCPs (recently synthesised and 1 year later) at different pH media.

6.3 Study of the functionalization of Au NPs

The hydrophobicity of the original NPs was due to their coating of OLAm molecules, which was used as surfactant in the synthesis. OLAm is an unsaturated fatty amine, so basically it has C-H, C-C, C=C and N-H bonds. In the infrared (IR) spectrum of Au-OLAm NPs (Figure 6.7), C-H stretching peaks are clearly observed below 3000 cm^{-1}. Besides,

the double band from asymmetrical and symmetrical N-H stretching of a primary amine between 3000 and 3300 cm^{-1} are also seen.

After the reaction, the presence of complex 1 in the nanocomposite was confirmed by the intense carboxylic C=O and pyridinic C=N stretching bands between 1500 and 1700 cm^{-1}. Besides, the intense peaks from the C-H stretching of OLAm (around 2900 cm^{-1}) suffered a drastic damping which indicates the significant removal of the surfactant from the surface of Au NPs. The peaks of the NCP spectrum, in comparison to free complex 1, suffered a small shift to lower wavelengths and are wider, suggesting the efficient chemisorption of the complex molecules to the surface of gold NPs.

Mass spectrum of Au-complex 1 NCP was also acquired. Basically, it showed characteristic peaks from complex 1 with additional atoms of gold. Most likely, gold atoms were knocked out from the surface of the NP during the ionization process of the sample and dragged to the detector together with the molecule fragments.

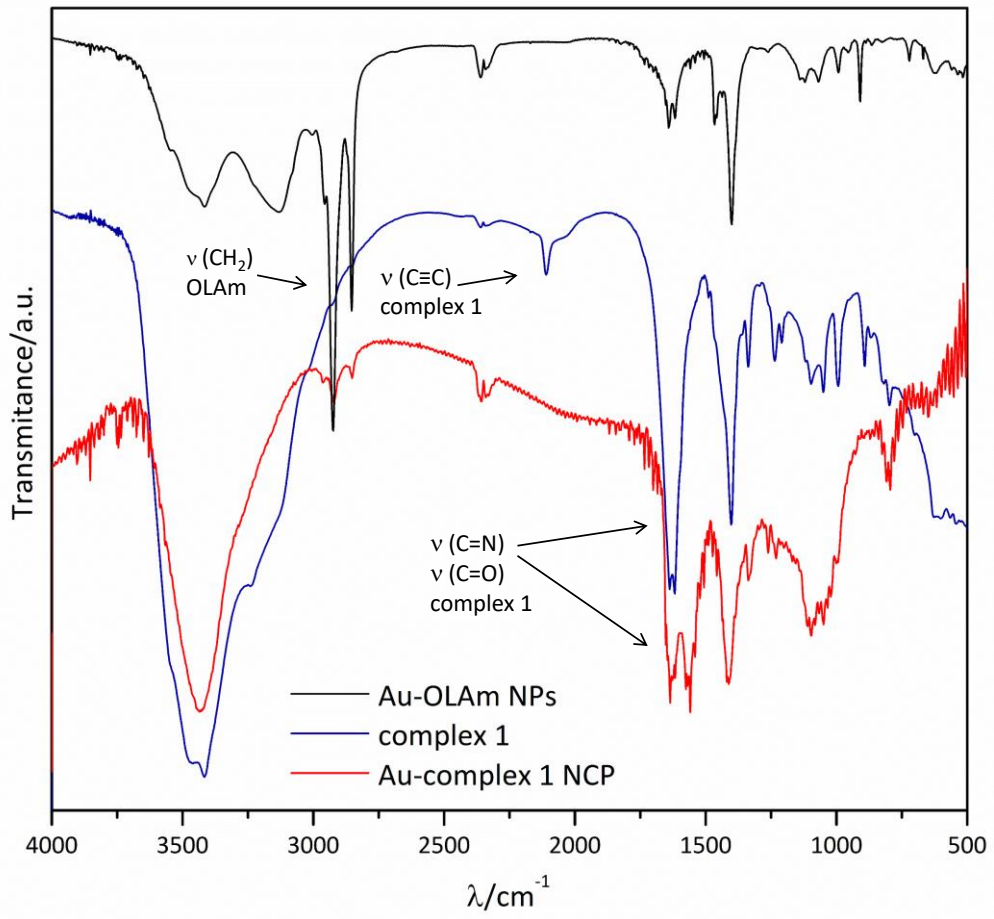

Figure 6.7: IR spectra of Au-OLAm NPs (black), free complex 1 (blue) and Au-complex 1 NCP (red).

Additionally, X-Ray Photoelectron Spectroscopy (XPS) was done by Dr. Jordi Llorca. In Figure 6.8A and B, XPS of Au-OLAm NPs and Au-complex 1 NCP verify the only

presence of Au(0) in the original NPs, as expected, and the coexistence of Au(0) and Au(I) in the NCP. As a consequence of the formation of the hybrid system, NCP contains both metallic Au NPs, with Au(0), and complex 1, with Au(I). Besides, the fitting of the XPS in N and P regions, indicates a N/P ratio of 3.6 in the NCP, which is in agreement with the theoretical ratio of 4 for complex 1. This fact further confirmed the quantitative substitution of the initial surfactant (OLAm) for the complex 1. In Figure 6.8C, the XPS survey spectrum is shown.

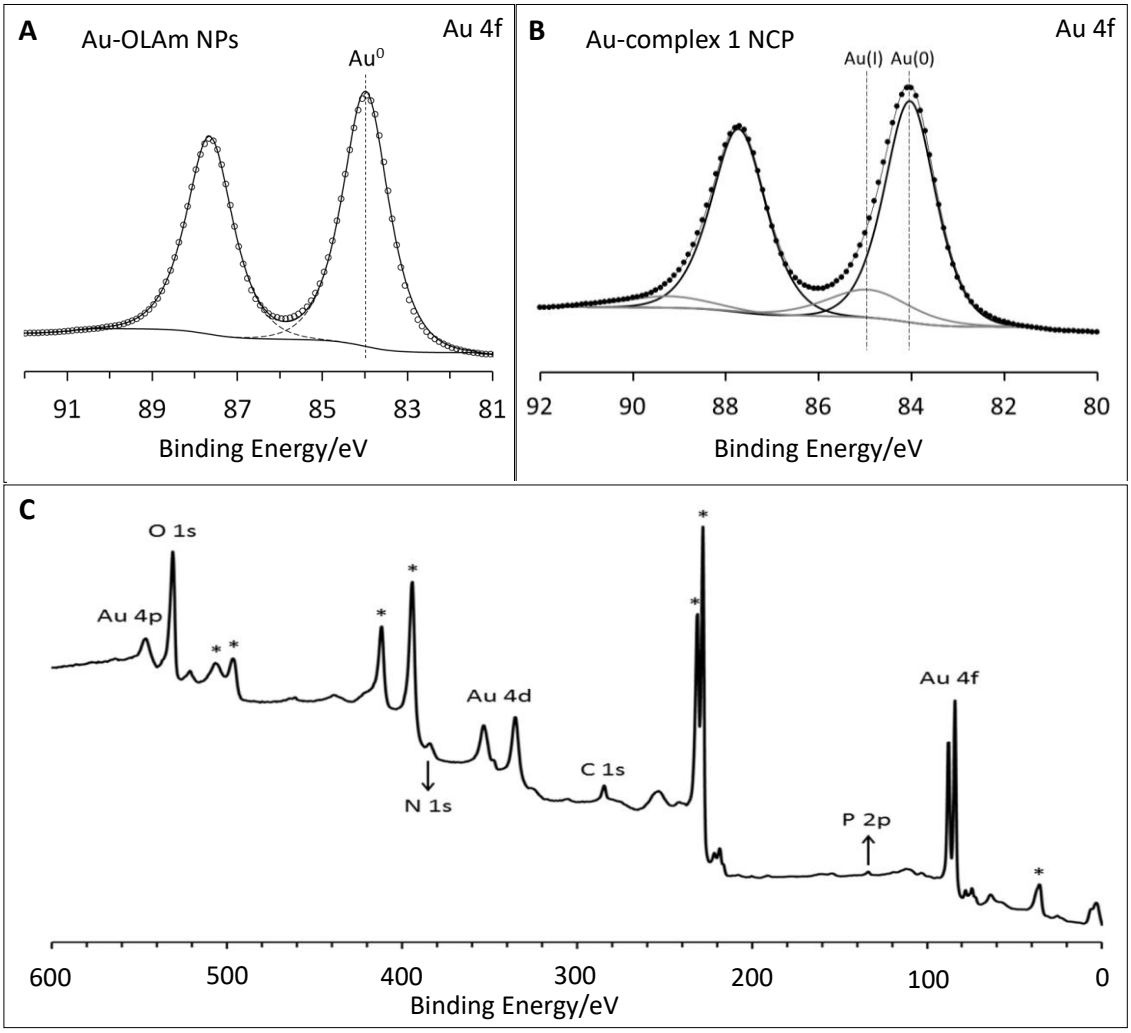

Figure 6.8: XPS spectra of (A) Au-OLAm NPs and (B) Au-complex 1 NCP. (C) XPS survey spectrum of Au-complex 1 NCP. *refers to the Mo signals coming from the sample holder.

6.4 Optical characterization of Au-complex 1 NCP

Finally, the optical characterization of the NCP was done. The absorption of the hybrid system in the UV-Vis range showed two remarkable bands (Figure 6.9). On the one side, there was a broad and intense band at 500-650nm, which was assigned to the LSPR of gold NPs. This band was broader and red-shifted with respect to that of the original Au NPs, which basically indicates some change in the dielectric properties of

the surface. The change of the solvent, an aggregation of the NPs or the presence of a different coating could be among the different responsible factors. On the other side, the band at 260nm was attributed to complex 1, which in its free form presents two bands in this region.

Moreover, the absorption of the nanocomposite at different pH was studied. The stability of the sample at different pH was studied previously by DLS and after one year (Figure 6.6). Curiously, the aqueous dispersions of the hybrid material at different pH had slightly different colours (Figure 6.9inset), going from violet at low pH (4 to 6) to blue at neutral pH (7 and 8) and coming back to violet at pH 9. Usually, in gold nanoparticles a red shift on the LSPR peak is an indicative of aggregation of NPs. However, DLS measurements at different pH (Figure 6.6) did not show very significant changes in size, so the variation of the absorption band may be due to the enhancement of the interparticle interactions.

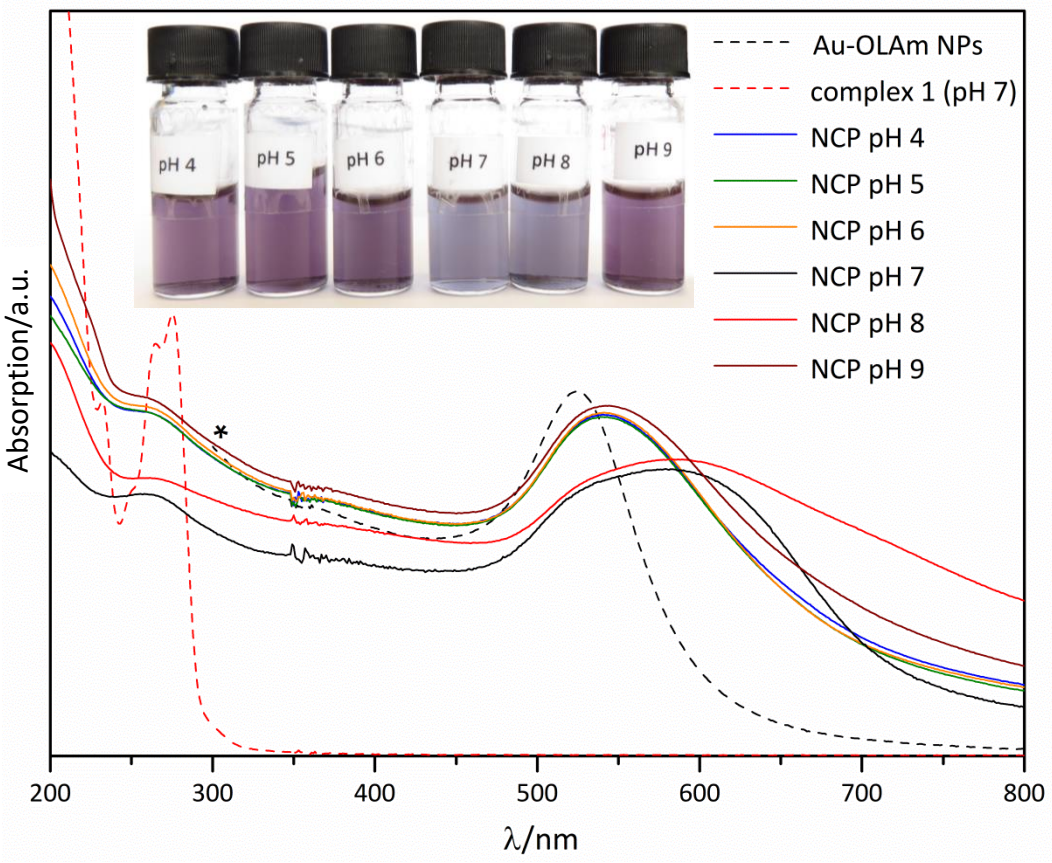

Figure 6.9: UV-Vis absorption spectra of Au-complex 1 NCP at different pH values, Au-OLAm NPs in toluene, and free complex 1 at neutral pH. *For ease of understanding, the spectrum of Au-OLAm NPs in toluene is shown only above 300 nm, which avoids the appearance of the absorption of the solvent. (Inset) Au-complex 1 NCP water dispersions at different pH.

In order to figure out the origin of these interparticle interactions a study of the UV-Vis absorption of free complex 1 was done (Figure 6.10). All bands of complex 1 had been

assigned previously.[326] The band at 240 nm was assigned to phosphine centred intraligand transitions and the peaks at 265-285nm were from the intraligand (IL) π-π* (C≡Cpy) transitions. The broad and weak band observed at 300 nm was assigned to the σ* (Au···Au)-π* transition. Hence, it is a consequence of the formation of aurophilic interactions. The significant intensification of this band at pH 7 could indicate a better capacity of the complex to create this kind of interactions at this pH, which are thought to be one of the anchoring forces between gold NPs and complex 1. This interaction may favour the creation of aggregates instead of just substituting the OLAm as coating of the nanoparticle. These observations matched perfectly with the fact that Au-complex 1 NCP showed a significant change of colour at this pH, indicating the presence of a higher nteraction of the metallic NPs.

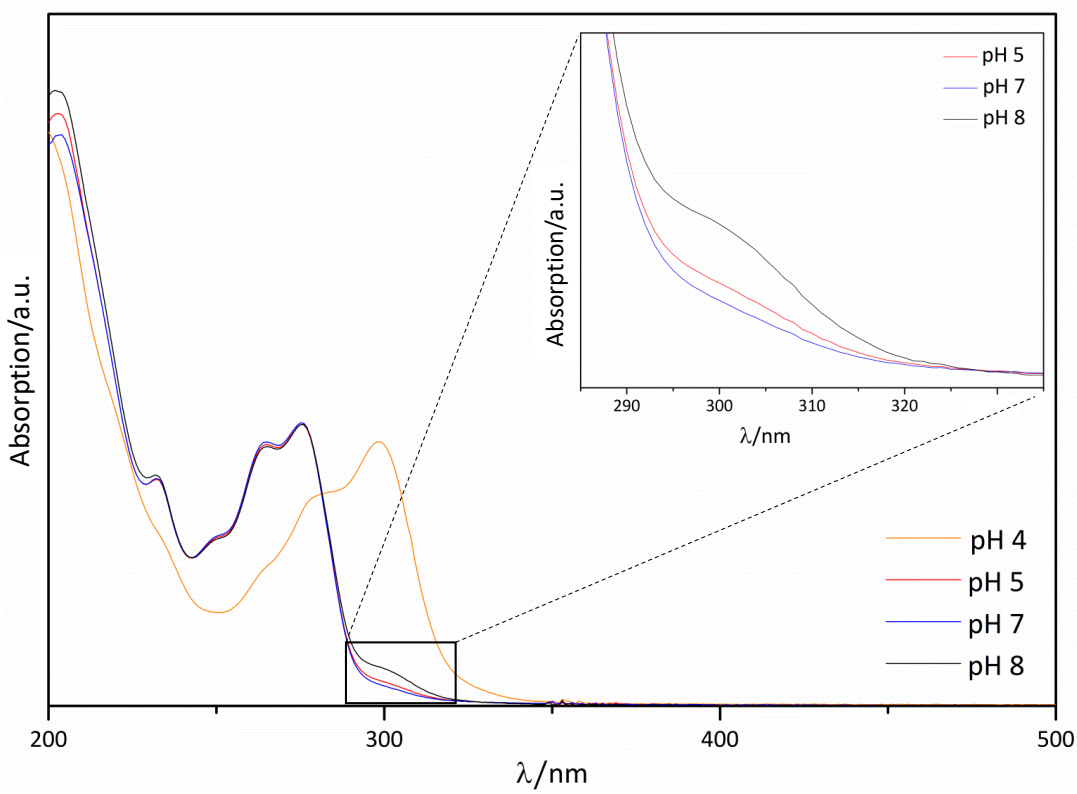

Figure 6.10: UV-Vis spectra of complex 1 at different pH values.

A schematic representation of the formation of the NPs is shown in Scheme 6.1.

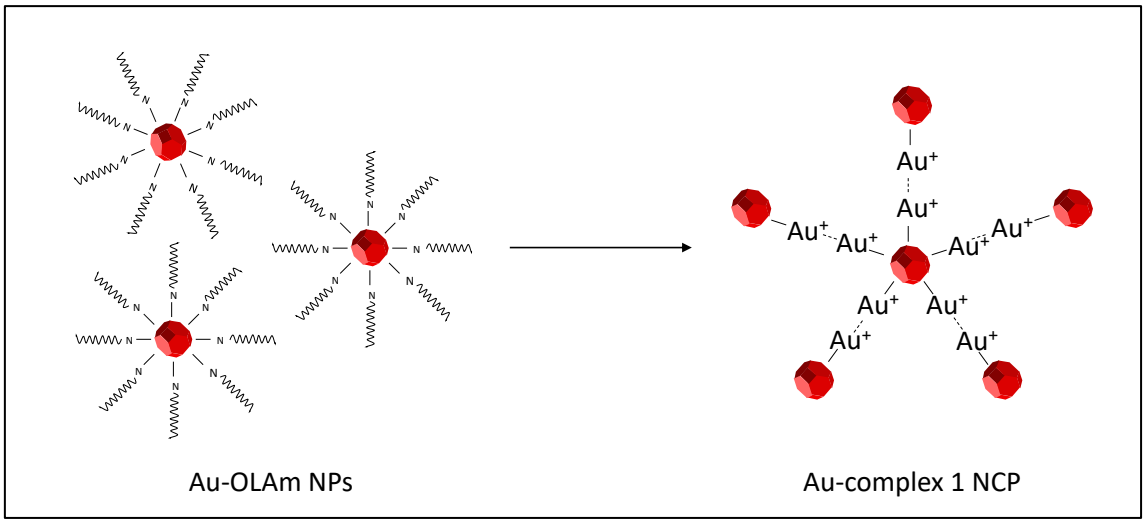

Scheme 6.1: Schematic representation of the formation of Au-complex 1 NCP from Au-OLAm NPs.

Additionally, two series of UV-Vis absorption spectra were recorded to study the formation of the NCPs. Both experiments were done fixing one of the components (complex 1 or Au-OLAm NPs) and by adding small amounts of the other, at pH 7.

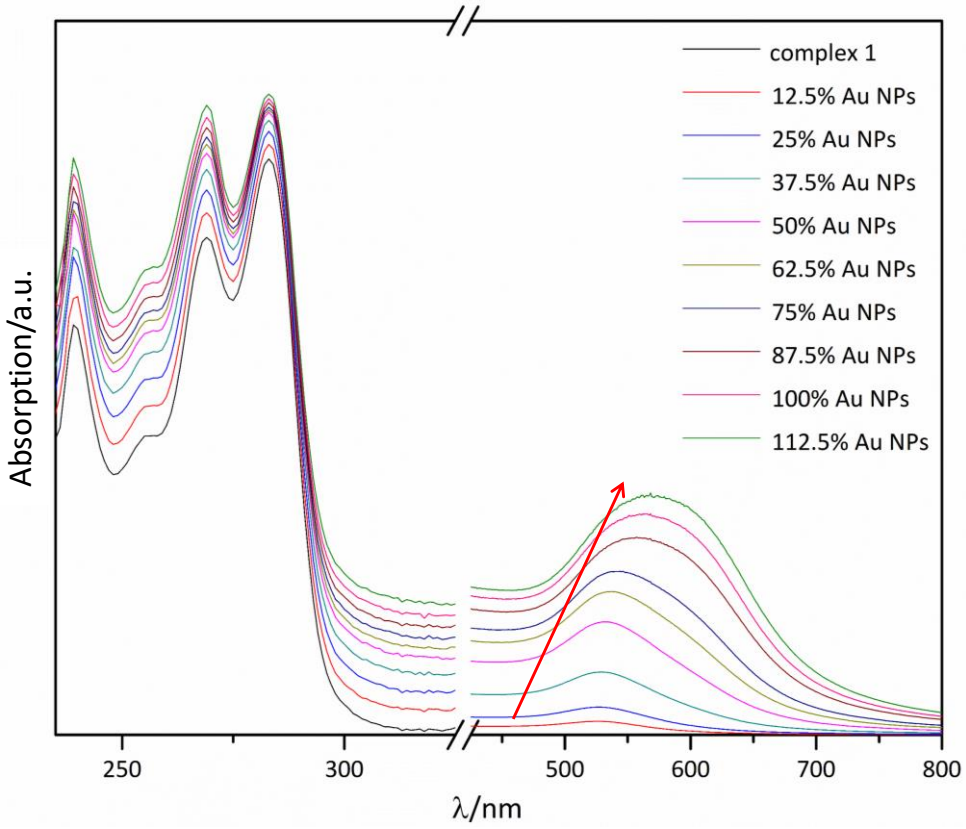

Figure 6.11: UV-Vis absorption spectra of complex 1 with an increasing of amount of Au-OLAm NPs.

Both experiments (Figures 6.11-12) showed clearly the red-shift and broadening of the LSPR bands of gold NPs with the reaction progress, an indicative of the increment of the interactions between the two compounds. In the experiment where the amount of Au-OLAm NPs was increasing, an increment of the intensity of the LSPR band is also observed, because of the increment of the amount of gold NPs in the solution.

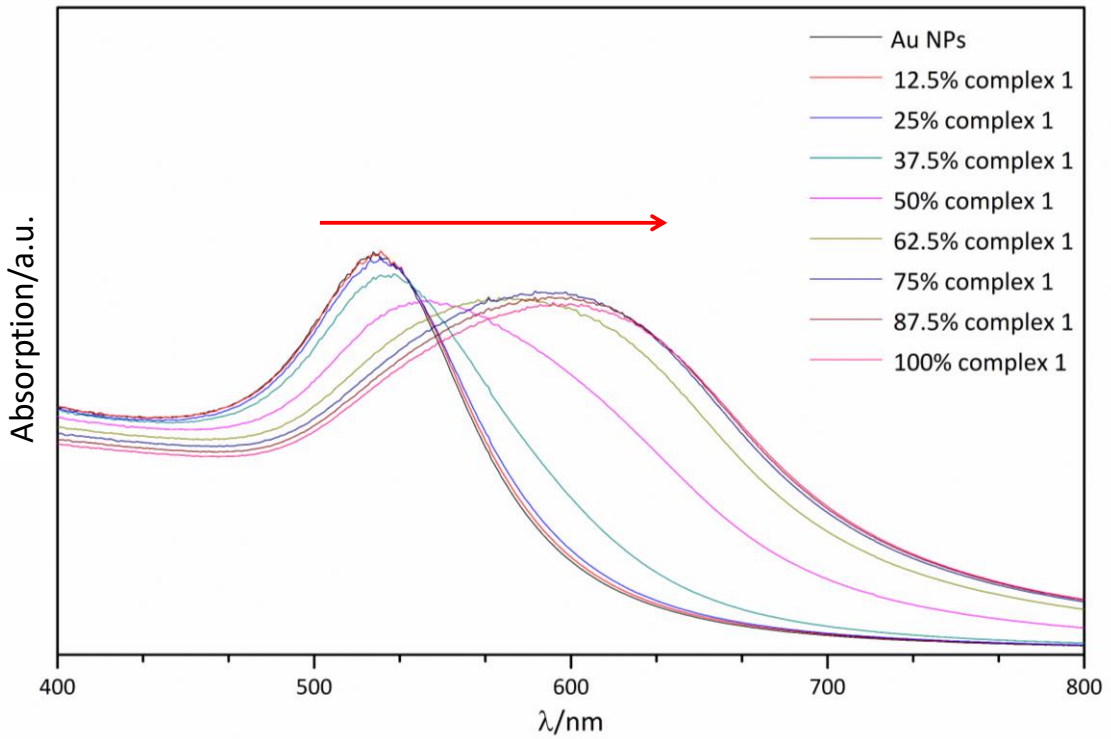

Figure 6.12: UV-Vis absorption spectra of Au-OLAm NPs with an increasing amount of complex 1.

6.5 Synthesis of the NCP with other inorganic nanoparticles

After confirming the successful synthesis of an hydrophilic nanocomposite of Au NPs and complex 1 mainly based on aurophilic interactions, a further study of the possibilities that this kind of interaction could provide was done by performing additional experiments replacing the Au NPs by other types of inorganic nanoparticles. Six different nanosystems of different chemical nature were studied.

Ag-complex 1 NPC

The first nanomaterial studied was OLAm-capped silver NPs, another noble metal. The procedure of synthesis was the same as the one used for Au-complex 1 NCP. Ag-OLAm NPs were quasi spherical and about 10 nm, as can be observed in TEM image of Figure 6.13A. The behaviour of this system was similar to the Au-complex 1 NCP. TEM and

SEM images and DLS measurements of Figure 6.13B-C and 6.14 show the formation of hydrophilic colloidally stable aggregates, formed as a result of the interaction between the Ag NPs and complex 1. However, this NCP was not as stable as Au-complex 1 NCP and DLS measurements clearly showed a broader distribution of aggregates sizes, going from 75 nm to 500 nm.

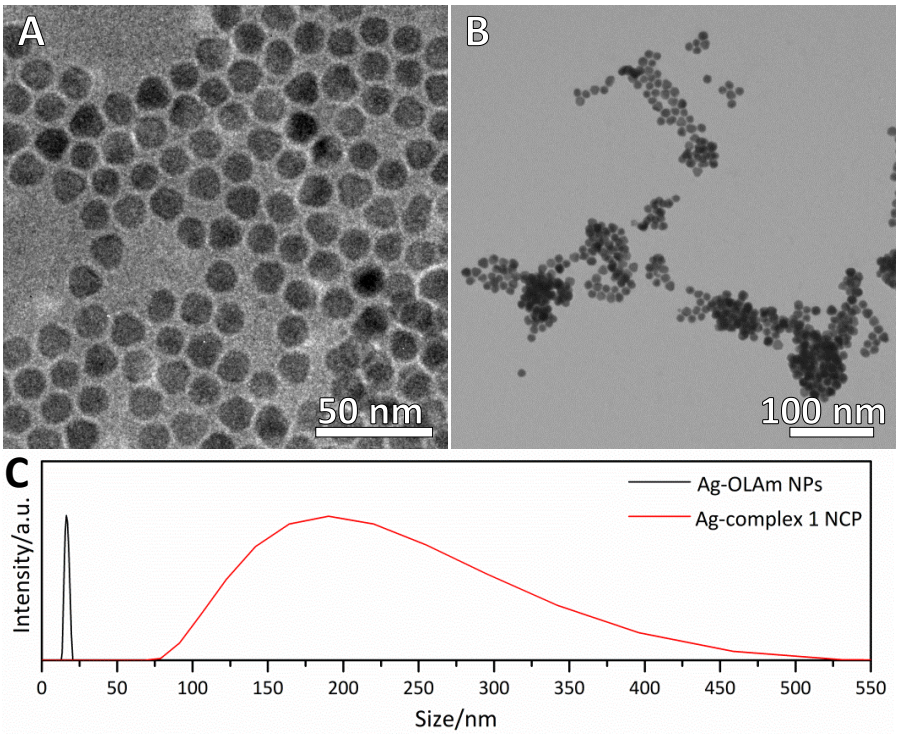

Figure 6.13: TEM micrograph of (A) hydrophobic Ag-OLAm NPs and (B) Ag-complex 1 NCP. (C) DLS measurements of Ag-OLAm NPs (black) and Ag-complex 1 NCP (red).

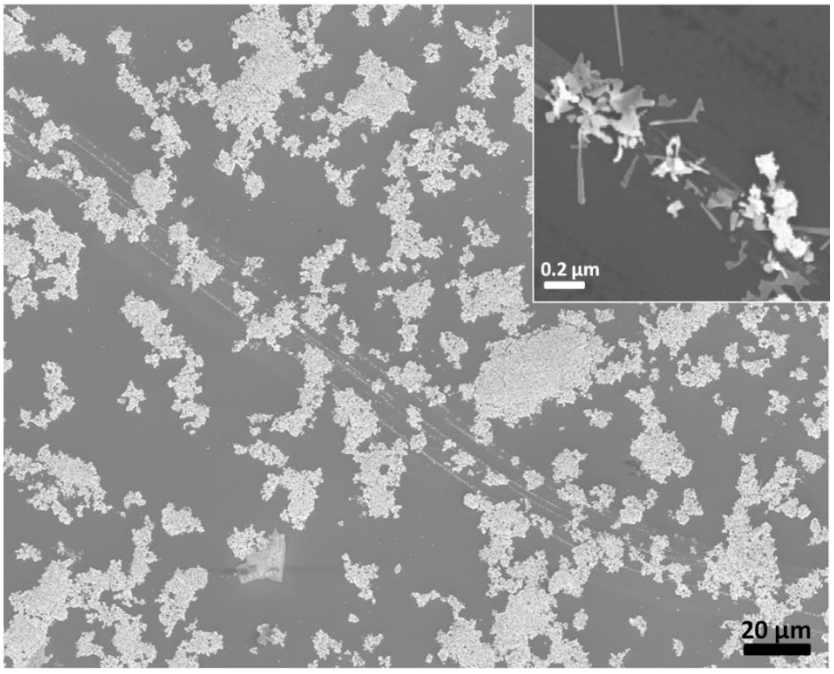

Figure 6.14: FESEM images of Ag-complex 1 NCP.

IR spectroscopy demonstrates (Figure 6.15) the substitution of OLAm for complex 1 in Ag-complex 1 NCP. OLAm characteristic peaks were significantly reduced whereas the peaks from complex 1 could be observed, even though the resolution of stretching C=N and C=O peaks was not clear in the spectra.

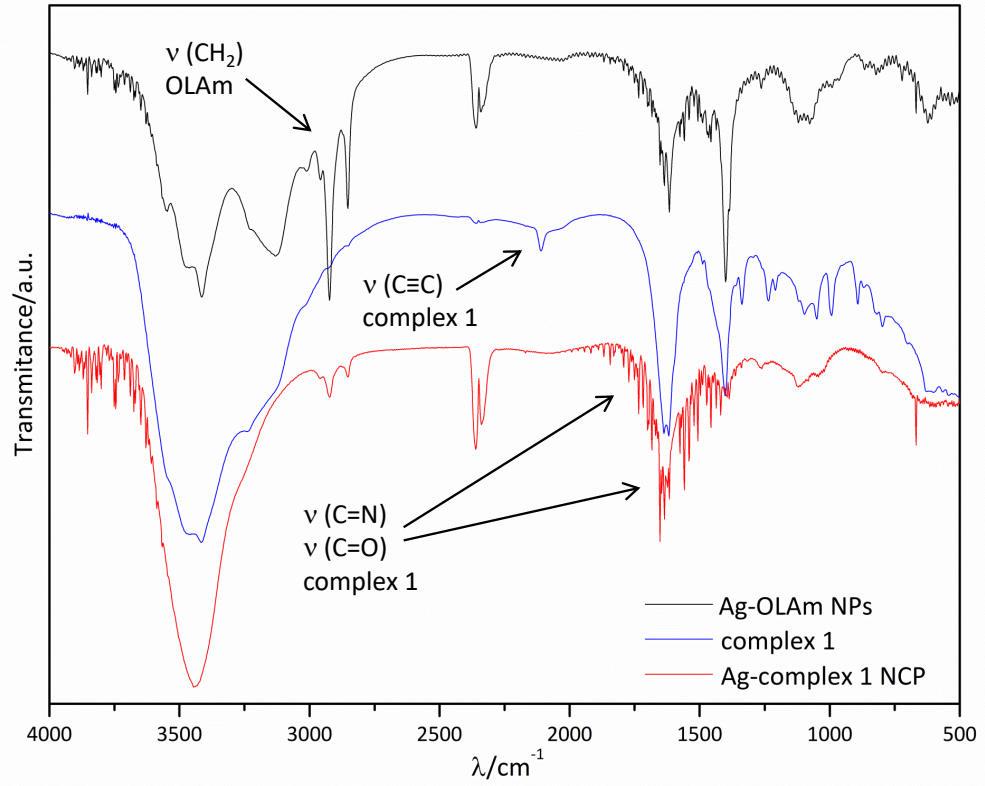

Figure 6.15: IR spectra of Ag-OLAm NPs (black), free complex 1 (blue) and Ag-complex 1 NCP (red).

To better corroborate the presence of complex 1 in the NCP, XPS was done (Figure 6.16). This technique showed the existence of Au(I) in the NCP, which came from complex 1. Apart from that, it also showed the coexistence of Ag(0), as expected from the metallic NPs, and Ag(I). At first sight, the presence of oxidized silver could result curious, but silver NPs usually have their surface partially oxidized. This fact was checked by performing XPS of Ag-OLAm NPs, which also presented the coexistence of the two oxidation states of silver. In this case, aurophilic interactions between the nanoparticle and the complex 1 were not possible; however, metallophilic Ag-Au interactions could play an important role in these assemblies.

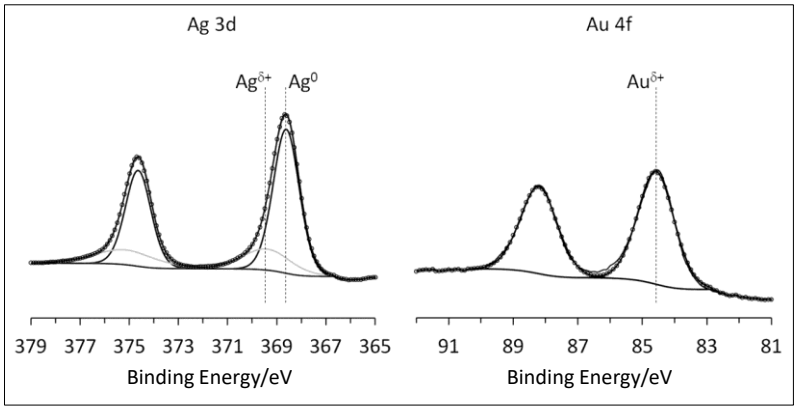

Figure 6.16: XPS spectra of Ag-complex 1 NCP.

UV-Vis absorption spectroscopy was also done for this sample (Figure 6.17). In this case, the NCP presented the characteristic broad band from complex 1 (between 250-300 nm) and the LSPR peak from silver NPs, which are known to present a characteristic LSPR peak at 400 nm. The broad peak, with two shoulders, observed in the spectrum of the NCP could be an indicative of the broad distribution of the aggregates, leading to a broad coupling of the two components in the Ag-complex 1 NCP. However, it is important not to discard the possibility that some part of the absorbance showed between 350 and 800 nm (attributed to the LSPR peak of silver NPs) could be from the dispersion of light, as a consequence of not having the sample completely stable in solution.

Error! Reference source not found.Semiconductor-complex 1 NCP

The next material tested was CdSe NPs, a well-known semiconductor with interesting luminescent-tunning properties. In this case, the unfeasibility of establishing metallophilic interactions lead to a lack of affinity between the surface of NPs and complex 1 and, consequently, analogous hydrophilic nanocomposites could not be obtained.

Interestingly, when other semiconductors with Ag^+ or Au^+ in their chemical formula were used, hybrid NCPs were obtained. It seems that the presence of this cations in the structure of the semiconductors was enough to improve the interactions, leading to the synthesis of the Ag_2Se-complex 1 NCP and Ag_3AuSe_2-complex 1 NCP. In Figure 6.18, the final solutions and DLS measurements of the samples are shown. Both samples presented a broad distribution of sizes, similar to the distribution showed by Ag-complex 1 NCP.

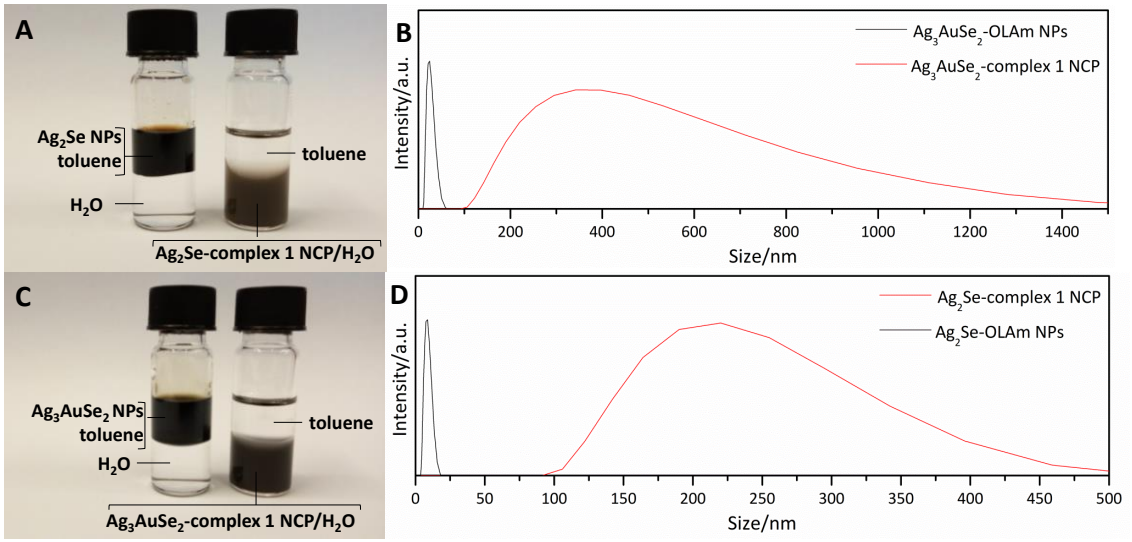

Figure 6.17: (A) Solubility and (B) DLS measurements of the initial hydrophobic Ag_2Se-OLAm NPs and final hydrophilic Ag_2Se-complex 1 NCP. (C) Solubility and (D) DLS measurements of the initial hydrophobic Ag_3AuSe_2-OLAm NPs and final hydrophilic Ag_3AuSe_2-complex 1 NCP.

Magnetic NP-complex 1 NCP

Another family of materials, the magnetic oxide materials, was tested. Specifically, Fe_3O_4 NPs were used. In this case, similar to the CdSe system, it was not possible to obtain the hydrophobic nanocomposite. However, when Fe_3O_4 NPs were coated with an atomic layer of metallic gold, the nanocomposite was formed, as can be observed in Figure 6.19. So, it seems that just an atomic layer of gold was enough to create the aurophilic interactions needed for the formation of the NCP.

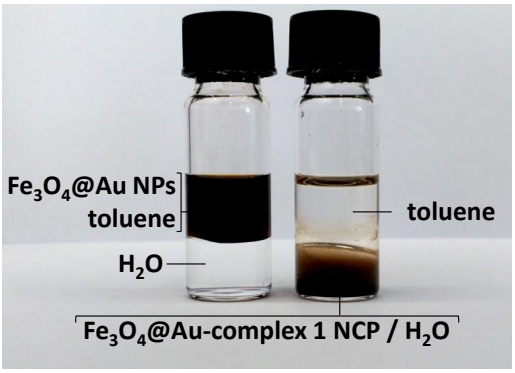

Figure 6.18: Solubility of the initial hydrophobic Fe_3O_4@Au-OLAm NPs and the final hydrophilic Fe_3O_4@Au-complex 1 NCP.

All these experiments with other inorganic nanomaterials consolidate the theory that aurophilic/metallophilic interactions play a key role in the formation of the hydrophilic nanocomposites formed by inorganic NPs and complex 1, opening a wide variety of possibilities for the synthesis of new hybrid nanomaterials.

6.6 Surface-Enhanced Raman Spectroscopy of Au-complex 1 and Ag-complex 1 NCPs

Raman Spectroscopy is a spectroscopic technique in which the sample is illuminated by a monochromatic light and the inelastically scattered photons are used to get information about the low-frequency modes of a molecule. It is well-known to be complementary to IR spectroscopy since the two techniques are governed by different selection rules and different low-frequency modes can be detected.

Surface-enhanced Raman Spectroscopy (SERS) is a variation of the traditional technique that allows the enhancement of the Raman signal, increasing its sensitivity and allowing in some cases the detection of single molecules. This improvement is observed when molecules are attached or close to a surface of a plasmonic nanomaterial.

This phenomenon was first observed in 1973 when McQuillan and co-workers were working with pyridine adsorbed on a roughened silver electrode.[327] However, the effect was not correctly interpreted until 1977 by Van Duyne and co-workers.[328] After some years of research, in 1997, two different groups published the first detections of single-molecules using this technique.[329,330] Since then, several groups have been working on the field and currently, SERS is used in sensing and imaging applications, single molecule detection, catalysis, bioanalytical applications, among others.[331–335]

Understanding the mechanism of this phenomenon is not easy, several mechanisms were proposed in the past and discarded. Nowadays, it is explained by the combination of two contributions: the electromagnetic mechanism and the chemical mechanism.[331,334,336–339]

The electromagnetic mechanism is based on the fact that the electromagnetic field of light can be enhanced and the incident light and the Raman scattered field amplified, when it interacts with a plasmonic surface. As it is well known, when photons of a particular frequency interact with the surface of some nanostructured metals, i.e. Ag, Au or Cu, the cloud of the conduction electrons of the metal start to oscillate following the oscillation of the incident light (Figure 1.3); this effect is known as the LSPR. As it was commented in the first chapter, the excitation of this LSPR has two important consequences: the selective absorption and scattering of the resonant radiation and the generation of a big electromagnetic field at the surface of the NP. In ordinary Raman experiments, the scattered radiation intensity depends on the magnitude of the electromagnetic field incident on the analyte. Nevertheless, when the analyte is close to a plasmonic NP, this is to say when there is SERS effect, the field generated by this LSPR effect is also influential, not only the electromagnetic field. Therefore, the SERS intensity is related to the electromagnetic field outside of the particle and is enhanced by a factor (EF) that can be approximately calculated by a direct comparison

of the intensities provided by the SERS and Raman experiments (Eq. 6.1) and normalized by the total number of molecules (N) in each experiment (Eq. 6.2).

$$EF_{\lambda} = \frac{I_{SERS}}{I_{Raman}} \cdot f \qquad (6.1)$$

$$f = \frac{N_R}{N_{SERS}} \qquad (6.2)$$

The chemical mechanism is related to the adsorption of the analyte to the metal NP surface. In some molecules, the highest occupied (HOMO) and the lowest unoccupied (LUMO) molecular orbitals have a similar energy level than the Fermi level of the metal. Then, a charge-transfer excitation could take place, which could be molecule to metal or metal to molecule (Figure 6.19). Even though the adsorption of the molecule to the NP could change the vibrational pattern due to the change in the molecular symmetry, the molecular orientation and light polarization on the surface of the NP, this charge-transfer excitation could also lead to larger enhanced factors (EF).

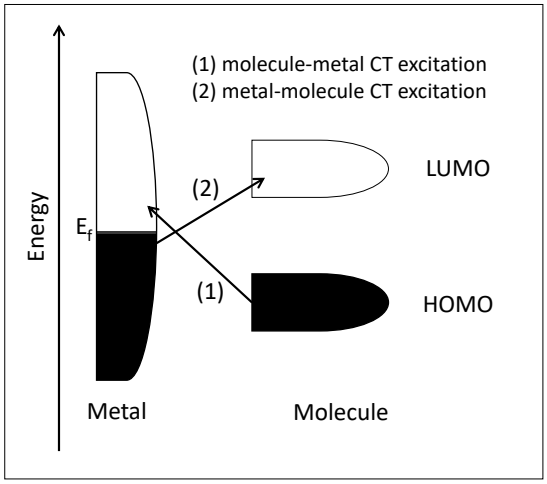

Figure 6.19: Illustration of the energy level diagram of a molecule adsorbed on a metal surface.

The classic plasmonic nanostructures, gold, silver and copper, are the most studied as SERS substrates. All three metals have LSPRs on the visible and near infrared region, where most Raman measurements are done, which make these metals even more convenient. Usually, silver and gold, because of their air stability are more used than copper, which is more reactive. Although gold is more stable and biocompatible, silver is a much more efficient optical enhancer, it presents EFs 2 or 3 orders of magnitude larger than those of gold. Apart from these metallic nanomaterials, other metals such as alkali metals (Li, Na, K, Rb and Cs), Al, Ga, In, Pt, Rh and metal alloys have been also tested as plasmonic substrates for SERS.

Au-complex 1 and Ag-complex 1 NCPs were thought to be suitable candidates to experience SERS effect, due to the presence of the plasmonic NPs. Free complex 1 presents strong fluorescence (Figure 6.1B) which impedes the observation of its Raman

scattering spectrum in its free form. However, the attachment of the molecules to the metallic NPs surface quenched the fluorescence. Hence, in this case, the study of the Raman scattering of complex 1 could be done, even though the low concentration of the molecules on the NCP (<0.1% in weight). Figure 6.21 shows the Raman spectra of Au-complex 1 and Ag-complex 1 NCPs.

In both spectra strong bands are observed at Raman shift of 1550-1600 cm^{-1} corresponding to the carbonyl (C=O) and C=N vibrations. The band at 1200 cm^{-1} is assigned to C–N vibrations and the one at 1000 cm^{-1}, to the C–P vibrations. The fact that silver SERS effect is stronger than the gold SERS effect was verified, as the Raman intensity for the Ag-complex 1 NCP spectrum are around two orders of magnitude higher than those for the Au analogue, measured at same concentration and under the same conditions. Besides, the Raman spectrum of Ag-complex 1 NCP exhibits an extra band at a Raman shift of about 2000-2100 cm^{-1}, which can be assigned to the C≡C vibration of complex 1.

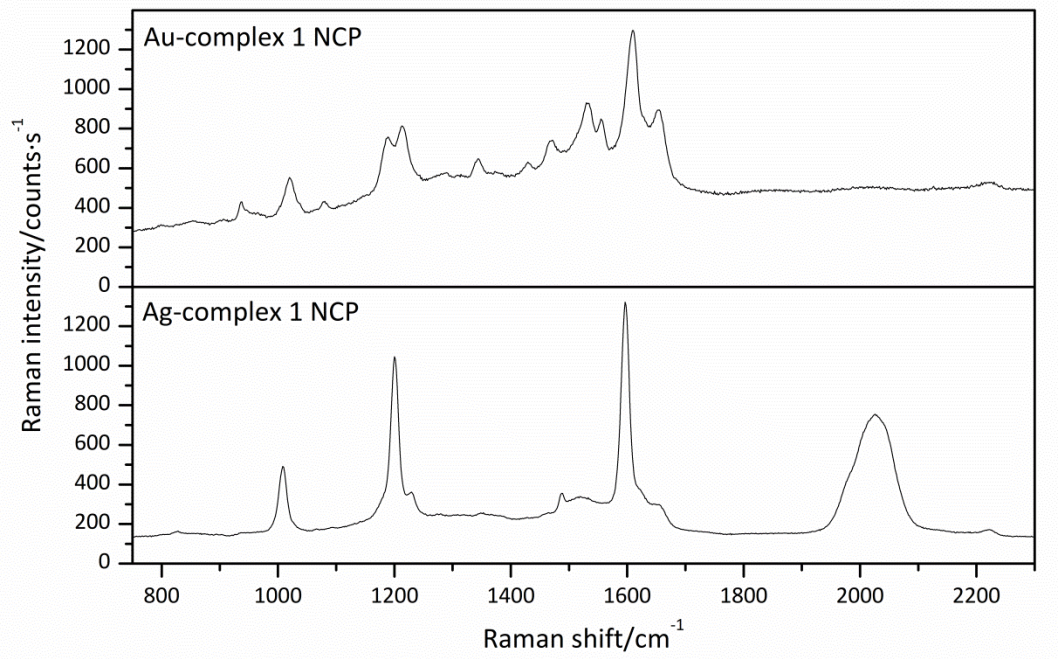

Figure 6.20: Raman spectra of Au-complex 1 NCP (top) and Ag-complex 1 NCP (bottom). The intensity of Au-complex 1 NCP spectrum has been multiplied by 100.

In summary, in this chapter new hydrophilic nanocomposites were synthesised and deeply characterized. The nanocomposites formation was based in the aurophilic/metallophilic interactions between complex 1, which contains an atom of Au(I) and the metallic atoms of the surface of the NPs. The ability of the complex 1 of going through a gelation process, allow the formation of the small aggregates of the NCP that makes them hydrophilic. The adsorption of the molecule on the NPs quenched totally the fluorescence of the molecules and allowed the characterization

of the material by Raman Spectroscopy, which in addition, due to the presence of a plasmonic material in the NCP, was enhanced by SERS effect.

6.7 Experimental part

Chemicals

Gold(III) chloride trihydrate ($HAuCl_4 \cdot 3H_2O$, ≥99.9%), silver nitrate ($AgNO_3$, ≥99%), iron(III) chloride ($FeCl_3$,97%), tetraoctylammonium bromide (TOAB, 98%), oleylamine (OLAm, 70%), oleic acid (OLAc, ≥99%), 1-octadecene (ODE, 90%), methanol (MeOH, ≥99.6%), and toluene (99.9%) were purchased from Sigma–Aldrich. Cadmium oxide (CdO, 99%), selenium powder (Se, 99.99%), silver chloride (AgCl, 99.9%), tri-n-octylphosphine oxide (TOPO, 99%), and tri-n-octylphosphine (TOP, 97%) were obtained from Strem Chemicals. Octadecylphosphonic acid (ODPA, 99%) was purchased from Polycarbon Industries. Sodium oleate (NaOL) was obtained from Tokyo Chemical Industry (TCI). 2-Propanol (iPrOH, for HPLC) and chloroform ($CHCl_3$, 99.2%) were purchased from VWR Chemicals. Absolute ethanol (99.5%), ethanol (EtOH, 96%v/v), and hexane (95%) were obtained from Panreac.

Synthesis of Au NPs (Au-OLAm NPs)

The synthesis of gold NPs was adapted from that described by Yu and co-workers[72] as follows: A mixture of ODE (30 mL), OLAc (4.5 mL), and OLAm (5.5 mL) was stirred in a 100 mL three-necked flask for 20 min at 120^{o}C under a vacuum. Meanwhile, in a glovebox $HAuCl_4 \cdot 3H_2O$ (120 mg, 0.30 mmol) was dissolved in ODE (7.5 mL) and OLAm (1.5 mL) in an auxiliary vial. Once the purge was complete and the system under N_2, the solution of gold precursor was injected into the flask and temperature was fixed at 150^{o}C. After 30 min of reaction, the heating was stopped, and the solution was washed with 2 equivalent volumes of iPrOH, and centrifuged at 4500 rpm for 4min. The product was redispersed in chloroform.

Synthesis of Ag NPs (Ag-OLAm NPs)

The synthesis of silver NPs was based on that reported by Shen and co-workers.[340] Briefly, in a 100 mL three-necked flask, $AgNO_3$ (85 mg, 0.50 mmol) and OLAm (2 mL) were dissolved in toluene (50 mL). Under nitrogen flow, the solution was heated to 110^{o}C and kept at this temperature for 6h. After this time, the mixture was cooled down naturally to room temperature, washed with EtOH (50 mL), and centrifuged for 5 min at 6000 rpm. The precipitate was redispersed in chloroform.

Synthesis of Fe_3O_4 NPs

The synthesis of the iron oxide NPs was based on that described by Park and co-workers.[341] Under a N_2 atmosphere, a mixture of iron oleate solution (5 mL, 1.00 mmol), NaOL (76 mg, 0.25 mmol), OLAc (88.5 mL, 0.25 mmol), and ODE (10 mL) was heated for 1h at 70^{o}C. Immediately thereafter, the temperature was raised to 100^{o}C, and the mixture was heated at a rate of 38^{o}Cmin^{-1} to 318–320^{o}C and kept at this temperature for 30 min. Heating was then stopped, and the crude solution was cooled to room temperature in air and left to stir for an additional 1h. The final solution was washed three times with iPrOH, centrifuging 4 min at 4000 rpm, and redispersing in toluene. The final precipitate was redispersed in chloroform. Iron oleate used as a precursor was prepared previously with $FeCl_3$ and NaOL.

Syntheis of CdSe NPs

The synthesis of the cadmium selenide NPs was performed by using the method published by Carbone and co-workers.[342] In a 25mL three-necked flask under continuous vacuum and stirring, TOPO (3.0 g), ODPA (280 mg, 0.84 mmol), and CdO (60 mg, 0.47 mmol) were heated at 150^{o}C for 2h. After degassing, and once under a N_2 atmosphere, the temperature was set up to 370^{o}C. Once at 300^{o}C, TOP (150 g, 4mmol) was injected into the solution. At 370^{o}C, a solution of Se (58 mg, 0.73 mmol) in TOP (360 mg, 0.97 mmol) was injected. After 15s of the TOP-Se injection, the reaction was stopped by removing the heating mantle and letting the flask cool down naturally. At 100^{o}C, toluene (5 mL) was added to the solution to avoid solidification. Once at room temperature, the solution was washed three times with MeOH, centrifuging 4 minutes at 4500 rpm and redispersing with toluene. Final precipitate was redispersed in chloroform.

Atomic gold coating of iron oxide NPs (Fe_3O_4@Au NPs)

Iron oxide NPs were gold coated by following a procedure published by Bronstein and co-workers.[343] Briefly, a solution of Fe_3O_4 NPs (4 mg), $CHCl_3$ (1 mL), and OLAm (0.8 mL) was stirred for 1h at room temperature. Meanwhile, $HAuCl_4{\cdot}3H_2O$ (98.5 mg, 0.25 mmol) and OLAm (0.2 mL) were dissolved in $CHCl_3$ (1 mL). This solution was added dropwise to the NP solution and stirred for 24 h. The final solution was purified with EtOH and then washed twice with a mixture of EtOH/hexane (5:1). The final precipitate was redispersed in chloroform.

Synthesis of Ag_2Se NPs and Ag_3AuSe_2 NPs

The synthesis of Ag_2Se NPs and Ag_3AuSe_2 NPs was done following the procedure reported in Chapter 2.

Synthesis of Au–complex 1 NCP

The functionalization of Au NPs with complex 1 was performed by a reaction at room temperature in $CHCl_3$. Complex 1 (4.2 mg, 8 mmol) was dissolved in $CHCl_3$ (8 mL) and mixed with a solution of Au NPs (0.17 nmol) in chloroform. The solution was shaken for 2h and centrifuged for 3 min at 4500 rpm. The precipitate was separated by centrifugation and redispersed in water.

The formation of NCPs of complex 1 with inorganic NPs other than Au (Ag NPs, Fe_3O_4 NPs, CdSe NPs, Fe_3O_4@Au NPs, Ag_2Se NPs, and Ag_3AuSe_2 NPs) was adapted from the protocol described above by using Ag/Fe_3O_4/CdSe/Fe_3O_4@Au/Ag_2Se/Ag_3AuSe_2 NPs instead of Au NPs.

Characterization methods

Transmission Electron Microscopy: A Hitachi H800 MP conventional transmission electron microscope equipped with Bioscan Gatan camera and a tungsten filament operating at an acceleration voltage of 200 kV and 3 mm spot size was used for the morphological study of all synthesized nanostructures. The samples were prepared by drop casting and evaporation of the solvent onto carbon-coated 300 mm mesh Cu grids.

Field-emission scanning electron microscopy: FESEM images were recorded with a Zeiss Neon40 scanning electron microscope Crossbeam Station equipped with a field-emission electron source operating at 5kV.

Dynamic Light Scattering: DLS measurements were done in a Zetasizer NanoS Spectrometer using quartz cuvettes.

Infrared Spectroscopy: IR spectra were recorded with a FTIR 520 Nicolet Spectrophotometer. For the measurements, a pellet of a mixture of the sample and KBr was used.

X-ray photoelectron spectroscopy: XPS was performed with a SPECS system equipped with an Al anode XR50 source operating at 150 mW and a Phoibos 150 MCD-9 detector. The pass energy of the hemispherical analyzer was set at 25 eV, and the energy step was set at 0.1 eV. The binding energy (BE) values were referred to the C1 speak at 284.8 eV.

ESI (+) mass spectroscopy: Mass spectra were recorded with a 4800 Plus MALDI TOF/TOF Analyzer Applied Biosystems MDS SCIEX.

UV-Vis absorbance spectroscopy: A Cary 100 Scan 388 Varian UV/Vis spectrophotometer was used with quartz cuvettes for optical characterization.

Raman spectroscopy: Raman spectra were acquired with a Jobin–Yvon Lab Ram HR 800 spectrophotometer coupled with an Olympus BXFM optical microscope by using a λ=532 nm laser.

The compositions and concentrations of the NP solutions were determined by inductively coupled plasma atomic emission spectroscopy (ICP-AES). The measurements were performed with an Optima 3200 RL PerkinElmer spectrometer. For the measurements, 50 mL of the solutions was precipitated in MeOH and redispersed in $CHCl_3$. The solution was evaporated in an oven overnight at 90^{o}C. Aqua regia (2.5 mL) and H_2O_2 (0.7 mL) were added to the precipitate before the vial was sealed and then heated to 90^{o}C for 72 h. The resulting solution was transferred to a 25mL volumetric flask and diluted with Milli-Q water. In the case of Ag_2Se and Ag_3AuSe_2 NPs, HNO_3 was used for the digestion of the samples instead of aqua regia to avoid the precipitation of silver chloride.

Conclusions

This thesis was focused in the design of novel compositionally controlled hybrid and ternary nanostructures and it was divided in six different parts, regarding to the system under study.

In the first part (chapter 2), which was centred in Ag-Au-Se the following conclusions can be extracted:

- a simple room temperature procedure (using pre-synthesised binary semiconductor NPs and a precursor gold solution) was designed for the synthesis of Ag-Au-Se hybrid and ternary materials

- the use of a reducing surfactant (DDA) leads to the total reduction of gold and the formation of a metallic domain, obtaining dimer-like hybrid nanostructures. The reaction time and the concentration of gold in the solution allow to control the structure of the semiconductor domain: the binary semiconductor is maintained when working at low reaction times and low concentrations (synthesis of Au-Ag_2Se HNPs), whereas the formation of the ternary semiconductor is favoured when long reaction times and high concentration of gold are used (synthesis of Au-Ag_3AuSe_2 HNPs).

- the use of a non-reducing surfactant (TOAB) avoids the formation of the metallic domain, leading to the synthesis of Ag_3AuSe_2 NPs

- Au(III) cations were suggested to be reduced by two different mechanisms. On the one side, the reduction to Au(0) and the formation of the metallic domain are driven by a reducing agent: the amine. On the other side, the reduction to Au(I) and the formation of the ternary material are induced by the Se^{2-} anions, which, consequently are oxidized to elemental selenium and originate an amorphous shell

- Au-Ag_3AuSe_2 HNPs can be also synthesised from the reaction of pre-synthesised Ag_2Se NPs and Au NPs in solution, even though more studies are necessary in this part in order to optimize the results. The same combinatory synthesis is not favoured in solid state

- optical characterization of Ag_2Se NPs showed a featureless absorption spectrum. The NPs do not show quantum confinement due to their large size, which is larger than the Bohr diameter

- the absorption spectra of Ag-Au-Se NPs systems show a shoulder around 600 nm, which can have two different origins: the LSPR of the gold domain or an intrinsic feature of the ternary material (Ag_3AuSe_2), still to be clarified

- Ag-Au-Se nanocomposite has a better thermoelectric performance in comparison with the binary semiconductor, even though the thermoelectric figure of merit is below the state-of-the-art

- Ag_3AuSe_2 NPs might be a promising material to be used as CT contrast agent. They show good contrast in CT with low toxicity effect, long blood circulation times and minimal mononuclear phagocyte system retention

The second part (chapter 3), focused in Ag-Au-S systems, leads to the succeeding conclusions:

- the same procedure designed in the former section can be used for the synthesis of Ag-Au-S systems

- three parameters (reaction time, Ag:Au ratio and surfactant) allow the gradual transformation of Ag_2S to Au_2S through sequential cation exchange reactions

- the formation of the metallic domain could not be avoided, even using a non-reducing surfactant, due to the high affinity of gold and sulphur. For instance, Au-Ag_3AuS_2 HNPs and Au-AgAuS HNPs were obtained using both, DDA and TOAB

- the use of a reducing agent permits, when working with low reaction times, the formation of the gold domain without the variation of the binary semiconductor (Au-Ag_2S HPs)

- the use of a non-reducing surfactant allows, when working with low Ag:Au ratios, the complete transformation of Ag_2S to Au_2S, with the formation of Au-Au_2S HNPs and hollow Au_2S NPs

- the presence of high concentration of bromides (when working with a high amount of Au(III)-TOAB complex solution) triggered the precipitation of silver

cations, which accelerate the outward rate of these ions, causing the Kirkendall effect and the formation of hollow nanostructures

- optical characterization of Ag-Au-S systems show similar results to their analogous system with selenide. The featureless absorption of Ag_2S and Au_2S NPs can be associated to the non-quantum confinement of these nanosystems due to their size. Au-Ag_3AuS_2 HNPs and Au-AgAuS HNPs showed a broad band around 600nm, which can be due to the LSPR of metallic domains or to an intrinsic feature of the ternary materials

- a transference from apolar solvents to water of Ag_2S NPs and Ag-Au-S nanostructured systems can be done by a ligand exchange procedure, substituting the oleylamine for an hydrophilic ligand (4-mercaptobenzoic acid)

Four conclusions can be extracted from the third part of this thesis (chapter 4), which was focused in Ag-Cu-S systems:

- a direct synthesis of AgCuS NPs by hot injection method was designed. Four different copper precursors (CuCl, CuI, $Cu(NO_3)_2$ and $CuCl_2$) can be used to obtain similar results in terms of morphology and crystallographic structure. However, Cu(I) precursors guarantee a better crystallinity in the final ternary system.

- two different mechanisms for the formation of AgCuS NPs were reported. The use of Cu(I) and Cu(II) chlorides as copper precursors lead to an early formation of Ag_2S NPs, which go through a gradual transformation, by cation exchange, to Ag_3CuS_2 and finally to AgCuS. The use of CuI favours the formation of Cu_2S and Ag_2S and the subsequent reaction of them to form directly the AgCuS

- AgCuS NPs show the two expected phase transitions of the material, going through a first phase transition from orthorhombic to hexagonal phase between 50 and 75°C and through a second phase transition from the hexagonal to the cubic phase between 175 and 200°C

- the synthesised AgCuS NPs does not show a good thermoelectric performance. Even though it presents acceptable thermal conductivity and Seebeck coefficients, it is not enough to compensate the low electrical conductivity values

In the fourth part (chapter 5), which was centred in Pt-Cu-Se systems, the following conclusions have been extracted:

- four different nanostructured materials, based on Pt, Cu and Se, were synthesised by a reaction between pre-synthesised $Cu_{2-x}Se$ NPs and a Pt(II) precursor in a hybrophobic medium and at high temperature,
- two different phases are formed, one Se-rich and another Pt-rich when working with small Pt:Cu ratios. These phases tend to homogenize to ternary Pt-Cu-Se phases when the amount of platinum is increased. If the amount of platinum is increased even more, the selenium is expelled of the material to lead to the formation of core-shell nanostructures, composed by a Pt shell and a Cu-containing core

- the optical characterization of the materials shows the well-known plasmonic band of Cu_2Se NPs, which is completely damped with the introduction of platinum in the structure

Finally, in the last part of the thesis (chapter 6), focused in the synthesis of an hybrid inorganic-organic nanostructured material, three conclusions can be reported:

- a room temperature procedure has been designed for the synthesis of an hybrid inorganic-organic nanocomposite formed by inorganic NPs (Au, Ag, Ag_3AuSe_2 and $Au@Fe_3O_4$) and a highly fluorescent low molecular weight Au(I) metallogelator. These NCPs are stable in water and alcohol solutions for a long period of time, at different temperatures and pH media

- the NCPs are composed by small aggregates of the inorganic nanoparticles surrounded by a shell of the metallorganic complex. The absorption spectroscopy studies of the NCPs at different pH, indicate the metallophilic interactions are one of the driving forces for the formation of these NCPs

- the coupling of the two building blocks of the NCPs are thought to be enhanced at neutral pH media, when the ability to create aurophilic interactions of the metallogelator is stronger

- Au-complex 1 NCP and Ag-complex 1 NCP can be used as enhancers in Raman spectroscopy (SERS effect). The strong coupling between the plasmonic nanomaterial and the Au(I) complex quenches the fluorescence of the latter and the Raman vibrations from the organic moiety can be detected even if its concentration in the sample is very low

References

(1) Poole, C. P.; Owens, F. J. *Introduction to nanotechnology*, 1st ed.; John Willey & Sons, Inc.: Hoboken, New Jersey, 2003.

(2) Faraday, M. *Philos. Trans. R. Soc. London* **1857**, *147* (0), 145–181.

(3) Burda, C.; Chen, X.; Narayanan, R.; El-Sayed, M. A. *Chem. Rev.* **2005**, *105* (4), 1025–1102.

(4) Mout, R.; Moyano, D. F.; Rana, S.; Rotello, V. M. *Chem. Soc. Rev.* **2012**, *41* (7), 2539–2544.

(5) Kundu, S.; Patra, A. *Chem. Rev.* **2017**, *117* (2), 712–757.

(6) Wu, W. *Nanoscale* **2017**, *9* (22), 7342–7372.

(7) Gong, S.; Cheng, W. *Adv. Electron. Mater.* **2017**, *3* (3), 1600314.

(8) Segev-Bar, M.; Haick, H. *ACS Nano* **2013**, *7* (10), 8366–8378.

(9) Kuno, M. *Introductory Nanoscience*, 1st ed.; Garland Science, Taylor & Francis Group, LLC: New York, 2012.

(10) Smith, A. M.; Nie, S. *Acc. Chem. Res.* **2010**, *43* (2), 190–200.

(11) Gaponik, N.; Hickey, S. G.; Dorfs, D.; Rogach, A. L.; Eychmüller, A. *Small* **2010**, *6* (13), 1364–1378.

(12) Jun, Y. W.; Seo, J. W.; Sang, J. O.; Cheon, J. *Coord. Chem. Rev.* **2005**, *249*, 1766–1775.

(13) Rogach, A. L.; Eychmüller, A.; Hickey, S. G.; Kershaw, S. V. *Small* **2007**, *3* (4), 536–557.

(14) Bera, D.; Qian, L.; Tseng, T.-K.; Holloway, P. H. *Materials (Basel).* **2010**, *3* (4), 2260–2345.

(15) Nozik, A. J.; Beard, M. C.; Luther, J. M.; Law, M.; Ellingson, R. J.; Johnson, J. C. *Chem. Rev.* **2010**, *110* (11), 6873–6890.

(16) Carey, G. H.; Abdelhady, A. L.; Ning, Z.; Thon, S. M.; Bakr, O. M.; Sargent, E. H. *Chem. Rev.* **2015**, *115* (23), 12732–12763.

(17) Kramer, I. J.; Sargent, E. H. *Chem. Rev.* **2014**, *114*, 863–882.

(18) Kramer, I. J.; Sargent, E. H. *ACS Nano* **2011**, *5* (11), 8506–8514.

(19) Shirasaki, Y.; Supran, G. J.; Bawendi, M. G.; Bulović, V. *Nat. Photonics* **2013**, *7* (1), 13–23.

(20) Qasim, K.; Lei, W.; Li, Q. *J. Nanosci. Nanotechnol.* **2013**, *13* (5), 3173–3185.

(21) Wang, Y.; Sun, H. *Prog. Quantum Electron.* **2018**, *60* (May), 1–29.

(22) Talapin, D. V; Lee, J.-S.; Kovalenko, M. V; Shevchenko, E. V. *Chem. Rev.* **2010**, *110* (1), 389–458.

(23) Kershaw, S. V.; Jing, L.; Huang, X.; Gao, M.; Rogach, A. L. *Mater. Horizons* **2017**, *4* (2), 155–205.

(24) Freeman, R.; Willner, I. *Chem. Soc. Rev.* **2012**, *41* (10), 4067–4085.

(25) Frasco, M. F.; Chaniotakis, N. *Sensors* **2009**, *9* (9), 7266–7286.

(26) Zhou, J.; Yang, Y.; Zhang, C. Y. *Chem. Rev.* **2015**, *115* (21), 11669–11717.

(27) Jamieson, T.; Bakhshi, R.; Petrova, D.; Pocock, R.; Imani, M.; Seifalian, A. M. *Biomaterials* **2007**, *28* (31), 4717–4732.

(28) Wegner, K. D.; Hildebrandt, N. *Chem. Soc. Rev.* **2015**, *44* (14), 4792–4834.

(29) Aldakov, D.; Lefrançois, A.; Reiss, P. *J. Mater. Chem. C* **2013**, *1* (24), 3756–3776.

(30) Lu, J.; Liu, H.; Zhang, X.; Sow, C. H. *Nanoscale* **2018**, *10*, 17456–17476.

(31) Regulacio, M. D.; Han, M.-Y. *Acc. Chem. Res.* **2016**, *49* (3), 511–519.

(32) Chen, M. M.; Xue, H. G.; Guo, S. P. *Coord. Chem. Rev.* **2018**, *368*, 115–133.

(33) Stroyuk, O.; Raevskaya, A.; Gaponik, N. *Chem. Soc. Rev.* **2018**, *47* (14), 5354–5422.

(34) Chen, B.; Pradhan, N.; Zhong, H. *J. Phys. Chem. Lett.* **2018**, *9* (2), 435–445.

(35) Kolny-Olesiak, J.; Weller, H. *ACS Appl. Mater. Interfaces* **2013**, *5* (23), 12221–12237.

(36) Cheshme Khavar, A. H.; Mahjoub, A. R.; Fakhri, H. *J. Inorg. Organomet. Polym. Mater.* **2016**, *26* (5), 1075–1086.

(37) Stanbery, B. J. *Crit. Rev. Solid State Mater. Sci.* **2002**, *27* (2), 73–117.

(38) Kessler, F.; Herrmann, D.; Powalla, M. *Thin Solid Films* **2005**, *480–481*, 491–498.

(39) Jackson, P.; Hariskos, D.; Wuerz, R.; Kiowski, O.; Bauer, A.; Friedlmeier, T. M.; Powalla, M. *Phys. Status Solidi - Rapid Res. Lett.* **2015**, *9* (1), 28–31.

(40) Khare, A.; Wills, A. W.; Ammerman, L. M.; Norris, D. J.; Aydil, E. S. *Chem. Commun.* **2011**, *47* (42), 11721–11723.

(41) Danilson, M.; Kask, E.; Pokharel, N.; Grossberg, M.; Kauk-Kuusik, M.; Varema, T.; Krustok, J. *Thin Solid Films* **2015**, *582*, 162–165.

(42) Zhou, H.; Hsu, W. C.; Duan, H. S.; Bob, B.; Yang, W.; Song, T. Bin; Hsu, C. J.; Yang, Y. *Energy Environ. Sci.* **2013**, *6* (10), 2822–2838.

(43) Wang, C.; Daimon, H.; Lee, Y.; Kim, J.; Sun, S. *J. Am. Chem. Soc.* **2007**, *129* (22), 6974–6975.

(44) Markovic, N. .; Schmidt, T. J.; Stamenkovic, V.; Ross, P. N. *Fuel Cells* **2001**, *1* (2), 105–116.

(45) Chen, J.; Lim, B.; Lee, E. P.; Xia, Y. *Nano Today* **2009**, *4* (1), 81–95.

(46) Wang, C.; Astruc, D. *Chem. Soc. Rev.* **2014**, *43* (20), 7188–7216.

(47) Wang, C.; Yin, H.; Chan, R.; Peng, S.; Dai, S.; Sun, S. *Chem. Mater.* **2009**, *21* (3), 433–435.

(48) Mayer, K. M.; Hafner, J. H. *Chem. Rev.* **2011**, *111* (6), 3828–3857.

(49) Motl, N. E.; Smith, A. F.; DeSantis, C. J.; Skrabalak, S. E. *Chem. Soc. Rev.* **2014**, *43* (11), 3823–3834.

(50) Nguyen, B. H.; Nguyen, V. H. *Adv. Nat. Sci. Nanosci. Nanotechnol.* **2015**, *6* (4), 43001.

(51) Wang, C.; Astruc, D. *Chem. Soc. Rev.* **2014**, *43* (20), 7188–7216.

(52) Doria, G.; Conde, J.; Veigas, B.; Giestas, L.; Almeida, C.; Assunção, M.; Rosa, J.; Baptista, P. V. *Sensors* **2012**, *12* (2), 1657–1687.

(53) Saha, K.; Agasti, S. S.; Kim, C.; Li, X.; Rotello, V. M. *Chem. Rev.* **2012**, *112* (5), 2739–2779.

(54) Guo, S.; Wang, E. *Nano Today* **2011**, *6* (3), 240–264.

(55) Jain, P. K.; Huang, X.; El-Sayed, I. H.; El-Sayed, M. A. *Acc. Chem. Res.* **2008**, *41* (12), 1578–1586.

(56) Arvizo, R. R.; Bhattacharyya, S.; Kudgus, R. a; Giri, K.; Bhattacharya, R.; Mukherjee, P. *Chem. Soc. Rev.* **2012**, *41* (7), 2943–2970.

(57) Boisselier, E.; Astruc, D. *Chem. Soc. Rev.* **2009**, *38* (6), 1759–1782.

(58) Sau, T. K.; Rogach, A. L.; Jäckel, F.; Klar, T. A.; Feldmann, J. *Adv. Mater.* **2010**, *22* (16), 1805–1825.

(59) Linic, S.; Christopher, P.; Ingram, D. B. *Nat. Mater.* **2011**, *10* (12), 911–921.

(60) Huang, J. A.; Luo, L. B. *Adv. Opt. Mater.* **2018**, *6* (8), 1701282.

(61) Carbone, L.; Cozzoli, P. D. *Nano Today* **2010**, *5* (5), 449–493.

(62) de Mello Donegá, C. *Chem. Soc. Rev.* **2011**, *40* (3), 1512–1546.

(63) Cozzoli, P. D.; Pellegrino, T.; Manna, L. *Chem. Soc. Rev.* **2006**, *35*, 1195–1208.

(64) Costi, R.; Saunders, A. E.; Banin, U. *Angew. Chem. Int. Ed. Engl.* **2010**, *49* (29), 4878–4897.

(65) Cortie, M. B.; McDonagh, A. M. *Chem. Rev.* **2011**, *111* (6), 3713–3735.

(66) Mastria, R.; Rizzo, A. *J. Mater. Chem. C* **2016**, *4* (27), 6430–6446.

(67) Selinsky, R. S.; Ding, Q.; Faber, M. S.; Wright, J. C.; Jin, S. *Chem. Soc. Rev.* **2013**, *42*, 2963–2985.

(68) Prusty, G.; Guria, A. K.; Mondal, I.; Dutta, A.; Pal, U.; Pradhan, N. *Angew. Chemie - Int. Ed.* **2016**, *55*, 2705–2708.

(69) Zhong, H.; Zhou, Y.; Yang, Y.; Yang, C.; Li, Y. *J. Phys. Chem. C* **2007**, *111*, 6538–6543.

(70) Kim, M. R.; Xu, Z.; Chen, G.; Ma, D. *Chem. - A Eur. J.* **2014**, *20* (36), 11256–11275.

(71) Enright, M. J.; Cossairt, B. M. *Chem. Commun.* **2018**, *54* (52), 7109–7122.

(72) Yu, H.; Chen, M.; Rice, P. M.; Wang, S. X.; White, R. L.; Sun, S. *Nano Lett.* **2005**, *5*, 379–382.

(73) Tian, X.; Zhang, L.; Yang, M.; Bai, L.; Dai, Y.; Yu, Z.; Pan, Y. *Wiley Interdiscip. Rev. Nanomedicine Nanobiotechnology* **2018**, *10* (1), 1476.

(74) Banin, U.; Ben-Shahar, Y.; Vinokurov, K. *Chem. Mater.* **2014**, *26* (1), 97–110.

(75) Mokari, T.; Rothenberg, E.; Popov, I.; Costi, R.; Banin, U. *Science* **2004**, *304* (5678), 1787–1790.

(76) Yang, G.; Liu, H.; Kong, X.; Lv, P.; Sun, Y.; Wang, Z.; Yuan, Z.; Yang, J. *Colloids Surfaces A Physicochem. Eng. Asp.* **2017**, *520*, 722–728.

(77) Dorfs, D.; Franzi, T.; Osovsky, R.; Brumer, M.; Lifshitz, E.; Klar, T. A.; Eychmüller, A. *Small* **2008**, *4* (8), 1148–1152.

(78) He, Z.; Meng, X. *J. Mater. Sci. Mater. Electron.* **2013**, *24* (9), 3365–3370.

(79) Shi, W.; Zeng, H.; Sahoo, Y.; Ohulchanskyy, T. Y.; Ding, Y.; Wang, Z. L.; Swihart, M.; Prasad, P. N. *Nano Lett.* **2006**, *6* (4), 875–881.

(80) Hodges, J. M.; Biacchi, A. J.; Schaak, R. E. *ACS Nano* **2014**, *8* (1), 1047–1055.

(81) Yang, J.; Elim, H. I.; Zhang, Q. B.; Lee, J. Y.; Ji, W. *J. Am. Chem. Soc.* **2006**, *128* (36), 11921–11926.

(82) Hu, W.; Liu, H.; Ye, F.; Ding, Y.; Yang, J. *CrystEngComm* **2012**, *14* (20), 7049–7054.

(83) Fernàndez-Altable, V.; Dalmases, M.; Falqui, A.; Casu, A.; Torruella, P.; Estradé, S.; Peiró, F.; Figuerola, A. *Chem. Mater.* **2015**, *27* (5), 1656–1664.

(84) Costi, R.; Saunders, A. E.; Elmalem, E.; Salant, A.; Banin, U. *Nano Lett.* **2008**, *8* (2), 637–641.

(85) Lindsay, S. M. *Introduction to Nanoscience*, First Edit.; Oxford University Press Inc.: New York.

(86) Murray, C. B.; Norris, D. J.; Bawendi, M. G. *J. Am. Chem. Soc.* **1993**, *115* (19), 8706–8715.

(87) LaMer, V. K.; Dinegar, R. H. *J. Am. Chem. Soc.* **1950**, *72* (11), 4847–4854.

(88) Kwon, S. G.; Hyeon, T. *Small* **2011**, *7* (19), 2685–2702.

(89) Yin, Y.; Alivisatos, A. P. *Nature* **2005**, *437* (7059), 664–670.

(90) Murray, C. B.; Kagan, C. R.; Bawendi, M. G. *Annu. Rev. Mater. Sci.* **2000**, *30*, 545–610.

(91) Van Embden, J.; Chesman, A. S. R.; Jasieniak, J. J. *Chem. Mater.* **2015**, *27* (7), 2246–2285.

(92) Rivest, J. B.; Jain, P. K. *Chem. Soc. Rev.* **2013**, *42*, 89–96.

(93) Beberwyck, B. J.; Surendranath, Y.; Alivisatos, A. P. *J. Phys. Chem. C* **2013**, *117*, 19759–19770.

(94) De Trizio, L.; Manna, L. *Chem. Rev.* **2016**, *116* (18), 10852–10887.

(95) Gupta, S.; Kershaw, S. V.; Rogach, A. L. *Adv. Mater.* **2013**, *25* (48), 6923–2944.

(96) De Trizio, L.; Prato, M.; Genovese, A.; Casu, A.; Povia, M.; Simonutti, R.; Alcocer, M. J. P.; D'Andrea, C.; Tassone, F.; Manna, L. *Chem. Mater.* **2012**, *24* (12), 2400–2406.

(97) Ramasamy, P.; Kim, M.; Ra, H. S.; Kim, J.; Lee, J. S. *Nanoscale* **2016**, *8* (15), 7906–7913.

(98) Lox, J. F. L.; Dang, Z.; Dzhagan, V. M.; Spittel, D.; Martín-García, B.; Moreels, I.; Zahn, D. R. T.; Lesnyak, V. *Chem. Mater.* **2018**, *30* (8), 2607–2617.

(99) Wang, Y.-X.; Wei, M.; Fan, F.-J.; Zhuang, T.-T.; Wu, L.; Yu, S.-H.; Zhu, C.-F. *Chem. Mater.* **2014**, *26* (19), 5492–5498.

(100) Mocatta, D.; Cohen, G.; Schattner, J.; Millo, O.; Rabani, E.; Banin, U. *Science (80-.).* **2011**, *332* (6025), 77–81.

(101) Zhang, J.; Di, Q.; Liu, J.; Bai, B.; Liu, J.; Xu, M.; Liu, J. *J. Phys. Chem. Lett.* **2017**, *8* (19), 4943–4953.

(102) Robinson, R. D.; Sadtler, B.; Demchenko, D. O.; Erdonmez, C. K.; Wang, L.-W.; Alivisatos, A. P. *Science (80-.).* **2007**, *317*, 355–358.

(103) Sadtler, B.; Demchenko, D. O.; Zheng, H.; Hughes, S. M.; Merkle, M. G.; Dahmen, U.; Wang, L.; Alivisatos, A. P. *J. Am. Chem. Soc.* **2009**, *131* (18), 5285–5293.

(104) Casavola, M.; Van Huis, M. A.; Bals, S.; Lambert, K.; Hens, Z.; Vanmaekelbergh, D. *Chem. Mater.* **2012**, *24* (2), 294–302.

(105) Fenton, J. L.; Steimle, B. C.; Schaak, R. E. *J. Am. Chem. Soc.* **2018**, *140* (22), 6771–6775.

(106) Lee, D.; Kim, W. D.; Lee, S.; Bae, W. K.; Lee, S.; Lee, D. C. *Chem. Mater.* **2015**, *27* (15), 5295–5304.

(107) Saruyama, M.; So, Y.; Kimoto, K.; Taguchi, S.; Kanemitsu, Y.; Teranishi, T. *J. Am. Chem. Soc.* **2011**, *133*, 17598–17601.

(108) Nedelcu, G.; Protesescu, L.; Yakunin, S.; Bodnarchuk, M. I.; Grotevent, M. J.; Kovalenko, M. V. *Nano Lett.* **2015**, *15*, 5635–5640.

(109) West, A. R. *Solid State Chemistry and its applications*, Second Edi.; Sons, J. W. &, Ed.; Chichester, 2014.

(110) Tubtimtae, A.; Lee, M. W.; Wang, G. J. *J. Power Sources* **2011**, *196* (15), 6603–6608.

(111) Tian, Q.; Deng, D.; Zhang, Z.; Li, Y.; Yang, Y.; Guo, X. *J. Mater. Sci.* **2017**, *52* (20), 12131–12140.

(112) Shen, H.; Jiao, X.; Oron, D.; Li, J.; Lin, H. *J. Power Sources* **2013**, *240*, 8–13.

(113) Hu, H.; Ding, J.; Zhang, S.; Li, Y.; Bai, L.; Yuan, N. *Nanoscale Res. Lett.* **2013**, *8*, 10.

(114) Perez-Taborda, J. A.; Caballero-Calero, O.; Vera-Londono, L.; Briones, F.; Martin-Gonzalez, M. *Adv. Energy Mater.* **2018**, *8* (8), 1702024.

(115) Xiao, C.; Xu, J.; Li, K.; Feng, J.; Yang, J.; Xie, Y. *J. Am. Chem. Soc.* **2012**, *134* (9), 4287–4293.

(116) Cadavid, D.; Ibáñez, M.; Shavel, A.; Durá, O. J.; López de la Torre, M. a.; Cabot, A.

J. Mater. Chem. A **2013**, *1* (15), 4864–4870.

(117) Yang, S.; Cho, K.; Yun, J.; Choi, J.; Kim, S. *Thin Solid Films* **2017**, *641*, 65–68.

(118) Jiang, W.; Wu, Z.; Zhu, Y.; Tian, W.; Liang, B. *Appl. Surf. Sci.* **2018**, *427*, 1202–1216.

(119) Liu, X.; Liu, Z.; Lu, J.; Wu, X.; Chu, W. *J. Colloid Interface Sci.* **2014**, *413*, 17–23.

(120) Meng, Z. Da; Zhao, W.; Kim, S. *Electron. Mater. Lett.* **2017**, *13* (6), 518–526.

(121) Mishra, S.; Du, D.; Jeanneau, E.; Dappozze, F.; Guillard, C.; Zhang, J.; Daniele, S. *Chem. Asian J.* **2016**, *11* (11), 1658–1663.

(122) Lin, Z.-H.; Shih, Z.-Y.; Roy, P.; Chang, H.-T. *Chem. Eur. J.* **2012**, *18* (39), 12330–12336.

(123) Xu, R.; Husmann, A.; Rosenbaum, T. F.; Saboungi, M. L.; Enderby, J. E.; Littlewood, P. B. *Nature* **1997**, *390* (6655), 57–59.

(124) Janek, J.; Mogwitz, B.; Beck, G.; Kreutzbruck, M.; Kienle, L.; Korte, C. *Prog. Solid State Chem.* **2004**, *32* (3–4), 179–205.

(125) Jang, J.; Pan, F.; Braam, K.; Subramanian, V. *Adv. Mater.* **2012**, *24*, 3573–3576.

(126) Jang, J. *AIP Adv.* **2016**, *6* (7), 75006.

(127) Nam, K.-H.; Kim, J.-H.; Cho, W.-J.; Chung, H.-B. *Appl. Phys. Lett.* **2013**, *102*, 192106.

(128) Batabyal, S. K.; Vittal, J. J. *Chem. Mater.* **2008**, *20* (18), 5845–5850.

(129) Husmann, A.; Betts, J. B.; Boebinger, G. S.; Migliori, A.; Rosenbaum, T. F.; Saboungi, M.-L. *Nature* **2002**, *417*, 421–424.

(130) Park, Y.; Jeong, S.; Kim, S. *J. Photochem. Photobiol. C Photochem. Rev.* **2017**, *30*, 51–70.

(131) Argueta-Figueroa, L.; Martínez-Alvarez, O.; Santos-Cruz, J.; Garcia-Contreras, R.; Acosta-Torres, L. S.; de la Fuente-Hernández, J.; Arenas-Arrocena, M. C. *Mater. Sci. Eng. C* **2017**, *76*, 1305–1315.

(132) Gui, R.; Jin, H.; Wang, Z.; Tan, L. *Coord. Chem. Rev.* **2015**, *296* (April), 91–124.

(133) Zhang, Y.; Hong, G.; Zhang, Y.; Chen, G.; Li, F.; Dai, H.; Wang, Q. *ACS Nano* **2012**, *6* (5), 3695–3702.

(134) Zhang, X. S.; Xuan, Y.; Yang, X. Q.; Cheng, K.; Zhang, R. Y.; Li, C.; Tan, F.; Cao, Y.-C.; Song, X.-L.; An, J.; Hou, X.-L.; Zhao, Y.-D. *J. Nanobiotechnology* **2018**, *16*, 42.

(135) Yang, T.; Tang, Y.; Liu, L.; Lv, X.; Wang, Q.; Ke, H.; Deng, Y.; Yang, H.; Yang, X.; Liu,

G.; Zhao, Y.; Chen, H. *ACS Nano* **2017**, *11* (2), 1848–1857.

(136) Tan, L.; Wan, A.; Li, H. *ACS Appl. Mater. Interfaces* **2013**, *5* (21), 11163–11171.

(137) Zhu, C.-N.; Chen, G.; Tian, Z.-Q.; Wang, W.; Zhong, W.-Q.; Li, Z.; Zhang, Z.-L.; Pang, D.-W. *Small* **2017**, *13* (3), 1602309.

(138) Ma, J.; Yu, M.; Zhang, Z.; Cai, W.; Zhang, Z.; Zhu, H.; Cheng, Q.; Tian, Z.; Pang, D. *Nanoscale* **2018**, *10*, 10699–10704.

(139) Dong, B.; Li, C.; Chen, G.; Zhang, Y.; Zhang, Y.; Deng, M.; Wang, Q. *Chem. Mater.* **2013**, *25*, 2503–2509.

(140) Yang, M.; Gui, R.; Jin, H.; Wang, Z.; Zhang, F.; Xia, J.; Bi, S.; Xia, Y. *Colloids Surfaces B Biointerfaces* **2015**, *126*, 115–120.

(141) Jin, H.; Gui, R.; Sun, J.; Wang, Y. *Colloids Surfaces B Biointerfaces* **2016**, *143*, 118–123.

(142) Delgado-Beleño, Y.; Martinez-Nuñez, C. E.; Cortez-Valadez, M.; Flores-López, N. S.; Flores-Acosta, M. *Mater. Res. Bull.* **2018**, *99* (November 2017), 385–392.

(143) Neelgund, G. M.; Oki, A.; Luo, Z. *Colloids Surfaces B Biointerfaces* **2012**, *100*, 215–221.

(144) Gates, B. B.; Mayers, B.; Wu, Y.; Sun, Y.; Cattle, B.; Yang, P.; Xia, Y. *Adv. Funct. Mater.* **2002**, *12* (10), 679–686.

(145) Son, D. H.; Hughes, S. M.; Yin, Y.; Alivisatos, P. A. *Science (80-.).* **2004**, *306* (5698), 1009–1012.

(146) Sahu, A.; Qi, L.; Kang, M. S.; Deng, D.; Norris, D. J. *J. Am. Chem. Soc.* **2011**, *133* (17), 6509–6512.

(147) Sahu, A.; Khare, A.; Deng, D. D.; Norris, D. J. *Chem. Commun. (Camb).* **2012**, *48* (44), 5458–5460.

(148) Wang, J.; Fan, W.; Yang, J.; Da, Z.; Yang, X.; Chen, K.; Yu, H.; Cheng, X. *Chem. Mater.* **2014**, *26* (5647–5653).

(149) Sahu, A.; Braga, D.; Waser, O.; Kang, M. S.; Deng, D.; Norris, D. J. *Nano Lett.* **2014**, *14* (1), 115–121.

(150) Johan, Z.; Picot, P.; Pierrot, R.; Kvacek, M. *Bull. la Soc. française minéralogie Cristallogr.* **1971**, *94*, 381–384.

(151) Bindi, L.; Cipriani, C. *Can. Mineral.* **2004**, *42*, 1733–1737.

(152) Wiegers, G. A. *J. Less-Common Met.* **1976**, *48*, 269–283.

(153) Feng, D.; Taskinen, P. *J. Alloys Compd.* **2014**, *583*, 176–179.

(154) Faizan, M.; Murtaza, G.; Azam, S.; Khan, S. A.; Mahmood, A.; Yar, A. *Mater. Sci. Semicond. Process.* **2016**, *52*, 8–15.

(155) Fang, C. M.; De Groot, R. A.; Wiegers, G. A. *J. Phys. Chem. Solids* **2002**, *63*, 457–464.

(156) Smit, T. J. M.; Venema, E.; Wiersma, J.; Wiegers, G. A. *J. Solid State Chem.* **1970**, *2* (2), 309–312.

(157) Liu, M.; Zeng, H. C. *Langmuir* **2014**, *30*, 9838–9849.

(158) Haldar, K. K.; Pradhan, N.; Patra, A. *Small* **2013**, *9* (20), 3424–3432.

(159) Mokari, T.; Rothenberg, E.; Popov, I.; Costi, R.; Banin, U. *Science (80-.).* **2004**, *304*, 1787–1790.

(160) Figuerola, A.; van Huis, M.; Zanella, M.; Genovese, A.; Marras, S.; Falqui, A.; Zandbergen, H. W.; Cingolani, R.; Manna, L. *Nano Lett.* **2010**, *10* (8), 3028–3036.

(161) Liu, X.; Lee, C.; Law, W. C.; Zhu, D.; Liu, M.; Jeon, M.; Kim, J.; Prasad, P. N.; Kim, C.; Swihart, M. T. *Nano Lett.* **2013**, *13* (9), 4333–4339.

(162) Leff, D. V.; Brandt, L.; Heath, J. R. *Langmuir* **1996**, *12* (20), 4723–4730.

(163) Newman, J. D. S.; Blanchard, G. J. *Langmuir* **2006**, *22*, 5882–5887.

(164) Marchetti, B.; Joseph, Y.; Bertagnolli, H. *J. Nanoparticle Res.* **2011**, *13* (8), 3353–3362.

(165) Subramaniam, C.; Tom, R. T.; Pradeep, T. *J. Nanoparticle Res.* **2005**, *7* (2–3), 209–217.

(166) Yang, J.; Sargent, E. H.; Kelley, S. O.; Ying, J. Y. *Nat. Mater.* **2009**, *8* (8), 683–689.

(167) Klug, H. P.; Alexander, L. E. *X-Ray Diffraction Procedures for Polycrystalline and Amorphous Materials*, 2nd Ed.; John Willey & Sons, Inc.: New York, 1974.

(168) Cullity, B. D.; Stock, S. R. *Elements of X-Ray Diffraction*, 3rd Ed.; Prentice Hall Inc.: New York, 2001.

(169) Gu, Y. P.; Cui, R.; Zhang, Z. L.; Xie, Z. X.; Pang, D. W. *J. Am. Chem. Soc.* **2012**, *134* (1), 79–82.

(170) Yarema, M.; Pichler, S.; Sytnyk, M.; Seyrkammer, R.; Lechner, R. T.; Fritz-Popovski, G.; Jarzab, D.; Szendrei, K.; Resel, R.; Korovyanko, O.; Loi, M. A.; Paris, O.; Hesser, G.; Heiss, W. *ACS Nano* **2011**, *5* (5), 3758–3765.

(171) Zhu, C.-N.; Jiang, P.; Zhang, Z.-L.; Zhu, D.-L.; Tian, Z.-Q.; Pang, D.-W. *ACS Appl. Mater. Interfaces* **2013**, *5* (4), 1186–1189.

(172) Shi, L. J.; Zhu, C. N.; He, H.; Zhu, D. L.; Zhang, Z. L.; Pang, D. W.; Tian, Z. Q. *RSC*

Adv. **2016**, *6* (44), 38183–38186.

(173) Langevin, M. A.; Lachance-Quirion, D.; Ritcey, A. M.; Allen, C. N. *J. Phys. Chem. C* **2013**, *117* (10), 5424–5428.

(174) Seebeck, T. J. *Phys. Abhandlungen der Königlichen Akad. der Wissenschaften zu Berlin* **1825**, *265*, 1822–1823.

(175) Peltier, J. C. *Ann. Chim. Phys.* **1834**, *56* (371).

(176) Gayner, C.; Kar, K. K. *Prog. Mater. Sci.* **2016**, *83*, 330–382.

(177) Hamid Elsheikh, M.; Shnawah, D. A.; Sabri, M. F. M.; Said, S. B. M.; Haji Hassan, M.; Ali Bashir, M. B.; Mohamad, M. *Renew. Sustain. Energy Rev.* **2014**, *30*, 337–355.

(178) Yang, L.; Chen, Z.-G.; Dargusch, M. S.; Zou, J. *Adv. Energy Mater.* **2018**, *8* (6), 1701797.

(179) Tritt, T. M.; Subramanian, M. A. *MRS Bull.* **2006**, *31* (3), 188–198.

(180) Bell, L. E. *Science (80-.).* **2008**, *321* (5895), 1457–1461.

(181) Medlin, D. L.; Snyder, G. J. *Curr. Opin. Colloid Interface Sci.* **2009**, *14* (4), 226–235.

(182) Bux, S. K.; Fleurial, J.-P.; Kaner, R. B. *Chem. Commun.* **2010**, *46* (44), 8311–8324.

(183) Ortega, S.; Ibáñez, M.; Liu, Y.; Zhang, Y.; Kovalenko, M. V.; Cadavid, D.; Cabot, A. *Chem. Soc. Rev.* **2017**, *3510* (46), 3510–3528.

(184) Ding, D.; Lu, C.; Tang, Z. *Adv. Mater. Interfaces* **2017**, *4*, 1700517.

(185) Day, T.; Drymiotis, F.; Zhang, T.; Rhodes, D.; Shi, X.; Chen, L.; Snyder, G. J. *J. Mater. Chem. C* **2013**, *1*, 7568–7573.

(186) Aliev, F. F.; Jafarov, M. B.; Eminova, V. I. *Semiconductors* **2009**, *43* (8), 977–979.

(187) Mi, W.; Qiu, P.; Zhang, T.; Lv, Y.; Shi, X.; Chen, L. *Appl. Phys. Lett.* **2014**, *104* (13), 133903.

(188) Han, C.; Sun, Q.; Cheng, Z. X.; Wang, J. L.; Li, Z.; Lu, G. Q.; Dou, S. X. *J. Am. Chem. Soc.* **2014**, *136*, 17626–17633.

(189) Hong, A. J.; Li, L.; Zhu, H. X.; Zhou, X. H.; He, Q. Y.; Liu, W. S.; Yan, Z. B.; Liu, J. M.; Ren, Z. F. *Solid State Ionics* **2014**, *261*, 21–25.

(190) Liu, W.; Shi, X.; Moshwan, R.; Hong, M.; Yang, L.; Chen, Z. G.; Zou, J. *Sustain. Mater. Technol.* **2018**, *17*, e00076.

(191) Guin, S. N.; Chatterjee, A.; Negi, D. S.; Datta, R.; Biswas, K. *Energy Environ. Sci.*

2013, *6*, 2603–2608.

(192) Gao, W.; Wang, Z.; Huang, J.; Liu, Z. *ACS Appl. Mater. Interfaces* **2018**, *10* (22), 18685–18692.

(193) Liu, Y.; Cadavid, D.; Ibáñez, M.; De Roo, J.; Ortega, S.; Dobrozhan, O.; Kovalenko, M.; Cabot, A. *J. Mater. Chem. C* **2016**, *4* (21), 4756–4762.

(194) Guin, S. N.; Srihari, V.; Biswas, K. *J. Mater. Chem. A* **2015**, *3* (2), 648–655.

(195) Pan, L.; Bérardan, D.; Dragoe, N. *J. Am. Chem. Soc.* **2013**, *135* (13), 4914–4917.

(196) Goto, Y.; Nishida, A.; Nishiate, H.; Murata, M.; Lee, C. H.; Miura, A.; Moriyoshi, C.; Kuroiwa, Y.; Mizuguchi, Y. *Dalt. Trans.* **2018**, *47* (8), 2575–2580.

(197) Chen, K. X.; Li, M. S.; Mo, D. C.; Lyu, S. S. *Front. Energy* **2018**, *12* (1), 97–108.

(198) Pernia Leal, M.; Rivera-Fernández, S.; Franco, J. M.; Pozo, D.; De La Fuente, J. M.; García-Martín, M. L. *Nanoscale* **2015**, *7* (5), 2050–2059.

(199) Leal, M. P.; Muñoz-Hernández, C.; Berry, C. C.; García-Martín, M. L. *RSC Adv.* **2015**, *5* (94), 76883–76891.

(200) Sharma, R. C.; Chang, Y. A. *Bull. Alloy Phase Diagrams* **1986**, *7*, 263–269.

(201) Barton, M. D.; Kief, C. T.; Burke, E. A. J.; Oen, I. S. *Can. Mineral.* **1978**, *16*, 651–657.

(202) Osadchii, E. G.; Rappo, O. A. *Am. Mineral.* **2004**, *89* (10), 1405–1410.

(203) Gurevich, V. M.; Gavrichev, K. S.; Osadchii, E. G.; Tyurin, A. V.; Ryumin, M. A. *Geochemistry Int.* **2011**, *49* (4), 422–428.

(204) Mikhlin, Y. L.; Nasluzov, V. a.; Romanchenko, A. S.; Shor, A. M.; Pal'yanova, G. a. *J. Alloys Compd.* **2014**, *617* (July 2015), 314–321.

(205) Pal'yanova, G. A.; Savva, N. E. *Theor. Found. Chem. Eng.* **2008**, *42* (5), 749–761.

(206) Seryotkin, Y. V; Bakakin, V. V; Pal 'yanova, G. A.; Kokh, K. A. *Growth Des* **2011**, *11*, 1062–1066.

(207) Seryotkin, Y. V.; Bakakin, V. V.; Pal'yanova, G. A.; Kokh, K. A. *CrystEngComm* **2014**, *16* (9), 1675.

(208) Bindi, L.; Stanley, C.; Seryotkin, Y.; Bakakin, V.; Pal'yanova, G.; Kokh, K. *Mineral. Mag.* **2016**, *80* (6), 1031–1040.

(209) Huang, H.; Qu, C.; Liu, X.; Huang, S.; Xu, Z.; Liao, B.; Zeng, Y.; Chu, P. K. *ACS Appl. Mater. Interfaces* **2011**, *3* (2), 183–190.

(210) Li, X.; Schaak, R. E. *Chem. Mater.* **2017**, *29*, 4153–4160.

(211) Bao, Z.; Sun, Z.; Xiao, M.; Tian, L.; Wang, J. *Nanoscale* **2010**, *2* (9), 1650–1652.

(212) Qu, J.; Liu, H.; Wei, Y.; Wu, X.; Yue, R.; Chen, Y.; Yang, J. *J. Mater. Chem.* **2011**, *21* (32), 11750–11753.

(213) Yang, J.; Ying, J. Y. *Chem. Commun. (Camb).* **2009**, *1* (22), 3187–3189.

(214) Yang, J.; Ying, J. Y. *J. Am. Chem. Soc.* **2010**, *132*, 2114–2115.

(215) Sadovnikov, S. I.; Gusev, A. I. *J. Mater. Chem. A* **2017**, *5* (34), 17676–17704.

(216) Wang, M.; Wang, Y.; Tang, A.; Li, X.; Hou, Y.; Teng, F. *Mater. Lett.* **2012**, *88*, 108–111.

(217) Lim, W. P.; Zhang, Z.; Low, H. Y.; Chin, W. S. *Angew. Chem. Int. Ed. Engl.* **2004**, *43* (42), 5685–5689.

(218) Hou, X.; Zhang, X.; Yang, W.; Liu, Y.; Zhai, X. *Mater. Res. Bull.* **2012**, *47* (9), 2579–2583.

(219) Liu, H.; Hu, W.; Ye, F.; Ding, Y.; Yang, J. *RSC Adv.* **2012**, *3*, 616–622.

(220) Wang, J.; Feng, H.; Chen, K.; Fan, W.; Yang, Q. *Dalt. Trans.* **2014**, *43* (10), 3990–3998.

(221) Jang, K.; Kim, S. Y.; Park, K. H.; Jang, E.; Jun, S.; Son, S. U. *Chem. Commun. (Camb).* **2007**, *11* (3), 4474–4476.

(222) Ishikawa, K.; Isonaga, T.; Wakita, S.; Suzuki, Y. *Solid State Ionics* **1995**, *79* (C), 60–66.

(223) Suárez, J. A.; Plata, J. J.; Márquez, A. M.; Sanz, J. F. *Theor. Chem. Acc.* **2016**, *135*, 70.

(224) Averitt, R. D.; Sarkar, D.; Halas, N. J. *Phys. Rev. Lett.* **1997**, *78* (22), 4217–4220.

(225) Morris, T.; Copeland, H.; Szulczewski, G. *Langmuir* **2002**, *18*, 535–539.

(226) Kuo, C. L.; Huang, M. H. *J. Phys. Chem. C* **2008**, *112* (31), 11661–11666.

(227) Gadgil, B.; Damlin, P.; Viinikanoja, A.; Heinonen, M.; Kvarnström, C. *J. Mater. Chem. A* **2015**, *3* (18), 9731–9737.

(228) Gobin, A. M.; Watkins, E. M.; Quevedo, E.; Colvin, V. L.; West, J. L. *Small* **2010**, *6* (6), 745–752.

(229) Liu, Y.; Ma, Y.; Zhou, J.; Li, X.; Xie, S.; Tan, R. *J. Nanomater.* **2015**, *2015*, 530631.

(230) Hu, C.; Chen, W.; Xie, Y.; Verma, S. K.; Destro, P.; Zhan, G.; Chen, X.; Zhao, X.; Schuck, P. J.; Kriegel, I.; Manna, L. *Nanoscale* **2018**, *10* (6), 2781–2789.

(231) Wang, X.; Liu, X.; Zhu, D.; Swihart, M. T. *Nanoscale* **2014**, *6* (15), 8852–8857.

(232) Wolf, A.; Kodanek, T.; Dorfs, D. *Nanoscale* **2015**, *7* (46), 19519–19527.

(233) Smigelskas, A. D.; Kirkendall, E. O. *Trans. Am. Inst. Min. Metall. Eng.* **1947**, *171*, 130–142.

(234) Fan, H. J.; Gösele, U.; Zacharias, M. *Small* **2007**, *3* (10), 1660–1671.

(235) Wang, W.; Dahl, M.; Yin, Y. *Chem. Mater.* **2013**, *25* (8), 1179–1189.

(236) El Mel, A. A.; Nakamura, R.; Bittencourt, C. *Beilstein J. Nanotechnol.* **2015**, *6* (1), 1348–1361.

(237) Anderson, B. D.; Tracy, J. B. *Nanoscale* **2014**, *6* (21), 12195–12216.

(238) Lee, J.; Kim, S. M.; Lee, I. S. *Nano Today* **2014**, *9* (5), 631–667.

(239) Yu, L.; Hu, H.; Wu, H. Bin; Lou, X. W. D. *Adv. Mater.* **2017**, *29* (15), 1604563.

(240) An, K.; Hyeon, T. *Nano Today* **2009**, *4* (4), 359–373.

(241) Lou, X. W.; Archer, L. A.; Yang, Z. *Adv. Mater.* **2008**, *20* (21), 3987–4019.

(242) Yin, Y.; Rioux, R. M.; Erdonmez, C. K.; Hughes, S.; Somorjal, G. A.; Alivisatos, A. P. *Science (80-.).* **2004**, *304* (5671), 711–714.

(243) Cabot, A.; Puntes, V. F.; Shevchenko, E.; Yin, Y.; Balcells, L.; Marcus, M. A.; Hughes, S. M.; Alivisatos, A. P. *J. Am. Chem. Soc.* **2007**, *129* (34), 10358–10360.

(244) Railsback, J. G.; Johnston-Peck, A. C.; Wang, J.; Tracy, J. B. *ACS Nano* **2010**, *4*, 1913–1920.

(245) Ibáñez, M.; Fan, J.; Li, W.; Cadavid, D.; Nafria, R.; Carrete, A.; Cabot, A. *Chem. Mater.* **2011**, *23* (12), 3095–3104.

(246) Mu, L.; Wang, F.; Sadtler, B.; Loomis, R. A.; Buhro, W. E. *ACS Nano* **2015**, *9* (7), 7419–7428.

(247) Liu, Y.; Liu, M.; Swihart, M. T. *J. Am. Chem. Soc.* **2017**, *139*, 18598–18606.

(248) Jiang, P.; Tian, Z.-Q.; Zhu, C.-N.; Zhang, Z.-L.; Pang, D.-W. *Chem. Mater.* **2012**, *24*, 3–5.

(249) Liu, Y.; Purich, D. L.; Wu, C.; Wu, Y.; Chen, T.; Cui, C.; Zhang, L.; Cansiz, S.; Hou, W.; Wang, Y.; Yang, S.; Tan, W. *J. Am. Chem. Soc.* **2015**, *137* (47), 14952–14958.

(250) Wang, X.; Qiu, P.; Zhang, T.; Ren, D.; Wu, L.; Shi, X.; Yang, J.; Chen, L. *J. Mater. Chem. A* **2015**, *3* (26), 13662–13670.

(251) Qiu, P. F.; Wang, X. B.; Zhang, T. S.; Shi, X.; Chen, L. D. *J. Mater. Chem. A* **2015**, *3*

(44), 22454–22461.

(252) Guin, S. N.; Sanyal, D.; Biswas, K. *Chem. Sci.* **2016**, *7*, 534–543.

(253) Guin, S. N.; Pan, J.; Bhowmik, A.; Sanyal, D.; Waghmare, U. V.; Biswas, K. *J. Am. Chem. Soc.* **2014**, *136*, 12712–12720.

(254) Savory, C. N.; Ganose, A. M.; Travis, W.; Atri, R. S.; Palgrave, R. G.; Scanlon, D. O. *J. Mater. Chem. A* **2016**, *4*, 12648–12657.

(255) Roychowdhury, S.; Jana, M. K.; Pan, J.; Guin, S. N.; Sanyal, D.; Waghmare, U. V.; Biswas, K. *Angew. Chemie - Int. Ed.* **2018**, *57* (15), 4043–4047.

(256) Breithaupt, C. *B. Hüttenmänn Z.* **1858**, *17*, 85.

(257) Djurle, S. *Acta Chem. Scand.* **1958**, *12* (7), 1427–1436.

(258) Trots, D. M.; Senyshyn, A.; Mikhailova, D. a.; Vad, T.; Fuess, H. *J. Phys. Condens. Matter* **2008**, *20*, 455204.

(259) Baker, C. L.; Lincoln, F. J.; Johnson, A. W. S. *Aust. J. Chem.* **1992**, *45*, 1441–1449.

(260) Chen, Z.; Zhang, W.; Yang, Z. *J. Cryst. Growth* **2009**, *311* (12), 3347–3351.

(261) Xing, C.; Zhang, Y.; Wu, Z.; Jiang, D.; Chen, M. *Dalt. Trans.* **2014**, *43* (7), 2772–2780.

(262) Liu, Z.; Han, J.; Guo, K.; Zhang, X.; Hong, T. *Chem. Commun.* **2015**, *51* (13), 2597–2600.

(263) Djurle, S. *Acta Chem. Scand.* **1958**, *12* (7), 1427–1436.

(264) Santamaria-Perez, D.; Morales-Garcia, A.; Martinez-Garcia, D.; Garcia-Domene, B.; Mühle, C.; Jansen, M. *Inorg. Chem.* **2013**, *52* (1), 355–361.

(265) Dutta, M.; Sanyal, D.; Biswas, K. *Inorg. Chem.* **2018**.

(266) Wang, Y.; Li, X.; Xu, M.; Wang, K.; Zhu, H.; Zhao, W.; Yan, J.; Zhang, Z. *Nanoscale* **2018**, *10* (5), 2577–2587.

(267) Wolf, A.; Kodanek, T.; Dorfs, D. *Nanoscale* **2015**, *7*, 19519–19527.

(268) Hu, J. Q.; Deng, B.; Zhang, W. X.; Tang, K. B.; Qian, Y. T. *Int. J. Inorg. Mater.* **2001**, *3*, 639–642.

(269) Skinner, B. *Econ. Geol.* **1966**, *61* (8), 1383–1389.

(270) Kolitsch, U. *Mineral. Mag.* **2010**, *74* (1), 73–84.

(271) Goble, R. J. *Can. Mineral.* **1985**, *23* (1), 61–76.

(272) Zhao, Y.; Pan, H.; Lou, Y.; Qiu, X.; Zhu, J.; Burda, C. *J. Am. Chem. Soc.* **2009**, *131* (I), 4253–4261.

(273) Liu, X.; Swihart, M. T. *Chem. Soc. Rev.* **2014**, *43* (11), 3908–3920.

(274) Comin, A.; Manna, L. *Chem. Soc. Rev.* **2014**, *43* (11), 3957–3975.

(275) Agrawal, A.; Johns, R. W.; Milliron, D. *Annu. Rev. Mater. Res.* **2017**, *47*, 1–31.

(276) Agrawal, A.; Cho, S. H.; Zandi, O.; Ghosh, S.; Johns, R. W.; Milliron, D. J. *Chem. Rev.* **2018**, *118* (6), 3121–3207.

(277) Niezgoda, J. S.; Rosenthal, S. J. *ChemPhysChem* **2016**, *17* (5), 645–653.

(278) Kriegel, I.; Scotognella, F.; Manna, L. *Phys. Rep.* **2017**, *674*, 1–52.

(279) Luther, J. M.; Jain, P. K.; Ewers, T.; Alivisatos, a P. *Nat. Mater.* **2011**, *10* (5), 361–366.

(280) Liu, X.; Wang, X.; Swihart, M. T. *Chem. Mater.* **2013**, *25* (21), 4402–4408.

(281) Dorfs, D.; Härtling, T.; Miszta, K.; Bigall, N. C.; Kim, M. R.; Genovese, A.; Falqui, A.; Povia, M.; Manna, L. *J. Am. Chem. Soc.* **2011**, *133* (29), 11175–11180.

(282) Li, W.; Zamani, R.; Rivera Gil, P.; Pelaz, B.; Ibáñez, M.; Cadavid, D.; Shavel, A.; Alvarez-Puebla, R. A.; Parak, W. J.; Arbiol, J.; Cabot, A. *J. Am. Chem. Soc.* **2013**, *135* (19), 7098–7101.

(283) Kriegel, I.; Jiang, C.; Rodríguez-Fernández, J.; Schaller, R. D.; Talapin, D. V; da Como, E.; Feldmann, J. *J. Am. Chem. Soc.* **2012**, *134* (3), 1583–1590.

(284) Song, G.; Shen, J.; Jiang, F.; Hu, R.; Li, W.; An, L.; Zou, R.; Chen, Z.; Qin, Z.; Hu, J. *ACS Appl. Mater. Interfaces* **2014**, *6* (6), 3915–3922.

(285) Manthiram, K.; Alivisatos, A. P. *J. Am. Chem. Soc.* **2012**, *134* (9), 3995–3998.

(286) Lee, S. H.; Nishi, H.; Tatsuma, T. *Chem. Commun.* **2017**, *53* (94), 12680–12683.

(287) Zhou, J.; Wang, Y.; Zhang, L.; Li, X. *Chinese Chem. Lett.* **2018**, *29* (1), 54–60.

(288) Balitskii, O. A.; Sytnyk, M.; Stangl, J.; Primetzhofer, D.; Groiss, H.; Heiss, W. *ACS Appl. Mater. Interfaces* **2014**, *6* (20), 17770–17775.

(289) Zou, Y.; Sun, C.; Gong, W.; Yang, X.; Huang, X.; Yang, T.; Lu, W.; Jiang, J. *ACS Nano* **2017**, *11* (4), 3776–3785.

(290) Maddinedi, S. B. *Environ. Toxicol. Pharmacol.* **2017**, *53* (January), 29–33.

(291) Wolf, A.; Hinrichs, D.; Sann, J.; Miethe, J. F.; Bigall, N. C.; Dorfs, D. *J. Phys. Chem. C* **2016**, *120*, 21925–21931.

(292) Fenton, J. L.; Hodges, J. M.; Schaak, R. E. *Chem. Mater.* **2017**, *29* (14), 6168–6177.

(293) Kim, J.; Piao, Y.; Hyeon, T. *Chem. Soc. Rev.* **2009**, *38* (2), 372–390.

(294) Banin, U.; Ben-Shahar, Y.; Vinokurov, K. *Chem. Mater.* **2014**, *26*, 97–110.

(295) Sánchez, C.; Belleville, P.; Popall, M.; Nicole, L. *Chem. Soc. Rev.* **2011**, *40*, 696–753.

(296) Sanchez, C.; Arribart, H.; Guille, M. M. G. *Nat. Mater.* **2005**, *4* (4), 277–288.

(297) Nicole, L.; Laberty-Robert, C.; Rozes, L.; Sanchez, C. *Nanoscale* **2014**, *6* (12), 6267–6292.

(298) Judeinstein, P.; Sanchez, C. *J. Mater. Chem.* **1996**, *6* (4), 511–525.

(299) Meek, S. T.; Greathouse, J. a; Allendorf, M. D. *Adv. Mater.* **2011**, *23* (2), 249–267.

(300) Allendorf, M. D.; Bauer, C. A.; Bhakta, R. K.; Houk, R. J. T. *Chem. Soc. Rev.* **2009**, *38* (5), 1330–1352.

(301) Carné, A.; Carbonell, C.; Imaz, I.; Maspoch, D. *Chem. Soc. Rev.* **2011**, *40* (1), 291–305.

(302) Li, J. R.; Kuppler, R. J.; Zhou, H. C. *Chem. Soc. Rev.* **2009**, *38* (5), 1477–1504.

(303) Yuan, S.; Feng, L.; Wang, K.; Pang, J.; Bosch, M.; Lollar, C.; Sun, Y.; Qin, J.; Yang, X.; Zhang, P.; Wang, Q.; Zou, L.; Zhang, Y.; Zhang, L.; Fang, Y.; Li, J.; Zhou, H. C. *Adv. Mater.* **2018**, 1704303.

(304) Zhang, H.; Liu, X.; Wu, Y.; Guan, C.; Cheetham, A. K.; Wang, J. *Chem. Commun.* **2018**, *54* (42), 5268–5288.

(305) Lee, J.; Farha, O. K.; Roberts, J.; Scheidt, K. A.; Nguyen, S. T.; Hupp, J. T. *Chem. Soc. Rev.* **2009**, *38* (5), 1450–1459.

(306) Sanchez, C.; Julián, B.; Belleville, P.; Popall, M. *J. Mater. Chem.* **2005**, *15*, 3559–3592.

(307) Parola, S.; Julián-López, B.; Carlos, L. D.; Sanchez, C. *Adv. Funct. Mater.* **2016**, *26* (36), 6506–6544.

(308) Vivero-Escoto, J. L.; Huang, Y.-T. *Int. J. Mol. Sci.* **2011**, *12* (12), 3888–3927.

(309) Divya, K. P.; Miroshnikov, M.; Dutta, D.; Vemula, P. K.; Ajayan, P. M.; John, G. *Acc. Chem. Res.* **2016**, *49* (9), 1671–1680.

(310) Mallia, V. A.; Vemula, P. K.; John, G.; Kumar, A.; Ajayan, P. M. *Angew. Chemie - Int. Ed.* **2007**, *46* (18), 3269–3274.

(311) Jyothish, K.; Vemula, P. K.; Jadhav, S. R.; Francesconi, L. C.; John, G. *Chem. Commun.* **2009**, *7345* (36), 5368–5370.

(312) Prakash, J.; Pivin, J. C.; Swart, H. C. *Adv. Colloid Interface Sci.* **2015**, *226*, 187–202.

(313) Nie, G.; Li, G.; Wang, L.; Zhang, X. *Polym. Chem.* **2016**, *7* (4), 753–769.

(314) Kumar, A.; Vemula, P. K.; Ajayan, P. M.; John, G. *Nat. Mater.* **2008**, *7* (3), 236–241.

(315) Jang, Y. H.; Jang, Y. J.; Kim, S.; Quan, L. N.; Chung, K.; Kim, D. H. *Chem. Rev.* **2016**, *116* (24), 14982–15034.

(316) Ye, W.; Long, R.; Huang, H.; Xiong, Y. *J. Mater. Chem. C* **2017**, *5* (5), 1008–1021.

(317) Enrichi, F.; Quandt, A.; Righini, G. C. *Renew. Sustain. Energy Rev.* **2018**, *82*, 2433–2439.

(318) Rodríguez, L.; Lima, J. C. *Inorganics* **2015**, *3*, 1–18.

(319) Schmidbaur, H.; Schier, A. *Chem. Soc. Rev. Chem. Soc. Rev* **2012**, *41*, 370–412.

(320) Kishimura, A.; Yamashita, T.; Aida, T. *J. Am. Chem. Soc.* **2005**, *127*, 179–183.

(321) Aguiló, E.; Gavara, R.; Lima, J. C.; Llorca, J.; Rodríguez, L. *J. Mater. Chem. C* **2013**, *1* (35), 5538–5547.

(322) Katz, M. J.; Sakai, K.; Leznoff, D. B. *Chem. Soc. Rev.* **2008**, *37* (9), 1884–1895.

(323) Johnson, A. L.; Willcocks, A. M.; Richards, S. P. *Inorg. Chem.* **2009**, *48* (17), 8613–8622.

(324) Gavara, R.; Llorca, J.; Lima, J. C.; Rodríguez, L. *Chem. Commun. Chem. Commun* **2013**, *49* (49), 72–74.

(325) Strassert, C. A.; Chien, C. H.; Galvez Lopez, M. D.; Kourkoulos, D.; Hertel, D.; Meerholz, K.; De Cola, L. *Angew. Chemie - Int. Ed.* **2011**, *50*, 946–950.

(326) Aguiló, E.; Gavara, R.; Lima, J. C.; Llorca, J.; Rodríguez, L. *J. Mater. Chem. C* **2013**, *1*, 5538–5547.

(327) Fleischmann, M.; Hendra, P. J.; McQuillan, A. J. *Chem. Phys. Lett.* **1974**, *26* (2), 163–166.

(328) Jeanmaire, D. L.; Van Duyne, R. P. *J. Electroanal. Chem.* **1977**, *84*, 1–20.

(329) Nie, S.; Emory, S. R. *Science (80-.).* **1997**, *275* (5303), 1102–1106.

(330) Kneipp, K.; Wang, Y.; Kneipp, H.; Perelman, L. T.; Itzkan, I.; Dasari, R. R.; Feld, M. S. *Phys. Rev. Lett.* **1997**, *78* (9), 1667–1670.

(331) Stiles, P. L.; Dieringer, J. A.; Shah, N. C.; Van Duyne, R. P. *Annu. Rev. Anal. Chem.* **2008**, *1* (1), 601–626.

(332) Sharma, B.; Frontiera, R. R.; Henry, A. I.; Ringe, E.; Van Duyne, R. P. *Mater. Today* **2012**, *15* (1–2), 16–25.

(333) Kneipp, J.; Kneipp, H.; Kneipp, K. *Chem. Soc. Rev.* **2008**, *37* (5), 1052–1060.

(334) Schlücker, S. *Angew. Chemie - Int. Ed.* **2014**, *53*, 4756–4795.

(335) McNay, G.; Eustace, D.; Smith, W. E.; Faulds, K.; Graham, D. *Appl. Spectrosc.* **2011**, *65* (8), 825–837.

(336) Campion, A.; Kambhampati, P. *Chem. Soc. Rev.* **1998**, *27*, 241–250.

(337) Moskovits, M. *J. Raman Spectrosc.* **2005**, *36* (6–7), 485–496.

(338) Le Ru, E. C.; Blackie, E.; Meyer, M.; Etchegoint, P. G. *J. Phys. Chem. C* **2007**, *111* (37), 13794–13803.

(339) Álvarez-Puebla, R. A. *J. Phys. Chem. Lett.* **2012**, *3* (7), 857–866.

(340) Shen, C.; Hui, C.; Yang, T.; Xiao, C.; Tian, J.; Bao, L.; Chen, S.; Ding, H.; Gao, H. *Chem. Mater.* **2008**, *20*, 6939–6944.

(341) Park, J.; An, K.; Hwang, Y.; Park, J.-G.; Noh, H.-J.; Kim, J.-Y.; Park, J.-H.; Hwang, N.-M.; Hyeon, T. *Nat. Mater.* **2004**, *3* (December), 891–895.

(342) Carbone, L.; Nobile, C.; De Giorgi, M.; Della Sala, F.; Morello, G.; Pompa, P.; Hytch, M.; Snoeck, E.; Fiore, A.; Franchini, I. R.; Nadasan, M.; Silvestre, A. F.; Chiodo, L.; Kudera, S.; Cingolani, R.; Krahne, R.; Manna, L. *Nano Lett.* **2007**, *7*, 2942–2950.

(343) Malyutin, A. G.; Easterday, R.; Lozovyy, Y.; Spilotros, A.; Cheng, H.; Sanchez-Felix, O. R.; Stein, B. D.; Morgan, D. G.; Svergun, D. I.; Dragnea, B.; Bronstein, L. M. *Chem. Mater.* **2015**, *27*, 327–335.


平和